**Carlos Alberto
Ferreira Marques**

**Componentes em Fibra Ótica para Comunicações
Óticas e Sensores**

**Fiber-Optic Components for Optical
Communications and Sensing**

Carlos Alberto Ferreira Marques

Componentes em Fibra Ótica para Comunicações Óticas e Sensores

Fiber-Optic Components for Optical Communications and Sensing

Dissertação apresentada à Universidade de Aveiro para cumprimento dos requisitos necessários à obtenção do grau de Doutor em Engenharia Física, realizada sob a orientação científica do Professor Doutor Rogério Nunes Nogueira, Investigador Principal do Instituto de Telecomunicações.

o júri / the jury

presidente / president
        Prof. Doutor Amadeu Mortágua Velho da Maia Soares
        Professor Catedrático da Universidade de Aveiro

vogais / examiners committee
        Prof. Doutor João de Lemos Pinto
        Professor Catedrático da Universidade de Aveiro

        Prof. Doutor Paulo Mateus Mendes
        Professor Associado da Escola de Engenharia da Universidade do Minho

        Prof. Doutor Orlando José dos Reis Frazão
        Professor Auxiliar Convidado da Faculdade de Ciências da Universidade do Porto

        Prof. Doutor Rogério Nunes Nogueira
        Investigador Principal do Instituto de Telecomunicações, pólo de Aveiro

palavras-chave	Redes de Bragg em fibra ótica, redes de período longo, comunicações óticas, sensores óticos, efeito ótico-acústico, filtros óticos, redes de Bragg regeneradas.

resumo	Nos últimos anos, a Optoelectrónica tem sido estabelecida como um campo de investigação capaz de conduzir a novas soluções tecnológicas. As conquistas abundantes no campo da óptica e lasers, bem como em comunicações ópticas têm sido de grande importância e desencadearam uma série de inovações. Entre o grande número de componentes ópticos existentes, os componentes baseados em fibra óptica são principalmente relevantes devido à sua simplicidade e à elevada de transporte de dados da fibra óptica.

Neste trabalho foi focado um destes componentes ópticos: as redes de difracção em fibra óptica, as quais têm propriedades ópticas de processamento únicas. Esta classe de componentes ópticos é extremamente atraente para o desenvolvimento de dispositivos de comunicações ópticas e sensores.

O trabalho começou com uma análise teórica aplicada a redes em fibra e foram focados os métodos de fabricação de redes em fibra mais utilizados.

A inscrição de redes em fibra também foi abordado neste trabalho, onde um sistema de inscrição automatizada foi implementada para a fibra óptica de sílica, e os resultados experimentais mostraram uma boa aproximação ao estudo de simulação. Também foi desenvolvido um sistema de inscrição de redes de Bragg em fibra óptica de plástico.

Foi apresentado um estudo detalhado da modulação acústico-óptica em redes em fibra óptica de sílica e de plástico. Por meio de uma análise detalhada dos modos de excitação mecânica aplicadas ao modulador acústico-óptico, destacou-se que dois modos predominantes de excitação acústica pode ser estabelecidos na fibra óptica, dependendo da frequência acústica aplicada. Através dessa caracterização, foi possível desenvolver novas aplicações para comunicações ópticas.

Estudos e implementação de diferentes dispositivos baseados em redes em fibra foram realizados, usando o efeito acústico-óptico e o processo de regeneração em fibra óptica para várias aplicações tais como rápido multiplexador óptico add-drop, atraso de grupo sintonizável de redes de Bragg, redes de Bragg com descolamento de fase sintonizáveis, método para a inscrição de redes de Bragg com perfis complexos, filtro sintonizável para equalização de ganho e filtros ópticos notch ajustáveis.

keywords

Fiber Bragg gratings, long period grating, optical communications, optical sensors, acousto-optic effect, optical filtering, regenerated fiber Bragg gratings.

abstract

In the last years, the Optoelectronics has been established as a top field of research able to drive towards new technological solutions. The abundant achievements in the field of optics as well in optical communications have been of great importance and triggered a number of innovations. Among the large group of existing optical components, optical fiber components are mainly relevant due to three factors: their simplicity, their nature as an optical fiber based component and the capability of optical fiber to carry information.

In this thesis the focus was on one of these optical components: optical fiber gratings, which have unique optical processing properties and are quite interesting for the development of devices for optical communications and sensing applications.

The work started with a theoretical analysis applied to fiber gratings and continues with the most used fiber gratings production methods.

The inscription of fiber gratings was also addressed in this work, where an automated inscription setup has been implemented for silica fiber, and experimental results showed a good approximation to the simulation study. Also, the inscription setup for gratings in polymer optical fiber was developed.

A detailed analysis of the acousto-optic modulation in fiber gratings in silica and polymer optical fiber was presented. By means of a detailed analysis of the mechanical excitation modes applied to the modulator set, it was noticed that two predominant modes of acoustic excitation can be found in the optical fiber depending on the applied acoustic frequency. Through this characterization, it was possible to develop new applications.

Studies and implementation of different devices based on fiber gratings were performed, using acousto-optic effect and regeneration process in optical fiber for photonic applications such as fast add-drop multiplexer, tunability of the fiber Bragg grating group delay, tunable phase-shift fiber Bragg grating, tunable mode coupler, method for inscription of complex fiber Bragg grating profiles, gain equalization filter and adjustable notch filters.

"São conhecimentos que fazem despertar os seres humanos, para saberem raciocinar e terem a certeza de que estão no caminho certo"

António Cottas

Aos meus pais e irmãos,
À Vera e Matilde.

Contents

List of Acronyms

ADM	*Add-Drop Multiplexer*
AMM	*Assumed Modes Method*
AO	*Acousto-Optic*
AO-ADM	*Acousto-Optic Add-Drop Multiplexer*
AOM	*Acousto-Optic Modulator*
AOSLM	*Acousto-Optic Superlattice Modulator*
ASE	*Amplified Spontaneous Emission*
AW	*Acoustic Wave*
AWG	*Arrayed Waveguide Gratings*
BER	*Bit Error Ratio*
BG-AOM	*Bragg Grating Acousto-Optic Modulator*
CCG	*Chemical Composition Grating*
CD	*Chromatic Dispersion*
CMOS	*Complementary Metal-Oxide-Semiconductor*
CW	*Continuous Wave*

DBR	Distributed Bragg Reflector
DWDM	Dense Wavelength Division Multiplexing
EDFA	Erbium Doped Fiber Amplifier
FBG	Fiber Bragg Grating
FC/APC	Ferrule Connector / Angled Physical Contact
FC/PC	Ferrule Connector / Physical Contact
FEM	Finite Element Method
FLM	Fiber-Loop Mirror
FWHM	Full Width at Half Maximum
GOSiP	Gratings Optical SImulation Platform
GDR	Group Delay Ripple
H_2	Hidrogen
He-Ne	Helium-Neon
HiBi	High birefringent
ITU	International Telecommunication Union
KrF	Krypton Fluoride
LBP	Laser Beam Profile
LP	Linear Polarized
LPG	Long Period Grating
LPG-AOM	Long Period Grating-Acousto-Optic Modulation
MM	Multi Mode
mPOF	microstructured Polymer Optical Fiber

mPOFBG-AOM	microstructured Polymer Fiber Bragg Grating- Acousto-Optic Modulation
MZ	Mach-Zehnder
NA	Numerical Aperture
NIR	Near-Infrared
NRZ	Non-Return to Zero
OCDMA	Optical Code Division Multiple Access
ONA	Optical Network Analyzer
OSA	Optical Spectrum Analyzer
OSNR	Optical Signal-to-Noise Ratio
PC	Polarization Controller
PANDA	Polarization-maintaining AND Attenuation-reducing
PCF	Photonic Crystal Fiber
PMMA	Poly(Methyl MethAcrylate)
POF	Polymer Optical Fiber
PFBG	Bragg Grating inscribed in Polymer Optical Fiber
PSFBG	Phase-Shifted Fiber Bragg Grating
PZT	Piezoelectric Transducer
RF	Radio Frequency
RFBG	Regenerated Fiber Bragg Grating
SF	Silica Fiber
SFBG	Silica Fiber Bragg Grating
SiO_2	Silica

SM   *Single Mode*

SMF   *Single Mode Fiber*

SPF-MMOW   *Side-Polished Fiber-Multimode Overlay Waveguide*

SSMF   *Standard Single Mode Fiber*

TEC   *Thermoelectric Cooler*

TFG   *Tilted Fiber Grating*

TMM   *Transfer Matrix Method*

TOF   *Tapered Optical Fiber*

UV   *Ultra Violet*

VI   *Virtual Instrument*

VIS   *Visivel*

VOA   *Variable Optical Attenuator*

WDM   *Wavelength Division Multiplexing*

List of Symbols

A	Acoustic beam area
$A(z)$	Amplitude of the forward propagating mode
A_{eff}	Effective transversal area
$A_n(z)$	Slowly varying amplitude of the nth mode travelling in the +z direction
$A_s(z)$	Variable size of the structure along the z-axis.
A_t	Transversal area
a	Fiber radius
a_{core}	Fiber core radius
a_m	Maximum value between distance phase mask / fiber
$B(z)$	Amplitude of the co-propagating mode
$B_n(z)$	Slowly varying amplitude of the nth mode travelling in the -z direction
b	Number of holes
C	Grating modulation depth
c	Speed of light in vacuum
c_{ext}	Speed of extensional mechanical waves in the material

$c_{PM\text{-}fiber}$	Distance of the phase mask /optical fiber
D	Dispersion coefficient
D_{jn}^{t}	Transverse coupling coefficient between j and n modes
D_{jn}^{z}	Longitudinal coupling coefficient between j and n modes
d	Distance between FBGs
d_f	Taper diameter
d_h	Hole diameter
d_{PZT}	PZT diameter
d_{sh}	Silica horn base diameter
d_{sht}	Silica horn tip diameter
d_p	Distance of the fiber to the normal of the boundary of the overlap region
D_w	Writing beam diameter
e	Local node
E	Young's modulus
E_a	total accumulated energy
E_{pulse}	Average energy per UV pulse
E^{T}	Transverse component of the electric field (Couple-Mode Theory)
$e_{n}^{T}(x,y)$	Transverse mode field
f	Acoustic frequency
F	Slit aperture
f_c	Cylindrical lens distance focal
F_{laser}	Laser frequency

F_V	Field of view
J_n	Bessel function coefficients
$\boldsymbol{K}$	Stiffness matrix
K	"ac" coupling coefficient
k_{AO}	Acousto-optic coupling coefficient
k_s	Acoustic wave vector
k_{jn}	"ac" coupling coefficient between j and n modes
l	Defect position
L	Length of a fiber grating
L_b	Intermodal beat length
l_b	Cavity length
L_{exp}	Exact length that the grating is written
L_i	Interaction length
LP_{0m}	Cladding modes
l_{pm}	Phase mask length
l_{sh}	Silica horn length
L_{TOF}	Tapered optical fiber length
$\boldsymbol{M}$	Mass matrix
M	Diffraction order
M_i	Uniform section
M_{lens}	Lens magnification
M_{SF}	Maximum camera sensor format

N	Number of grating planes
n	Refractive index
n_1	Refractive index of the incident wave
n_2	Refractive index of the diffracted wave
$n_{cladding}$	Refractive index of the cladding
n_{core}	Refractive index of the core
n_{eff}	Effective refractive index
$n_{eff,1}$	Effective refractive index of the incident wave medium
$n_{eff,2}$	Effective refractive index of the diffracted wave medium
n_{ex}	External refractive index
n_{pulses}	Total number of pulses
n_{core}^{eff}	Effective index of the core mode
$n_{cladding,m}^{eff}$	Effective indices of the mth cladding mode
p	Acoustic wave propagation phase
P_{ASE}	Pump Power
$P(t)$	External excitation
$\boldsymbol{P_0}$	Nodal force of the first component
P_c	Power of a reflected optical channel
p_e	Photo-elastic coefficient (also called as stress-optical coefficient)
p_{ij}	Components of the strain optic tensor
P_s	Acoustic power
P_{s-o}	Strain-optic coefficient

P_φ		Position of the value of φ on the FBG
q		Generalized coordinates vector
r		Power reflection coefficient
R		Reflectivity
r_{max}		Maximum reflectivity
s		LPG sensitivities to the external media refractive indices
$t_=$		Bar transmission
t_b		Time between bursts
T_{bt}		Burst time
t_{exp}		Exposure time
t_{GDR}		Group delay ripple coefficient
T^m		Minimum transmission of LPG
t_{PZT}		PZT thick
t_s		Switching time
t_{st}		Time to change the spectrum
t_x		Cross transmission
$t_{x,max}$		Maximum cross transmission
u		Axial displacement
$\mathbf{u}$		Nodal displacement vector
$\ddot{\mathbf{u}}$		Nodal acceleration vector
$\mathbf{u_0}$		Displacement vector solution
u_∞		mth root of the Bessel function

u_f	Transverse acoustic wave amplitude
v	Grating visibility
v_F	Velocity which the fiber is moved
v_f	Speed of flexural wave
v_{PM}	Velocity which the phase mask is moved
V_{PZT}	PZT load
v_{sc}	Scanning beam velocity
$v(z)$	Fringe visibility of the index change
α_{neff}	Thermo-optic coefficient
$\alpha_{neff,m}$	Thermal-optic coefficient (LPG)
α_Λ	Thermal expansion coefficient
β	Mode propagation constant
β_1	Propagation constant of the incident wave
β_2	Propagation constant of the diffracted wave
Δn	Amplitude modulation of the refractive index
$\triangle z_0$	Separation between two grating sections
$\triangle z$	Length of the ith uniform section
$\Delta\varepsilon(x,y,z)$	Permittivity perturbation constant
$\Delta\beta$	Phase mismatch factor
$\Delta\beta_{AO}$	Phase difference (Acousto-Optic)
$\Delta\Theta$	Change in temperature
$\Delta\lambda$	Wavelength difference

$\Delta\lambda_0$	Measurable bandwidth between the first zeros of a uniform grating
$\Delta\varphi$	Phase shift
ΔP	Peak-to-peak power variation
δ	Detuning
δn	Effective refractive index variation
δn_0	"dc" index change
$\delta n_{eff}(z)$	Induced perturbation on the effective refractive index along z
$\delta\lambda_0$	Dip wavelength shift
δn_{core}	Photo-induced index change in the core
$\overline{\delta n_{core}}$	Variation in the average refractive index value of the fiber core
$\overline{\delta n_{eff}}$	"dc" index change spatially averaged over a grating period
ε	Longitudinal strain field
η	Fraction of light coupled from mode 1 to 2 after the interaction length
Θ	Mutual angle of the UV beams
Θ_w	Angle between diffracted wave and the normal incidence
Θ_1	Angle of the incident wave
Θ_2	Angle of the diffracted wave
Θ_i	Angle of the incident UV beam of prism wavefront-splitting interferometer
Θ_m	Angle of the diffracted order of prism wavefront-splitting interferometer
Θ_{PM}	Tilt angle of the phase mask
Θ_{TFG}	Tilt angle
κ_m	Coupling coefficient for the mth cladding mode

Λ	Grating period
Λ_0	Period to the grating input
Λ_h	Pitch (holes)
Λ_{pm}	Phase mask period
$\Lambda_{sampled}$	Sampled period
Λ_{static}	Grating period in a static situation
Λ_{TFG}	Tilted FBG period
λ	Wavelength
$\lambda_{acoustic}$	Acoustic wavelength
λ_B	Bragg wavelength
λ_{BS}	FBG switched wavelength generated by acoustic wave
λ_c	Wavelength in vacuum
$\lambda_{central}$	Central wavelength
λ_D	Design wavelength
λ_m	Dip wavelength
λ_{max}	Maximum wavelength in a grating
λ_{res}	Resonant wavelength
λ_s	Flexural acoustic wavelength
λ_{UV}	Wavelength of the writing radiation
ρ	Reflectivity
ρ_D	Density
ρ_{eff}	Effective density

σ	Poisson's ratio
τ	Group delay
τ_{max}	Maximum group delay
τ_s	Specific group delay
τ_{sta}	Stabilization time
υ_{gs}	Acoustic group velocity
ϕ	Phase(or phase shift value for PSFBG)
ϕ_i	Shift in the phase of the grating
$\phi(z)$	Grating chirp (FBG)
$\varphi(z)$	Trial or assumed modes function
$\phi(z')$	Grating chirp (TFG)
ϕ_a	Accumulated phase
ω	Optical frequency
ω_s	Angular frequency
ψ_{jn}	"dc" coupling coefficient between j and n modes
ψ'	General "dc" self-coupling coefficient
$\{f(t)\}$	Generalized excitation vector

Chapter 1

Introduction

Fiber optics have been developed in such an extent that over the last decades, the use of optical fibers has revolutionized the way the world exchanges and processes information [Bates2001]. Dramatic advances in optical fiber technology have led to the boost of the Internet and the demand for higher bandwidth applications providing high-speed communications that impacts all facets of modern life. Due to the advantages of non-electromagnetic interference, light weight, flexibility, low-loss and high temperature tolerance, optical fibers not only have developed and commercialized in optical communications but also boosted the fast growing technology of sensing and metrology.

1.1. Motivation and Outline

In 2009, Prof. Charles K. Kao was awarded half of Novel Prize in Physics for the groundbreaking achievements concerning the transmission of light in optical fiber for communication. Optical fiber has been regarded as one of the most important inventions of the last decades and has revolutionized telecommunication since it was developed. The development of the optical fiber technology allowed scientists to develop long haul telecommunications links [Makovejs2010, Millar2011] as well as construct different all-fiber devices [Ortega1999, Saval2005, Drummond2011]. Many of these devices were built particularly for data transfer applications, using the technology of the wavelength division multiplexing (WDM). Actually, the success of the Internet is based on the tremendous fast data transmission over the use of optical fiber [Zhao2012]. Optical fiber has a great deal of advantages, including small size and weight, low

transmission loss, enormous bandwidth, immunity to cross talk, electrical isolation, signal security, ruggedness and flexibility, low cost, and reliability. The many unique features of optical fibers lead to the fact that they are not restricted to telecommunications and their application extends to many other areas, including laser [Liaw2007,Wang2010], sensing [Zhu2008, Miao2009] and medical sciences [Mohanty2007, Mishra2011], which are some of the fields that optical fiber has revolutionized.

The possibility of writing diffraction gratings (short period gratings known as fiber Bragg gratings (FBGs) and long period gratings (LPGs)) in optical fiber opened a vast field of research. It has been considered by many scientists as one of the most active fields in optics. This field of FBGs has more thirty years old, dating back to its discovery by Hill and co-workers in Canada [Hill1978]. It grew slowly in the beginning but an important technological breakthrough by Meltz and co-workers 10 years later [Meltz1988, Meltz1989] renewed worldwide interest in FBGs. Thenceforth, fiber grating technology has been recognized as key technology in a variety of applications [Erdogan1997a, Erdogan1997b, Othonnos1997]. Their unique properties and versatility as in-fiber device is illustrated by their use in optical communication systems, microwave photonic systems and fiber sensors.

These optical components will be discussed throughout this thesis, covering theoretical background and their fabrication for several applications. Many times can be associated different mechanisms that can be used to change and control several of the properties of gratings in optical fibers. Accordingly, the study of the interaction between sound and light arises as a sustainable mechanism for increasing this approach. This interaction, known as acousto-optic effect, is the key to construct several all-fiber photonic devices, such as frequency shifters [Kim1986], tapers and couplers [Birks1996, Fernandes2012], filters [Feced1999, Diez2003], lasers [Delgado2006], among others [Barmenkov2010, Oliveira2010a, Oliveira2010b]. Another mechanism for this approach is the use of the regeneration phenomenon in fiber gratings. Lately, this phenomenon is attracting the interest of several areas, such as sensors technology [Lindner2009, Valmir2011, Chen2011], fiber laser sector [Aslund2010, Canning2013], oil/gas, and others [Silva2007]. In this thesis, experimental and simulated results of these mechanisms in fiber gratings are largely focused. New applications, not reported before in literature of these mechanisms in the optical communications and sensing fields are also described.

During the PhD, the author has been involved in some projects, which allowed interacting with multiple MSc and PhD students creating a positive dynamic for progress and success of the work presented in this thesis. Consequently, the cooperation with many colleagues at Instituto de Telecomunicações, with different work topics, opened great possibilities for a thesis with great results.

Furthermore, international collaborations with research groups were performed namely with Prof. Dr. Alexandre Pohl and his PhD student (now Dr. Roberson Oliveira at Volvo - Brazil) at the Federal University of Technology – Curitiba, Brazil in 2008, about acousto-optic effect in optical fiber. Another collaboration was made with the research group of prof. Dr. David J. Webb at the Aston University – United Kingdom in 2012, which has expertise in the fabrication of Bragg gratings in polymer optical fiber (PFBG). During one month, a short-term visit was made by the author to earn scientific knowledge about this topic. Following the design and implementation of a manufacturing system of PFBGs at the Instituto de Telecomunicações, already giving great results concerning the narrow bandwidth Bragg gratings in different types of polymer fibers and also different spectral windows were achieved, including the 600 nm region, for the first time. Finally, another longstanding collaboration with the group of Prof. Dr. Hypolito J. Kalinowsky and prof. Dr. Valmir de Oliveira at the Federal University of Technology – Curitiba, Brazil was relevant for this PhD thesis. In this case, the collaboration contributed with the topic about regeneration process in silica fibers using Bragg gratings inscribed with the manufacturing system presented in this thesis.

The following chapters present an analysis of components in optical fiber technology for optical communications and sensing. This thesis has six chapters, organized as follows.

Chapter 1 discusses the motivation and the organization of the thesis structure as well as its main scientific contributions.

Chapter 2 reviews the state of the art of the theoretical background on fiber gratings principles. The discussion of the fiber gratings principles is organized in a way that includes the two most important simulation models found in the literature: coupled-mode equations and transfer-matrix method. In both cases, the corresponding algorithms and associated computer programs validate the experimental results displayed throughout the thesis and proved to be an

excellent tool for further research. This chapter also reviews the most used fiber gratings fabrication methods.

The structure of this thesis is, to a large extent, centered on the development and implementation of the silica and polymer optical fiber gratings manufacturing workstations discussed in chapter 3, where a significant period of the research time elapsed. The proposed setup for silica optical fiber gratings is planned in terms of the automation of the fiber grating fabrication process while encompassing an upgrade and revision of the control software and hardware. This infrastructure is a central platform concerning the activity related to fiber gratings fabrication for both dispersion management and spectral filtering. The goal was to link the experience and maturity that fiber grating technology reached in the research group to a more sophisticated system that is, at the same time, suitable to be used by a larger number of people through the user friendly software developed. The hardware aspects and control software diagram of the fabrication unit implemented are addressed in chapter 3. Chapter 3 also gives special emphasis to characterization of inscribed fiber gratings achieved for both manufacturing workstations, i.e., for silica and polymer fibers.

Chapter 4 addresses a detailed description of the acousto-optic modulation in silica and polymer fiber. The methods used to simulate the mechanical structure and the experimental assemblies are also presented in this chapter. The chapter 4 ends up with the experimental characterization of the modulator and; numerical simulations and experimental evidences are used to verify the way acoustic waves modulates the diffraction grating spectra.

In the Chapter 5, the applications are described and their respective experimental assemblies detailed. The devices performance are also presented and discussed in this chapter.

Chapter 6 overviews the developed work, summarizes the main conclusions and achievements, and presents suggestions for future work.

1.2. List of Publications

The work accomplished during the elaboration of this thesis resulted in 17 papers published in internationally peer reviewed journals, 37 conference proceedings and a book chapter. The publications are listed below.

1.2.1. Book Chapter

[BC1] M. V. Drummond, C. A. F. Marques, P. Monteiro, R. N. Nogueira. "Optical Network Analyser for characterization of optical devices", Book chapter to appear in the EURO-FOS scientific handbook of experimental fiber-optic systems for telecommunicationns.

1.2.2. Journal Articles

[J17] C. A. F. Marques; L. Bilro; N. Alberto; D. J. Webb; R. N. Nogueira ; "Narrow Bandwidth Bragg Gratings Imprinted in Polymer Optical Fiber for Different Spectral Windows", Optics Communications, Vol. 307, pp. 57 - 61, October, 2013.

[J16] C. A. F. Marques; L. Bilro; L. Khan; R. A. Oliveira; D. J. Webb; R. N. Nogueira ; "Acousto-Optic Effect in Microstructured Polymer Fiber Bragg Gratings: Simulation and Experimental Overview", IEEE/OSA Journal of Lightwave Tech., Vol. 31, No. 10, pp. 1551 - 1558, May, 2013.

[J15] A. Pohl; R. A. Oliveira; R. Ezequiel Silva; C. A. F. Marques; P.T. Neves; K. Cook; J. Canning; R. N. Nogueira ; "Advances and new applications using the acousto-optic effect in optical fibers - review paper", Photonic Sensors, Vol. 3, No. 1, pp. 1 - 25, March, 2013.

[J14] C. A. F. Marques; R. A. Oliveira; A. Pohl; R. N. Nogueira ; "Tunability of the FBG group delay through acousto-optic modulation", Optical Fiber Technology, Vol. 19, No. 2, pp. 121 - 125, March, 2013.

[J13] A. Sousa; C. A. F. Marques; R. N. Nogueira ; P. S. André; "OSNR Monitoring Using Fiber Bragg Grating In High Birefringent Optical Fibers", Microwave and Optical Tech. Letters, Vol. 55, No. 1, pp. 6 - 8, January, 2013.

[J12] C. A. F. Marques; R. A. Oliveira; A. Pohl; R. N. Nogueira ; "Tunable acoustic bursts for customized tapered fiber Bragg structures", Journal of the Optical Society of America B-Optical Physics , Vol. 29, No. 12, pp. 3367 - 3370, December, 2012.

[J11] C. A. F. Marques; R. A. Oliveira; A. Pohl; R. N. Nogueira ; "Adjustable EDFA Gain Equalization Filter for DWDM Channels Based on a single LPG excited by Flexural Acoustic Waves", Optics Communications, Vol. 285, No. 18, pp. 3770 - 3774, August, 2012.

[J10] P. Antunes; C. A. F. Marques; H. Varum; P. S. André; "Biaxial Optical Accelerometer and High-Angle Inclinometer With Temperature and Cross-Axis Insensitivity", IEEE Sensors Journal, Vol. 12, No. 7, pp. 2399 - 2406, July, 2012.

[J9] C. A. F. Marques; V. Oliveira; H. Kalinowsky; R. N. Nogueira ; "Production of optical notch filters with fine parameter control using regenerated Fiber Bragg Gratings", Optics Letters, Vol. 37, No. 10, pp. 1697 - 1699, May, 2012.

[J8] R. A. Oliveira; C. A. F. Marques; J. Canning; R. N. Nogueira ; A. Pohl; "Complex Bragg Grating Writing using Direct Modulation of the Optical Fibre with Flexural Waves", Applied Physics Letters, Vol. 99, No. 16, pp. 161111 - 161111-3, October, 2011.

[J7] C. Vicente; R. Venkatachaam; B. Ferreira; P. Marques; C. A. F. Marques; E. Pecoraro; L. D. Carlos; P. S. André; R. A. Sá Ferreira; "Thin film optimization design of organic-inorganic hybrids for waveguide high-rejection optical filters", Physica Status Solidi (RRL), Vol. 5, No. 8, pp. 280 - 282, July, 2011.

[J6] R. A. Oliveira; G. R. C. Possetti; C. A. F. Marques; P.T. Neves; K. Cook; R. C. Kamikawachi; J. L. Fabris; R. N. Nogueira ; J. Canning; A. Pohl; "Control of the long period grating spectrum through low frequency flexural acoustic waves ", Measurement Science & Technology, Vol. 22, No. 4, pp. 045205 - 6pp, April, 2011.

[J5] C. A. F. Marques; R. A. Oliveira; A. Pohl; J. Canning; R. N. Nogueira ; "Dynamic Control of a Phase-Shifted FBG through Acousto-Optic Modulation", Optics Communications, Vol. 284, No. 5, pp. 1228 - 1231, March, 2011.

[J4] M. V. Drummond; C. A. F. Marques; P. Monteiro; R. N. Nogueira ; "Photonic Instantaneous Frequency Measurement System Using Complementary Modulation", IEEE Photonics Technology Letters, Vol. 23, No. 3, pp. 143 - 145, February, 2011.

[J3] N. Alberto; C. A. F. Marques; J. L. Pinto; R. N. Nogueira ; "Three-parameter optical fiber sensor based on a tilted fiber Bragg grating", The Virtual Journal for Biomedical Optics, Vol. 6, No. 1, pp. 6085 - 6091, January, 2011.

[J2] N. Alberto; C. A. F. Marques; J. L. Pinto; R. N. Nogueira ; "Three-parameter optical fiber sensor based on a tilted fiber Bragg grating", Applied Optics, Vol. 49, No. 31, pp. 6085 - 6091, November, 2010.

[J1] M. V. Drummond; C. A. F. Marques; P. Monteiro; R. N. Nogueira ; "Photonic Instantaneous Microwave Frequency Measurement System based on Signal Remodulation", IEEE Photonics Technology Letters, Vol. 22, No. 16, pp. 1226 - 1228, August, 2010.

1.2.3.   National and International Conferences

[C38] R. N. Nogueira, L. Bilro, C. A. F. Marques, R. Oliveira, J.Heidarialamdarloo, "Bragg gratings in plastic optical fiber for communications and sensing applications", Proc International Conference on Plastic Optical Fibers - POF, Búzios, Brazil, pp. 1 - 4, September, 2013.

[C37] C. A. F. Marques; A. Pohl; R. N. Nogueira, "Time Response of Bragg Gratings in microstructured Polymer Optical Fiber", Proc International Conference on Plastic Optical Fibers - POF, Búzios, Brazil, pp. 1 - 4, September, 2013.

[C36] R. N. Nogueira, L. Bilro, C. A. F. Marques, R.Oliveira, J.Heidarialamdarloo, "Optical filtering in plastic optical fibers – invited paper", Proc International Conf. on Transparent Networks – ICTON , Cartagena, Spain, Vol. Procedings, pp. 1 - 4, June, 2013.

[C35] C. A. F. Marques; L. Bilro; D. J. Webb; R. N. Nogueira ; "Inscription of narrow bandwidth Bragg gratings in polymer optical fibers", Proc European Workshop on Optical Fibre Sensors, Krakow, Poland, Vol. Procedings, pp. 8794-120 - , May, 2013.

[C34] C. A. F. Marques; R. A. Oliveira; A. Pohl; R. N. Nogueira ; "Adjustable EDFA Gain Equalization Filter Based on a Single LPG Excited by Flexural Acoustic Waves for Future DWDM Networks", Proc Photonics, Chennai, India, Vol. , pp. 1 - 3, December, 2012.

[C33] C. A. F. Marques; L. Bilro; L. Khan; R. A. Oliveira; D. J. Webb; R. N. Nogueira ; "Controlling the Properties of Microstructured Plastic Optical Fiber Bragg Gratings using Acousto-Optic Excitation", Proc IEEE Photonics Global Conf. - PGC , Singapore, Singapore, Vol. Procedings, pp. - , December, 2012.

[C32] C. A. F. Marques; V. Oliveira; H. Kalinowsky; R. N. Nogueira ; "Optical Notch Filters with Precise Production Control using Regenerated Fiber Bragg Gratings", in International Conference on Fibre Optics and Photonics, OSA Technical Digest (online) (Optical Society of America, 2012), paper T2C.3, 2012.

[C31] L. Bilro; C. A. F. Marques; L. Khan; R. A. Oliveira; D. J. Webb; R. N. Nogueira ; "Acousto-optic modulation in a microstructured plastic optical fibre Bragg grating", Proc Optical Fiber Sensors Conf., Beijing, China, Vol. Proc. of Spie, pp. 1 - 4, October, 2012.

[C30] N. Alberto; J. Santos Santos; C. A. F. Marques; V. Neto Neto; R. N. Nogueira ; "Nanodiamond coated Bragg gratings for sensing applications", Proc Optical Fiber Sensors Conf., Beijing, China, Vol. 8421, pp. 842120-1 - 842120-4, October, 2012.

[C29] G. Fernandes.; M. Niehus; C. A. F. Marques; R. N. Nogueira; A. N. A. N. Pinto; "Acousto-Optic Tunable Mode Coupler", Proc OSA Optical Fiber Communications - OFC, Los Angeles, United States, Vol. CD, pp. JTh2A.2, March, 2012.

[C28] C. Leitão Leitão; H. Lim;, L. Bilro; P. Antunes; C. A. F. Marques; J. Prata; P. S. André; R. N. Nogueira ; J. L. Pinto; "Development and characterization of new sensors for hemodynamic evaluation: fibre Bragg sensor for arterial pulse waveform acquisition ", Proc Portuguese chapter of IEEE EMBS Portuguese Meeting in Bioengineering, Coimbra, Portugal, Vol. --, pp. 1 - 4, February, 2012.

[C27] R. A. Oliveira; C. A. F. Marques; K. Cook; J. Canning; R. N. Nogueira ; A. Pohl; "Inscription of Bragg gratings using flexural acoustic waves", Proc European Conf. on Optical Communications - ECOC, Geneva, Switzerland, Vol. CD, pp. Tu.3.LeCervin.4 - , September, 2011.

[C26] L. Melo; V. Oliveira; C. A. F. Marques; N. Ângelo; N. Alberto; L. Bilro; R. N. Nogueira ; "Influence of hydrogenation in the thermal regeneration of FBGs", Proc International Commission for Optics General Congress of the International Commission for Optics - ICO, Puebla, Mexico, Vol. --, pp. 1 - 4, August, 2011.

[C25] R. Vilar; C. A. F. Marques; R. N. Nogueira ; A. Teixeira; R. Llorente; F. Ramos; "Flexible Optical-Comb-Based Multi-Wavelength Conversion for Optical Switching and Multicast", Proc European Conf. on Networks and Optical Communications - NOC, Newcastle, United Kingdom, Vol. , pp. 1 - 4, July, 2011.

[C24] M. V. Drummond; C. A. F. Marques; P. Monteiro; R. N. Nogueira ; "Photonic Instantaneous RF Frequency Measurement System based on Complementary E/O Modulation", Proc Optoelectronics and Communications Conf. - OECC, Kaohsiung, Taiwan, Vol. 6G2-2, pp. 1 - 2, July, 2011.

[C23] A. Sousa; C. A. F. Marques; R. N. Nogueira ; P. S. André; "OSNR monitoring using Hi-Bi FBG for 10 Gbit/s optical networks", Proc International Conf. on Transparent Networks – ICTON , Stockholm, Sweden, Vol. , pp. 1 - 4, June, 2011.

[C22] R. A. Oliveira; G. R. C. Possetti; C. A. F. Marques; P.T. Neves; C. A. Bavastri; R. C. Kamikawachi; J. L. Fabris; R. N. Nogueira ; J. Canning; A. Pohl; "Acousto-optic control of the LPG spectrum for sensing applications", Proc Optical Fiber Sensors Conf., Ottawa, Canada, Vol. OFS11-OFS21-223, pp. 1 - 4, May, 2011.

[C21] C. A. F. Marques; L. Melo; R. A. Oliveira; A. Pohl; P. S. André; R. N. Nogueira ; "Adaptive gain equalization on optical amplifiers based on the acousto-optic modulation using a long period grating", Proc International Conf. on Applications of Optics and Photonics - AOP2011, Braga, Portugal, Vol. , pp. - , May, 2011.

[C20] L.M. Sá ; C. A. F. Marques; N. Alberto; R. N. Nogueira ; P. S. André; "Multichannel dispersion compensation using a simplified approach SFBG design", Proc International Conf. on Applications of Optics and Photonics - AOP2011, Braga, Portugal, Vol. , pp. - , May, 2011.

[C19] N. Alberto; C. A. F. Marques; J. L. Pinto; R. N. Nogueira ; "Simultaneous temperature and refractive index sensor based on a tilted fibre Bragg grating", Proc International Conf. on Applications of Optics and Photonics - AOP2011, Braga, Portugal, Vol. -, pp. - - -, May, 2011.

[C18] N. Alberto; C. A. F. Marques; P. Antunes; J. L. Pinto; R. N. Nogueira ; "Three parameters simultaneous measurement with a single TFBG", Proc Optical Fiber Sensors Conf., Ottawa, Canada, Vol. 7753, pp. 77537Z - 1 - 77537Z - 4, May, 2011.

[C17] C. A. F. Marques; R. A. Oliveira; A. Pohl; P. S. André; R. N. Nogueira ; "Adaptive gain equalization on optical amplifiers based on the Acousto-Optic effect using a single Long Period Grating", Proc EUROCON and CONFTELE 2011, Lisbon, Portugal, Vol. cd, pp. 1 - 3, April, 2011.

[C16] C. A. F. Marques; R. A. Oliveira; J. Canning; A. Pohl; R. N. Nogueira ; "Controlling the properties of Fiber Bragg Gratings based on the Acousto-Optic modulation ", Proc EUROCON and CONFTELE 2011, Lisbon, Portugal, Vol. cd, pp. 1 - 3, April, 2011.

[C15] A. Sousa; C. A. F. Marques; R. N. Nogueira ; P. S. André; "Optical signal to noise ratio monitoring with Hi-Bi fiber Bragg grating", Proc EUROCON and CONFTELE 2011, Lisboa, Portugal, Vol. , pp. 1 - 3, April, 2011.

[C14] M. V. Drummond; C. A. F. Marques; P. Monteiro; R. N. Nogueira ; "Photonics Instantaneous RF Frequency Measurement System based on Complementary Modulation", Proc International Conf. on Applications of Optics and Photonics - AOP2011, Braga, Portugal, Vol. 1, pp. 1 - 4, March, 2011.

[C13] R. A. Oliveira; C. A. F. Marques; J. Canning; R. N. Nogueira ; A. Pohl; "Tunable Narrow Dispersion Compensation for Independent CWDM Channels using Acousto-Optic Effect", Proc Workshop on Photonic Sensors for the Industry - WPSI, Paraná, Brazil, Vol. , pp. 1 - 2, October, 2010.

[C12] C. A. F. Marques; R. A. Oliveira; A. Pohl; J. Canning; R. N. Nogueira ; "Control of the Properties of Fiber Bragg Gratings Based on the Accousto-Optic Effect", Proc European Conf. on Optical Communications - ECOC, Torino, Italy, Vol. , pp. - , September, 2010.

[C11] N. Alberto; C. A. F. Marques; J. L. Pinto; R. N. Nogueira ; "Simultaneous strain and refractive index sensor based on a TFBG", Proc European Workshop on Optical Fibre Sensors, Porto, Portugal, Vol. 7653, pp. 765324-1 - 745324-4, September, 2010.

[C10] A. Pohl; R. A. Oliveira; C. A. F. Marques; K. Cook; R. N. Nogueira ; J. Canning; "Novel Applications of the Acousto-Optic Effect in the Control of Fibre Bragg Grating Parameters – invited paper", Proc International Conf. on Transparent Networks – ICTON , Munique, Germany, Vol. Mo.C1.4, pp. 1 - 4, June, 2010.

[C9] L.M. Sá ; C. A. F. Marques; R. N. Nogueira ; P. S. André; "Simple Approach to Design a Multichannel Sampled FBG for Dispersion Compensation", Proc Symp. on Enabling Optical Networks - SEON, Porto, Portugal, Vol. , pp. 1 - 2, June, 2010.

[C8] C. A. F. Marques; R. A. Oliveira; A. Pohl; J. Canning; R. N. Nogueira ; "Tunable Optical Notch Filter Based On The Acousto-optic Effect In A Fbg", Proc OSA Bragg Gratings, Photosensitivity and Poling in Glass Waveguides - BGPP, Karlsruhe, Germany, Vol. CD, pp. BTuC5 - , June, 2010.

[C7] R. A. Oliveira; C. A. F. Marques; C. Mayer; J. Pereira; R. N. Nogueira ; A. Pohl; "Single Device for Excitation of Both Flexural and Longitudinal Acousto-Optic Effects in Fiber Bragg Gratings", Proc International Microwave and Optoelectronics Conf. - IMOC, Pará, Brazil, Vol. Proceedings, pp. 546 - 549, November, 2009.

[C6] R. A. Oliveira; C. A. F. Marques; R. N. Nogueira ; A. Pohl; "Fast Acousto-Optic Add-Drop based on Fiber Bragg Grating", Proc IEEE Lasers and Electro Optics Society Annual Meeting - LEOS, Belek, Turkey, Vol. Proceedings, pp. 573 - 574, October, 2009.

[C5] R. N. Nogueira ; M. V. Drummond; C. A. F. Marques; A. Teixeira; P. S. André; Rocha, R. F.; "Advanced Applications of Fiber Bragg Gratings for Telecom Systems", Proc Progress in Electromagnetics Research Symp. - PIERS, Moscow, Russia, Vol. Proceedings, pp. 00 - 00, August, 2009.

[C4] R. N. Nogueira ; M. V. Drummond; C. A. F. Marques; A. Teixeira; P. S. André; Violas, M.; P. Monteiro; P.-Y. Fonjallaz; "All-optical signal processing techniques with fiber based devices ", Proc International Conf. on Transparent Networks – ICTON , Azores, Portugal, Vol. -, pp. - - -, July, 2009.

[C3] J. M. M. Santos; C. A. F. Marques; O. Abe; R. N. Nogueira ; "Long Period Fiber Grating as EDFA Gain flattening", Proc Symp. on Enabling Optical Networks - SEON, Amadora, Portugal, Vol. -, pp. 1 - 2, June, 2009.

[C2] F. Conradin; C. A. F. Marques; R. N. Nogueira ; L. Almásy; "Analysis of Different Writing Techniques for Chirped Fibre Bragg Gratings", Proc Conf. on Telecommunications - ConfTele, Santa Maria da Feira, Portugal, Vol. Proceedings, pp. 403 - 406, May, 2009.

[C1] C. A. F. Marques; M. V. Drummond; F. Conradin; R. N. Nogueira ; "Implementation of an Automated Fiber Bragg Grating Writing System", Proc Conf. on Telecommunications - ConfTele, Santa Maria da Feira, Portugal, Vol. Proceedings, pp. 399 - 402, May, 2009.

1.3. Main Achievements

In the author opinion, the most important results reported in this thesis are the following:

- Development and implementation of the automatized fiber gratings manufacturing workstation for silica optical fiber [C1-C5].

- Development and implementation of the Bragg gratings fabrication setup for polymer optical fiber [J16, J17, C35, C36].

- Modeling of the interaction between acousto-optic effect and FBG/LPGs for potential photonic applications [J6, C7, C12, C22, C29].

- Modeling of the interaction between acousto-optic effect and microstructured polymer optical fiber for photonic applications [J16, C31, C33].

- Fast acousto-optic add-drop multiplexer using a uniform Bragg grating [C6, C37].

- New technique for tunability of the group delay based on acousto-optic modulation. It can be applied for tunable dispersion compensator for WDM channels and optical delay lines [J14, C13, C16].

- Novel adjustable notch filter using a phase-shifted fiber Bragg grating with fine tuning based on acousto-optic effect [J5, C8, C10, C12, C16].

- New method based on acousto-optic effect for writing complex fiber Bragg gratings such as customized phase-shifts and sampling modulation of uniform Bragg gratings [J8, J12, C27].

- Adjustable EDFA gain equalization filter for DWDM channels based on a single long period grating excited by flexural acoustic waves [J11, C17, C21, C34].

- Acousto-optic tunable mode coupler using a multimode tapered optical fiber [C29].

- Novel technique for fabrication of tunable optical notch filter with a precise parameter control based on regenerated fiber Bragg gratings [J9, C32].

The remaining journal and conference papers do not focus exclusively on the operation principles covered in this thesis. In addition to these contributions, a book chapter [BC1] was written within the frame of the EURO-FOS Network of Excellence. All contributions are referenced at section 1.2.

Chapter 2

Theoretical Background

2.1. Introduction

An optical fiber is a cylindrical dielectric waveguide. It consists of a core which is surrounded by a cladding layer. To confine the light guiding in the core, the refractive index of the core n_{core} is greater than that of the cladding $n_{cladding}$ to form the total internal reflection at the core cladding boundary. One of the key parameters of optical fibers is Numerical Aperture (NA) which is determined by the two indices [Ghatak1998],

$$NA = n \sin \theta_{max} = \sqrt{n_{core}^2 - n_{cladding}^2}$$

(2.1)

where θ_{max} is the acceptance angle. The larger the value of NA, hence, the greater acceptance angle, the more amount of light the fiber can collect and also the wider the output beam will expand from the fiber end.

Another widely used key parameter is the V-parameter [Hill1978] which defines the mode volume of the core region in step index (SI) fiber:

$$V = \frac{2\pi a_{core}}{\lambda_c} \sqrt{n_{core}^2 - n_{cladding}^2} = 2\pi a_{core} NA$$

(2.2)

where a_{core} is the radius of the core region and λ_c is the wavelength in vacuum. For single-mode (SM) optical fiber, the value of the V-parameter should fulfill V ≤ 2.405.

Fiber gratings consist of a periodic variation of the refractive index in the core of an optical fiber, which is normally produced by exposing the fiber to a spatially varying pattern of ultraviolet (UV) light. The discovery of the photosensitivity in optical fiber happened in 1978 at the Communications Research Center Canada, during experiments of non-linear effects. At the time, a photoinduced permanent change was observed in the refractive index of the fiber core through an intense exposure to core-launched visible light from an argon ion laser [Hill1978]. Since then, the study of fiber gratings started to call the attention of the scientific community. The periodic structure, shown in Figure 2.1 can couple a portion of light from the forward propagating core mode to the backward propagating core mode. In 1978, K. O. Hill et al. first demonstrated the internal writing of an fiber grating in silica fiber [Hill1978] and Z. Xiong et al. were the first to report inscribing FBG in polymer optical fiber (POF) in 1999 [Xiong1999].
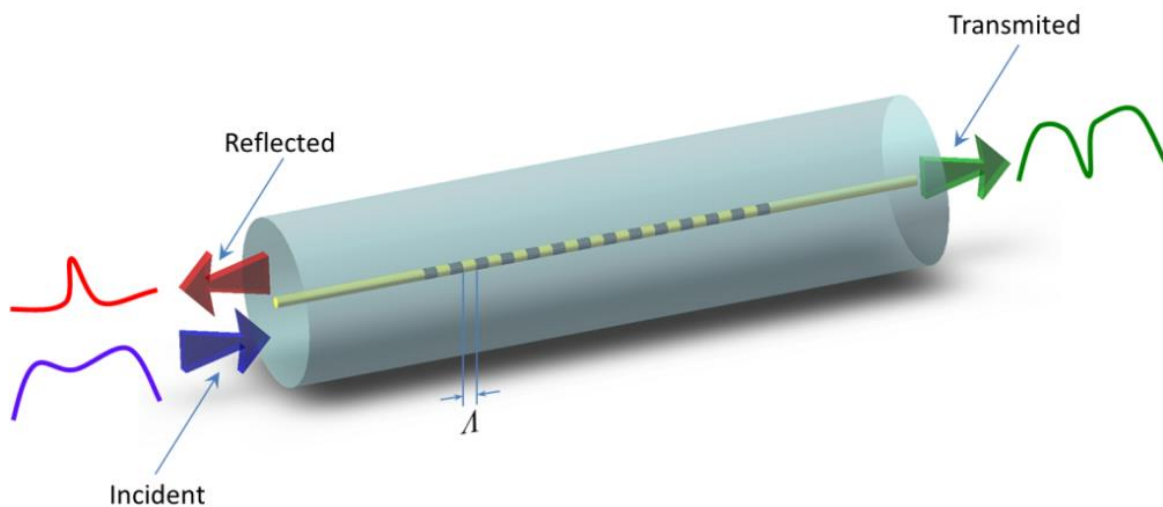
Figure 2.1 – Illustration of the diffraction effect of a fiber grating.

Fiber devices such as optical filters [Kawasaki1978], optical sensors [Bhatia1996, Vengsarkar1996], and distributed Bragg reflector fiber lasers (DBR) [Kringlebotn1994] were fabricated, making this technology a crucial solution for all-fiber communication and sensing devices.

In 1988 Meltz et al. reported the fabrication of a fiber diffraction grating by exposing the fiber core externally to an intense UV interference pattern [Meltz1989]. This was an important advance in the fiber grating fabrication technology [Hill1993a]. As the research in the field evolved, two kinds of fiber gratings were developed: one based on the reflection of the light, with short-period modulation, similar to those inscribed by Hill et al. [Hill1978, Hill1993a], the so called FBG, and the other formed by long periods of modulation, known as LPG [Vengsarkar1996].

The Bragg grating length can vary from a few millimeters to several centimeters in length. The amplitude of refractive index modulation, Δn, usually does not exceed values of the order of 10^{-2}, being the values typical of order $\Delta n \sim 10^{-4}$. For a Bragg grating operating in the 1,5 µm window, usual in optical communications, the typical periodicity of the modulation is $\Lambda \approx 0,5$ µm.

A complementary structure of the Bragg grating is the LPG [Vengsarkar1996, Bhatia1996]; whose their use is often combined with Bragg gratings and their fundamentals share a common path. Indeed, whereas a Bragg grating, or short period grating, has typically a modulation period of several hundred nanometers, in an LPG the period rounds typically hundreds of micrometers.

Fiber gratings are simply an optical diffraction grating, and thus its effect upon a light wave incident on the grating at an angle θ_1 can be described by equation [Born1987]

$$n_2 \sin(\theta_2) = n_1 \sin(\theta_1) + M \frac{\lambda}{\Lambda} \tag{2.3}$$

where θ_2 is the angle of the diffracted wave and the integer M determines the diffraction order (see Figure 2.2). This equation predicts only the directions into which constructive interference occurs, but it is nevertheless capable of determining the wavelength at which a fiber grating most efficiently couples light between two modes. Fiber gratings can be broadly classified into two types: Bragg gratings (also called reflection and short-period gratings), in which coupling occurs between modes traveling in opposite directions; and transmission gratings (also called long-period gratings), in which the coupling is between modes traveling in the same direction. Figure 2.3 (a) illustrates reflection by a Bragg grating of a mode with a bounce angle of θ_1 into the same mode traveling in the opposite direction with a bounce angle of $\theta_2 = -\theta_1$. Since the mode propagation constant β is simply $\beta = (2\pi/\lambda) n_{eff}$ where $n_{eff} = n_{core} \sin\theta$, we may rewrite (2.3) for guided modes as

$$\beta_2 = \beta_1 + M\frac{2\pi}{\Lambda} \tag{2.4}$$
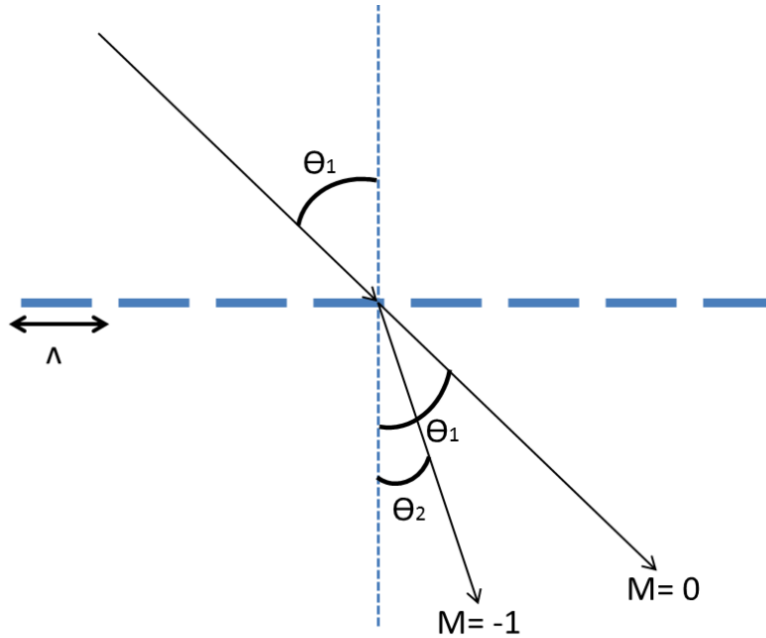
Figure 2.2 – Diffraction of a light wave by a fiber grating [Erdogan97].

For first-order diffraction, which usually dominates in a fiber grating, *M = -1*. This condition is illustrated on the *β* axis shown below the fiber. The solid circles represent bound core modes $\left(n_{cladding} < n_{eff} < n_{core}\right)$, the open circles represent cladding modes $\left(1 < n_{eff} < n_{cladding}\right)$, and the hatched regions represent the continuum of radiation modes. Negative β values describe modes that propagate in the *−z* direction. By using (2.4) and recognizing $\beta_2 \le 0$, we find that the resonant wavelength for reflection of a mode of index $n_{eff,1}$ into a mode of index $n_{eff,2}$ is

$$\lambda = \left(n_{eff,1} + n_{eff,2}\right)\Lambda \tag{2.5}$$

If the two modes are identical, we get the familiar result for Bragg reflection: $\lambda = 2n_{eff}\Lambda$. Diffraction by a transmission grating of a mode with a bounce angle of θ_1 into a co-propagating mode with a bounce angle of θ_2 is illustrated in Figure 2.3 (b). In this illustration the first mode is a

core mode while the second is a cladding mode. Since here $\beta_2 > 0$, (2.4) predicts the resonant wavelength for a transmission grating as

$$\lambda = \left(n_{eff,1} - n_{eff,2} \right) \Lambda \qquad (2.6)$$

For co-propagating coupling at a given wavelength, evidently a much longer grating period is required than for counter-propagating coupling.
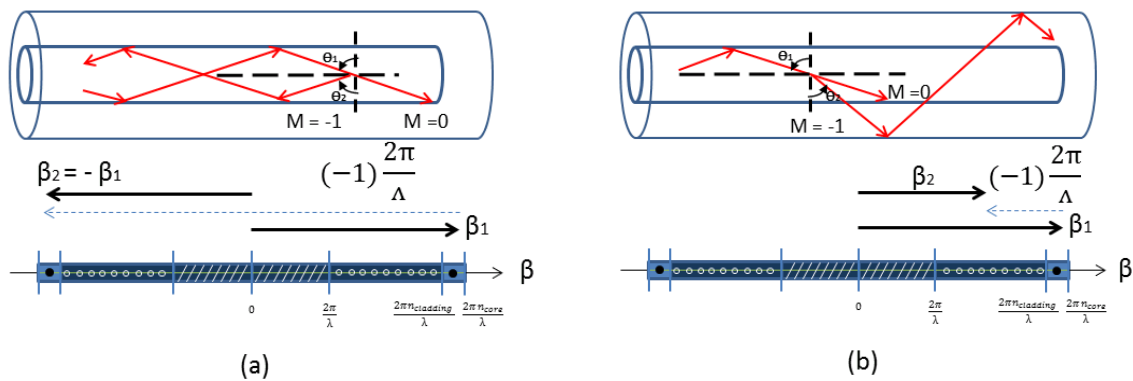
Figure 2.3 – Ray-optic illustration of (a) core-mode Bragg reflection by an FBG and (b) cladding-mode coupling by a fiber transmission grating for M =-1 [Erdogan1997a].

2.2. Coupled Mode Theory

Coupled-mode theory is a widely used technique to obtain an approximate solution for electromagnetic wave propagating in periodically layered medium and is capable of providing the quantitative information about the spectral response of fiber gratings. This theory is a simple and an accurate model employed to describe the characteristic and optical properties of most in-fiber gratings.

Detailed derivation of couple-mode theory and description of its applications in guided mode and gratings was given by Yariv [Yariv1973], Kogelnik [Kogelnik1972] and Erdogan [Erdogan1997a, Erdogan1997b]. Here a brief and abridged part of these reports is presented that is most related to the material of this thesis and the derivation in this section closely follows the proposed work by Erdogan.

We shall consider the ideal mode approximation to coupled mode theory in which the transverse components of the electric field are written as a superposition of the ideal modes. Modes should be considered in an ideal waveguide that does not experience a grating perturbation. If modes are labeled with index n, we will have:

$$E^T(x,y,z,t) = \sum_n \left[A_n(z) \cdot e^{i\beta_n z} + B_n(z) \cdot e^{-i\beta_n z} \right] \cdot e_n^T(x,y) \cdot e^{-i\omega t} \tag{2.7}$$

where ω is the optical frequency of field, n is the label of modes, $A_n(z)$ and $B_n(z)$ represent the slowly varying amplitudes of the nth mode travelling along the fiber axis direction (*+z* and *-z* directions).

$e_n^T(x,y)$ is the transverse mode field, which may describe a bound-core, cladding or radiation mode. As already mentioned, β is the propagation constant and simply given by:

$$\beta = \frac{2\pi}{\lambda} n_{eff} \tag{2.8}$$

where n_{eff} represents the effective refractive index of nth mode.

The mode coupling occurs in the presence of a dielectric perturbation and, as a result, the amplitudes A_n and B_n of the nth mode evolve along the *z* direction based on the following equations:

$$\frac{dA_n}{dz} = i \sum_j A_j \left[D_{jn}^t + D_{jn}^z \right] \cdot e^{i(\beta_j - \beta_n)z} + i \sum_j B_j \left[D_{jn}^t - D_{jn}^z \right] \cdot e^{-i(\beta_j + \beta_n)z} \tag{2.9}$$

$$\frac{dB_n}{dz} = -i \sum_j A_j \left[D_{jn}^t - D_{jn}^z \right] \cdot e^{i(\beta_j + \beta_n)z} - i \sum_j B_j \left[D_{jn}^t + D_{jn}^z \right] \cdot e^{-i(\beta_j - \beta_n)z} \tag{2.10}$$

where D_{jn}^t and D_{jn}^z are the transverse and longitudinal coupling coefficients between the j and n modes, respectively.

The longitudinal coupling coefficient, D_{jn}^z, is analogous to transverse component, D_{jn}^t. However, for fiber, mode D_{jn}^z is usually neglected since it is half magnitude of the transverse components for fiber modes. The transverse coupling coefficient in the above equations is given by equation (2.11).

$$D_{jn}^{t}(z)=\frac{\omega}{4}\iint_{\infty}\Delta\varepsilon(x,y,z)\cdot e_{j}^{T}(x,y)\cdot e_{n}^{T*}(x,y)dxdy \tag{2.11}$$

$\Delta\varepsilon(x,y,z)$ from the above equation is the permittivity perturbation and its value is approximately *2nδn$_{eff}$* where *δn$_{eff}$* is the (effective) refractive index variation and small compared with the local index, *n*, in the ideal fiber. Considering an ideal waveguide situation, i.e. no perturbation exists so $\Delta\varepsilon=0$, the coupling coefficient $D_{jn}^{t}(z)=0$ and the transverse modes are orthogonal and do not exchange energy.

By exposing an optical fiber to a spatially varying pattern of UV intensity, it induces a perturbation on the effective refractive index (*δn$_{eff}$*) along the propagation axis z and is given by the expression [Erdogan1997]:

$$\delta n_{eff}(z)=\overline{\delta n_{eff}}(z)\left\{1+v(z)\cos\left[\frac{2\pi}{\Lambda}z+\phi(z)\right]\right\} \tag{2.12}$$

where $\overline{\delta n_{eff}}(z)$ is the "dc" index change spatially averaged over a grating period, $0\leq v(z)\leq 1$ is the fringe visibility of the index change, Λ is the period, and $\phi(z)$ describes grating chirp. Note that the visibility does not change the average value of refractive index, only changes the variation amplitude of this. It is verified by simulating of a Bragg grating portion for three different values of visibility. Figure 2.4 shows that the average value of variations (dashed) is the same.

Depending on the parameters such as $\overline{\delta n_{eff}}(z)$, $v(z)$, $\phi(z)$, grating writing angle or spatial arrangement of the different gratings, the Bragg gratings can have different types of properties and applications. Thus, it is crucial to classify them according to the spatial variation type they possess. This classification will be discussed in the following sections.
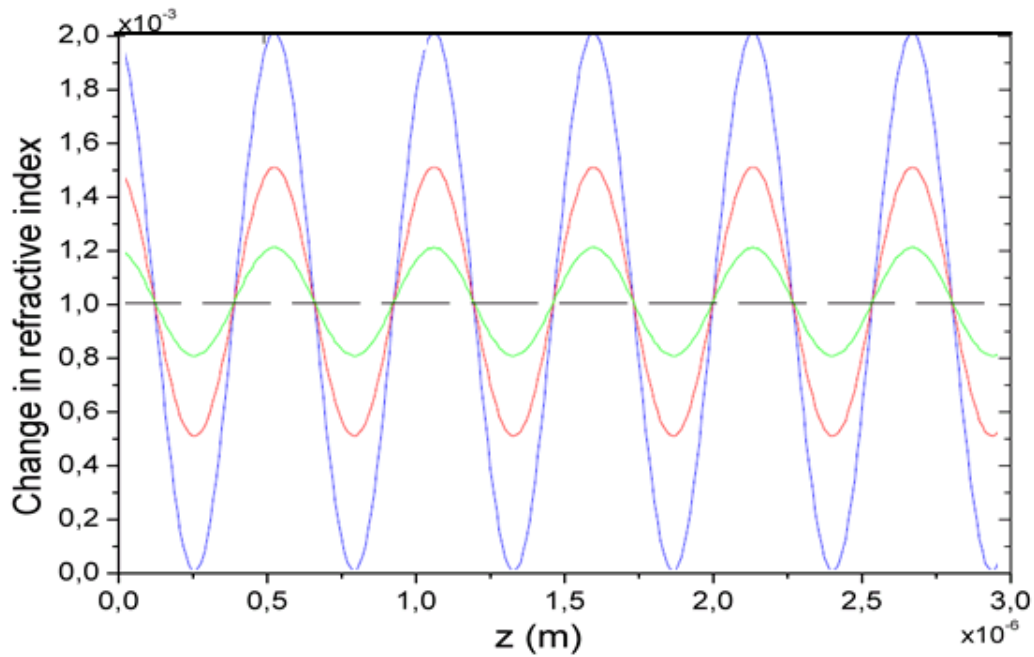
Figure 2.4 - Refractive index modulation in the core of a fiber along z, with varying visibility of the fringe pattern (v =1 – blue; v=0,5 – red; v=0,2 – green) [Nogueira2005].

In most fiber gratings, the photo-induced index modulation is almost uniform across the core and negligible outside the core so the dc index change $\overline{\delta n_{eff}}(z)$ can be replaced by $\overline{\delta n_{core}}(z)$ and based on what has already been explained $\Delta\varepsilon(x,y,z)$ can be replaced by $2n_{core}\overline{\delta n_{core}}(z)$. By applying these substitutions, the general coupling coefficient, $D_{jn}^{t}(z)$ can be rewritten in the form of the following equation:

$$D_{jn}^{t}(z)=\psi_{jn}(z)+2k_{jn}(z)\cos\left(\frac{2\pi}{\Lambda}z+\phi(z)\right) \tag{2.13}$$

$\psi_{jn}(z)$ and $k_{jn}(z)$ in the above equation are defined as "dc" and "ac" coupling coefficients respectively and can be calculated as:

$$\psi_{jn}(z)=\frac{\omega n_{core}}{2}\overline{\delta n_{core}}(z)\iint\limits_{core}e_{j}^{T}(x,y)e_{n}^{T*}(x,y)dxdy \tag{2.14}$$

$$k_{jn}(z)=\frac{v}{2}\psi_{jn}(z) \tag{2.15}$$

2.2.1. Backward Mode Coupling

In backward mode coupling, near the wavelength for which reflection of a mode of amplitude *A(z)* into an identical counter-propagating mode of amplitude *B(z)* is the dominant interaction in a Bragg grating [Erdogan1997a]. Under such conditions, equations ((2.9) and 2.10)) are simplified to the following equations:

$$\frac{dR}{dz} = i\psi'R(z) + ikS(z)$$
(2.16)

$$\frac{dS}{dz} = -i\psi'S(z) - ik^*R(z)$$
(2.17)

In above equations, *k* is the "ac" coupling coefficient and ψ' is the general "dc" self-coupling coefficient which is defined as:

$$\psi' = \delta + \psi - \frac{1}{2}\frac{d\phi}{dz}$$
(2.18)

where δ is the detuning and independent of *z*:

$$\delta = \beta - \frac{\pi}{\Lambda} = \beta - \beta_D = 2\pi n_{eff}\left[\frac{1}{\lambda} - \frac{1}{\lambda_D}\right]$$
(2.19)

$\lambda_D = 2n_{eff}\Lambda$ is the "design wavelength" for Bragg scattering by an infinitesimally weak grating ($\delta n_{eff} \rightarrow 0$).

The amplitude *R* and *S* in equations (2.16 and 2.17) are defined as:

$$R(z) = A(z) \cdot e^{i\delta z - \frac{\phi(z)}{2}}$$
(2.20)

$$S(z) = B(z) \cdot e^{-i\delta z + \frac{\phi(z)}{2}}$$
(2.21)

For a SM Bragg grating, one may use the following simplified relations:

$$\psi = \frac{2\pi}{\lambda}\overline{\delta n}_{eff}$$
(2.22)

$$k = k^* = \frac{\pi}{\lambda} v \overline{\delta n_{eff}} \tag{2.23}$$

If the grating is uniform along z, then $\overline{\delta n_{eff}}$ is constant and $d\phi(z)/dz = 0$. Thus, k, ψ and ψ' are all constants. This simplifies equations (2.20) and (2.21) into coupled first-order ordinary differential equations with constant coefficients. The closed-form solutions may be found when appropriate boundary conditions are specified. The reflectivity of a uniform fiber grating of length L can be found by assuming that the propagation wave is incident from $z \to -\infty$ (i.e., $R(-L/2)=1$) and there is no backward propagation wave exists from $z \geq L/2$ (that means $S(L/2)=0$). Thus, the amplitude ρ is given by:

$$\rho = \frac{S(-L/2)}{R(-L/2)} = \frac{-k \sinh\left(\sqrt{k^2 - \psi'^2}\, L\right)}{\psi' \sinh\left(\sqrt{k^2 - \psi'^2}\, L\right) + i\sqrt{k^2 - \psi'^2}\, \cosh\left(\sqrt{k^2 - \psi'^2}\, L\right)} \tag{2.24}$$

The power reflection coefficient r is given by:

$$r = \left|\rho^2\right| = \frac{\sinh^2\left(\sqrt{k^2 - \psi'^2}\, L\right)}{-\dfrac{\psi'^2}{k^2} + \cosh^2\left(\sqrt{k^2 - \psi'^2}\, L\right)} \tag{2.25}$$

And the phase, ϕ can be expressed by

$$\phi = \arctan\left(\frac{\text{Im}(\rho)}{\text{Re}(\rho)}\right) \tag{2.26}$$

The induced group delay by the grating can be estimated from phase. In this way, it is necessary to replace the function ϕ with phase jumps of *2π* (due to the arctan function) by another equivalent with phase continuous variation ϕ_a, called accumulated phase. Thus, the induced group delay by the grating can be calculated from

$$\tau = \frac{d\phi_a}{d\omega} = -\frac{\lambda^2}{2\pi c}\frac{d\phi_a}{d\lambda} \tag{2.27}$$

Moreover, the dispersion factor defined as the variation of the group delay as a function of wavelength, is computed from

$$D = \frac{d\tau}{d\lambda} = \frac{2\tau}{\lambda} - \frac{\lambda^2}{2\pi c}\frac{d^2\phi_a}{d\lambda^2} = -\frac{2\pi c}{\lambda^2}\frac{d^2\phi_a}{d\omega^2}.$$ (2.28)

Using the power reflection coefficient equation, different reflection spectral responses can be plotted with different *kL* values, as shown in Figure 2.5. It should be noted here that curves in the figure are plotted against the normalized wavelength

$$\frac{\lambda}{\lambda_{max}} = \frac{1}{1 + \psi'L/\pi N}$$ (2.29)

where $N = L/\Lambda$ is the number of grating planes. For a given *kL* value, the bandwidth of a grating will decrease with increasing *N*.
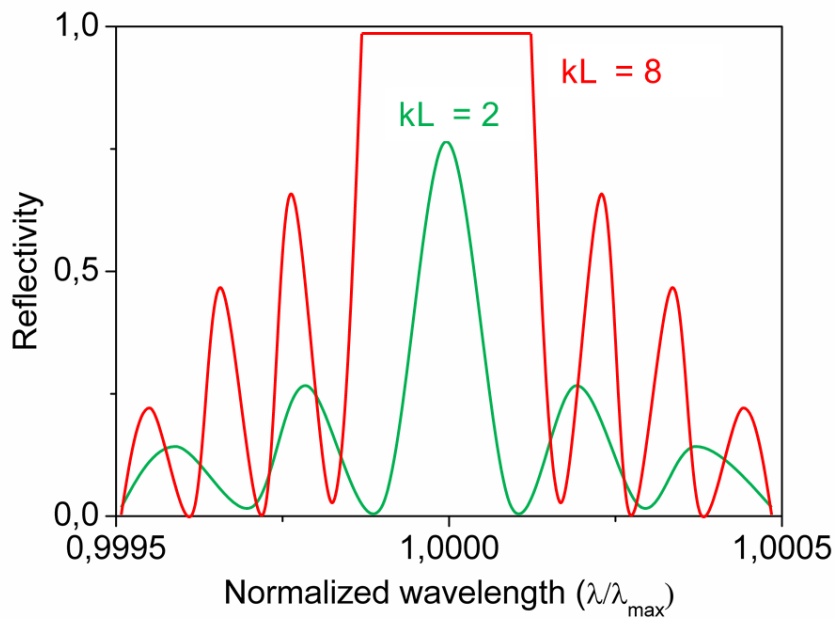
Figure 2.5 - Reflection spectral response versus normalized wavelength (λ/λ_{max}) for a uniform Bragg grating with kL= 2 and 8.

Still from equation 2.29, when $\psi' = 0$, or at the wavelength $\lambda_{max} = \left(1 + \frac{\overline{\delta n_{eff}}}{n_{eff}}\right)\lambda_D$ **,** the maximum reflectivity can be achieved, given by:

$$r_{max} = \tanh^2(kL)$$ (2.30)

The bandwidth for a uniform Bragg grating is the width between the first zeros on either side of the maximum reflectivity [Erdogan1997a]. From equation, it can be found:

$$\frac{\Delta\lambda_0}{\lambda} = \frac{v\overline{\delta n_{eff}}}{n_{eff}}\sqrt{1 + \left(\frac{\lambda_D}{v\overline{\delta n_{eff}}L}\right)^2}$$ (2.31)

In the grating illustrated in Figure 2.4 the respective spatial properties remains constant throughout its longitudinal extent. That means the $\overline{\delta n_{eff}}(z)$, $v(z)$ and $\phi(z)$ parameters are constant and independent of z. Such gratings are called uniform Bragg gratings and the reflection spectrum is similar to that shown in Figure 2.6. Figure 2.7 shows the schematic diagram of the backward mode coupling in an FBG.
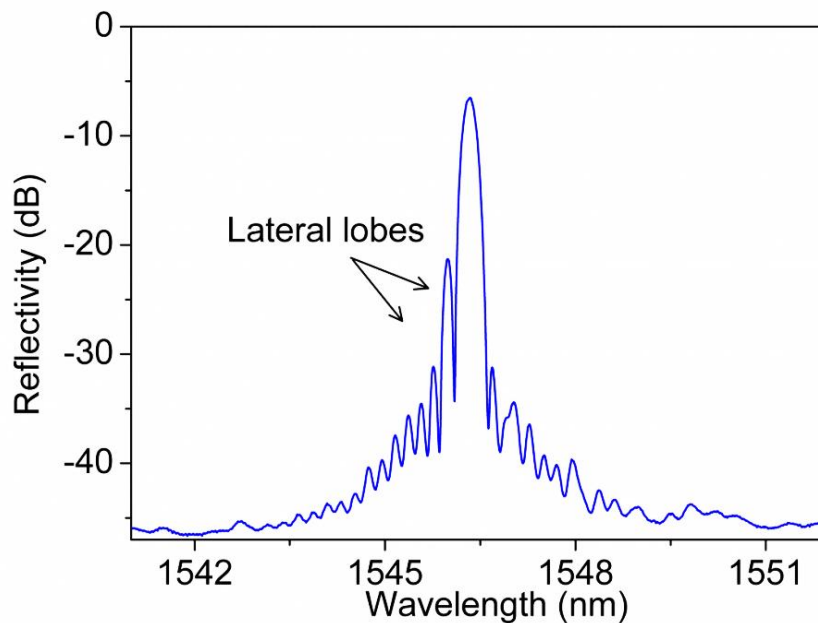
Figure 2.6 – Example of a possible reflection spectrum of a uniform Bragg grating.

Even though the spatial properties of uniform FBGs are constant along z in these gratings is possible to control the reflectivity and bandwidth, by controlling the amplitude of modulation and FBG length. The advantages of such gratings are related to its simplicity of inscription; however,

the reflection spectrum exhibits side lobes with high amplitudes, which can be a drawback for optical communications since they favor the existence of crosstalk between channels very close in wavelength. However, recently it was demonstrated that side lobes can be used for photonic instantaneous frequency measurement systems to suppress a particular optical carrier by 20 dB, where the optical carrier frequency was aligned with a first-order zero of the FBG reflectivity, providing the narrowest notch filtering [Drummond2011].

These side lobes appear due to the abrupt boundaries of the Bragg grating giving a similar effect to Fabry-Perot cavities. The side lobes of the uniform FBGs can be reduced substantially if the amplitude of refractive index modulation, in the endpoints of the Bragg grating, start and to end gradually, to avoid the interfaces responsible for the effect Fabry-Perot cavity. To this technique is called apodization and was presented by Hill and Matsuhara as an effective way of side lobes reduction [Hill1974, Matsuhara1974]. From equation (2.12), the apodization control is made through the parameters $\overline{\delta n_{eff}}(z)$ and $v(z)$, directly related to the exposure time and the visibility of optical fringes, respectively.

In general, it shall be noted that the apodization profile consists on the variation of average value of the effective refractive index, and the visibility profile is the amplitude of the sinusoidal variation of the effective refractive index. The most common apodization techniques consist of varying the amplitude of modulation through greater or shorter exposure time. Detail information about apodization profiles can be found in [Nogueira2005].
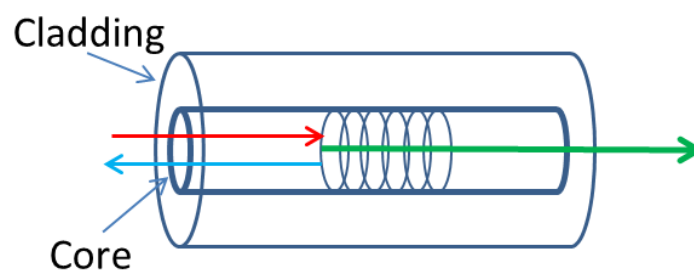
Figure 2.7 – Schematic diagram of backward-mode coupling in FBG.

2.2.2. Forward Mode Coupling

The Theory Matrix Method (TMM) formulation applied for transmission gratings is similar to the one presented for reflection grating. The change is that, instead of considering the energy coupled to a counter-propagating mode, the light is coupled to a co-propagating mode, for instance light propagating in mode "1" being coupled to a co-propagating mode "2". Figure 2.8 shows the quadrupole characteristics of the LPG, where now *R* represents the amplitude of the forward propagating mode and *S* the amplitude of the co-propagating field.
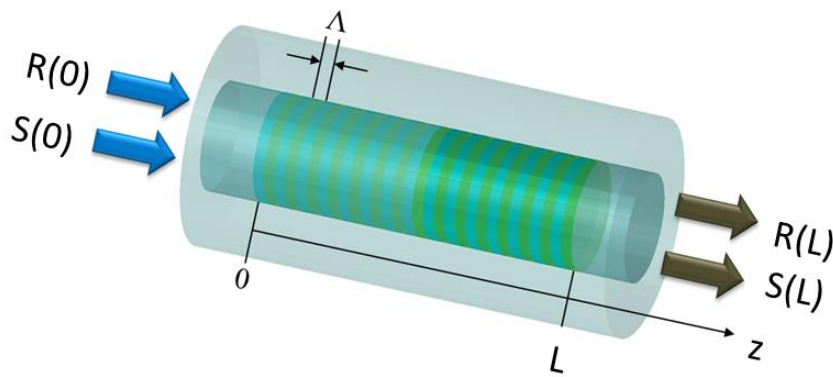
Figure 2.8 - LPG represented as a quadrupole in the TMM.

Forward mode coupling is the condition in which a forward propagating mode with amplitude *A₁(z)* is strongly coupled into a co-propagating mode of amplitude *A₂(z)* close to the wavelength in which forward mode coupling occurs, then equations (2.9) and (2.10) can be rewritten in the form of the amplitudes of these two modes and making the usual "synchronous approximation"

$$\frac{dR}{dz} = i\psi' R(z) + ikS(z) \tag{2.32}$$

$$\frac{dS}{dz} = -i\psi' S(z) + ik^* R(z) \tag{2.33}$$

And *R* and *S* are new amplitudes and defined as:

$$R(z) = A_1(z) \cdot e^{i(\psi_{11}+\psi_{22})\frac{z}{2}} \cdot e^{i\delta z - \frac{\phi}{2}} \tag{2.34}$$

$$S(z) = A_2(z) \cdot e^{-i(\psi_{11}+\psi_{22})\frac{z}{2}} \cdot e^{-i\delta z + \frac{\phi}{2}}$$

(2.35)

ψ_{11} and ψ_{22} are "*dc*" coupling coefficients as defined earlier in equation (2.14) and k is "*ac*" cross coupling coefficient defined in equation (2.15). Here $k = k_{21} = k^{*}_{12}$ and ψ' is the general "*dc*" self-coupling coefficient and is introduced as:

$$\psi' = \delta + \left(\frac{\psi_{11} - \psi_{22}}{2} \right) - \frac{1}{2} \frac{d\phi}{dz}$$

(2.36)

If δ is considered constant along z direction then, will follow the below equation:

$$\delta = \frac{1}{2}(\beta_1 - \beta_2) - \frac{\pi}{\Lambda} = \pi \Delta n_{eff} \left[\frac{1}{\lambda} - \frac{1}{\lambda_D} \right]$$

(2.37)

As it was introduced before, $\lambda_D = \Delta n_{eff} \Lambda$ is the design wavelength for a grating approaching zero index modulation and the correspondent grating condition for FBGs is $\lambda = \lambda_D$. In FBGs, the forward-coupling equations, equations (2.32) and (2.33) are first-order ordinary differential equations with constant coefficients. Thus when the appropriate boundary conditions are given, the closed form solutions can be found. However in the case of a uniform forward-coupled grating, ψ' and k are constants and in contrast to the FBG, here the coupling coefficient k may not be written as simple as defined in equation (2.23) and required the numerical evaluation. The transmission can be found by assuming only one mode is incident from $z \rightarrow -\infty$ (i.e. $R(0) = 1$ and $S(0) = 0$). The respective power bar and cross transmission

$$t_= = \frac{|R(z)|^2}{|R(0)|^2}$$

(2.38)

and

$$t_\times = \frac{|S(z)|^2}{|R(0)|^2} ,$$

(2.39)

can be shown to be [Yarin1973]:

$$t_{=} = \cos^2\left(\sqrt{k^2 + \hat{\psi}^2}\, z\right) + \frac{1}{1 + \dfrac{k^2}{\hat{\psi}^2}} \sin^2\left(\sqrt{k^2 + \hat{\psi}^2}\, z\right) \tag{2.40}$$

and

$$t_{\times} = \frac{1}{1 + \dfrac{\hat{\psi}^2}{k^2}} \sin^2\left(\sqrt{k^2 + \hat{\psi}^2}\, z\right), \tag{2.41}$$

respectively. The maximum cross transmission (which occurs when $\hat{\psi} = 0$) is found to be

$$t_{\times,max} = \sin^2\left(kL\right), \tag{2.42}$$

and it occurs at the wavelength

$$\lambda = \frac{1}{1 - \left(\psi_{11} - \psi_{22}\right)\dfrac{\Lambda}{2\pi}} \lambda_D. \tag{2.43}$$

For coupling between a core mode '*1*' and a cladding mode '*2*' with an induced index change in the core only, $\psi_{11} = \psi$ from (2.22), $\psi_{22} \ll \psi_{11}$. Therefore, (2.43) can be approximated as

$$\lambda \cong \left(1 + \frac{\overline{\delta n_{eff}}}{\Delta n_{eff}}\right)\lambda_D, \tag{2.44}$$

where $\overline{\delta n_{eff}} \ll \Delta n_{eff}$.

In an LPG, forward-mode coupling between the core and cladding modes occurs in which the resonant wavelength satisfies:

$$\lambda_{res} = \left(n_{core}^{eff} - n_{cladding,m}^{eff}\right)\Lambda \tag{2.45}$$

In the above equation, n_{core}^{eff} and $n_{cladding,m}^{eff}$, are the effective indices of the core and *mth* cladding mode, respectively. As the difference between core and cladding mode effective indices are far

less than unity, the period of LPG is much larger than that of FBG. In fact, the investigated periods for LPGs are factors of hundred microns, where the period of FBG is less than one micron [Bhatia1996, Vengsarkar1996].

Around λ_{res}, the energy of the propagating cladding modes is lost due to absorption and scattering in the surrounding environment, creating a rejection band in the transmission spectrum, strongly dependent of the external medium (temperature, refractive index, pressure and so on). The minimum transmission at λ_{res} is given by the expression

$$T^m = 1 - sin^2\left(kL\right),$$

(2.46)

where L is the length of the LPG and k is the coupling coefficient for the *mth* cladding mode, which is determined by the overlap integral of the core and respective cladding mode and by the amplitude of the periodic modulation of the mode propagation constants [James2003]. An LPG transmission spectrum is shown in Figure 2.9, which presents five attenuation bands [Bhatia1997]. Each one of these bands can be used to measure a specific parameter.
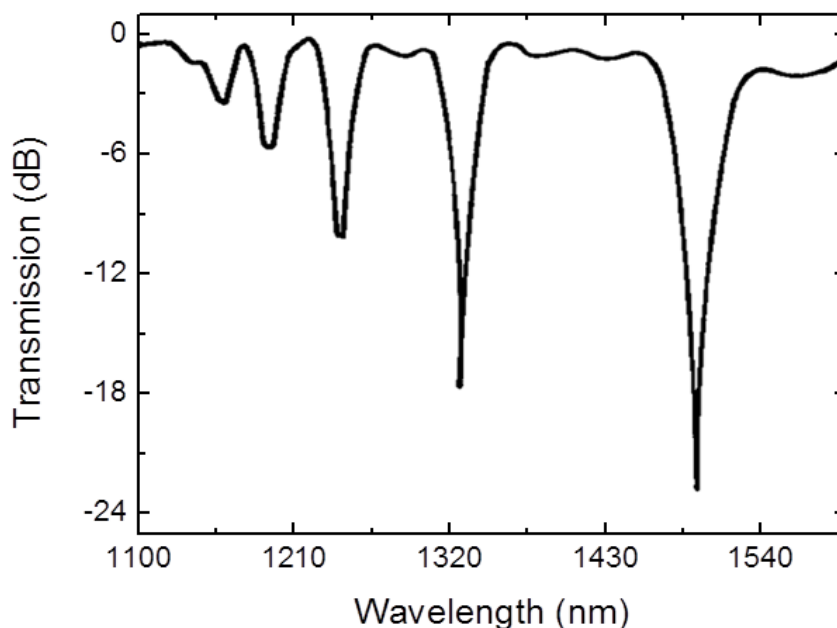
Figure 2.9 - Transmission spectrum of an LPG inscribed in a SMF-28 fiber with period 320 μm, by Bhatia [Bhatia1997].

2.2.3. Phase Match Condition

In the presence of the grating perturbation in the fiber core, the bound wave can be coupled to either backward or forward propagating modes. Fiber gratings can be categorized in two main types according to the direction of mode coupling. One category contains the gratings which are backward-coupled including FBGs with uniform and chirped structures and tilted fiber grating (TFG) with small tilt angles, while the other group includes LPGs and TFGs with large tilt angle in which coupling occurs between forward propagating modes. So to transfer energy from one mode of amplitude $A_1(z)$ into a counter- or co- propagating mode of amplitude $B_2(z)$, the phase mismatch factor is defined as a detuning:

$$\Delta\beta = \beta_1 \pm \beta_2 - \frac{2\pi}{\Lambda}M\cos\theta_{TFG} \qquad (2.47)$$

β_1 and β_2 are the propagation constants for incident and diffracted modes respectively. θ_{TFG} is a tilt angle and M is the diffraction order. Also "±" sign defines the propagation direction of "∓ (z)". To transfer a significant portion of energy the phase mismatch factor should be zero or phase matching condition satisfies $\Delta\beta = 0$, therefore:

$$\beta_1 \pm \beta_2 = \frac{2\pi}{\Lambda}M\cos\theta_{TFG} \qquad (2.48)$$

In backward propagation, β_1 and β_2 both have identical positive signs where for co-propagation β_1 and β_2 have opposite signs. In most cases, the first order diffraction is dominant and therefore, *M = 1*. By substituting equation (2.8), the resonant wavelength this satisfied in the following relationship:

$$\lambda = \left(n_{eff,i} \pm n_{eff,j}\right)\frac{\Lambda}{\cos\theta_{TFG}} . \qquad (2.49)$$

2.3. Tilted Fiber Grating

TFGs are created when the grating structure is tilted by an angle θ_{TFG}. In such gratings, the mode coupling is not as simple as normal gratings. As illustrated in Figures 2.10 (a) and (b) in TFGs mode coupling can occur in either forward or backward direction depending on the tilt angle.
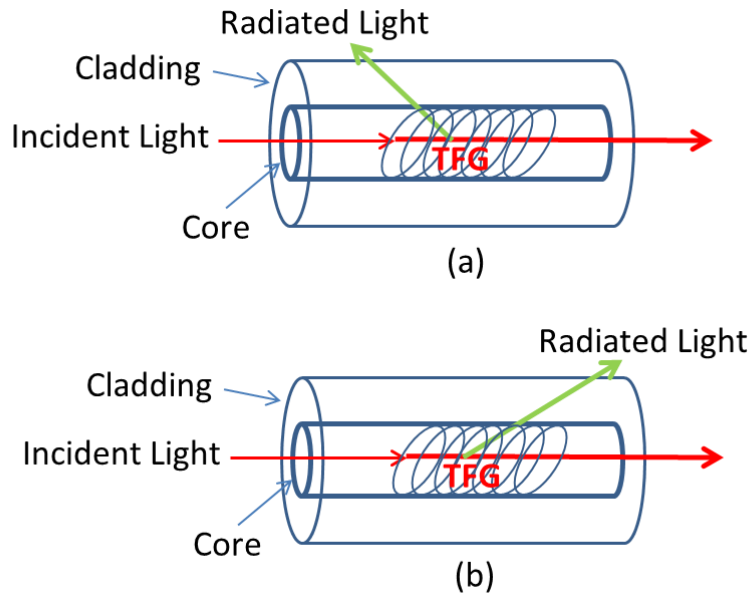
Figure 2.10 – Schematic diagram of (a) backward-mode and (b) forward coupling in TFG.

In the case of tilted gratings, the resonant wavelengths are [Erdogan1996, Bhatai1996]:

$$\lambda_{res} = \left(n_{core}^{eff} \pm n_{cladding,m}^{eff} \right) \frac{\Lambda}{\cos\theta_{TFG}}$$

(2.50)

The sign of "+" and "-" in the above equation indicate the direction of the mode propagation toward - z or + z direction respectively. As it is schematically presented in Figure 2.11, in TFGs, the grating period along the fiber axis is simply identified by the following relationship:

$$\Lambda_{TFG} = \frac{\Lambda}{\cos\theta_{TFG}}$$

(2.51)
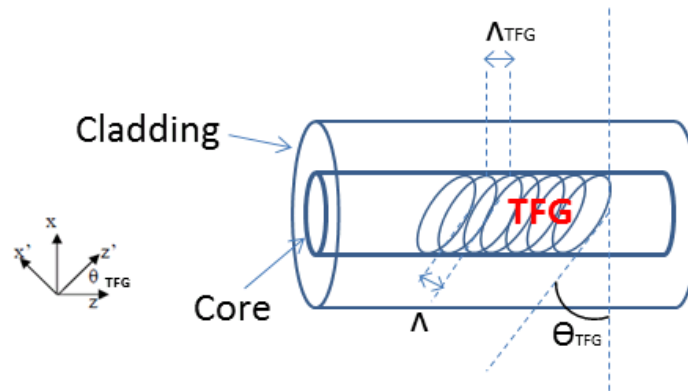
Figure 2.11 – Schematic diagram of TFG.

The photo-induced index change in the core of a SM optical fiber, δn_{core}, follows the below relationship:

$$\delta n_{core}(z) = \overline{\delta n_{core}}(z')\left\{1 + v\cos\left[\frac{2\pi}{\Lambda}z' + \phi(z')\right]\right\}$$
(2.52)

z' (illustrated in Figure 2.11) in equation (2.52) is defined as $z' = x\sin\theta_{TFG} + z\cos\theta_{TFG}$. But for slightly varying functions $\overline{\delta n_{core}}(z')$ and $\phi(z')$, it can be considered as $z' = z\cos\theta_{TFG}$. Then by taking the projectile of these functions along the fiber axis (z), the general coupling coefficient (previously introduced in equation (2.13) can be rewritten in the following format:

$$D_{\mp\pm}^{t}(z) = \psi(z) + 2k_{\mp\pm}(z)\cos\left(\frac{2\pi}{\Lambda_{TFG}}z + \phi(z\cos\theta_{TFG})\right)$$
(2.53)

where subscript "*n*" in equation (2.13) is associated with forward propagating mode (+ sign) and subscript "*j*" describes the backward propagating mode (− sign). The self-coupling coefficient and cross coupling coefficient now become:

$$\psi(z) = \frac{wn_{core}}{2}\overline{\delta n_{core}}(z\cos\theta_{TFG})\iint\limits_{core} e_{\mp}^{T}(x,y) \cdot e_{\pm}^{T*}(x,y)dxdy$$
(2.54)

and

$$k_{\mp\pm}(z,\theta_{TFG})=\frac{v}{2}.\frac{wn_{core}}{2}\overline{\delta n_{core}}(z\cos\theta_{TFG})\iint\limits_{core}e^{\left(\pm i\frac{2\pi}{\Lambda_{TFG}}x\tan\theta_{TFG}\right)}.e_{\mp}^{T}(x,y).e_{\pm}^{T*}(x,y)dxdy \qquad (2.55)$$

It is worthy to note that $k_{\mp}=k_{\pm}^{*}$. The effect of tilting the structure of the grating is correspondent to "effective fringe visibility" defined as $v_{\mp\pm}(\theta)$ in the following relationship:

$$\frac{v_{\mp\pm}(\theta_{TFG})}{v}=\frac{\iint\limits_{core}e^{\left(\pm i\frac{2\pi}{\Lambda_{TFG}}x\tan\theta_{TFG}\right)}.e_{\mp}^{T}(x,y).e_{\pm}^{T*}(x,y)dxdy}{\iint\limits_{core}e_{\mp}^{T}(x,y).e_{\pm}^{T*}(x,y)dxdy} \qquad (2.56)$$

So it can be rewritten

$$k_{\mp\pm}(z,\theta_{TFG})=\frac{v_{\mp\pm}(\theta_{TFG})}{2}\psi(z) \qquad (2.57)$$

in direct analogy to equation (2.15). The result indicates that tilting the grating structure leads to reduction of the effective fringe visibility by amount presenting in equation (2.56). Also this result describes the effect of the grating perturbation in backward scattering.

2.4. Nonuniform Gratings

Most fiber gratings designed for practical applications are not uniform gratings. Often the main reason for choosing a nonuniform design is to reduce the undesirable side lobes prevalent in uniform-grating spectra; but there are many other reasons to adjust the optical properties of fiber gratings by tailoring the grating parameters along the fiber axis. Chirping the period of a grating enables the dispersive properties of the scattered light to be tailored [Kogelnik1976]. Chirped fiber gratings are useful for dispersion compensation [Ouellette1987], for controlling and shaping short pulses in fiber lasers [Fermann1995], and for creating stable continuous wave (CW) and tunable mode-locked external-cavity semiconductor lasers [Morton1994], [Morton1993].

Sometimes it is desirable to create discrete, localized phase shifts in an otherwise periodic grating. Discrete phase shifts can be used to open an extremely narrow transmission resonance in a reflection grating or to tailor the passive filter shape.

Considering the non-uniformity of the grating, the reflection and transmission spectra from the two-mode coupling can be calculated by considering a piecewise approach, whereby the grating is divided into discrete uniform sections that are individually represented by a matrix. The solution is found by multiplying the matrices associated with each one of the sections. The characteristic equation is solved by making the matrix determinant equal to zero and the resulting polynomial enables the eigenvalues to be found.

The FBG of length *L* can be treated as a quadrupole, as show in Figure 2.12, where *R* and *S* represent the co-propagating and counter-propagating modes, respectively. For convenience, the amplitude *R(0)* of the incident wave is normalized, in such a way that the maximum value is equal to unit at the origin (*z = 0*).
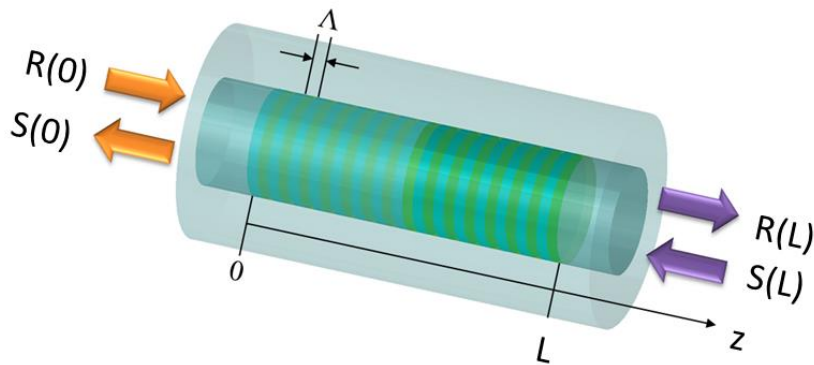
Figure 2.12 - Bragg grating schematic as a quadrupole. R and S represent the co-propagating and counter-propagating modes, respectively.

Splitting the grating in M_i uniform sections and defining R_i and S_i as amplitudes of the fields across the section *i*, the propagation through the section is described by the equation

$$\begin{bmatrix} R_i \\ S_i \end{bmatrix} = F_i \begin{bmatrix} R_{i-1} \\ S_{i-1} \end{bmatrix},$$ (2.58)

For Bragg gratings the matrix $\mathbf{F}_i^B$ is given by

$$F_i^B = \begin{bmatrix} \cosh(\gamma_B \Delta z) - i\dfrac{\psi'}{\gamma_B}\sinh(\gamma_B \Delta z) & -i\dfrac{k}{\gamma_B}\sinh(\gamma_B \Delta z) \\[2em] i\dfrac{k}{\gamma_B}\sinh(\gamma_B \Delta z) & \cosh(\gamma_B \Delta z) + i\dfrac{\psi'}{\gamma_B}\sinh(\gamma_B \Delta z) \end{bmatrix}, \qquad (2.59)$$

where Δz is the length of the *i-th* uniform section and

$$\gamma_B \equiv \sqrt{k^2 - \psi'^2} . \qquad (2.60)$$

For transmission gratings the matrix F_i^c is shown as

$$F_i^c = \begin{bmatrix} \cosh(\gamma_c \Delta z) + i\dfrac{\psi'}{\gamma_c}\sinh(\gamma_c \Delta z) & i\dfrac{k}{\gamma_B}\sinh(\gamma_B \Delta z) \\[2em] i\dfrac{k}{\gamma_c}\sinh(\gamma_c \Delta z) & \cosh(\gamma_c \Delta z) - i\dfrac{\psi'}{\gamma_c}\sinh(\gamma_c \Delta z) \end{bmatrix}, \qquad (2.61)$$

with

$$\gamma_c \equiv \sqrt{k^2 + \psi'^2} . \qquad (2.62)$$

Once all of the matrices for the individual sections are known, the output amplitude are given by:

$$\begin{bmatrix} R_M \\ S_M \end{bmatrix} = F_M \cdot F_{M-1} \cdot .... \cdot F_i \cdot .... \cdot F_1 \begin{bmatrix} R_0 \\ S_0 \end{bmatrix}. \qquad (2.63)$$

To implement the piecewise approach for apodized and chirped gratings, it is only assign constant values ψ, k, and $(1/2)d\phi/dz$ to each uniform section, where these might be the z-dependent values of $\psi(z)$, $k(z)$, and $(1/2)d\phi/dz$ evaluated at the center of each section. For phase-shifted gratings, a phase-shift matrix F_π is inserted between the factors F_i and F_{i+1} in the product in (2.63) for a phase shift after the *ith* section. For Bragg gratins the phase-shift matrix is of the form

$$F_\pi^B = \begin{bmatrix} e^{\left(\frac{-i\phi_i}{2}\right)} & 0 \\ 0 & e^{\left(\frac{i\phi_i}{2}\right)} \end{bmatrix},$$ (2.64)

and for transmission gratings

$$F_\pi^c = \left(F_\pi^B\right)^*,$$ (2.65)

since the field amplitudes propagate in the *-z* direction for Bragg gratings but the *+z* direction for transmission gratings. ϕ_i is the shift in the phase of the grating itself for discrete phase shifts, and for sampled gratings

$$\frac{\phi_i}{2} = \frac{2\pi n_{eff}}{\lambda}\Delta z_0,$$ (2.66)

where Δz_0 is the separation between two grating sections.

2.4.1. Chirped FBGs

The aperiodic Bragg gratings are known in the literature for gratings with chirp and generally refer to gratings in which the resonance condition varies along its length. If the variation of the periodicity is small, it can be considered locally uniform. Because of this, each part of the grating will reflect different wavelengths without affecting each other [Byron93]. The most common aperiodic FBGs are gratings with variable period along its longitudinal extension. The aperiodicity type is controlled by the parameter $\phi(z)$ in equation (2.12). The aperiodicity has effect in two properties of Bragg gratings: the bandwidth and group delay. In aperiodic FBGs the resonance condition occurs for various wavelengths, resulting in a grating with a bandwidth much higher than conventional FBGs. This property is sometimes used in applications where it is necessary optical filters with a high rejection band. As mentioned, the group delay characteristics of the grating are different from conventional gratings. Since different wavelengths are reflected in different positions on the fiber, it causes a group delay dependent on the wavelength. If the aperiodicity is linear, the delay group will also be linear, can be used in devices dispersion compensation in optical communications as proposed originally by Ouellete [Ouellete1987].

Subsequently, several studies followed using aperiodic gratings to compensate the dispersion in different situations [Loh1996, Laming1997 or Garrett1998]. Besides gratings with linear aperiodicity, the aperiodic gratings were also tested with quadratic aperiodicity [Eggleton1994] or even with jumps in the period [Farries1994]. Another use for these FBGs is the temporal reformatting of short pulses in fiber lasers [Fermann1995].

Generally, the period of an aperiodic FBG can be expressed by a polynomial of *N* degree given by

$$\Lambda(z) = \Lambda_0 + \Lambda_1 z + ... + \Lambda_N z^N \tag{2.67}$$

where Λ_0 is the period to the grating input. Figure 2.13 shows schematically the period variation over an FBG with linear aperiodicity.
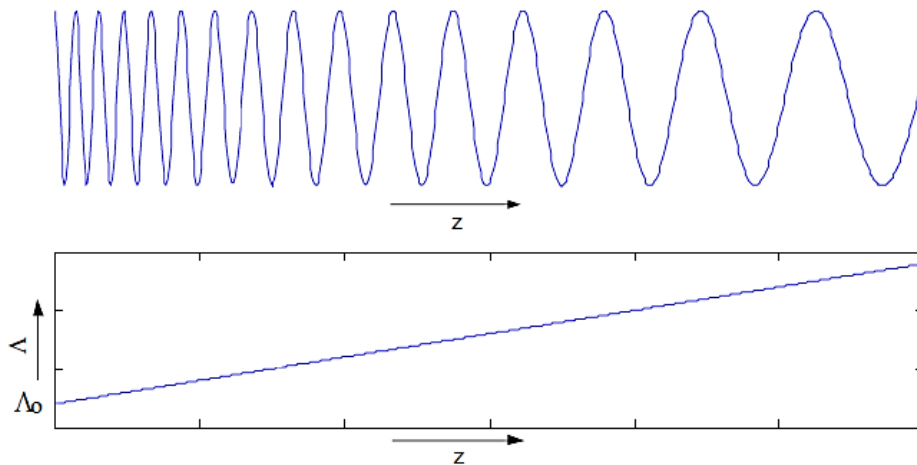
Figure 2.13 – Illustration of the refractive index variation in a linear aperiodic grating (above) and the respective period variation (below) [Nogueira2005].

The group delay dependent on wavelength of aperiodic gratings can be used for various purposes, including dispersion compensation. Figure 2.14 shows the reflectivity of a Bragg grating aperiodic without apodization, wherein the linear aperiodicity coefficient of equation (2.67) is Λ_1= 0,8 nm/cm.

Being the linear aperiodicity, the group delay also shows a linear behavior. The simulation was carried out considering the grating input shows larger period, so that the slope is negative. An approximation for the maximum group delay induced by the grating, τ_{max}, can be easily calculated

from the physical parameters of the grating. Whereas minimum group delay is zero, τ_{max} is the time that field takes to travel the grating to the end and to back to the beginning (*2L*). Thus:

$$\tau_{\max} \approx \frac{2Ln_{eff}}{c} \tag{2.68}$$

In case of Figure 2.14 the obtained τ_{max} is ~242 ps, which is in agreement with the measured value graphically.
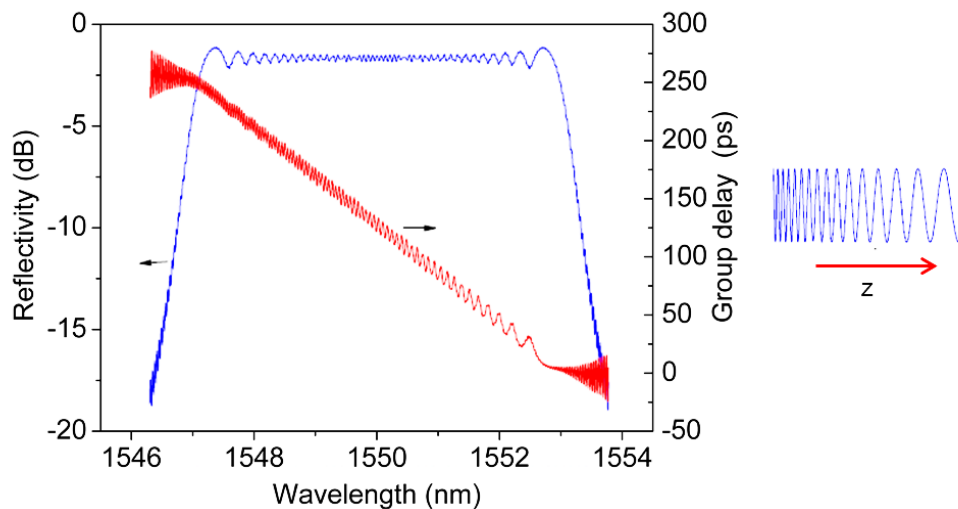
Figure 2.14 – Reflection spectrum and group delay of an aperiodic Bragg grating. L = 25 mm;
Λ_1 = 0,8 nm/cm (Adapted from [Nogueira2005]).

Note that the period variation in the Bragg grating is not the only method to change the resonance condition along its extension, despite being the most common. It is also possible to obtain the same effect by variation of average refractive index along the z-axis and keeping the constant period. However, it is more difficult to obtain this kind of gratings with high quality since it is necessary to control accurately the average value of refractive index. This technique although apparently be easier to implement, it is necessary to have in account the non-linear dependence of refractive index variation with exposition time. This is a technique that can be used when there is no technical means to inscribe a grating with variable period. The Figure 2.15 shows a simulated grating with this technique.
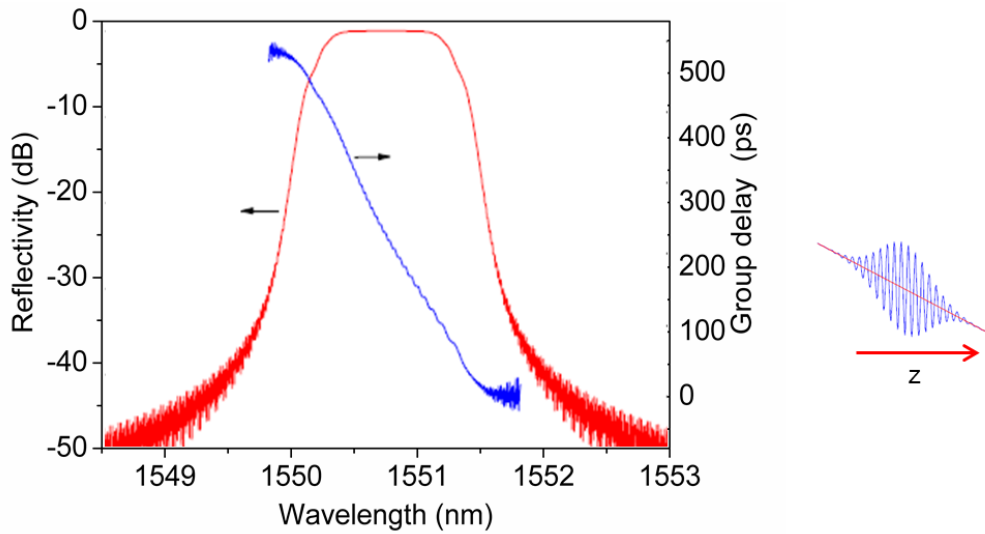
Figure 2.15 - Bragg grating with uniform period and linear value variation of the refractive index average value. Simulation parameters: L = 50 mm; $\overline{\delta n_{eff}}(z)=(z/L)\times 10^{-4}$. Right: Illustration of the refractive index profile (Adapted from [Nogueira2005]).

2.4.2. Fabry-Perot Cavities and Phase-Shifted FBGs

These structures, which were first documented by Huber [Huber1991] consists of two Bragg gratings spaced apart appropriately, forming one resonant cavity (Figure 2.16). One of the characterizing parameters of such structures is the Free Spectral Range (FSR). This parameter designates the spacing between maxima of the spectral response of the cavity. In the case of Fabry-Perot cavity formed by two mirrors off, spaced by a distance d, the FSR can be calculated by

$$FSR(\lambda)=\frac{\lambda^2}{2dn_{eff}(\lambda)}$$

(2.69)

For an equivalent Fabry-Perot cavity formed by two Bragg gratings, the FSR is not possible to calculate from a single distance d. In fact, d becomes a function dependent on the wavelength [Kashyap1999]. Under these conditions, the FSR is maximum at the reflection peak and can be calculated in good approximation by expression (2.69) and considering d as the distance between the inner ends of the cavity. The wavelengths farther away from the resonance condition penetrate more easily into two gratings, so that the distance d will be greater. Thus, the

FSR will decrease as the wavelength deviate from the condition resonance to a minimum value given by (2.69) where *d* is the distance between the opposite extremes. It is concluded that for the FSR is constant (for instance, optical clock recovery), it is necessary that FBGs have the smallest possible length. Similarly, for the FSR is the highest possible, it is necessary to reduce the distance between the gratings to the fullest.

In either case, both the reduction in gratings length, and the reduction of distance between them have higher demands technical standpoint.
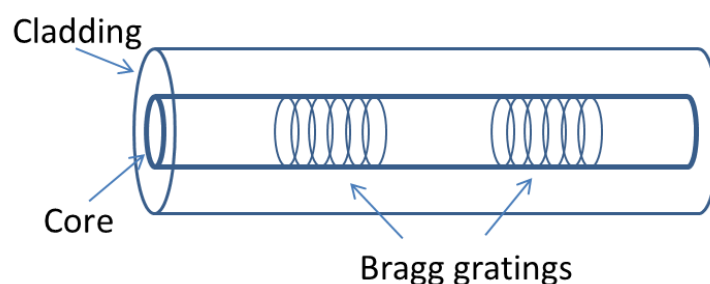
Figure 2.16 – Schematic representation of a Fabry-Perot cavity in optical fiber.

When used in transmission, this type of FBGs has a set of very narrow filters with interest in optical communications. As mentioned above, the spacing between the maximum resonance depends on the distance between gratings. The Figure 2.17 allows observing the transmission spectra of three cavities based on these Bragg gratings, but distances different between them. The distance between the maximum transmission for distances *d* = 5 mm, *d* = 10 mm and *d* = 20 mm is respectively FSR_5 = 0,131 nm, FSR_{10} = 0,074 nm and FSR_{20} =0,039.

The Bragg gratings with phase shift can be considered as a particular case of Fabry-Perot cavities based on fiber Bragg gratings, where the distance between the inner ends are lower than the modulation period. This technique results an adaptation of other similar technique used in semiconductor lasers with Distributed Feedback (DFB) to allow the laser operate on a single frequency [Haus1976]. In spectral terms, the phase shift in the modulation index causes a transmission filter on the rejection band of the grating. The wavelength of this filter can be selected through the grating position of the phase jump, the type of induced phase jump, or both. Generally, the tuning is made with different phase shifts amplitudes between 0 and 2π, placed in

the center of the grating, or by fixed phase shifts of π, corresponding to a spacing of $\lambda/4$ at different grating locations [Agrawal1994]. The phase-shifted FBGs can also be used in other applications such as in optical switches [Melloni2000] or formatting impulses [Curatu2002].
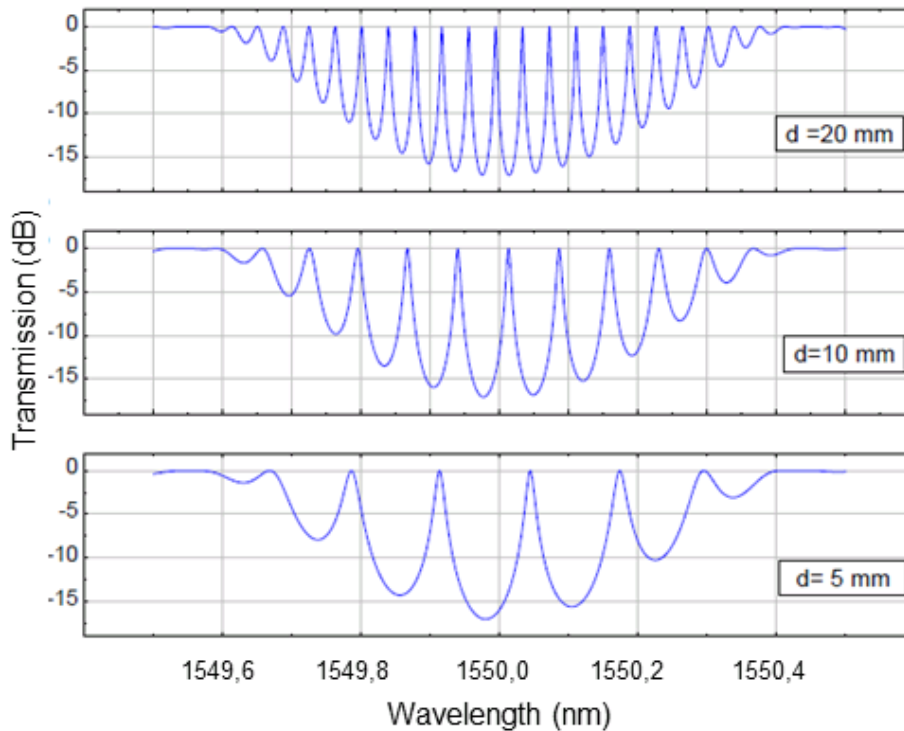
Figure 2.17 – Transmission spectra of Fabry-Perot cavities based on Bragg gratings with different distance between gratings. L = 2 mm [Nogueira2005].

2.5. Bragg Gratings Fabrication Methods

Advanced fabrication methods are essential for obtaining high quality and low cost Bragg gratings for telecom and sensing applications. An ideal Bragg grating technique should present some important features. First of all, it must allow the inscription of gratings with good physical and optical qualities. The mechanical strength of a grating should not be degraded significantly after fabrication when compared with the strength of a good quality fiber. Also, a narrow and well defined spectral linewidth and a low excess loss are normally required to achieve high resolution measurements. Secondly, a fabrication technique should allow good repeatability, mainly of the central wavelength and the reflectivity in order to make Bragg gratings standard devices under

the condition of mass production and interchangeable without calibration. Thirdly, it should be flexible, since reflectivities and central wavelengths of the produced gratings should be easily selectable. Finally, and in a commercial point of view, it should provide an economical mass production capability, since low cost Bragg gratings would be available if they could be mass produced at high speed.

The Bragg grating fabrication techniques most used broadly fall into two categories: the interferometric and the phase mask approaches. In the first category, a single UV input beam is divided into two, interfering then at the fiber plane. The second depends on an exposure of the fiber through an optical diffractive element. Currently, within these two categories there are four major different techniques for FBGs fabrication in optical fibers: amplitude-splitting interferometer, wavefront-splitting interferometer, phase mask technique, long FBG inscription and point-by-point Inscription. The mechanism of the different inscription techniques will be presented and described very briefly. More details on each inscription method can be easily found in [Othonos1999, Kashyap1999].

2.5.1. Amplitude-Splitting Interferometer

The interferometer method for transversal inscription of FBGs was first demonstrated by Meltz et al. in 1989 [Meltz1989]. The configuration of a typical amplitude-splitting interferometer for a high coherence UV laser source utilized in FBG fabrication is shown in Figure 2.18 (a). During the inscription, the UV Laser beam is divided into two equal intensity beams by the beam splitter and then these two beams are reflected to intersect at angle θ from two UV mirrors, while the fiber was held at the intersection of the beams. The Bragg grating period is equal to the interference fringe period, which is given by

$$\Lambda = \frac{\lambda_{UV}}{2n_{eff} \sin\dfrac{\theta}{2}}$$

(2.70)

where λ_{UV} is the wavelength of the writing radiation and θ is the mutual angle of the UV beams.
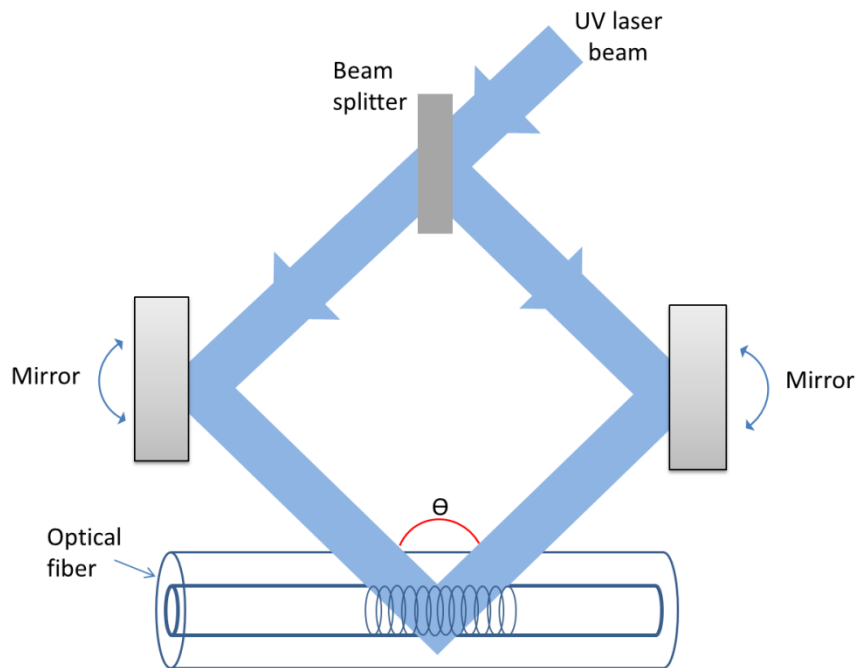
(a)
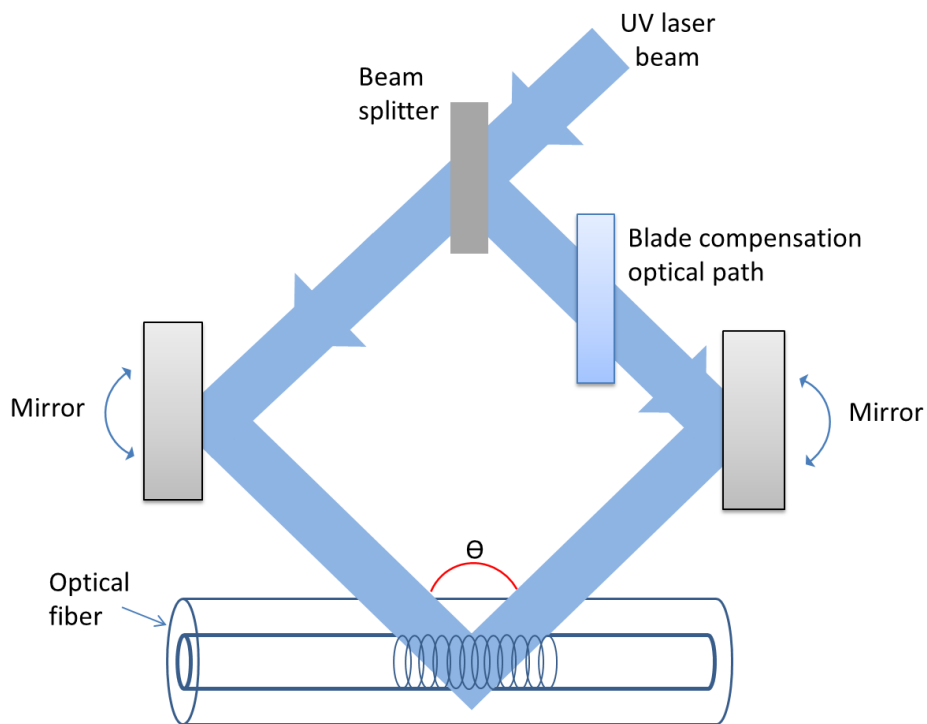
(b)

Figure 2.18 - (a) A typical amplitude-splitting interferometer configuration for high coherence UV laser utilized in the fabrication of Bragg gratings in optical fibers; (b) An improved amplitude splitting interferometer for low spatial coherence source. [Othonos1999]

Sometimes, a low spatial coherence laser source, for example, the excimer laser is used. For this kind of source, the fringe pattern for laser beams produced by the arrangement in Figure 2.18 (b) will be in low quality, because there exists different number of reflections in each optical path, leading to one interfering beam acquire lateral orientation compared with the other one. Thus, it is necessary to correct the difference optical paths induced by beam splitter. Typically, a SiO_2 blade with correct thickness will solve the problem, as shown in Figure 2.18 (b).

The advantage and disadvantage of amplitude-splitting interferometer are both quite clear. The most important advantage of the interferometric method is that by changing the intersection angle, this setup can inscribe a Bragg grating at any desired wavelength. However, like all other interferometers, entirely isolating the optical components in the setup from mechanical vibrations and air flows is very important and actually is unachievable. Sub-micrometer displacements of the laser beam caused by vibrations and air currents can affect the quality of the interference fringe pattern, which lead to low fringe visibility, thus low strength of the grating.

2.5.2. Wavefront-Splitting Interferometer

There are two typical configuration of the wavefront-splitting interferometer used to fabricate Bragg gratings in optical fiber: the prism interferometer [Kashyap1990] and the Lloyd´s mirror interferometer [Kashyap1999]; both interferometers are shown in Figure 2.19. The dominant principle of this interferometric method is that if a collimated UV beam is incident at a reflective surface, for example, a mirror or prism edge, then half of the beam is reflected across the path of the incident beam so that there is interference occurring in the region where the reflected and unreflected beams overlap and the interference fringe pattern is focused to the core of the fiber by a cylindrical lens. With a wavefront-splitting interferometer, the grating quality is less affected by the environment, since the reduction of the optical components together with the optical path in the system. It is easy to inscribe Bragg gratings at tunable wavelength; however the tuning range is limited by the interferometer arrangement. In addition, the length of the Bragg grating fabricated with this kind of system is restricted to the half of the incident UV beam width.
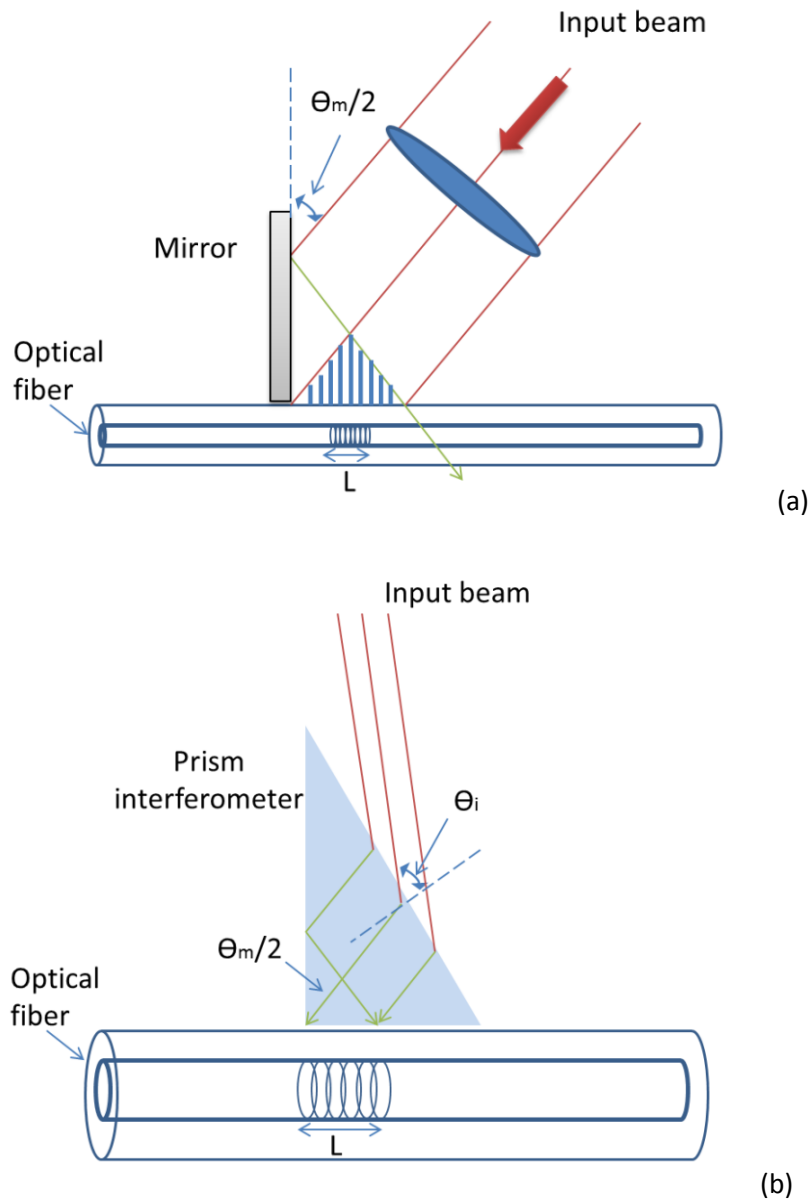
Figure 2.19 - (a) Schematic of a Lloyd´s mirror wavefront-splitting interferometer; (b) Schematic of a prism wavefront-splitting interferometer [Othonos1999]. $\theta_m/2$ is the angle of the diffracted order, θ_i is the angle of the incident UV beam.

2.5.3. Phase Mask Method

The phase mask method has been reported as an improved technique for the fabrication of Bragg gratings [Hill1993, Anderson1993], allowing easier alignment and inscription. The UV light beam is

spatially phase modulated and diffracted by the phase mask, as shown in Figure 2.20. The produced interference pattern is then used to photoimprint a refractive index modulation in the photosensitive fiber placed in proximity and parallel behind the phase mask.
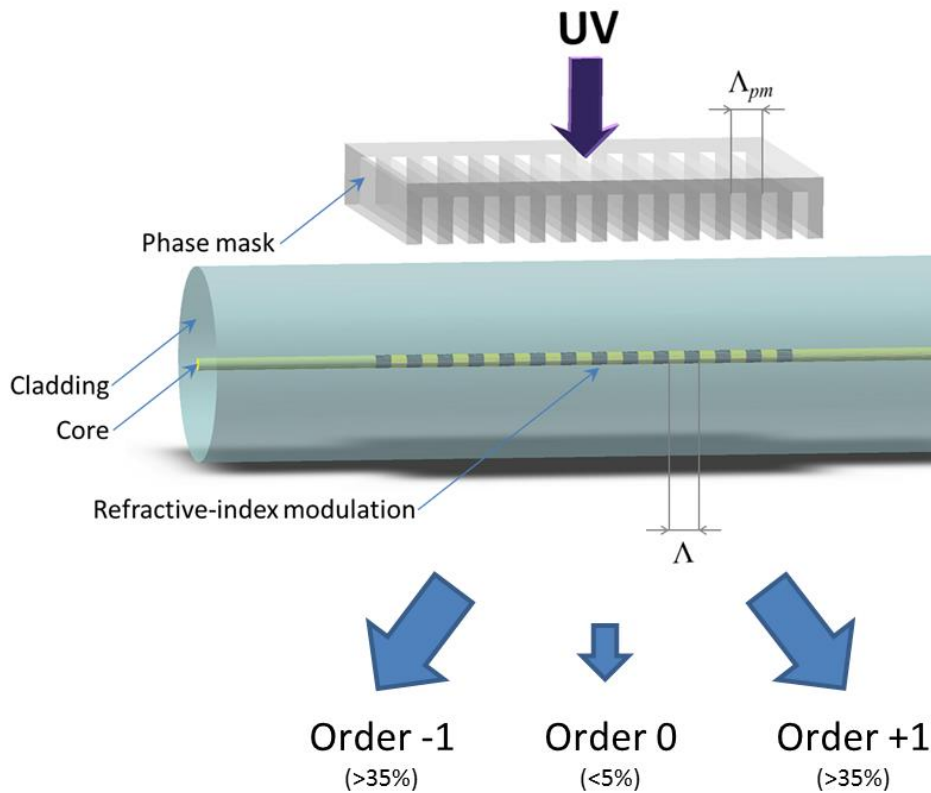
Figure 2.20 – Schematic diagram of the phase mask method.

As it can be seen from Figure 2.20, the phase mask is basically a grating etched in a high quality silica plate with well controlled space ratio and depth of the etched grooves. The principle of operation is based on the diffraction of an incident UV beam into several orders, $M = 0, \pm1, \pm2….$ The incident and diffracted orders satisfy the general diffraction equation, with the period of the phase mask, Λ_{pm}, being given by

$$\Lambda_{pm} = \frac{M\lambda_{UV}}{\sin\left(\frac{\theta_m}{2}\right) - \sin(\theta_i)}$$

(2.71)

where $\theta_m/2$ is the angle of the diffracted order, and θ_i is the angle of the incident UV beam. For normal incidence ($\theta_i = 0$), as represented in Figure 2.20, the diffracted radiation is split into $M = 0$ and ±1 orders. By a proper adjustment of the grooves depth, the zero diffraction order can be suppressed to values below 5 %, while each of the main diffracted beam orders (+1 and -1) contain more than 35 % of the incident radiation. Each phase mask has a zero order minimized for a single incident wavelength and so should be used with care at other wavelengths since this factor can influence the grating pattern. The interference pattern of the two beams of orders ±1 brought together has a period Λ given by

$$\Lambda = \frac{\lambda_{UV}}{2\sin\left(\dfrac{\theta_m}{2}\right)} = \frac{\lambda_{UV}}{2\dfrac{\lambda_{UV}}{\Lambda_{pm}}} = \frac{\Lambda_{pm}}{2} \tag{2.72}$$

which is exactly half the value of the phase mask period and is independent of the UV wavelength. The Bragg wavelength, λ_B, required for the grating in the waveguide is determined by the period of the grating etched in the mask, Λ_{pm}. Thus, relating equations (2.72) and $\lambda = 2n_{eff}\Lambda$ becomes

$$\lambda_B = n_{eff}\Lambda_{pm} \tag{2.73}$$

The apparatus that implements the phase mask method is very compact and in general less sensitive to vibrations. But one of the most important advantages is the small coherence needed in the UV illuminating source to create the desired interference pattern. Associated with the fact that the Bragg wavelength is determined by the pitch of the phase mask and is independent of the wavelength of the UV source, this makes this technique much more attractive than the one described in 2.5.1 or 2.5.2. It also offers a high probability of mass production with good repeatability at low cost. However, for each Bragg wavelength a different phase mask is required. In order to remove this disadvantage, several approaches and modified schemes based in this technique have been presented. The easiest approach is to apply some mechanical tension to the optical fiber which allows to shift down the Bragg wavelength to a maximum of ~3 nm [Zhang1993]. Another approach is the placement of a reducing lens before the phase mask, allowing the tuning of the Bragg wavelength of ~2 nm [Prohaska1993]. Other modifications have been proposed, like for example, where the phase mask is used as a beam splitter (see

Figure 2.21) [Kashyap1994]. In this case, one or two of the mirrors are rotatable and/or displaceable, building a small size interferometer integrating the flexibility of the mirror interferometer and the compactness of the phase mask scheme. This scheme allows wide wavelength tunability and it may have any type of grating which can also be replicated and translated to different wavelengths.
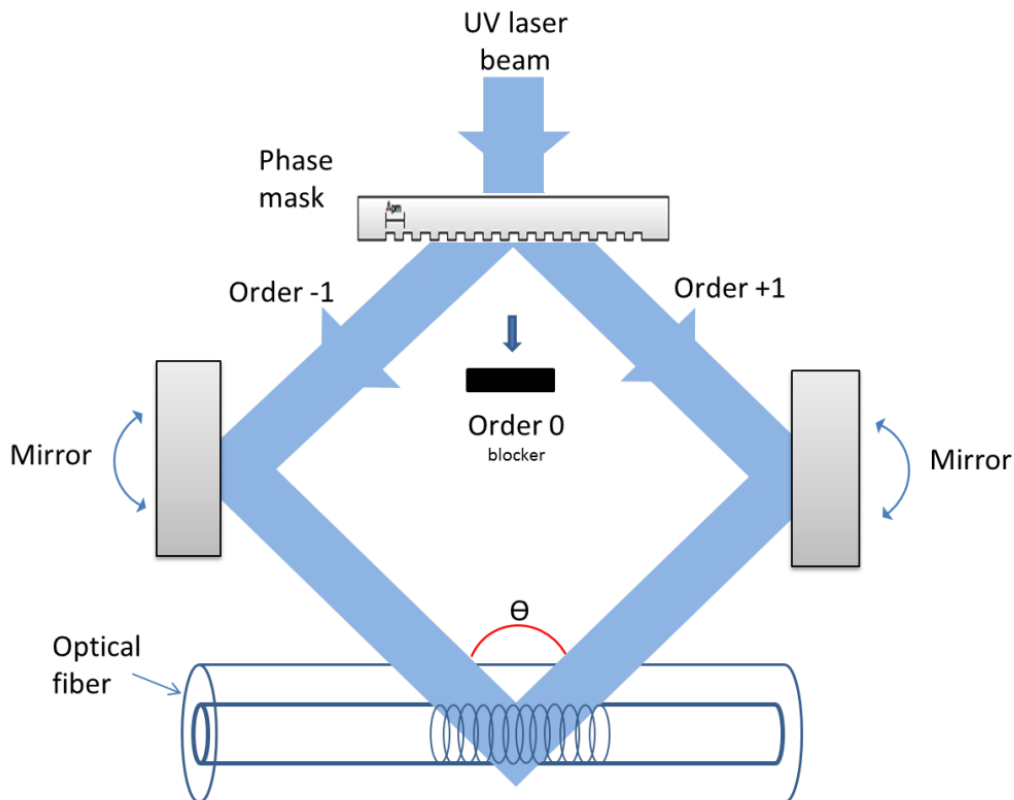
Figure 2.21 – Phase mask used as beam splitter. [Kashyap1999]

2.5.4. Long FBG Inscription

In the methods described above, the length of the grating is inscribed approximately equal to the diameter of the UV beam. On the other hand, it is difficult to develop lasers with large diameter, due to instability problems. Thus, the FBGs inscribed by the described methods do not have dimensions greater than 10 mm (phase mask length). This limitation can be important for some applications based on Bragg gratings. One way to around this is to use the scanning technique. This technique, which can be used in both phase mask and interferometer techniques, consist in

use of a laser scanning in the writing plane. If the whole system, with the exception of laser beam, remains static, the effect is the same inscription with a beam diameter equal to the sweep amplitude for the same power density. Thus, the FBG length is limited by sweep amplitude, the mirrors width or by the phase mask length used. However, in applications where extremely long FBGs are required, it becomes necessary to inscribe in other inscription method which permits FBGs production without the limitations mentioned above. One way to surpass this limitation is to inscribe a set of sequentially adjacent FBGs in fiber. The used translation stage will be sufficiently accurate to avoid phase jumps between exposure lengths or sections. The inscription process of an FBG with a length higher than the length of the phase mask pattern takes advantage of the accurate translation stage. Once the first exposition is completed, the high precise translation stage moves so that another exposition is performed after the first one. This process continues until the target length is achieved. The apodization profile can be controlled by varying the exposure time of each exposition. In the end, the FBG is composed by various sections (one section by exposition) stitched together. These exposure length/sections must be a multiple of the grating period to minimize phase errors and it is another important aspect. As such, the cited technique is based on the stitching method. A detail theoretical description on the stitching method formulation can be found in [Marques2008]. Although the phase mask can produce virtually any pattern, the available phase masks produce an uniform FBG with a length dependent on the slit aperture used and a period given by expression (2.72). The inscription of FBGs with different periods can be achieved by stretching the fiber, or by switching the phase mask. If the inscription is carried out with a fixed phase mask, only able to inscribe FBGs with wavelength defined by the phase mask. To surpass this situation, one can using an interferometer to inscribe a sequential set of gratings with desired wavelength. Thus, it is possible to program the translation stages controller to adjust the interferometer according to the position of the fiber. This technique has some requirements of the technical point of view, since it needs also an adjustment of the fiber position so that it remains in overlap zone of the two orders. Alternatively, one can be used a single mask phase which is moved at a velocity, v_{PM}, while the fiber is moved at a velocity, v_F. In this case, the difference between inscribed and original wavelength is given by

$$\Delta\lambda = \Lambda_{static}\,\frac{v_F}{v_{PM}} \qquad\qquad (2.74)$$

where Λ_{static} is the grating period inscribed in a static situation. Through this method it is possible to program different periodicities along the fiber, sufficing for this, to control the fiber and phase mask velocities.

2.5.5. Point-by-Point Inscription

The first demonstration of the point-by-point technique for fabricating Bragg reflectors was reported by Malo et al. [Malo1993]. This technique uses a UV pulse laser or femtosecond laser to inscribe individual grating planes one step at a time along the core of the fiber. A single pulse of light passes through a slit and then is focused onto the core of the optical fiber. After the refractive index at the irradiation point is changed, the fiber is translated a distance Λ, which is the grating period, from the original place by a precision translation stage. This procedure is repeated until the desired grating structure is obtained. The main advantage of this technique is that the grating parameters, like period, length, can be adjusted flexibly, however, the accuracy control of the translation stage movement is very crucial. This technique is more used in LPGs fabrication as will be seen on the next section.

2.6. Long Period Grating Fabrication Methods

During the inscription of an LPG on optical fiber, the mechanism which facilitates coupling of optical power from the guided mode into co-propagating cladding modes is produced. The most used inscription techniques of LPGs are based on induced changes in the refractive index of the fiber core in a periodic manner, however another class of fabrication methods exists that relies on physical deformation of the fiber to create the required optical modulation [James2003]. Most commonly, the aim technique to produce LPGs is the exposure of photosensitive optical fibers to UV laser radiation using an amplitude mask, a phase mask or an interferometric beam pattern [Vengsarkar1996, Bhatia1996, Erdogan1997a, Bhatia1999, Eggleton2000b]. There are a number of others ways to fabricate LPGs by changing the refractive index of the core without illumination of the fiber by UV laser, such as: irradiation from a carbon-dioxide laser [Wang2010], with femtosecond laser pulses [Mihailov2006] and by applying electric-arc discharges have been used

to inscribe LPGs on a period-by-period basis [Petrovic2007]. Ion implantation through a metal amplitude mask, dopant diffusion into the fiber core, mechanically induced and temporary LPGs using the acousto-optic modulation are other techniques used [Fujimaki2000, Cho2002, Bock2007, Li2002] however, only the most used will be discussed in this thesis. A broad and brief overview of some fabrication techniques will be given here namely, laser UV light, mechanically induced and electric-arc discharges.

2.6.1. Laser UV Light Technique

The most popular fabrication method is inscribed the LPG by exposure to UV light (193-360nm). This was due to the fact when LPG inscription became widely studied [Vengsarkar1996], the UV-inscription systems were already in place for the manufacture of FBG, becoming this method more feasible [James 2003].There are two common techniques to inscribe an LPG in optical fiber by using the UV light: the amplitude mask and the point-to-point techniques [Vengsarkar1996, Kashyap2010]. All processes that depend on illumination by UV light require first that the optical fiber be receptive to this irradiation, in other words, the fiber must be made photosensitive before writing the grating. This can be achieved by doping the fiber silica core with impurity atoms such as germanium or boron; or by hydrogen loading [Kashyap2010] exposing the fiber to high pressure H_2 gas for a significant period of time so that hydrogen diffusion into the core material takes place. Then, it will be made a brief description of the processes most used to fabricate LPGs by UV technique.

2.6.1.1. Amplitude Mask Technique

One of the most common methods for inscribing LPG using UV light is the amplitude mask technique with the desired period [Kashyap2010, Vengsarkar1996]. The amplitude mask contains an array of transparent windows that forms an illuminated-shadow periodical pattern over the fiber as shown in Figure 2.22, yielding a LPG with the same periodicity as that of the mask. The amplitude mask is made from chrome-plated silica [Vengsarkar1996] or alternatively a metal foil is milled or etched with rectangular gaps between grooves whose widths correspond to the required grating period [James2003].
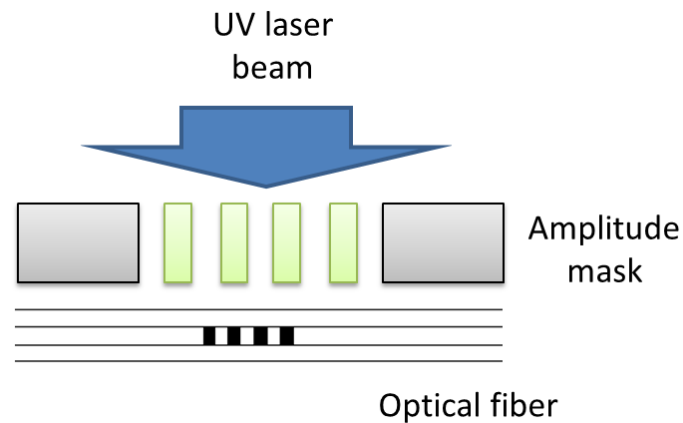
Figure 2.22 – Illustration of the amplitude UV radiation writing.

The fiber is placed in contact with the amplitude mask so that its axis is oriented perpendicular to the mask grooves. Inscription occurs by UV exposure through the amplitude mask and onto the fiber in alternate bands of maximum or minimum intensity, causing corresponding peaks in the refractive index modulation of the photosensitive fiber core. The UV exposition is repeated until the index modulation has reached a desired level to provide the attenuation depth in the LPG transmission spectrum.

2.6.1.2. Point-by-Point UV Technique

This technique already was mentioned in sub-section 2.5.5 however, more information will be given because this technique is very used in LPGs fabrication. In this technique, which the UV beam illuminates a section the optical fiber by a thin slit aperture, point-by-point modulation of the core refractive index is induced by single-spot illumination at different points along the fiber separated by the grating period, until the desired grating length is achieved. There are two distinct configurations in practical implementations: first, the fiber is translated continuously in a direction parallel to its axis past a regularly pulsed UV source [Kashyap2010]; or the fiber is stopped at each point and a single high energy UV pulse can illuminate a specific section [Hill1990]. Both are shown schematically in Figure 2.23. The UV beam irradiates the fiber through a slit that is aligned so that the longest dimension of the slit´s image remains normal to the fiber axis [Malo1993]. Significant improvement is achieved when the laser beam is focused through the

slit and after of the slit is placed a cylindrical lens to converge the beam until the fiber increasing the power density be irradiated on the fiber.
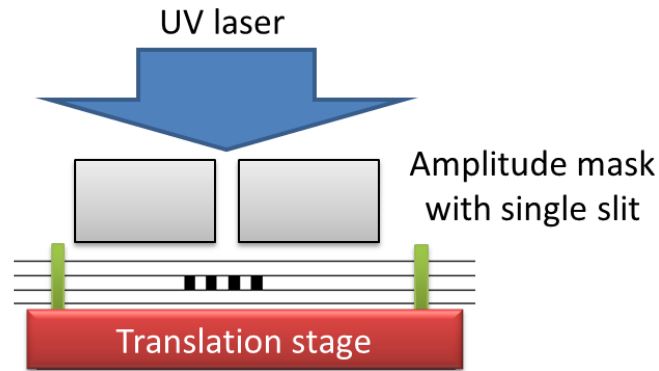
Figure 2.23 – Illustration of the point-to-point UV radiation writing.

Both of these methods have inherent advantages and disadvantages. Regarding the amplitude mask, the advantages of this technique are that the UV source need not to have a high degree of spatial and temporal coherence [James2003] and the intensity pattern does not depended on the beam position in relation to the mask itself as long as some overlap occurs [Bennion1996]. The disadvantages are that the grating period and length are restricted by the dimensions of the amplitude mask [Zhang1999], but masks with different parameters are easy to obtain [Kashyap2010]. Furthermore, the amplitude masks can easily be damaged if they are exposed to UV light whose intensity exceeds their damage threshold. Regarding the point-to-point method, the main advantages are that it is cheaper than the amplitude mask and it is extremely flexible: the grating periodicity, length and blaze are all independent parameters, which can be separately adjusted to obtain the desired LPG specifications [Hill1990, Zhang1999, Malo1993]. Summary, LPGs are most suited to the point-by-point inscription technique because of their dimensions: longer length and period can be easily achieved by convenient controlling the translation stage and position of the fiber during inscription [Kashyap2010].

2.6.2. Mechanically induced Long Period Grating

In order to produce mechanical LPGs, several techniques were published in the literature [Chen2004, Eijkelenborg2004, Rego2003, Probst1989, Cardenas2009]. These techniques have the same aim, in other words, induce periodic stress and/or microbending in a fiber by squeeze the fiber between a set of grooved plates. Two examples of these techniques are shown in Figure 2.24. They have in fact abundant similarities with regard to the effects in the fiber. Indeed, it seems reasonable to assume that the mechanisms of microbending and stress work simultaneously to the formation of the mechanically Induced LPG. The relative contribution of each mechanism to the formation of the grating depends on the fabrication technique used. For instance, the basic fabrication configurations consist in a fiber laying on a flat surface that is periodically pressed by a coiled wire [Probst1989], a grooved plate [Savin2000] (see Figure 2.24 (a)) or graphite rods [Sohn2004] (see Figure 2.24 (b)). The configurations presented in [Savin2000, Probst1989] enable wavelength tunability through adjustment of the angle between the fiber and the mechanical grooves and control of the transmission loss by applying loads to the gratings. Regarding the wavelength tunability, these techniques are not so flexible.

(a)   (b)
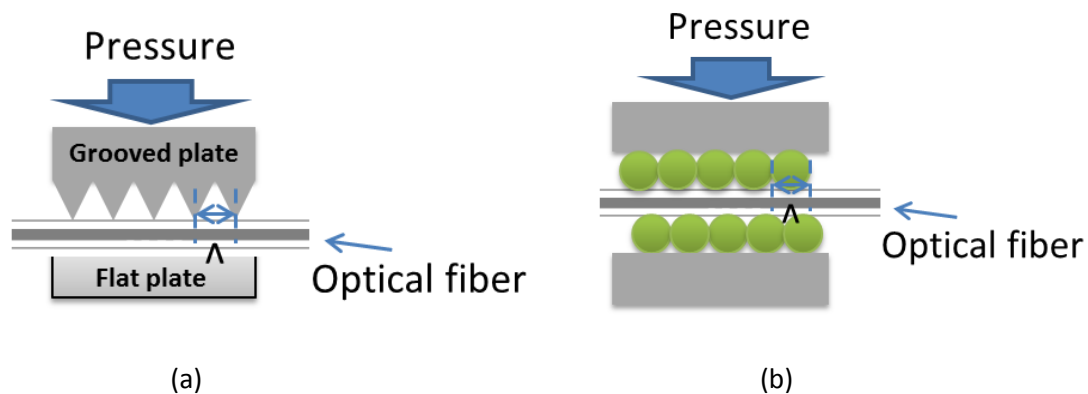
Figure 2.24 – Fabrication methods: (a) Grooved plate [savin2000]; (b) two out-of phase arrays of graphite rods [Sohn2004].

2.6.3. Electric-arc Discharge Technique

Another process used to inscribe LPGs is the electric-arc technique using arc discharges from a commercial fiber fusion splice machine or similar system [Palai2001, Rego2005] as shown in

Figure 2.25. This technique does not require photosensitive optical fibers to obtain an LPG and, unlike UV-induced LPGs for which the resonant wavelengths depend on the grating strength, the spectral properties only depend on the length and the grating period [Humbert2002]. The electric-arc discharge technique has evident advantages: the technology is cheaper (no need to use expensive laser) and flexible since it is a point-to-point inscription process; it is fast (the electric-arc discharges are often times fastest than UV exposure time) and is applicable to any type of fiber like silica, photonic crystal fibers (PCF) and microstructured fibers. Another great advantage: If the temperature is kept below the point at which residual stresses are annealed and stress relaxation begins [Rego2001], the fabricated gratings are very stable at high temperatures. However, the principal disadvantage is some lack of reproducibility. Albeit the resonant wavelengths are a lot stable, the attenuation bands can vary a bit for gratings inscribed under the same conditions. The causes for this behavior are: 1) the changes on the relative position between the fiber and the electrodes, 2) electrodes degradation and their repositioning on replacement, 3) dust on the fibers or on the electrodes and, 4) changes on the environment conditions. Therefore, to have a reasonable reproducibility of LPG with same characteristics, a precise alignment of the fiber is required, as well as electrode holders enabling accurate repositioning and a clean controlled environment. Another drawback of the technique is the limit imposed on the shortest period (around 240 μm) that can be manufactured.
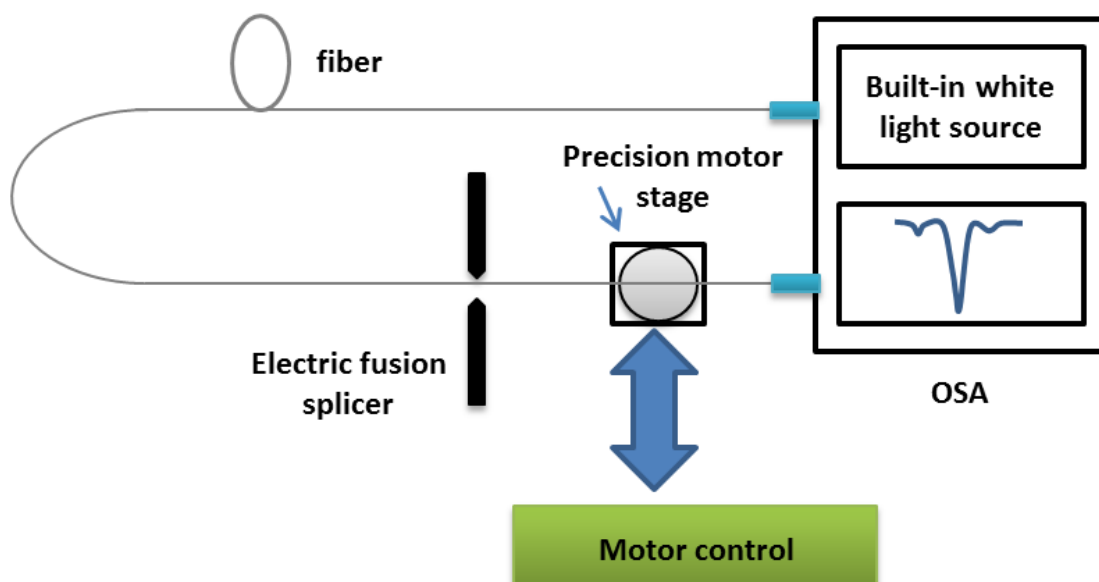
Figure 2.25 – Illustration of the electric-arc technique [Palai2001].

Detailed discussion on fabrication and characterization of fiber gratings are presented in chapter 3 of this thesis.

2.7. Chapter Summary

In this chapter, a review of the theoretical background on fiber gratings principles is done. The discussion of the fiber gratings principles is organized in a way that includes the two most important simulation models found in the literature: coupled-mode equations and transfer-matrix method. The revision of mode coupling theory for different types of grating was given, namely, for FBG, LPG, TBG and including nonuniform gratings. Fiber gratings inscription methods for Bragg gratings and LPGs have been introduced.

Chapter 3

Optical Fiber Grating Manufacturing

3.1. Introduction

The great demand for high performance optical fiber gratings with very tight tolerances in their spectral profile has led to the improvement of fiber grating design processes. Similarly, the progress that has recently been made in sophisticated modeling techniques, based on generic inverse scattering theory, has produced powerful design tools for arbitrary grating design that require a manufacturing system with accurate phase control along the grating length [Plougmann2004, Skaar1998, Feced1999]. A standard technique to solve the inverse problem is the layer peeling algorithm adapted for FBGs, which converts the complex impulse response into a grating structure defined by apodization and phase functions [Skaar2001]. Then, once the target grating spectral response is defined, the model calculates the spatial distribution of the refractive index modulation along the grating length, which contains phase and amplitude distributions.

The development of advanced production processes has become effective when new and more sophisticated hardware and software control tools were made available. In this context, new workstations were set up for fabrication of advanced fiber gratings for silica and polymer optical fiber. These optical devices play various roles in several applications related to this area, being extensively used in DWDM systems. They are an integral part of devices for gain equalization, optical Add/Drop multiplexers and act as optical elements for dispersion compensation.

Due to the demands of technology, the need for these optical devices in different applications is increasing.

3.2. Gratings Fabrication in Silica Optical Fiber

Historically, FBGs were firstly recorded using internal writing [Hill1978] and the transversal holographic technique [Meltz1989]. Both these methods have been superseded by the phase mask technique, which is schematically described in the diagram of Figure 3.1. The phase mask is placed in contact or near contact with the fiber, and the UV beam impinges normally to the fiber axis. The beam passes through the mask and is spatially diffracted to create an interference pattern with pitch Λ along the fiber axis [Hill1993b]. Since the period of the phase mask (Λ_{pm}) and the effective index of the fiber are known, the wavelength reflected by the grating can be estimated according to the Bragg condition for the *zeroth*

$$\lambda_B = n_{eff}\Lambda_{pm} = 2n_{eff}\Lambda \qquad (3.1)$$

where λ_B is the Bragg wavelength and n_{eff} is the effective mode index at the grating.
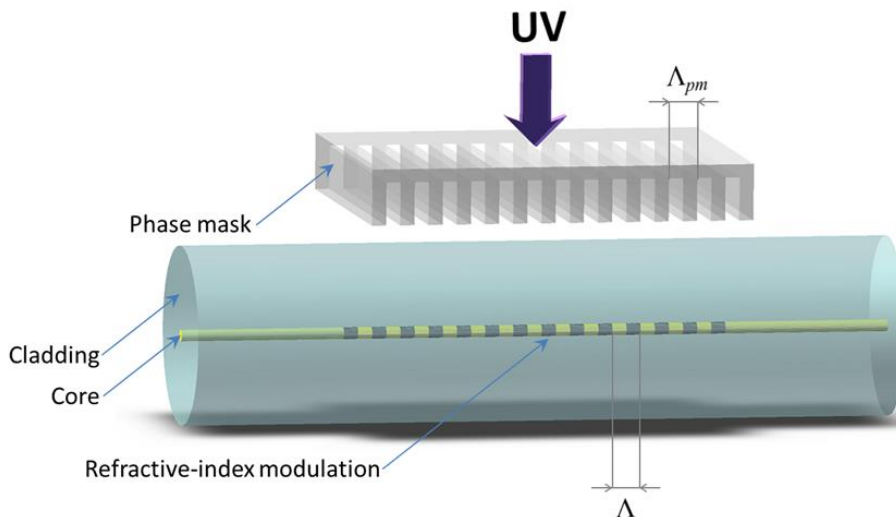
Figure 3.1 – Bragg grating fabrication apparatus based on the phase mask technique.

3.2.1. Workstation

As mentioned in chapter 1, the implementation of the fiber grating manufacturing workstation was a relatively long campaign throughout this thesis, which was only possible due to the maturity and cumulative experience that the research group acquired on fiber grating fabrication technology. The individual blocks that constitute the implemented workstation, as well as the control software developed in LabVIEW, are described. This section discriminates the technical features of the workstation parts, which were designed to enable a high level of automation while providing a flexible solution for advanced fiber grating fabrication. Figure 3.2 shows a simple schematic illustration of the fiber grating manufacturing.
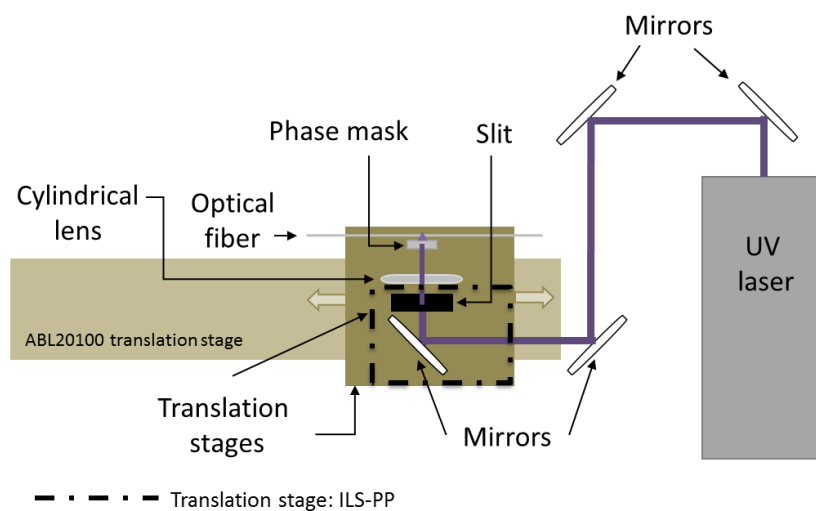
Figure 3.2 – Simple schematic illustration of the fiber grating manufacturing.

The list below summarises the system features, while anticipating the detailed item-by-item description:

- Excimer laser operating with KrF at 248 nm with cooling system (BraggStar Industrial-LN, Coherent)

- Ultra-stable linear air bearing scan stage (Aerotech)

- Machine vision alignment system, that ensures optical fiber to phase mask alignment below micrometer resolution (Edmund Optics)

- Cylindrical lens mount that adjusts the focus offset (Thorlabs)

- Adjustable fiber strain to improve wavelength repeatability (Thorlabs)

- Vacuum mask fixture, for quick change of phase masks

- Magnetic fiber clamps to fix the optical fiber

- Motorized mask swing-out, to move mask away from fiber for loading, then back into position for writing (Newport)

- Control software drivers to control auto strain, mask position, and beam scanning functions

- Optical table, tilt platform three-axis, motorized translation stages, brackets, mirrors, focusing cylindrical lens, phase masks, adjustable slit (Thorlabs, Newport, Melles Griot products).

The optical fiber used for writing is fixed by the magnetic clamps, whose height is determined by two damped posts. In one there is a motorized translation stage MFA-CC (Newport) to enable the application of mechanical tension to the fiber while in the other there is a three-axis manual stage to align the fiber. The second MFA-CC translation stage, which contains the phase mask support, is placed on a three-axis tilt platform for writing tilted Bragg gratings. It is used to control the distance between the phase mask and the fiber. The MFA-CC has a travel range of 25 mm, the minimum incremental motion is 0,1 μm with a repeatability of 0,3 μm. The maximum speed is 2,5 mm/s. The ABL20100 translation stage (Aerotech) supports not only the three-axis tilt platform, but also a motorized translation stage ILS-PP (Newport). The ABL20100 has a travel range of 1000 mm and the minimum incremental motion is 10 nm. On the other hand, the ILS-PP stage supports a mirror to redirect the UV beam, a slit defining the width beam and a cylindrical lens. The ILS-PP has a travel range of 150 mm, the minimum incremental motion is 1 μm with a repeatability of 1,5 μm. The maximum speed is 100 mm/s.

The ABL20100 stage allows gradual displacement of this whole assembly, so that the UV beam focusing on the phase mask and it is projected in the fiber section intended for writing fiber grating.

In general, during the writing process, the fiber is connectorized to an optical network analyzer (ONA) to measure parameters such as group delay, the reflectivity or transmission of the grating in real time.

The MFA-CC, ILS-PP and ABL20100 stages are linked to a computer by specific drivers. Thus, it is possible to communicate with these devices and to control the stage parameters in the writing process.

All the Newport stages are connected to a controller XPS (Newport) that uses Ethernet interface to communicate with the computer. The stage ABL20100 is controlled by software from the Unidex 500 board (Aerotech), which is placed in the computer for this purpose. A high resolution camera acquires the image of the alignment phase mask with optical fiber and it communicates with the computer via USB.

Most of these components are over an optical table which is suspended by means of compressed air in order to minimize mechanical perturbations. Furthermore, part of the assembly is protected from dust and air vibration by an acrylic box as shown in Figure 3.3.
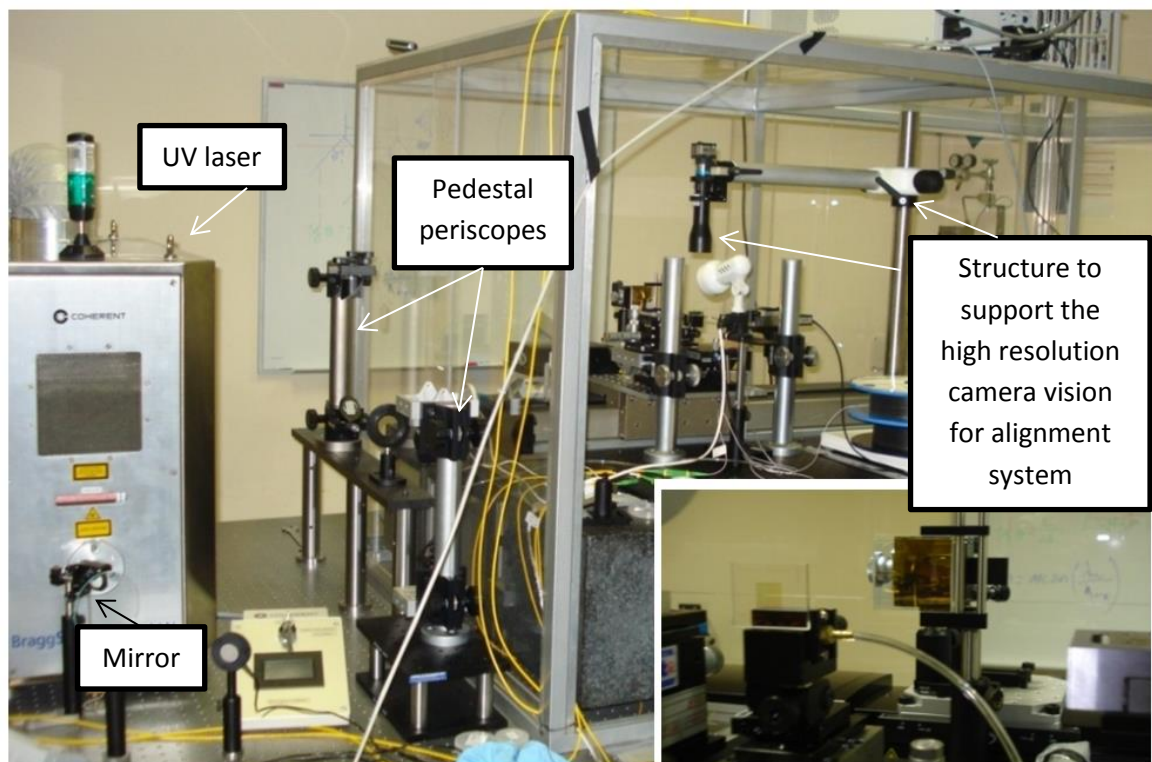

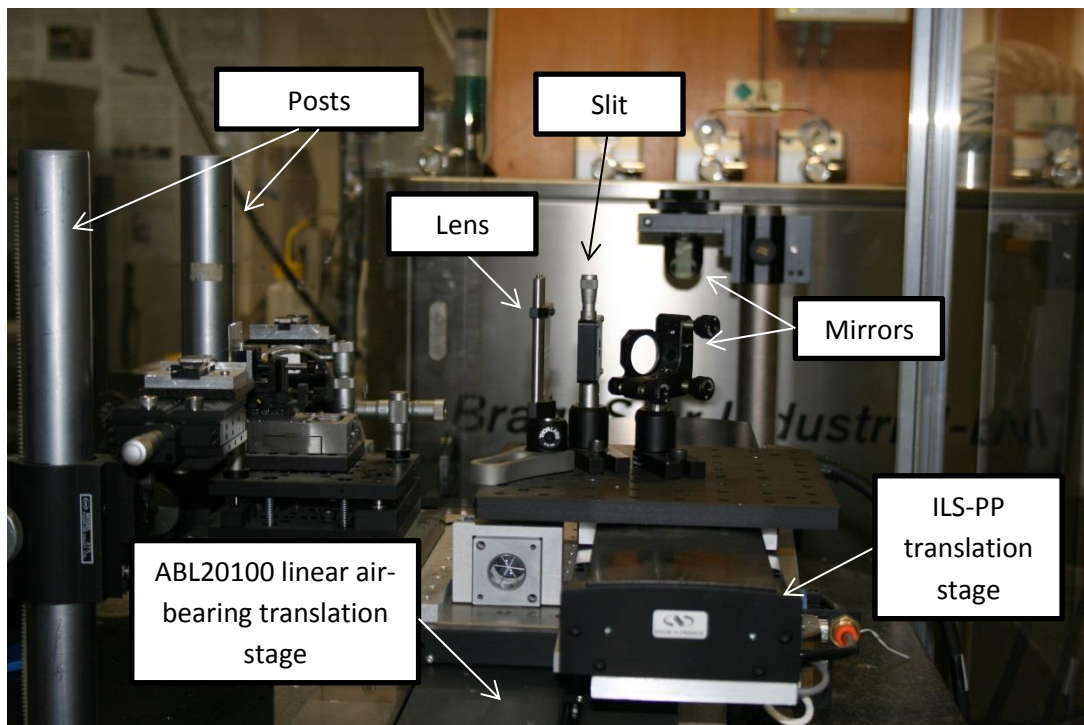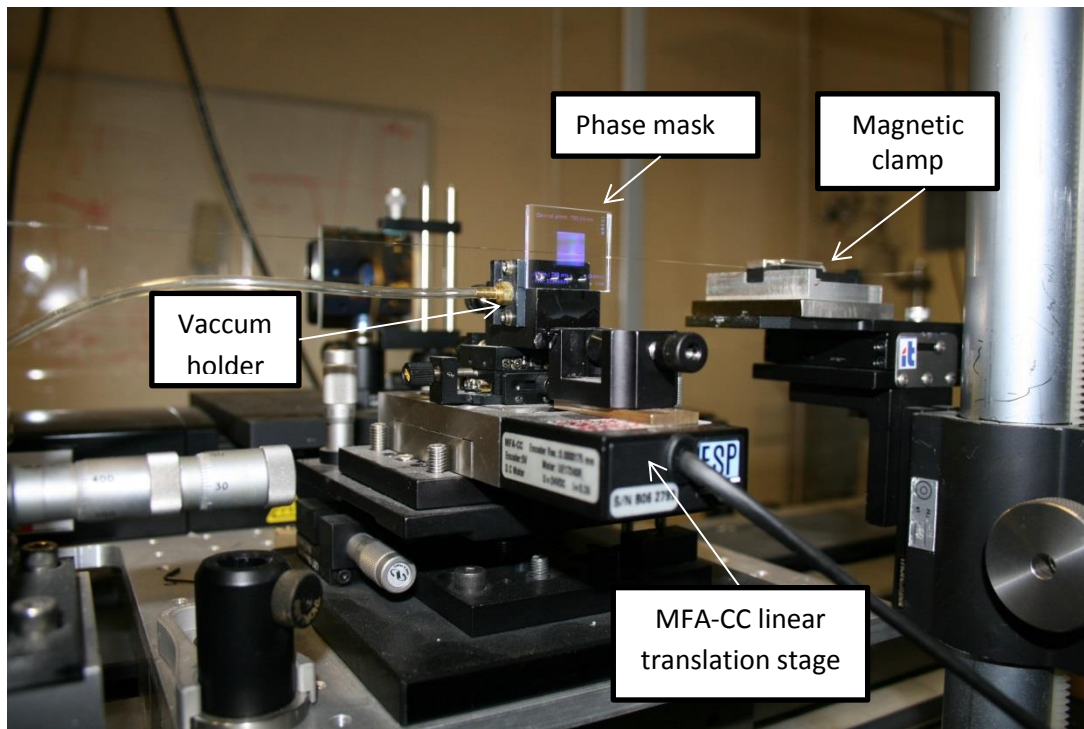Figure 3.3 – General view of the fiber grating manufacturing workstation.

Figure 3.4 – Pictures of the main scanning stage sub-assembly.

Figure 3.4 shows the scanning stage sub-assembly. This sub-assembly provides beam scan capability using a linear air-bearing translation stage, and is capable of interfacing with existing hardware and software through the control system. The scanning stage provides the means to perform multiple scans of the laser beam/phase mask during the writing operation. The scanning beam velocity can be set from 0,1 mm/s to 10,0 mm/s, and may be fixed between positions, or vary continuously according to a profile defined by a data table. In turn, the beam can be scanned from 0 mm to 1000 mm length, with a position resolution of 10 nm in the scan direction across the desired beam scan length.

 The system incorporates two pedestal periscopes as shown in Figure 3.3. The beam steerers allow to easily set the laser beam height and precisely control the azimuth and elevation angles of the beam leaving the periscope device. The beam steerer has two fully adjustable mirror mounts, allowing entering beams to be non-parallel to the table surface. The height and angle of the mirrors are manually adjusted, to redirect the incident beam from the laser source to the system beam entrance, i.e., cylindrical lens and precision optical slit. Thus, the beam laser is reflected by a mirror set (four mirrors), passing later by a precise optical slit, where the beam width can be controlled. This width is adjustable from 0 to 5 mm, with a resolution of 1 μm. There is then a cylindrical focusing lens (30 mm x 30 mm) having a focal length of 20 cm, followed by a phase mask near the focal point. The lens focuses the beam and optimizes its energy on the core of the fiber. The fiber to be irradiated is trapped by a set of magnetic clamps and is positioned in the overlap zone of diffracted orders +1 and -1.

The fiber handling is an issue very important in fiber grating manufacturing. Two independent translation stages, one motorized MFA-CC (one-axis) and other manual (three-axis), mounted on two mechanical vertical positioning posts enable the adjustment of optical fiber height with respect to the beam height. These stages allow a perfect parallelism of the optical fiber plane relative to the beam scanning plane. The minimum interior span between magnetic clamps was designed to be 180 mm, to allow maximum flexibility in multiple FBG manufacturing. The fiber handling sub-assembly, shown in Figure 3.5, provides the capability to load and unload the optical fiber, to apply mechanical tension with the motorized translation stage and to adjust the height position with manual translation stage (three-axis). The mechanical tension applied to the fiber by the motorized translation stage is adjustable. It also provides means to apply and record a constant longitudinal tension along the axis of the fiber. The mechanism provides a constant

tension after the fiber is properly fixed and positioned, during the exposure process. The axial tension sensor platform has a load capacity and a sensitivity of 30 N and 0,03 N, respectively. To read the axial tension applied to the fiber is used a strain gauge reader.

The phase-mask sub-assembly includes the phase mask support and stage that enables reliable mounting and positioning of the phase-mask while ensuring an outstanding fiber to phase mask relative positioning precision (see Figure 3.4 and 3.5). The phase-mask support is fixed to a high-resolution stage. The assembly includes: a vacuum holder for toggling the mask in and out of position; a tilt platform to provide three-axis angular alignment of the phase mask and an ultra-compact size and high reliability motorized stage for phase mask to optical fiber positioning. Therefore, the phase-mask may be placed at a desired longitudinal position with respect to the fiber, while keeping their proximity. To enable transverse positioning of the phase mask in respect to the optical fiber, the phase mask assembly includes a motorized stage that deviates the phase mask from fiber position for safe loading and unloading of the optical fiber. The maximum separation distance is 25 mm and the minimum incremental motion is 0,1 μm. The phase-mask assembly additionally provides angular alignment capability, so that the phase mask can be placed in a desired orientation with respect to the optical fiber. For this, a multi-axis tilt platform is used, which has three-axis angular orientation freedom. It features two tilt adjustments plus rotation that allow a component to be oriented parallel with an arbitrary plane. The tilt range for each axis is ±8 degrees, with a precision of less than 2 arcseconds.

Finally, the manufacturing workstation possesses an high resolution machine vision alignment system that provides the capability to precisely position the phase mask with respect to the optical fiber. A key issue in fiber grating manufacturing is the alignment between the phase mask and the optical fiber and its distance. The system includes a high resolution camera, equipped with a high magnification video lens (see Figure 3.3). The machine vision alignment system provides the capability to verify the position of the phase mask with respect to the fiber over a range from 30 μm to 500 μm, measured from the phase mask surface to the surface of the optical fiber. This system allows a position reproducibility within ±5 μm of the desired value. The machine vision alignment system also identifies and locates the position of the optical fiber, and measures its angle with a resolution of 0,1 degrees.
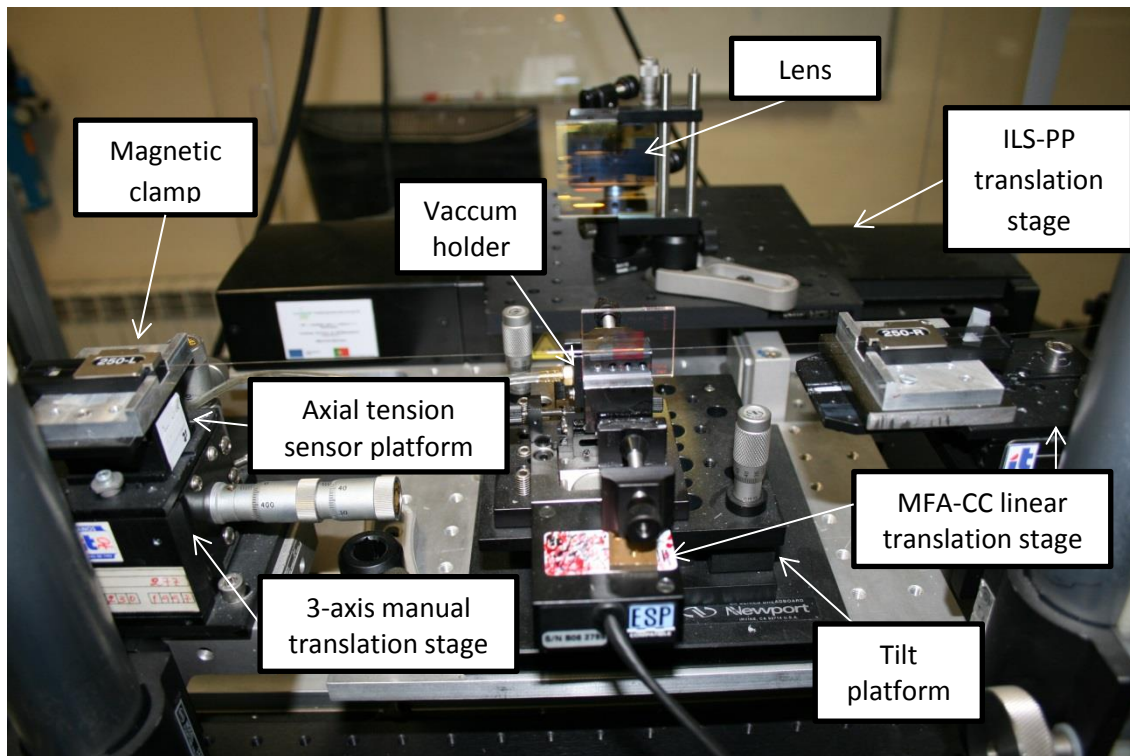
Figure 3.5 – Fiber handling sub-assembly.

3.2.2. Alignment Phase Mask/Optical Fiber and their Optimal Distance

As already mentioned, one of the key for successful writing of Bragg gratings by phase mask is to obtain a precise alignment between phase mask and the optical fiber. This alignment should be as accurate as possible and the distance from the phase mask to the fiber should be as small as possible, without contact to avoid damage of the phase mask. Therefore, an image acquisition system in order to achieve a better alignment was chosen as the better solution. For this process was performed an analysis of the camera and lens to use in order to obtain an image with a considerable magnification of the phase mask/optical fiber.

Since the optical fiber presents a diameter in the range 125 μm, it was taken a high-resolution monochrome camera with resolution 1280x1024 pixels. The camera has a vertical resolution of 1024 pixels with 5,2 μm each, and then the fiber diameter occupies about 25 pixels in the image. The image obtained with 1280x1024 pixels could be visualized with pixel equivalence 1:1 ("no

magnification") on the computer screen, where the fiber diameter corresponds about 5,75 mm measured on the screen (assuming that the dot pitch of the screen is 0,25 mm). The idea is to magnify the fiber image (125 µm) and to have access an image with a field of view between 10 and 13 mm. Since the maximum camera sensor format is 6,6 mm, the lens magnification (M_{lens}) is given:

$$M_{lens} = \frac{M_{SF}}{F_V} = \frac{6,6}{11,5} = 0,57X \qquad (3.2)$$

where M_{SF} is maximum camera sensor format and F_V is the field of view. A lens with 0,6x magnification is needed. Another factor to consider is the working distance, i.e. depending on the magnification of each lens, the working distance varies. This was also taken into account, since the distance between the lens and the phase mask / optical fiber cannot be too large, because the system is within an acrylic box, nor too small to have handling space in placement of the fiber in magnetic clamps. A telecentric lens was chosen because it eliminates parallax errors more easily. It is possible to calculate the written length taking into account the distance of the phase mask /optical fiber and the slit aperture defining the width of the laser beam (Figure 3.6). *F* corresponds to the slit aperture, $c_{PM\text{-}fiber}$ is the distance of the phase mask /optical fiber, a_m is the maximum value that can vary the distance phase mask / fiber, d_p is the distance of the fiber to the normal of the boundary of the overlap region, L_{exp} is the exact length that the grating is written, and θ_w is the angle between diffracted wave and the normal incidence.
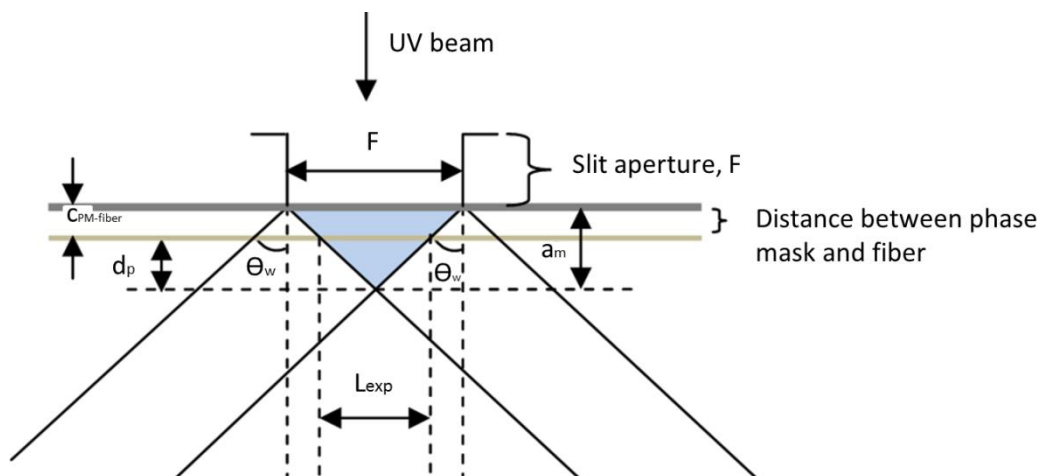
Figure 3.6 – Scheme showing the distance of the phase mask /optical fiber and the slit aperture defining the width of the laser beam.

The phase mask must be at a distance of the fiber between $0 < z \leq a_m$, since the phase mask cannot be in contact with the fiber or outside the overlap region. The following trigonometric relations apply:

$$\tan(\theta_w) = \frac{L/2}{d_p} \tag{3.3}$$

Consequently,

$$L_{exp} = 2\tan(\theta_w)d_p \tag{3.4}$$

It is known that $c_{PM\text{-}fiber} + d_p = a_m$, i.e. $d_p = a_m\text{-}c_{PM\text{-}fiber}$. Then substituting the expression (3.4) has:

$$L_{exp} = 2\tan(\theta_w)\left(a_m - c_{PM-fiber}\right) \tag{3.5}$$

It is also known that the relationship between F and a is given by:

$$\tan(\theta_w) = \frac{F/2}{a_m} \tag{3.6}$$

Therefore, (3.6) can be written as:

$$L_{exp} = 2\tan(\theta_w)\left(\frac{F}{2\tan(\theta_w)} - c_{PM-fiber}\right) \tag{3.7}$$

or

$$L_{exp} = F - 2c_{PM-fiber}\tan(\theta_w) \tag{3.8}$$

For the determination of angle θ_w, using the equation for diffraction gratings given in (2.3), considering M = 1 and assuming a normal incidence ($\theta_1 = 0$), we have:

$$\theta_w = \arcsin\left(\frac{\lambda_{UV}}{\Lambda_{pm}}\right) \tag{3.9}$$

Hence, the FBG length written depends of slit aperture, distance between the phase mask and the optical fiber and the angle θ_w . Note that the angle θ_w depends on the phase mask period that is used. The FBG length written is always lowest than slit aperture. For example, for a phase mask period Λ_{pm} = 1065 nm, with $c_{PM\text{-}fiber}$ = 70 μm, and F = 200 μm, it is obtained a L_{exp} = 166 μm.

3.2.3. Developed Control Software

All the control software of such devices in order to obtain the writing of fiber gratings has been developed in LabVIEW. All devices have driver libraries that enable this programming type. LabVIEW is suitable for this type of implementation and it consists in a graphical programming environment by block diagrams. In LabVIEW, each routine is based on Virtual Instrument (VI) containing a code sequence that constitutes a program that can act independently.

In this implemented program, created in LabVIEW, it is possible control all of the available hardware by reading the parameters inherent and instructions execution of according to the logical process of writing the fiber gratings. Thus, the user can activate the system in an easy way and perform the writing with the insertion of some data related with the laser source and the writing type to be made. The developed software is divided into three main parts: motion control position (ABL20100 and ILS-PP stages), the phase mask alignment/ fiber and laser control.

3.2.3.1. Motion Control Position

The Newport XPS is an integrated motion controller, easy to use with effective and high performance. The stages connected to it can be manipulated for an high precision control from most basic motion sequences to the most complex. Communication is done through an Ethernet cable. To control the ABL20100 stage it is necessary and indispensable to use the Unidex 500 board. This board makes the connection to the DR500 amplifier, which receives motion feedback from the stage. This feedback is received by a multiplier which provides a square wave describing the motion. Then this information is sent to the Unidex 500 board. To obtain the control of this stage via LabVIEW, snippets code were developed for each action needed for its operation such as

basic files needed to move the stage, reading real-time feedback from the stage, as well as the error associated to each motion [Marques2008].

It was developed another part that reads files containing motion sequences of position for writing fiber gratings. In Figure 3.7 the interface created for controlling the motion of two main stages is displayed. In a succinct way, the software loads the file and reads the first value of the file, moves the stage according that value, the exposure is made with the desired energy, then reads the next value to move and makes new exposure and so on until the last value file. This process will be presented and explained in detail below, when the writing methods of fiber gratings implemented in this work are discussed.
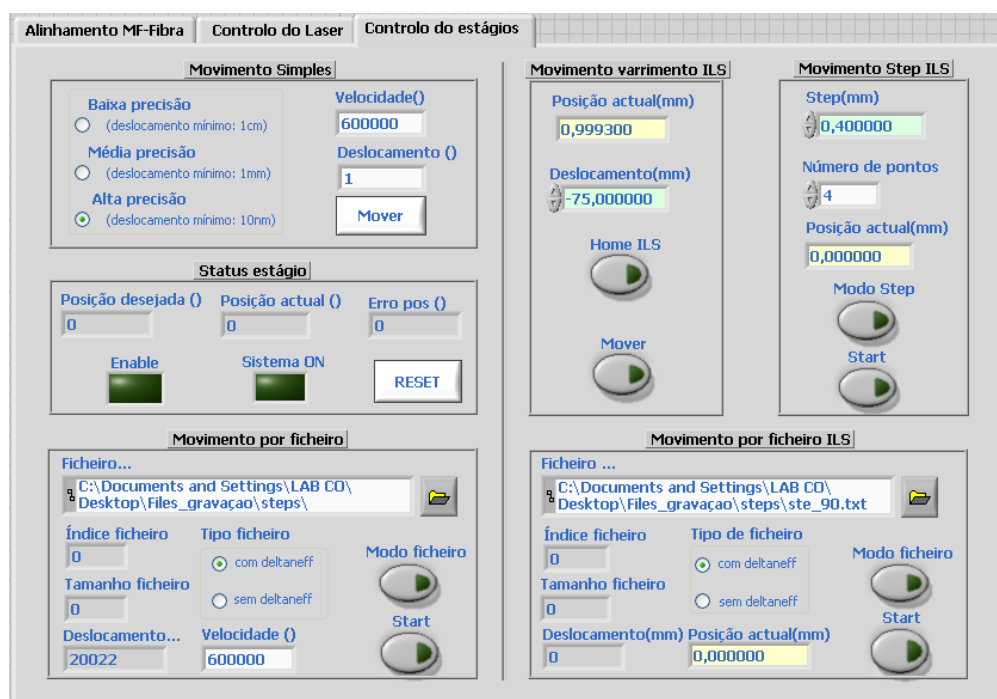
Figure 3.7 – Control interface of the main stages of motion.

3.2.3.2. Phase Mask/Optical Fiber Alignment

It is necessary to align the phase mask with the optical fiber so that the phase mask is positioned as close as possible to the optical fiber so that it is positioned in the area of overlap of the +1 and - 1 orders.

The phase mask must have a fully parallel alignment to the optical fiber, with the shortest possible distance, which is typically on the order of few micrometers. To this end, it is used a motorized MFA-CC translation stage, which approximates the phase mask to the optical fiber. It was also developed the control software code in order to make this process automated [Marques2008]. The developed software allows to control this distance from acquired image in real time by a monochrome camera, wherein are detectable the pixels of the frontal limits, either of the phase mask, or of the fiber, and thereby the distance between these pixels is calculated during the approximation the phase mask to fiber. It is noted that there is a change in velocity, since if the gap distance is still high stage moves rapidly; otherwise it moves slowly, leading a high precision distance control. The Figure 3.8 shows the control interface of the phase mask/ fiber alignment.

Figure 3.8 – Control interface of the phase mask – fiber alignment.

3.2.3.3. Laser Control

To control the laser BraggStar Industrial via LabVIEW is required to create a serial communication with the computer. All commands, including control of the frequency, number of pulses per burst, the burst number, temperature, pressure, etc., are explained in [Marques2008].

In the parameter setting block of shooting mode, it is possible to switch between continuous mode and burst mode, and set parameters associated with burst, the frequency of continuous shooting mode that corresponds to the frequency of the pulses constituting a burst sequence. A burst can be defined as a sequence of pulses which will depend on the frequency. To save the changes of the laser information, the update button must be pressed, and can be observed changing in parameters laser status. The interface can be seen in Figure 3.9.
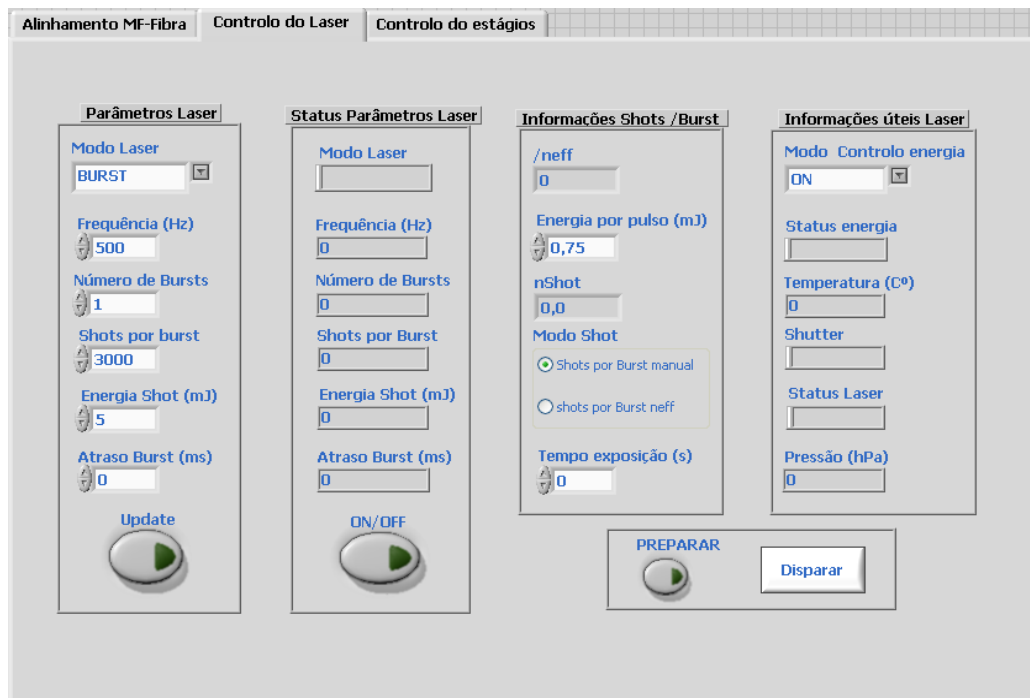
Figure 3.9 – Control interface of the laser.

3.2.4. Implemented Methods of Inscription of Fiber Gratings

The aim this system is to be able to inscribe simple fiber gratings (uniform FBG) to the most complex (phase-shifted FBG (PSFBG), chirped FBG, Fabry-Pérot cavity, LPGs) with quality when compared to simulation results of the profile of those fiber gratings. It is possible the inscription of gratings using four writing methods: phase mask method, UV beam scanning phase mask technique, stitching method and point-to-point method.

3.2.4.1. Phase Mask Method

As mentioned above, the inscription by phase mask is a simple method where it is possible to inscribe fiber gratings via a single uniform exposure of laser light, which is defined by the slit aperture the length of grating inscribed, without the need to move the translation stage, i.e., no motion of the phase mask relative to the fiber. The grating length is limited by the slit aperture and laser beam width.

3.2.4.2. UV Beam Scanning Phase Mask Technique

Fiber gratings can be inscribed by scanning the beam across the phase mask. It can be defined the slit aperture, and here there is no motion of the phase mask with respect to the optical fiber. However, there is motion of the ILS-PP translation stage that supports a mirror, the slit and the focusing lens. This motion sweeps the width of the phase mask that is static relative to the fiber. The duration of this motion is defined by the fiber grating characteristics that is desired to inscribe, which defines the speed of the ILS-PP stage. The fiber grating length is limited to the phase mask length.

3.2.4.3. Stitching Method

This method is widely used for inscription of several FBGs with specific characteristics such as chirped Bragg gratings. In this method there is a motion of the ABL20100 translation stage i.e., the whole platform that contains the ILS-PP translation stage and the tilt platform containing the phase mask is moved relative to the static optical fiber. This method depends of exposure length (L_{exp}) that the user wishes to use for writing: lower L_{exp} values result in higher precision at the expense of a slower writing speed. The steps evolve according a file that lists the displacements, which correspond to the displacement values of the translation stage being considered in order to inscribe a FBG with a given visibility ($v\,(z)$), length (L) and change in the refractive index. These steps must be a multiple of the grating period to minimize phase errors. Also, the high precision translation stage (ABL20100) is the key this method, also to avoid phase errors when various sections are stitched together. Each exposition inscribes the pattern defined by the phase mask

onto the fiber; when the first exposition is completed, the set moves and then another exposition is performed after the first one. This process continues until the desired length is obtained. At the end of the process, the FBG is composed by various sections (sub-gratings) stitched together in phase.

3.2.4.4. Point-to-Point Method

Fiber gratings can be inscribed by point-to-point method, each grating plane is produced singly, by incidence of an UV pulse in the optical fiber. After the inscription of a point, the laser beam path is displaced (with help the ILS-PP motorized stage) with respect the static optical fiber, corresponding this distance to the grating period. This method is most used for the inscription of LPGs as will be presented later. The advantage of this method compared to those previously is the flexibility it offers to change the grating parameters such as period and grating length.

The design and simulation of several fiber gratings described in this thesis were performed on a Matlab software, which is an in-house software written in Matlab and called gratings in optical simulation platform (GOSiP). The GOSiP is based on the TMM [Erdogan1997]. Through this simulator can be obtained simulations of Bragg gratings mentioned in the previous chapter, being able to manipulate various parameters, such as grating length, visibility, variation of the effective refractive index, L_{exp}, phase shift value and its position, among others. Also some of the presented simulations were performed using a commercial software designated OptiGrating.

3.2.5. Writing Process

In this section a detailed description will be made of the entire process of writing gratings in optical fiber. All steps are contemplated since the material preparation until the final characterization of the fiber grating.

All equipment used in the system are turned 'on': computer, DR500 amplifier, compressed air system supplying the optical table and the ABL20100 stage, XPS controller, the laser cooling system, purging system and the laser.

It is checked the type of fiber grating for writing, the used method (phase mask method, or UV beam scanning phase mask technique or Stitching method), to define the slit aperture.

It is checked the desired central wavelength for the inscription of the grating to use the correct phase mask (if needed). It shall be noted that there are various phase masks with different periods, which covers entire C-Band, plus some for the visible, 1100 nm and L-Band spectral windows.

It withdrawing a cladding portion of the optical fiber to allow the fiber grating writing. The optical fiber is pre-connectorized to the ONA to check the grating spectrum growth in reflection and / or transmission in real time. The fiber is then placed in the magnetic clamps with a controlled tension, to ensure the fiber is stretched.

The user runs the control software and system initialization is performed allowing the preparation and initial positioning of all motorized stages.

The imaging system is activated in real time by placing the desired distance from the mask to the fiber, in pixels, allowing the automatic approach of the phase mask to the fiber, which distance is ~ 14 pixels (~ 70 µm).

In the parameter setting block of the laser the values required for the writing process are inserted, such as frequency, continuous or burst shooting, and in the case of burst shooting, placing the burst number, the delay between bursts, the number of pulses per burst and the energy of each pulse. The shooting type will depends on the adopted method for writing the fiber grating.

Upon completion of the automatic writing of grating, the next step is to perform the deviation of the mask phase in respect to the optical fiber. The aim is to remove the fiber of the magnetic clamps to avoid any contact between phase mask and optical fiber.

Finally, the spectrum will be saved in reflection and/or transmission of the produced fiber grating. In Figure 3.10, there is a flowchart explaining the relative sequence of the inscription of fiber gratings.

```
┌─────────────────────────┐
│ Activation of equipment │
│ inherent to the setup   │
└─────────────────────────┘
            │
            ▼
┌─────────────────────────┐
│ Checking the type of    │
│ grating and writing     │
│ method                  │
└─────────────────────────┘
            │
            ▼
┌─────────────────────────┐
│ Defining the slit       │
│ aperture                │
└─────────────────────────┘
            │
            ▼
┌─────────────────────────┐
│ Checking of desired     │
│ wavelength              │
└─────────────────────────┘
```

According between phase mask and λ?

Changing the phase mask

Positioning the fiber in the magnetic clamps with coating previously removed

Image acquisition and phase mask approximation of the desired distance

Phase mask – fiber distance

Update laser parameters according to the type of writing method

Choosing the motion type

Fiber grating writing

Automatic termination of the fiber grating writing

Deviation of phase mask in relation to the fiber for avoid damage
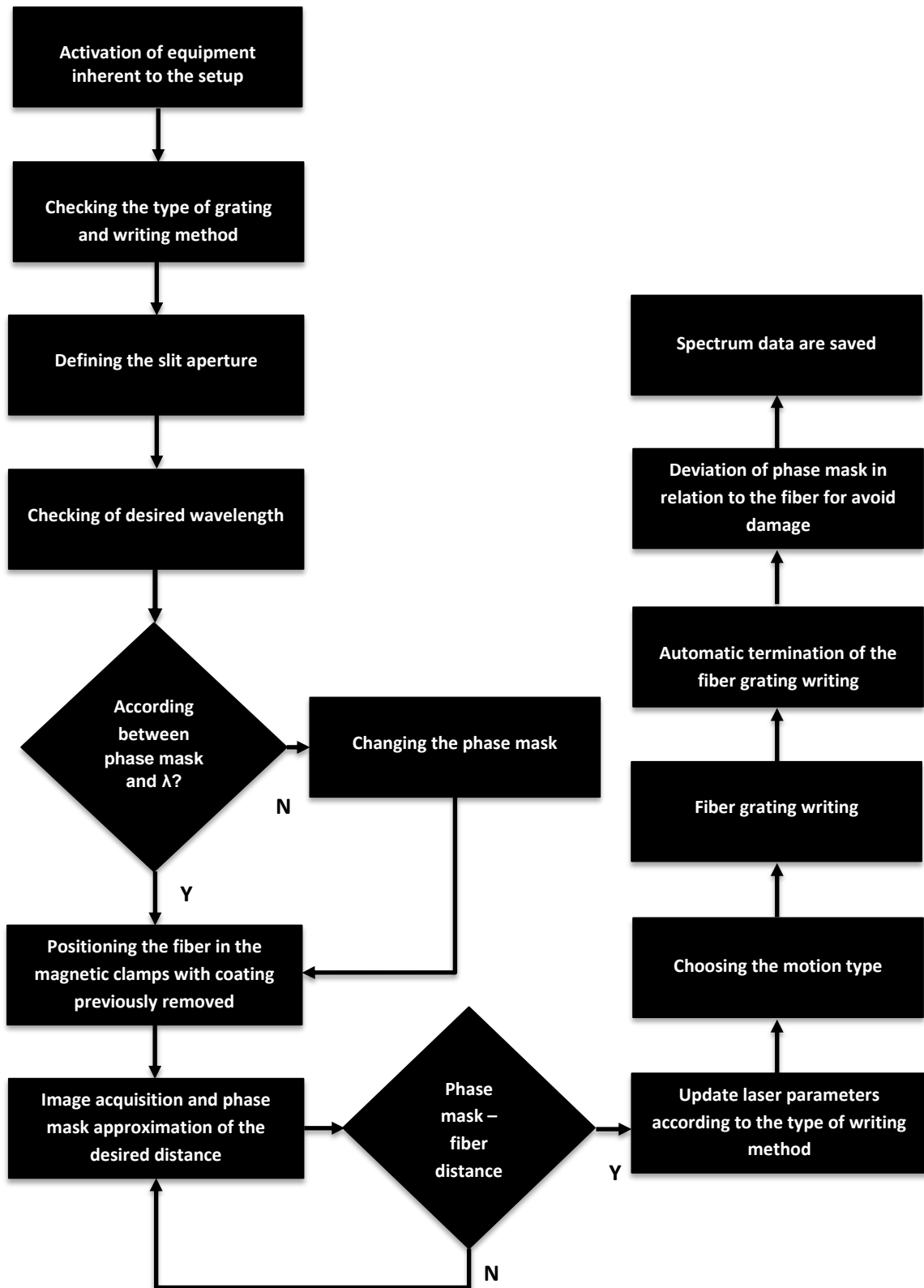
Spectrum data are saved

N

Y

Y

N

Figure 3.10 – Flowchart of the sequence for writing the fiber gratings.

3.2.6. Characterization of Inscribed Fiber Gratings

Once the system has been given with the purpose of writing gratings, its characterization in terms of reproducibility compared to that obtained by simulation shows particular interest. Before this detailed analysis it is appropriate to present a study that reports the total accumulated energy at the time of inscription of fiber grating with the refractive index variation for the purpose of understand their behavior.

3.2.6.1. Variation Study of Refractive Index with the Total Accumulated Energy

Experimental tests were performed to understand the behavior of the refractive index variation with the total accumulated energy. Thus, the average energy per UV pulse was measured (E_{pulse}) immediately before the phase mask by means of a power meter, where successive exposures were made, and progressively increasing the total number of pulses per exposure. For each exposure was noted the wavelength variation and from this was calculated the refractive index variation through the relationship:

$$\Delta n_{eff} = \frac{\Delta \lambda}{\Lambda_{pm}}$$ (3.10)

The total accumulated energy, E_a, of each exposure according to:

$$E_a = n_{pulses} \cdot E_{pulse}$$ (3.11)

where n_{pulses} is the total number of pulses, which is given by:

$$n_{pulses} = F_{laser} \cdot t_{exp}$$ (3.12)

where F_{laser} is the laser frequency and t_{exp} is the exposure time. Figure 3.11 depicts a linear relationship between the refractive index variation and the total accumulated energy for a refractive index variation of 2×10^{-4}. For higher values, we are in the presence of a non-linear behavior.
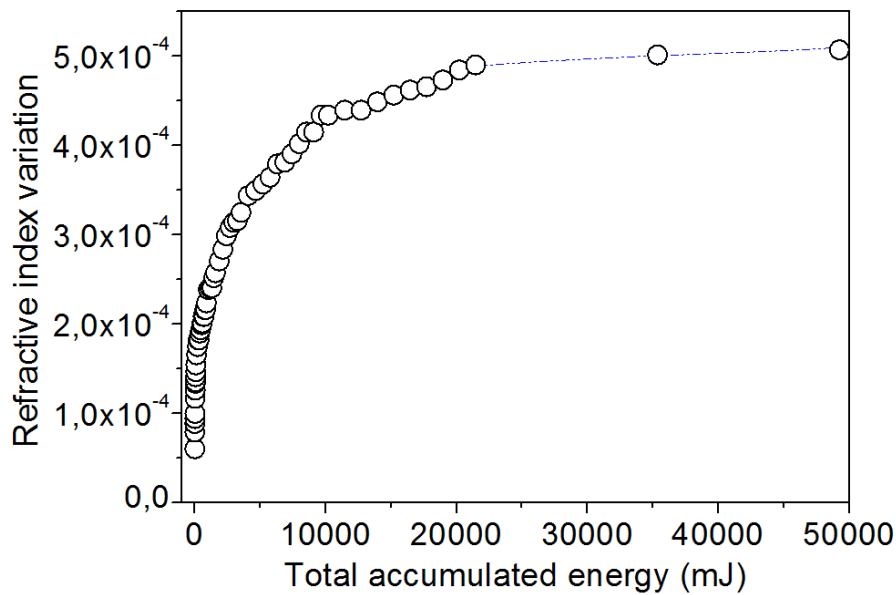
Figure 3.11 - Refractive index variation behavior as a function of total accumulated energy.

3.2.6.2. Uniform FBGs

The uniform FBGs, as mentioned above, are easier to obtain. A first test was conducted in order to verify the reproducibility of writing uniform FBGs. Hence, four FBGs were inscribed, each with a slit aperture of F = 1 mm and with the same exposition conditions. From Figure 3.12 it can be seen that the four FBGs have a spectral response very similar with slight deviation from the maximum amplitude.

Another test was to produce and to compare a uniform FBG with length L = 1 mm by using the phase mask and stitching methods. For the phase mask method the slit aperture was set to 1 mm and a specific total accumulated energy, E_a. For the stitching method the slit aperture was 100 µm. The calculated displacement step for the stitching method is rounded to the nearest multiple of 100 µm according to the grating period. Consequently, a file with 10 steps was calculated and it was made an exposure of energy, E_a for each. Figure 3.13 shows the spectral responses for the two cases as well as the simulation response. The parameters used for the simulated FBG were Δn_{eff} = 1x10^{-4}, L = 1,1x10^{-3} m, υ = 1. There is a good spectral response of the two methods in comparison with the FBG simulated. However, there is a small difference in

amplitude and period of the FBG side lobes in relation to the simulated FBG. This difference may be explained by an inhomogeneity of the laser beam profile, inducing a slight apodization.
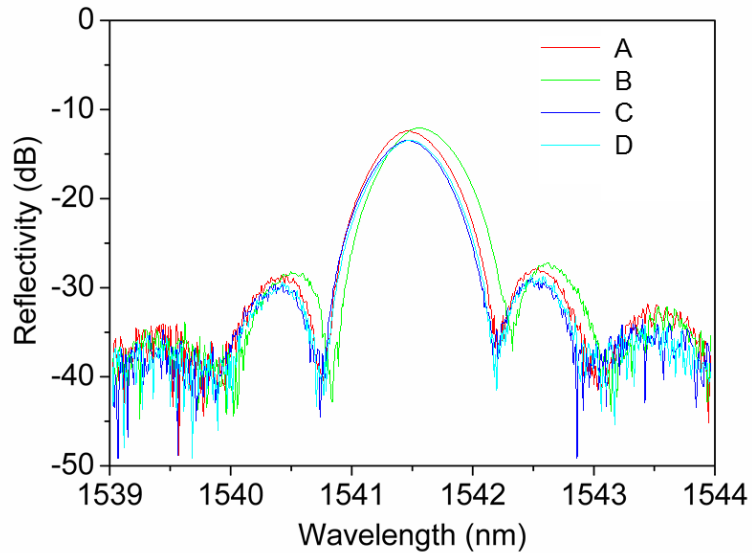

Figure 3.12 - Spectral response of four uniform FBGs inscribed under the same conditions.
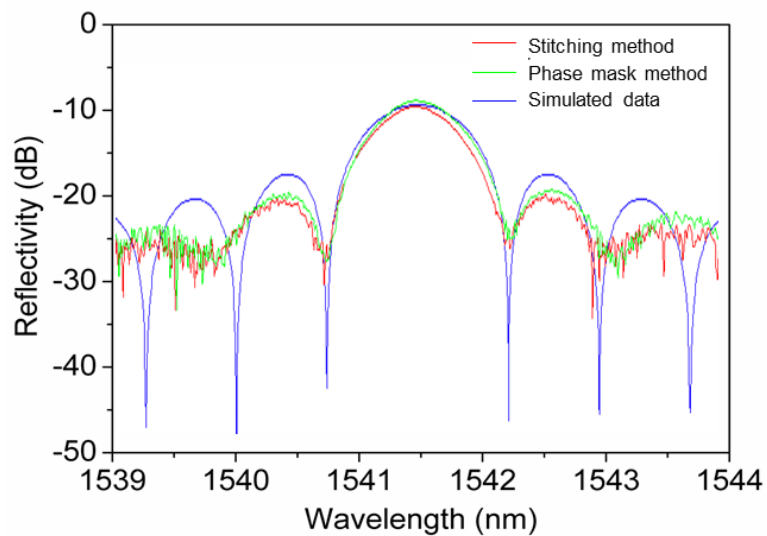

Figure 3.13 – Response of uniform FBGs inscribed by the phase mask and stitching methods; and their simulated FBG.

3.2.6.3. Phase-Shifted FBGs

This type of FBG, called as PSFBG, is characterized by introducing a phase shift in the modulation of refractive index. The stitching method was used to obtain a file of steps for writing such FBG with a phase shift of $\phi = \pi$ at position L = 10 mm. The total FBG length has a length L = 20 mm. The parameters used for the simulated FBG were: Δn_{eff} = 2,2x10^{-4}, L = 20,4x10^{-3} m. It was obtained a similar FBG to the simulated FBG in terms of spectral properties. The 3-dB bandwidth of the narrow transmission band of the π-PSFBG was measured to be ~47 pm, showing a good agreement with the simulated result (~44 pm). The experimental spectrum also presents a maximum notch depth around 22 dB, which is similar to the simulated result (25 dB) as shown in Figure 3.14.
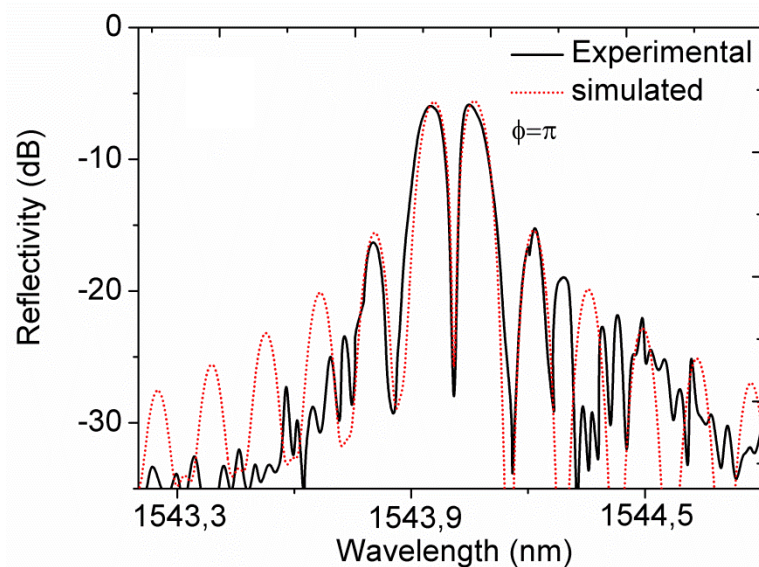
Figure 3.14 – Experimental and simulated results of a phase shifted FBG inscribed by stitching method.

3.2.6.4. Chirped FBGs

By varying the periodicity of the refractive index modulation throughout the grating it is possible to achieve a much broader reflection band. If the variation of the periodicity is small, it can be considered locally uniform. Because of this, each part of the grating will reflect different wavelengths without affecting each other. The resulting reflection spectrum is a much broader but weaker reflection band. To achieve the same strength of the reflection, a much stronger FBG

is needed. Thus, one consequence of this linear variation of the period is a higher bandwidth compared to an uniform FBG.

This type of FBG was also inscribed by the stitching method. The FBG length is L = 10 mm, the used L_{exp} was 150 µm and the displacement step according L_{exp} (a multiple of the phase mask period used - 150,165 µm). It was designed a chirped FBG and parameters such as reflectivity, bandwidth and group delay were evaluated. Figure 3.15 illustrates the comparison of FBG writing in terms of reflection and group delay. The chirped FBG was simulated with 66 sub-gratings, showing that the experimental and simulation results are in good accordance.
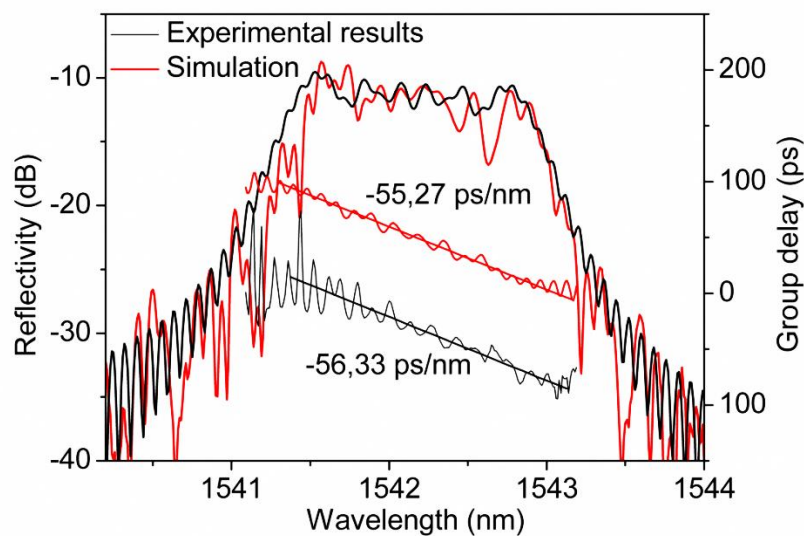
Figure 3.15 - Reflectivity and group delay response of a chirped FBG.

Table 3.1 – Comparison between simulation and experimental data with respect to the chirped FBG.

	Reflectivity (dB)	Bandwidth (nm)	Dispersion (ps/nm)
Theoretical	28,48	1,63	-55,27
Experimental	28,48	1,49	-56,33

Table 3.1 shows the experimental and simulated results. The dispersion, D, is calculated from equation (2.28) of the Chapter 2, which is defined as the rate of change of group delay, τ, with wavelength. A good agreement between both experimental and simulated results is achieved for

the reflectivity. In the case of the bandwidth, a difference of 140 pm was achieved between the experimental and simulated data. Finally, Figure 3.15 also shows a similar slope between them and it is also verified by the dispersion values.

3.2.6.5.   **Notch FBGs**

Narrow optical notch filters are optical devices widely used in in broadband wireless access networks such as radio-over-fiber and universal mobile telecommunication systems [Zheng2005, Zhang2009], whose usefulness is to filter signals with reduced bandwidth, such as RF signals.

The aim is to achieve an FBG with a reduced bandwidth and a high transmission. Thus, a FBG was inscribed with a bandwidth of 62 pm (measured at -30 dB) and wavelength centered in 1549,948 nm. The uniform FBG with a length of L = 25 mm and L_{exp} = 200 µm was inscribed by the stitching technique. Figure 3.16 illustrates the comparison between the experimental and simulated FBG. Table 3.2 shows a comparison between experimental and simulated data such as central wavelength, bandwidth and transmission. The bandwidth is close to the expected and a good transmission with respect to the simulated FBG was achieved successfully.
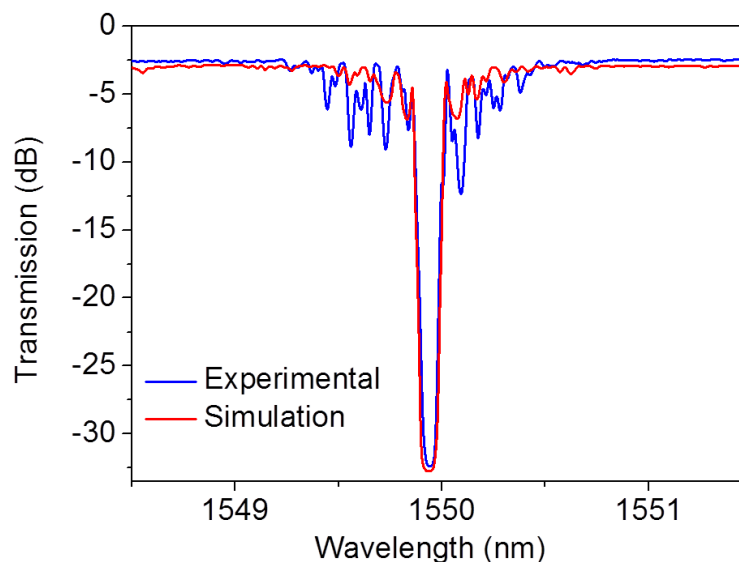

Figure 3.16 – Experimental and simulated results of a narrow notch FBG inscribed by stitching method.

Table 3.2 – Comparison between parameters of the inscribed and simulated Bragg grating.

	$\lambda_{central}$ (nm)	Bandwidth (nm)	Transmission (dB)
Theoretical	1549,886	87	-32,1
Experimental	1549,948	62	-31,01
Error	0,138	25	-1,09

3.2.6.6.   FBG Arrays

An array of FBGs with wavelengths in the C-band is widely used in photonic applications such as Optical Code Division Multiple Access (OCDMA) networks, sensors, and so on. An OCDMA network allows multiple users share the same transmission media by assigning different optical codes to different users.

An array of FBGs is used as OCDMA coders because it is possible to reflect multiple wavelengths with different delays on the same fiber. As such, if a light pulse is sent to the grating, the reflected signal consists on several pulses with different wavelengths and time delays. The time delays depend on the spacing between the individual FBGs. The receiver must have an array of FBGs with wavelength in the inverse order, this will cause the initial pulse is reconstructed. Figure 3.17 shows a keyword user and the corresponding provision of the encoding array of FBGs.
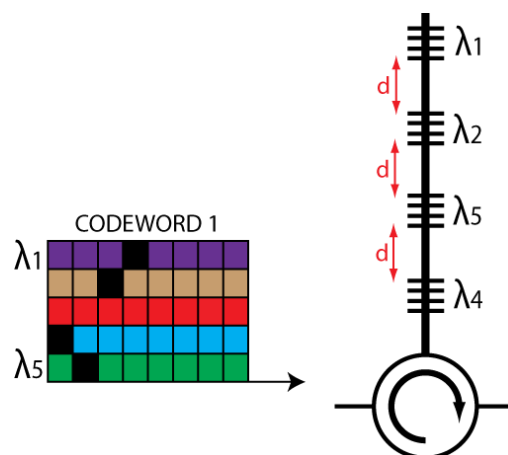

Figure 3.17 – User code and corresponding provision of coding.

An array of FBGs consists in writing of FBGs along an optical fiber, they being spaced by a distance *d*. This distance can be calculated by:

$$d = \frac{c\tau_s}{2n_{eff}}$$

(3.13)

where τ_s is the specific group delay.

It was written an array with four gratings delayed by 50 ps among them, which corresponds to *d* = 5.17789 mm. The required wavelengths for ODCMA system are in the range of 1548,20 nm and 1554.60 nm and spaced of 1.6 nm. The four FBGs have similar reflectivities, difference of 50 ps in terms of group delay between FBGs and relative spacing between adjacent FBGs of 1.6 nm was also achieved. The inscription of this array, it is necessary after writing the first FBG moving the translation stage *d* = 5,17789 mm and then changing the phase mask for the inscription of the next FBG, and so on.

The resulting FBGs present a good agreement with the projected FBGs in respect to the values of relative spacing between wavelengths (Table 3.3), group delay between FBGs (Table 3.4) and central wavelength (table 3.5). Figure 3.18 also shows similar reflectivities for four FBGs.
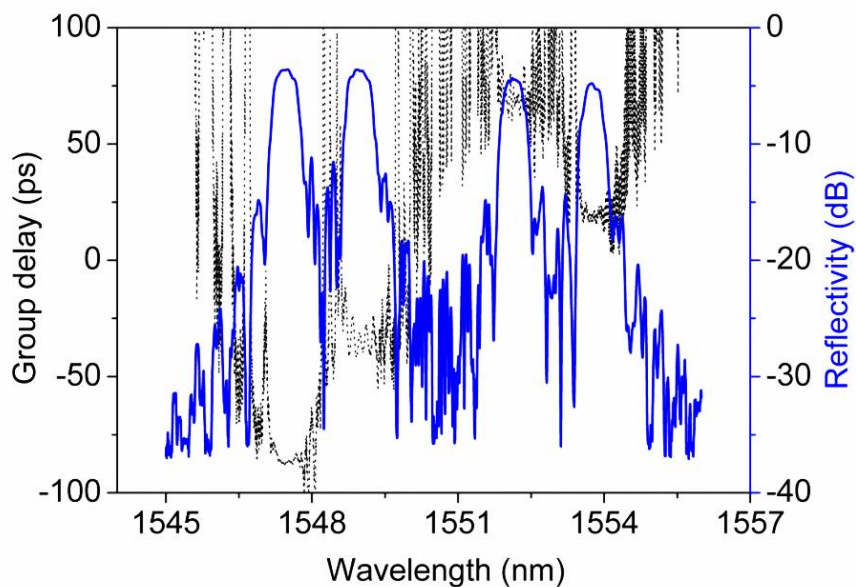

Figure 3.18 – Amplitude and group delay responses of a FBGs array.

Table 3.3 – Comparison between Bragg gratings inscribed in terms of spacing.

	1stFBG |spacing| (nm)	2ndFBG |spacing| (nm)	3rdFBG |spacing| (nm)	4thFBG |spacing| (nm)
Theoretical	--	1,6	4,80	1,6
Experimental	--	1,61	4,79	1,58
Deviation	--	0,01	0,01	0,02

Table 3.4 – Comparison between Bragg gratings inscribed in terms of group delay.

	1stFBG Group delay (ps)	2ndFBG Group delay (ps)	3rdFBG Group delay (ps)	4thFBG Group delay (ps)
Theoretical	--	50	50	50
Experimental	--	50,11	50,17	50,09
Deviation		0,11	0,17	0,09

Table 3.5 – Comparison between Bragg gratings inscribed in terms of central wavelength.

	1stFBG $\lambda_{central}$ (nm)	2ndFBG $\lambda_{central}$ (nm)	3rdFBG $\lambda_{central}$ (nm)	4thFBG $\lambda_{central}$ (nm)
Theoretical	1553,00	1554,60	1549,80	1548,20
Experimental	1552,86	1554,47	1549,68	1548,10
Deviation	0,14	0,13	0,12	0,10

3.2.6.7.   Tilted FBGs

As mentioned in previous chapter, the inscription of a TFG implies that the interference fringes pattern make an angle to the axis of the optical fiber. This condition can be obtained by tilting of the phase mask relative to the z-axis of the optical fiber, as shown in Figure 3.19.

In the inscription of TFGs, the angle between the optical fiber axis and normal to the fringe pattern, tilt angle of the phase mask (θ_{PM}) does not match the tilt angle of the FBG inscribed (θ_{TFG}). In 2001, Laffont et al. justified this difference with the refraction suffered by the UV beam, especially in the air-cladding interface [Laffont2001]. In the same year, Mihailov et al. showed an expression that related these two angles and took into account the cylindrical structure of the optical fiber. In this case it was considered that the angular distortion of the virtual image of the

fringe pattern occurred when it passes through a cylinder full, which was equivalent to the fiber in its whole [Mihailov2001]. However, in 2002, the same research group presented a corrected version for the calculation of distortion. In this new model considered the fringe pattern across only half cylinder, since what matters to know it is the distortion, which is obtained on the core of the optical fiber. The relationship between the two angles is given by [Mihailov2002]:

$$\theta_{TFG} = \frac{\pi}{2} - tg^{-1}\left(\frac{1}{n_{eff}\,tg\,\theta_{PM}}\right)$$
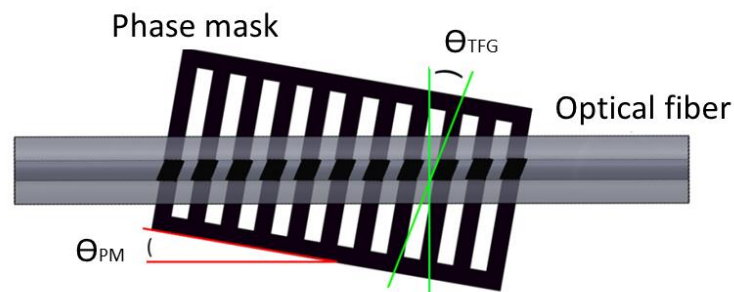
(3.14)

Figure 3.19 – Scheme showing the tilting phase mask relative to the z-axis of the fiber. Θ$_{TFG}$: tilt angle of TFG; Θ$_{PM}$: tilt angle of the phase mask [Alberto2011].

In Figure 3.20 (a) is shown a graph of θ_{TFG} as a function of θ_{PM}, built based on the expression (3.14).

Figure 3.20 (b) shows the transmission spectrum of a TFG. In this case, the TFG was inscribed in a standard SM photosensitive fiber (FiberCore PS1250/1500) using the UV beam scanning phase mask technique. The fiber was previously subjected to a hydrogenation process that occurred at a pressure of 150 bars, during two weeks, in order to enhance its photosensitivity. The resulting tilted FBG has a length and a tilt of 15 mm and 8°, respectively. TFGs are used extensively for sensing and optical communication, especially for multi-parameter fiber sensor [Suo2008, Alberto2010], modal power distribution measurers [Chun2005], add-drop filters [Castro2004], among others.

$$\theta_{TFG} = 1{,}39\theta_{PM} + 0{,}25$$
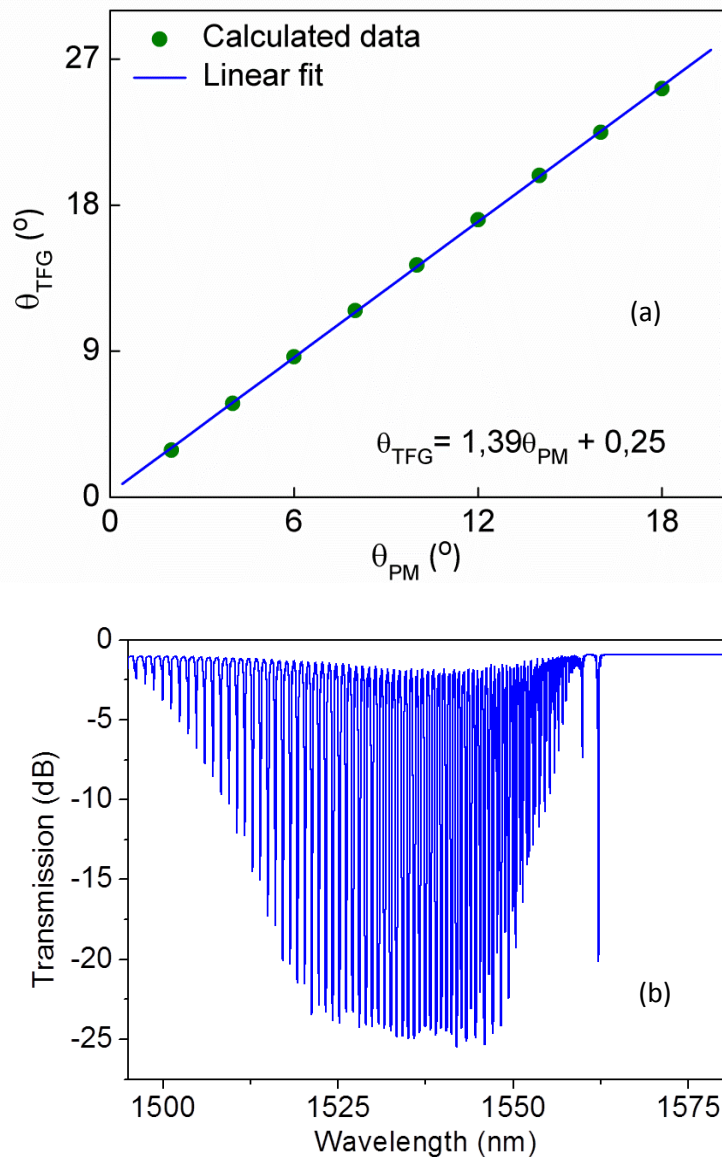
Figure 3.20 – (a) Representation of the tilt angle of the TFG as a function of the tilt angle of the phase mask. (b) Transmission spectrum of a TFG with 15 mm of length and an 8° tilt angle.

3.2.6.8.   Long Period Gratings

Long period gratings, periodic index perturbation on the order of hundreds of micrometers in period are used extensively for sensing and optical communication, especially for WDM systems [Varshney2007, Harumoto2002], as they can reduce the undesirable side lobes prevalent in uniform-grating spectra, and shape spectra extremely sharp.

An LPG was inscribed into a hydrogen loaded standard SM photosensitive fiber through the direct written point-by-point method. The LPG was inscribed with an exposure time t_{exp} = 17 s in each point. The LPG period is Λ = 410 µm and the exposure length is L_{exp} = 200 µm. The LPG was inscribed with energy of 3 mJ per pulse and laser frequency of 500 Hz. The LPG length is L = 52 mm, leading to an attenuation peak wavelength at λ ~ 1556 nm. The simulation and experimental results are shown in Figure 3.21 showing a good agreement.
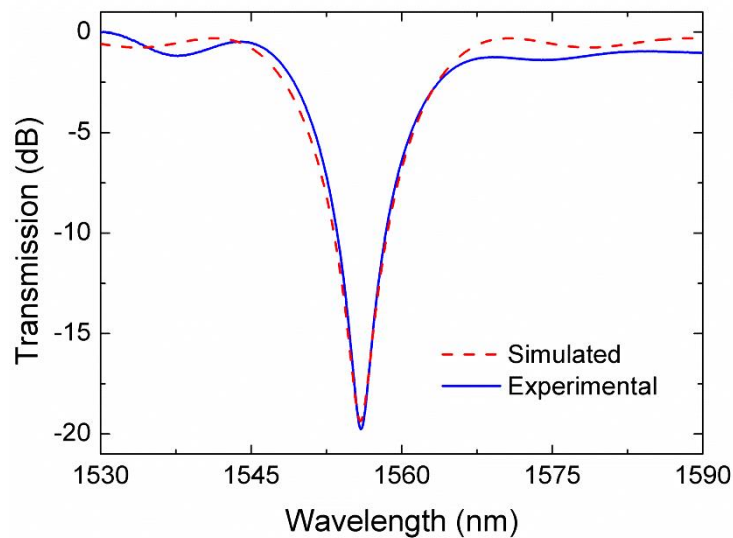
Figure 3.21 - Simulated (dashed line) and experimental (solid line) spectrum of the LPG.

3.2.6.9.   High Birefringent (HiBi) FBGs

High birefringent FBG (HiBi FBG) are used widely for sensing [Abe2004] and optical communication [Andre2004, Teixeira2005] for OCDMA systems [Nogueira2006] and Optical Signal-To-Noise Ratio (OSNR) monitoring systems [Pratas2013]. Because of its geometry, a HiBi fiber has two effective refractive index values, corresponding to the principal optical axes. For an incident signal with polarization components along these two principal optical axes, each of them will experience a different refractive index value. Therefore, by imprinting a Bragg grating in these fibers, two reflection bands will arise, being the reflection response of a HiBi FBG equivalent to the convolution of two uniform Bragg gratings, centered at different Bragg wavelengths, each one corresponding to a different polarization direction (x and y).

HiBi FBGs were produced by imprinting a 35 mm long grating in a hydrogen loaded PANDA type optical fiber HP-1550 (Thorlabs), using scanning phase mask (1073,85 nm) method. The grating was inscribed with energy of 3 mJ per pulse that swept the fiber with a sweep velocity (v_{sc}), v_{sc} =0,2 mm/s. The resulting grating imposes reflection at two spectral bands, in which one matches the signal wavelength. The Figure 3.22 (a) shows the reflection spectrum of a 35 mm HiBi FBG. A 10 mm long grating was imprinted using a phase mask with period of 1071,45 nm, an exposition time of 70 s (v_{sc} =0,14 mm/s) and an energy of 2,5 mJ per pulse (Figure 3.22 (b)).
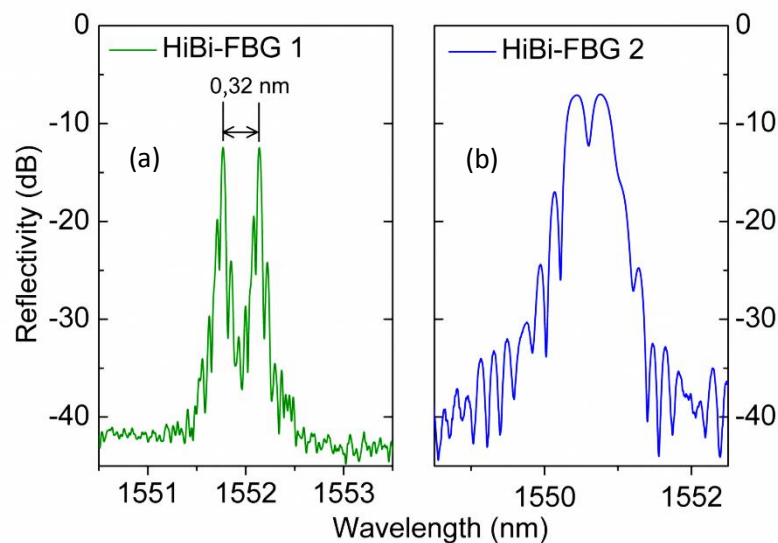
Figure 3.22 – Reflection spectra of a HiBi FBG inscribed in Panda type optical fiber HP-1550 using the phase mask technique for (a) 35 mm and (b) 10 mm long gratings.

3.2.6.10. Fabry-Pérot Cavities

Fabry-Pérot cavities are used widely for multi-wavelength lasers generation and optical clock recovery. For the purpose of optical clock recovery, it requires that the distance between peaks of the spectrum in frequency is approximately constant.

The Figure 3.23 (a) shows the reflection spectrum of a Fabry-Pérot filter for optical clock recovery at 40 Gbit/s [Albuquerque2009]. Two FBGs were imprinted using a phase mask method, an exposition time of 20 s and energy of 2,5 mJ per pulse. Each FBG has a length of 0,5 mm and the distance between them is 2,051 mm. The figure 2.16 illustrates a scheme for inscription of a

Fabry-Pérot filter containing two FBGs and one cavity between them. The production of very short Fabry-Pérot filters is more complex and its reflectivity is too small. For very high transmission rates (for instance 100 Gbit/s), number of peaks within the envelope function of the central peak is smaller because the peaks are more distant from each other, i.e., the FSR is greater. Thus, this type of filter has worse results for higher transmission rates [Albuquerque2009].
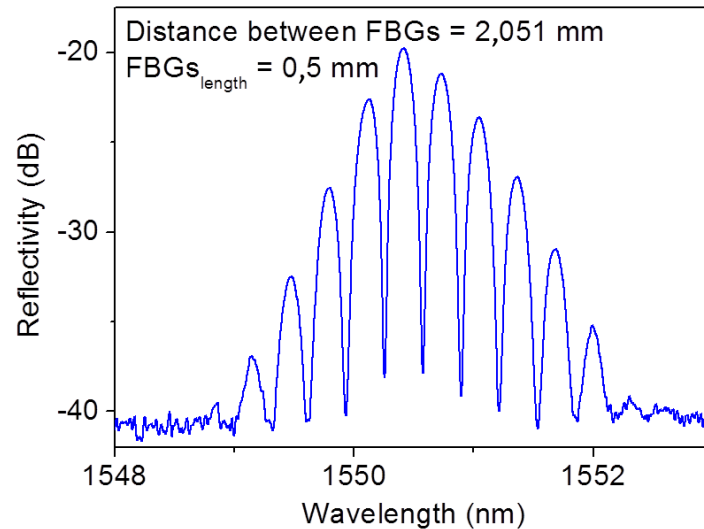
Figure 3.23 – (a) Reflection spectrum of a Fabry-Pérot cavity inscribed in standard SM photosensitive fiber (FiberCore PS1250/1500) using the phase mask technique.

3.2.6.11.   Regenerated FBGs

As is known, FBGs are used in many industrial and technological applications. Within standard telecommunications applications, for example, type I FBGs that can operate at 80 °C for 25 years are required – such gratings can in principle operate for lengthy periods up to 300 °C. Gratings that can operate at temperatures well above standard telecommunication requirements are critical to the success of many real time sensing applications. In industries involving high temperature furnaces, such as aluminum smelting or coal based power stations, it would be of interest to be able to monitor temperatures in excess of 1000 °C. Similar temperature requirements span many other types of industries such as structural health monitoring of buildings [Cardozo2007], or engine turbines in various vehicle formats, particularly aircraft

[Epaarachchi2009]. Another particularly important industry is the fiber laser sector [Canning2006].

In recent years, there has been an effort by the scientific community to increase the thermal resistance of an FBG. Previous studies have already established that the operable temperature of FBGs can be increased by several means, including tailoring the glass composition [Butov2006], pre-processing with seed irradiation [Åslund2000], the formation of type-In (or type IIA) [Xie1993, Groothoff2004] gratings and type-II [Archambault1993] gratings, including those inscribed using femtosecond IR lasers [Grobnic2006]. Another variant with superior high temperature stability is the so-called "chemical composition grating (CCG)" [Fokine2002] where a periodic index modulation can be regenerated after erasure of the UV induced type-I grating written in H-loaded germanosilicate fiber, which happens to contain fluorine, if annealed ~1000 °C. The prediction was a local reduction, or increase, of fluorine in the UV-exposed zones at that high temperature through diffusion of hydrogen fluoride. After, the general phenomenon of regeneration has been found in simple H-loaded germanosilicate fiber [Zhang2007]. Canning et al. demonstrated that if a seed FBG (grating inscribed into a hydrogen loaded standard SM photosensitive fiber) is heated to high temperatures (~900 °C) we obtain a new structure called regenerated FBG (RFBG), resistant to temperatures around 1000 °C [Canning2008a, Canning2010]. Recent work demonstrates that regeneration can be achieved without hydrogen, although for much lower temperature operation [Linder2009]. The heating causes the FBG spectral reflection band to initially disappear or decrease dramatically, followed by the growth of another spectral reflection band normally close to the same central wavelength.

Fabrication of seed FBG

In order to precipitate the structural change associated with regenerated gratings, a seed grating is necessary. In practice, it is confirmed that the stronger the seed grating, the stronger the final regenerated grating. For this case, conventional Bragg gratings inscribed into fibers with germanium or others dopants, with or without hydrogen have been presented [Canning2010]. For example, Figure 3.24 shows the reflection of a very strong type I Bragg grating inscribed in photosensitivity Fibercore PS1250/1500 SM fiber using the phase mask technique. The illumination was carried out using UV light from our KrF excimer laser at 248 nm. The fiber

samples were previously subjected to a hydrogenation process that occurred at a pressure of 150 bars during two weeks, in order to enhance its photosensitivity.
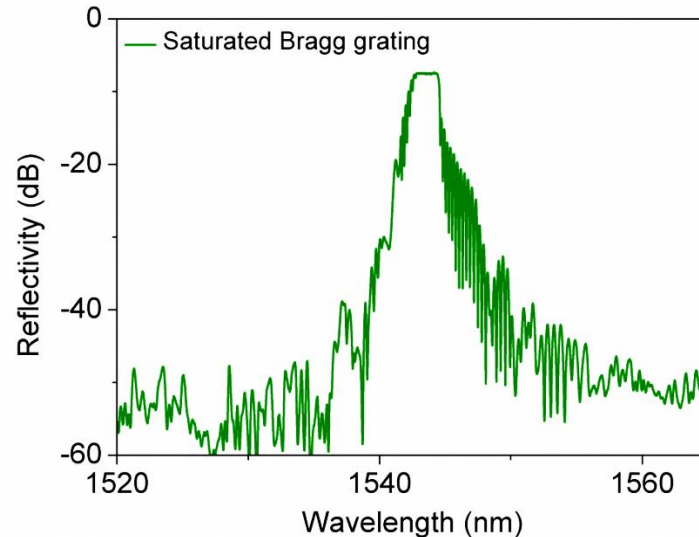

Figure 3.24 – Reflection spectrum of a very strong type I Bragg grating inscribed photosensitivity Fibercore PS1250/1500 SM fiber using the phase mask technique. L = 4 mm and exposure time of 20s.

Fabrication of RFBG

After the production, the FBGs were initially characterized in terms of their spectral response and afterwards put in an electrical oven for heating [Valmir2010]. Using a processing procedure identical to that optimized in [Canning2008b] strong seed gratings were thermally processed. Figure 3.25 shows the experimental setup used in the regeneration of FBGs. It is based on a tubular oven (Carbolite, MTF 12/25A model) and a quartz tube, where is placed the optical fiber containing the FBG. During the period between production and thermal characterization, the gratings were kept at dark. Two thermocouples were used to monitor and control the oven temperature. One of them was put at the center of the usable volume of the oven and the FBGs were placed surrounding it. The oven temperature can be kept with a fluctuation below ± 0.5 °C.

In this particular case, regeneration was obtained by heating the seed gratings in the oven laboratory to temperatures in the range of 550 °C until the seed signal vanishes and the regenerated grating signal stabilizes. The initial spectrum of the grating was obtained at room

temperature before starting the heating cycle, whereas the final spectrum is measured at the end of the process, after the grating cooled to room temperature again.
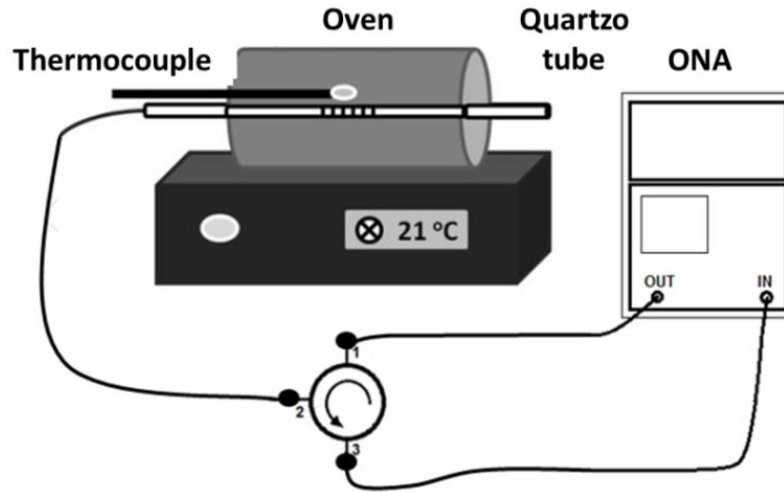
Fig. 3.25 – Experimental setup used for production of RFBGs (adapted from [Alberto2011, Valmir2012]).

Figure 3.26 shows the seed FBG reflectivity with a length L = 4 mm together with that of the respective RFBG. The reflectivity spectra of the seed show characteristics of a saturated grating. The considerable shift in the Bragg wavelength can be assigned to the changes in the refractive index profile [Canning2010]. A Bragg wavelength blue shift of the order of 2 nm is achieved. This value is in agreement with literature [Canning2008b].

Figure 3.26 – Regenerated grating spectrum.

The regeneration cycle for the mentioned grating is shown in Figure 3.27. The grating was annealed at 550 °C and afterwards it was kept in the oven. The evolution of the grating reflectivity is representative of the UV induced refractive index modulation during isothermal annealing. The grating reflectivity decreases during the first 78 min before a secondary growth. This secondary growth leads to an index change in the fiber core which is more temperature-stable than normal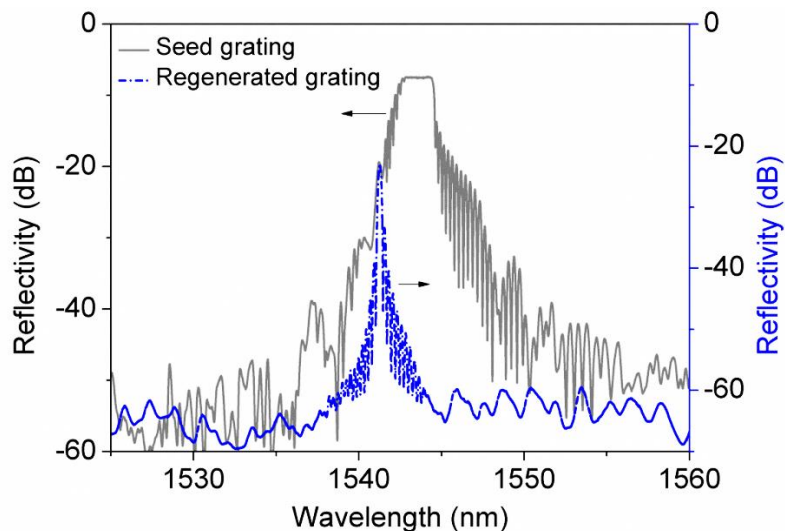 Type I FBGs. The reflection spectra show that the grating has been regenerated in approximately 72% of reflection relatively to the initial saturated grating, which corresponds to a signal ~35 dB above noise background. This secondary growth happens the first 5 min just after the grating vanishes. The heating process was only interrupted after 140 min test, where no significant signal variation is seen. It presents a similar behavior for any regeneration process using saturated FBGs, regardless of grating length and fiber saturation level.
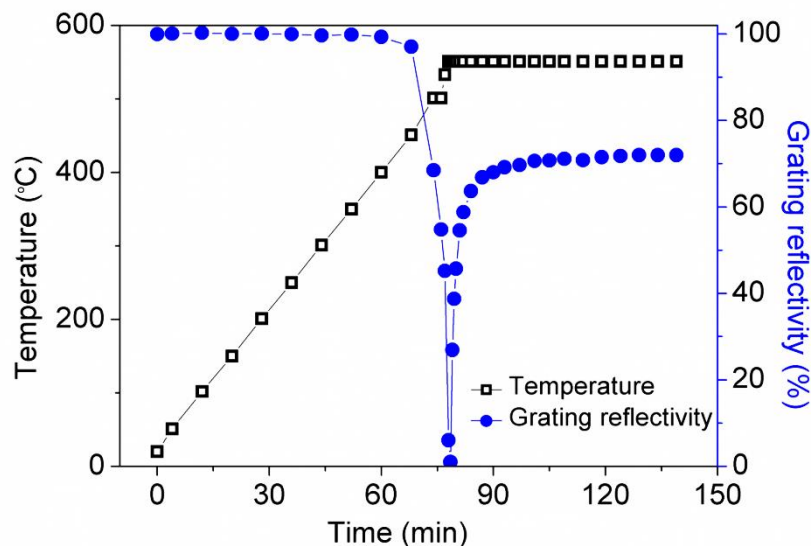
Figure 3.27 - The regeneration cycle for a grating.

In conclusion, it shall be noted that the mounted workstation for fiber gratings fabrication in silica optical fiber contributed not only for several devices used and presented by the author in this thesis, but also for several devices used and tested in other scientific works resulting in papers published in internationally peer reviewed journals [J1-J4, J7, J10, J13] and conference proceedings [C2-C5, C9, C11, C14, C15, C18-C20, C23-C26, C28, C30].

3.3. Gratings Fabrication in Polymer Optical Fiber

Polymer optical fibers (POFs) are starting to be considered a viable alternative to silica fibers in photonic applications [Atef2012a, Shi2013, Yuan2011a, Zhang2012], mainly due to their flexibility, easy non-skilled handling, higher mechanical resistance to impacts and vibrations, relative low cost and ruggedness. POF has exhibited increasing potential in the short distance moderate bandwidth data communication applications [Daum2001, Möllers2009] including high rate data transmission in automotive industry [Kibler2004]. As a potentially low cost sensing solution, it has several advantages compared with its silica counterpart, including higher thermal and strain sensitivity the ability to survive much higher strain levels [López2005]. In addition, POF development also focused on microstructured designs, allowing endlessly SM and air guiding operation with larger cores when compared to SI fibers [Large2011].

These advantages make POF very attractive for use in short-range optical communications as in media oriented system transport, industrial control, in-building networks [Polishuk2006, Ziemann2008], and radio over fiber systems [Lethien2005]. However, one of the major drawbacks pointed to POFs is the greater attenuation coefficient as compared to silica fiber (≤0.2 dB/km at 1550 nm for conventional standard SM fiber), a fact that limits their applications. In fact, POFs made of standard poly(methyl methacrylate) (PMMA) [Zhang2012,Stefani2011] and TOPAS [Yuan2011a] have very high attenuation of more than 50 dB/m at wavelengths near 1550 nm. This makes it hard to work with POFs at the C-band region, unless using very short sections of fiber. However, recent studies show that the use of perfluorinated polymers as core materials significantly reduces losses [Koike2009, Lethien2011, Makino2012]. It means all the hydrogen in the polymer is replaced by fluorine. The heavier fluorine atoms reduce the frequency of molecular vibrations and shift the associated absorption lines to longer wavelengths, increasing the transparency in the visible (VIS) and near infrared (NIR) [Argyros2013]. Certain perfluorinated polymers such as poly(perfluoro-butenylvinyl ether) are preferred, as they exhibit much lower propagation losses and can be operated at longer wavelengths, where transmitters and receivers as developed for silica fibers can be used. For instance, in one of the best transmission POF, graded-index POF (GI-POF), the core is perflurinated GI presenting low losses, low dispersion, high bandwidth, low cost, and good transmission characteristics already achieved in the literature[Yang2009, Shao2012].

A significant decrease in the material loss can be achieved by working at a lower wavelength, in particular, the 0,06 and 0,2 dB/m [Atef2012b, Makino2012] target is possible at wavelength (between 520 and 850 nm) at which CMOS (complementary metal-oxide-semiconductor) technology is available [Atef2012b]. For this reason, there is currently a strong push in the sensor and optical communications (such as POF transmission systems) community to develop polymer devices in VIS and NIR window, allowing thereby to solve this drawback easily.

Bragg gratings in POF (PFBGs) are well attractive due the easy integration in optical components and to be cost effective for data communication [Atef2012a, Shi2013, Polishuk2006, Ziemann2008, Lethien2005, Lethien2011, Atef2012b, Makino2012, Park2011], and sensor applications [Yuan2011a, Zhang2012, Stefani2011]. PFBGs have been reported in both SI-POF [Stefani2011] and microstructured POFs (mPOF) [Yuan2011a, Stefani2011] including SM FBGs and multimode FBGs (MM FBGs). The most PFBGs reported to date had a resonance wavelength around 1550 nm, primarily because of the availability of low cost telecom equipment at that wavelength. To date, total exposure times of 45-100 minutes for step index fibers [stefani2011, Yuan2011b] and 60-270 minutes for mPOF [Stefani2011, Yuan2012] are usually necessary for writing the FBGs (between 2 and 10 mm). Furthermore, in most cases these FBGs have 10 dB of rejection or less in the case of MM PFBGs [Luo2011]. Recently, it was reported a narrow bandwidth FBG at 850 nm in two types of few-moded POFs (mPOF and SI-POF) with 10 mm long FBG, achieving bandwidths of 0,29 nm and 0,17 nm, respectively, and 10 dB of rejection using an expanded beam for writing the FBGs [Stefani2011]. However, in some applications, including sensors and WDM POF communications, narrower filters with higher reflectivities are needed.

Bragg gratings have been inscribed in polymer optical fibers using conventional techniques that have been utilized for the inscription of gratings in silica optical fibers, for example, PFBG has been fabricated using the phase mask technique [Dobb2005] or a ring interferometer arrangement [Liu2001], with grating inscription undertaken using CW or pulsed laser sources operating at either 325 nm [Dobb2005] or 355 nm [Liu2001]. One of the strongest PFBG achieved is with 28 dB transmission rejection and a linewidth less than 0,5 nm [Liu2002]. The inscription time can vary from a few minutes [Yu2004] to over one hour [Peng1999], depending on the different photosensitivity induced into the core of the fiber. Upon those successful experiences, FBGs are successfully inscribed in several kinds of POF in this thesis, i.e. standard PMMA based mPOF, PMMA based doped and undoped SM and MM POF.

3.3.1. POF Bragg Grating Inscription Setup

A continued-wave helium cadmium laser (Kimmon IK3301R-G) operating at 325 nm and ~30 mW of laser power is used in the system. The schematic diagram is shown in Figure 3.28.
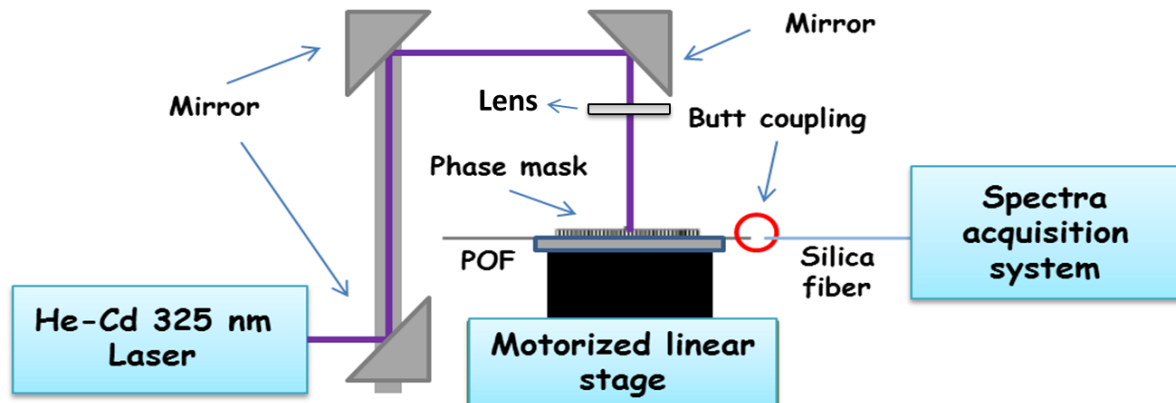

Figure 3.28 – Schematic diagram of PFBG inscription system.

After cleaving of the fiber, POF is mounted into v-grooves on both sides with a gap in between to avoid reflection, and it was taped down to ensure that the fiber did not sag. Furthermore, the POF is supported along its length in order to minimize the effects of air currents and laser-induced heating on the fiber position. The v-grooves are attached to a three-axis translation stage. This setup must allow the fiber to be fixed firmly, preventing any motion which would result in a grating being smeared or destroyed. A static laser beam (beam width = 1,2 mm) is focused vertically onto the fiber by a cylindrical lens (focus length = 10 cm) through the phase mask. The cylindrical lens is used to focus vertically downward the laser light on the optical fiber in order to increase the power density onto the fiber's core. The pattern imprinted into the fiber is determined by the phase mask (Ibsen Photonics), placed just above the fiber, whose uniform periods of 405,4 and 557,2 nm are optimized for polymer fibers to give 605 and 830 nm gratings in the CMOS window, and a period of 1042,7 nm for 1550 nm spectral range.

The long FBGs are obtained through scanning along the phase masks that is made by a motorized linear stage (MFA- CC), which containing the fiber and the phase mask, with a specific speed defined by the total exposure time (t_{exp}) and long FBGs are produced for various kinds of POFs.

The MFA-CC has a travel range of 25 mm, the minimum incremental motion is 0,1 μm with a repeatability of 0,3 μm. The maximum speed is 2,5 mm/s. The general view of the gratings manufacturing workstation for POF is shown in Figure 3.29 containing the motorized linear stage, which supports the fiber and phase mask.

With this set-up, at 1550 nm, the reflected spectra were monitored by an interrogation system (Micron Optics 125-500) with wavelength accuracy of 1 pm. The growth of the 830 nm and 600 nm FBGs was monitored in reflection with a spectral resolution of 0,33 nm using an 850 nm or 650 nm 1x2 silica fiber couplers (SM or MM accordingly), a broadband light source HL-2000 (Ocean Optics) and a spectrometer USB2000+VIS-NIR (Ocean Optics).
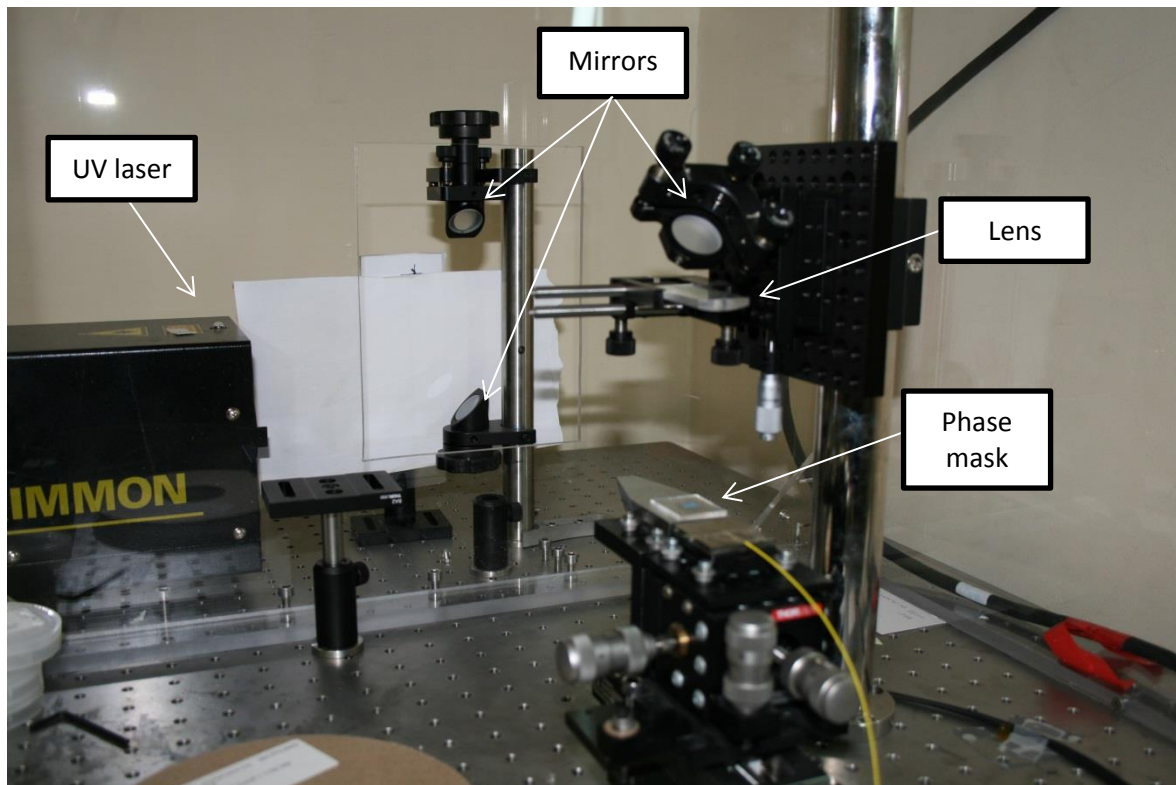

Figure 3.29 – General view of the manufacturing workstation for PFBGs.

A very essential factor must be mentioned, the cleaving of the POF. POF cannot be cleaved by cleavers for silica fibers but by blade cutting. There are a few studies [Law2006, Abdi2009] investigating the cleaving of POFs and they claim that the quality of the cutting surface of the

fiber is mainly affected by the temperature of the fiber and blade together with the speed of the cut. In this thesis, the PMMA based fibers are found to be well cleaved by hand on a hot plate with a razor blade (SH-2 Magnetic stirrer) at approximately 80°C for both the blade and fiber, which gives a high quality end facet. The quality of the cut is verified using a microscope (Olympus BH2-UMA) and will be shown in the next section. A silica fiber pigtail (SM or MM accordingly) was butt-coupled to the POF using an angle cleaved end-facet (8° angled Cleaver, model CI-08, Ilsintech) and a small amount of refractive index matching gel in order to reduce Fresnel reflections, which manifested themselves as background noise. The butt-coupling is aided for an XYZ translation stage.

Thus, one out arm of the coupler is spliced with FC/APC pigtail which was used to couple the light into the POF. The two input arms of the coupler, spliced with FC/PC pigtails were correspondingly connected to the light source and the spectrometer. At first, the light source was a He-Ne laser working at 633 nm. By adjusting the three-axis translation stage, the maximum throughput of POF at 633 nm is obtained (the core-to-core alignment is aligned by red light source at 633 nm). Then the light source is switched to the broadband light source. This is due to the invisible infra-red Bragg wavelength of the grating. In addition, the gratings can also be monitored in transmission. Instead of using the coupler, light can be directly coupled into one end of the fiber from the broadband light source and out of the fiber from the other end to the spectrometer by using butt coupling method and FC/PC patch cord.

3.3.2. Implemented Methods of Inscription of Fiber Gratings

3.3.2.1. Phase Mask Method

As mentioned in the section 3.2.3, the inscription by phase mask is a simple method where it is possible to inscribe fiber grating via a single uniform exposure of laser light, which is defined by laser beam width (~ 2 mm), without the need of a translation stage. However, greater FBG lengths can be achieved with this technique if the beam is expanded, but with a lower use of laser power.

3.3.2.2. Scanning Inscription Method

Long FBGs can be inscribed by a scanning method. A translation stage supports whole the structure that containing phase mask/optical fiber and the laser beam path remains static. The FBG length is limited to the phase mask length. Figure 3.30 shows the scanning stage sub-assembly.
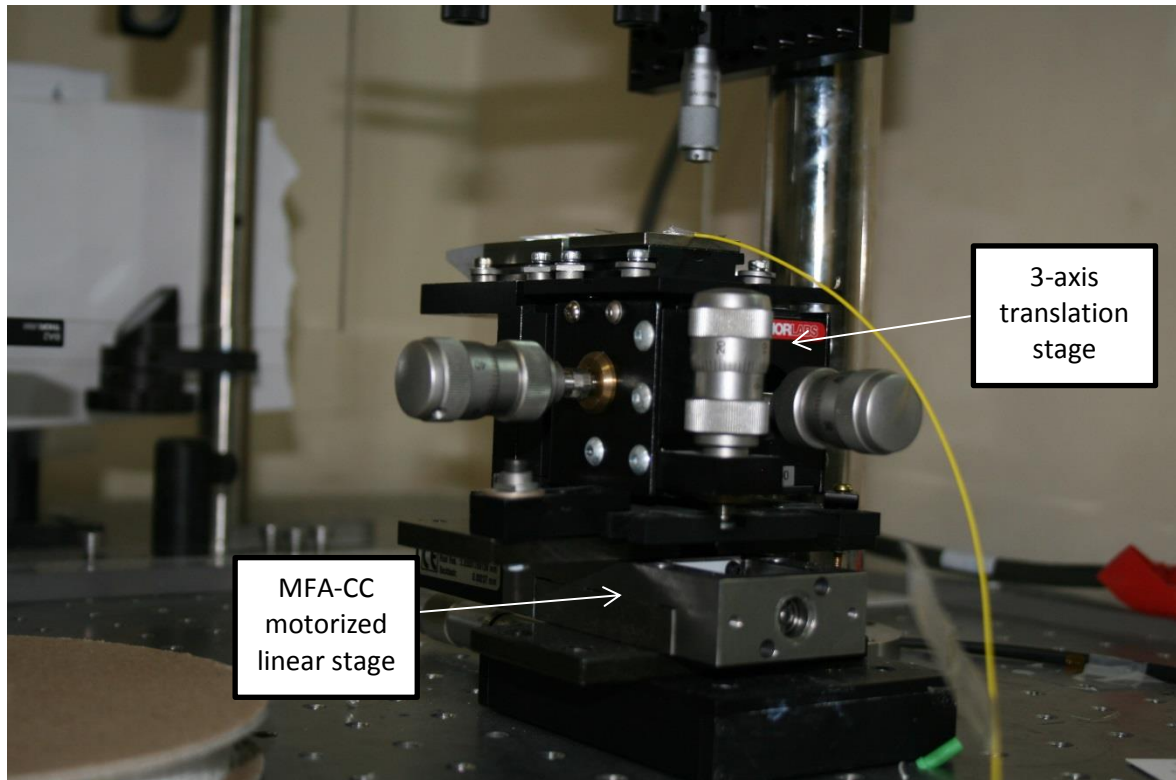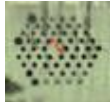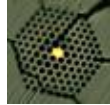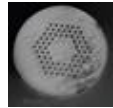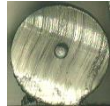
Figure 3.30 – Motorized linear stage sub-assembly, which supports the POF and phase mask.

3.3.3. Characterization of inscribed fiber gratings

First, the inscription of 10-mm-long FBGs at 1550 nm is carried out by checking their response and afterwards, FBGs are inscribed at 600 and 850 nm spectral windows with the same length to obtain a comparison for these three spectral windows. The gratings fabrication conditions and POF specifications are described in Table 3.6. All POFs in study are commercially available.

Table 3.6. POFs parameters and FBGs fabrication conditions

POF specification and FBGs fabrication conditions					
Mode	**Fiber name**	**Core / Outer diameter (μm)**	**Rings of holes**	**t$_{exp}$ (min)**	**Fiber cross section**
Few-mode	mPOF (Kiriama)	15 / 150	4	45	
Single-mode	MORPOF02 (Paradigm Optics)	3,13 / 115	-	20	
	mPOF (Kiriama)	6 / 125	6	45	
Multimode	mPOF G3 (Kiriama)	34 / 250	1	83	
	mPOF (Kiriama)	50 / 150	3		
	GI-POF (Chromis Fiberoptics)	50 / 490	-	60	

3.3.3.1. Step Index POF Bragg Gratings

The photosensitive SM SI-POF (MORPOF02 Paradigm Optics) used in grating fabrication experiments is supplied by Paradigm Optics. The fiber (shown in Table 3.6) possesses a 115 μm diameter pure PMMA cladding with a 3,13 μm diameter core based on PMMA but containing dopants (details are not provided by the supplier) to raise the refractive index and enhance the photosensitivity to 325 nm UV light so as to enable the faster inscription of the Bragg grating. So for this kind of fiber, the scanning inscription method is chosen for grating fabrication and this will enable a longer grating length, leading to the narrower bandwidth. Upon the bandwidth equation of a uniform Bragg grating (equation (2.31) of the previous chapter), the longer the grating (more grating planes) is, the smaller the bandwidth will be.

The Bragg grating is inscribed in the doped photosensitive MORPOF02 with the scanning inscription. The total exposure time is related with FBG length and velocity of the motorized linear stage. For a total exposure time of 20 min and FBG length of 10 mm, the sweep velocity was set to be 8×10^{-3} mm/s. Figure 3.31 shows the amplitude response and 3-dB bandwidth for PFBG achieving 21 dB of rejection and 3-dB bandwidths of 0,11 nm. The MORPOF02 fiber is SM at 1300 nm (or greater). This fiber has a quoted NA of 0,27 at 1100 nm. The normalized frequency $V = \left(2\pi a_{core}/\lambda\right)NA$, is then 3.98 at 850 nm, which indicates that the fiber will support 6 modes at 850 nm.
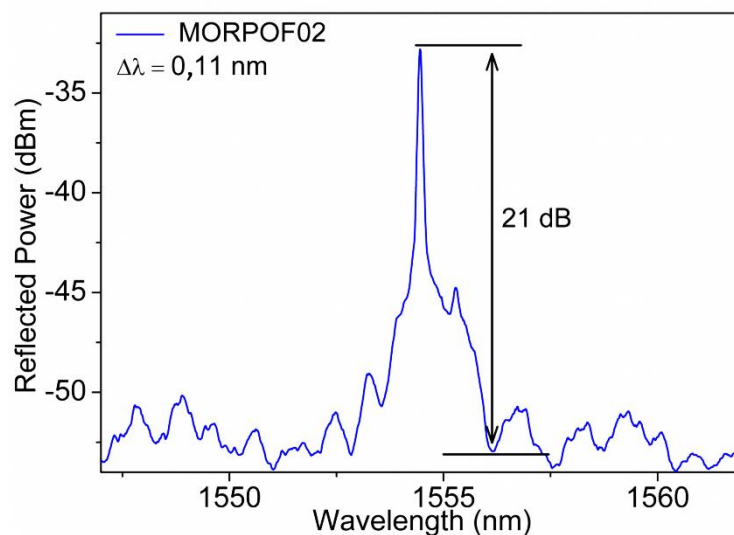
Figure 3.31 - Reflection spectrum of FBGs written in SM MORPOF02 at 1550 nm.

For PFBG at 850 nm it is achieved a 3-dB bandwidth of 0,09 nm, which is less than the previously published [Stefani2011] (see Figure 3.32).
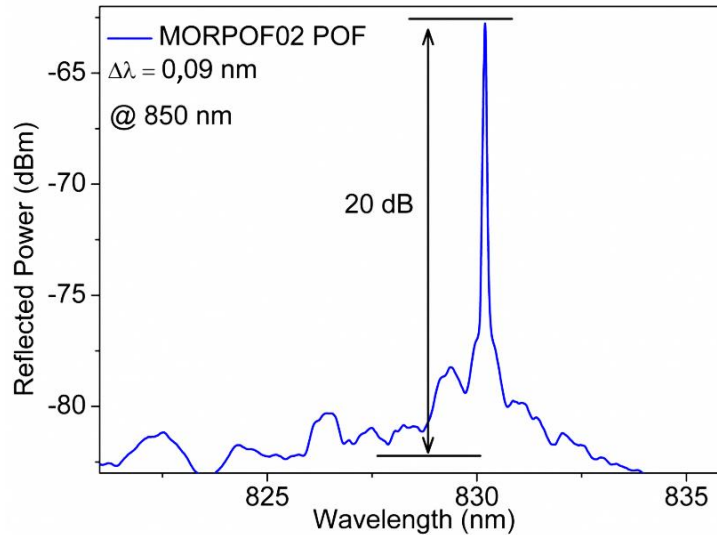
Figure 3.32 - Reflection spectrum of FBG written in SM MORPOF02 at 850 nm spectral range.

3.3.3.2. Graded Index POF Bragg Gratings

The first inscription of a Bragg grating in GI-POF was achieved as shown in Figure 3.33.
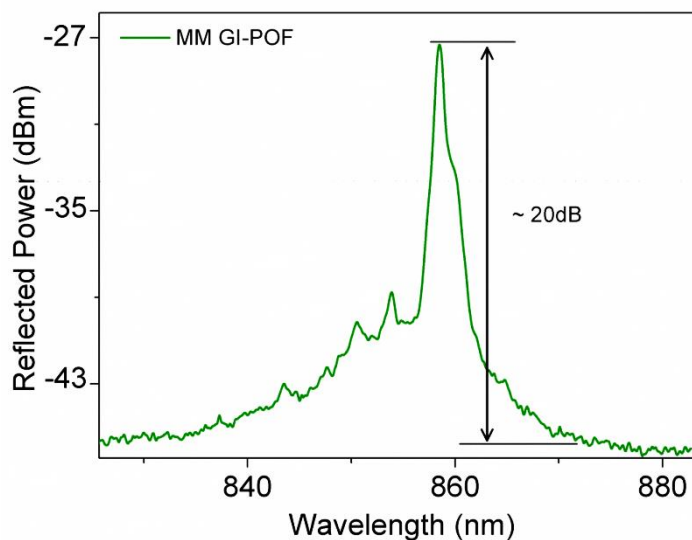
Figure 3.33 - Reflection spectrum of FBG written in MM GI-POF at 850 nm spectral range.

For this fiber (supplied by Chromis Fiberoptics), the core is perfluorinated graded index and it has a diameter of 50 μm. The outer region of this fiber is about 490 μm. Table 3.6 also shows the microscope image of the end facet of the GI-POF. The FBG has an optical rejection of 20 dB and presents a typical inscription time of 60 min. The Bragg wavelength of the inscribed grating was in the region of 860 nm with a length of 2 mm, determined by the width of the UV laser beam.

3.3.3.3. Microstructured POF Bragg Gratings

Few-mode fiber

The PMMA mPOF used in Bragg grating fabrication is supplied by Kiriama, Australia. The cross section of the fiber after cleaving is shown in Table 3.6. The fiber used consisted of pure PMMA and was fabricated using the method described in reference [Barton2004]. The fiber has an outside diameter of 150 μm and a core diameter of 15 μm. This mPOF has with 4 rings of holes separated with a pitch (Λ_h) of 9,61 μm and a hole diameter (d_h) of 4,2 μm. The hole diameter to pitch ratio (d_h/Λ_h) of 0,44 means that the mPOF is few-mode at 850 nm [Kuhlmey2002]. Simulating the mPOF for 600 nm, 850 nm and 1550 nm, it is confirmed that this fiber is SM for 1550 nm. In the case of 600 and 850 nm the fiber have three modes and their respective polarizations as is shown in Figures 3.34 (a-d). Figure 3.34 (e) depicts a FBG optical rejection of 15 dB above noise background and a 3-dB bandwidth of 0,16 nm at 1550 nm range.
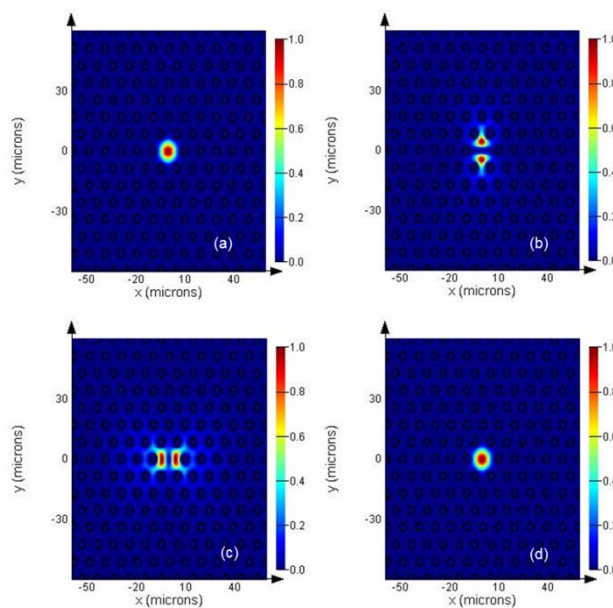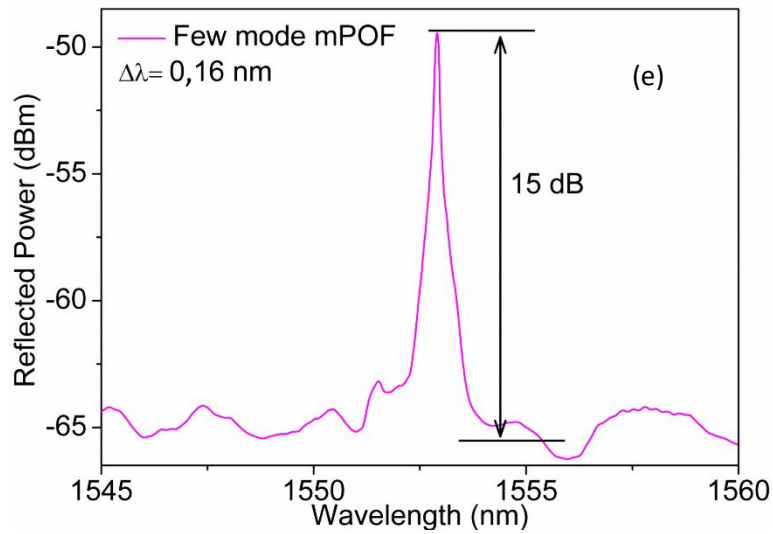
Figure 3.34 - (a-c) Simulated spectral modes of the mPOF for 850 nm presenting three modes and their respective polarizations. (d) The fiber presents a SM at 1550 nm. (e) Reflection spectrum of a few-mode mPOF FBG.

Figure 3.35 (a) shows the reflection spectrum of a 25 mm PFBG fabricated with this mPOF, which presents a narrow 3-dB bandwidth of 0,045 nm and 17 dB of rejection at 1550 nm window. The spectrum was recorded before saturation after a writing time of 105 min. The first PFBG at 600 nm spectral region is also reported as shown in Figure 3.35 (b). The 10-mm long PFBG has a narrow 3-dB bandwidth of 0,13 nm and the optical rejection is 17 dB.
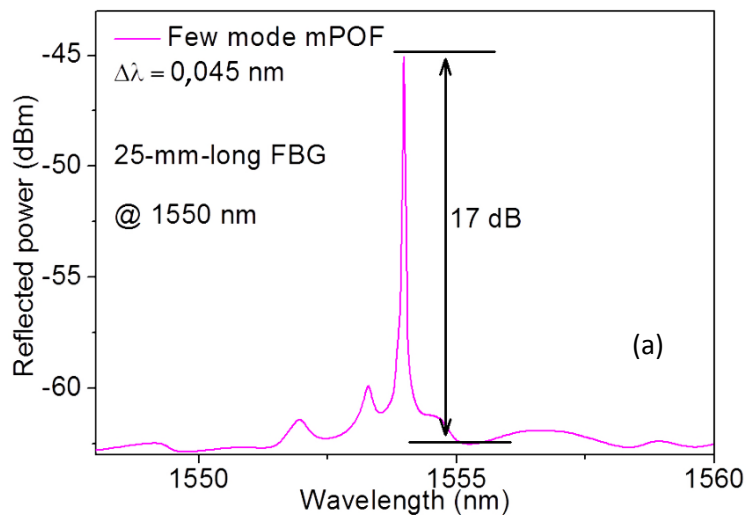
Figure 3.35 - Reflection spectra (a) of a few-mode mPOF FBG at 1550 nm (25-mm-long FBG) and (b) few-mode mPOF FBG at VIS spectral window (10-mm-long FBG).

The necessary total exposure time to write a FBG in an mPOF is longer than to inscribe a grating in a solid POF of the similar diameter and leads to relatively weak gratings. This is because the holes around the core of the mPOF scatter a significant part of the laser power during the writing process [Marshall2007].

Single-mode fiber

The cross section of the other SM mPOF after cleaving is shown in Table 3.6. The fiber has an outside diameter of 125 µm, a core diameter of 6 µm and 6 rings of holes. Figure 3.36 (a) shows the amplitude response and 3-dB bandwidth for mPOF achieving 16 dB of rejection and 3-dB bandwidth of 0,19 nm at 850 nm spectral range. A similar result is shown in Figure 3.36 (b) at 1550 nm spectral range with 15 dB of rejection and 0,22 nm of bandwidth.
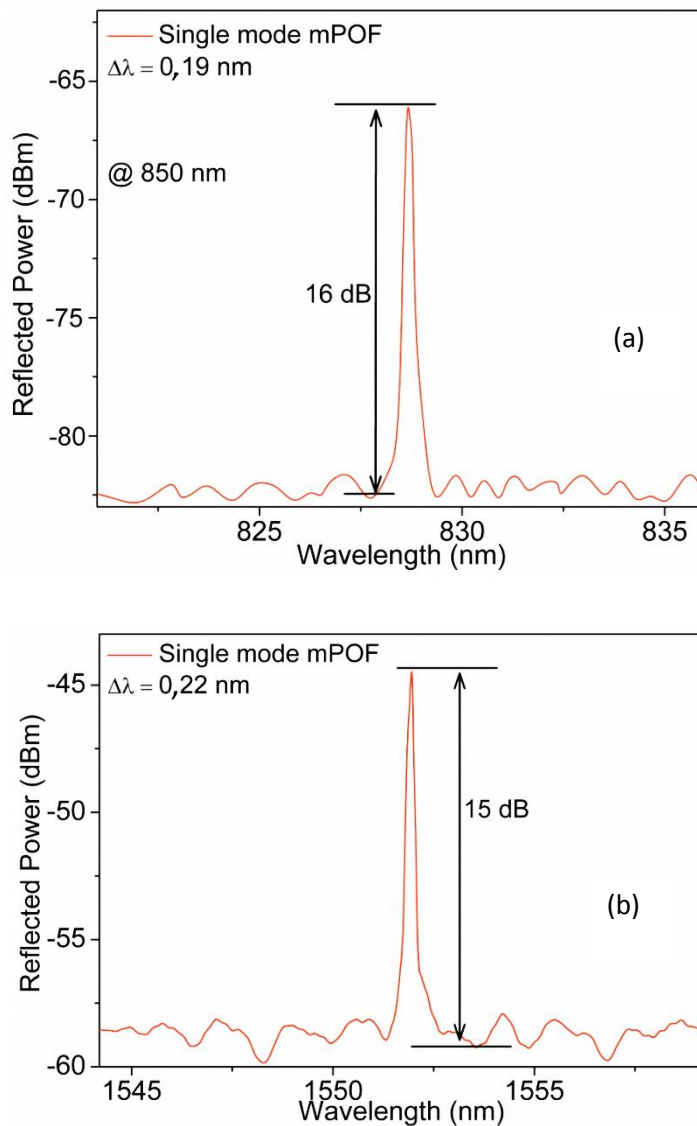
Figure 3.36 - (a) Reflection spectrum of the SM mPOF FBG at 850 nm with 3-dB bandwidth of 0,19 nm with 16 dB rejection. (b) Spectrum at 1550 nm.

Multimode fiber

Bragg gratings in MM mPOF (Kiriama) were also obtained. At 1550 nm both MM mPOF FBGs display a similar rejection level for the same total exposure time however, the 3-dB bandwidth is 0,15 nm for the MM mPOF G3 (Figure 3.37 (a)) and 0,08 nm for the MM mPOF with three rings of holes (Figure 3.37 (b)). This difference between both values may be due to the distinct geometry of air holes and fiber diameter (core and outer). The lower than expected 3-dB bandwidth

obtained for MM mPOF when compared to SM mPOF can be due to the excitation of only one mode because a SM fiber optic cable was used to link the grating to the interrogating system. The MM mPOF FBG is shown in Figure 3.37 (c) at 850 nm spectral window and it exhibits an optical rejection and 3-dB bandwidth around 15 dB and 0,11 nm, respectively. It is also reported the first MM PFBG at 600 nm spectral region as shown in Figure 3.37 (d). The 10-mm long FBG has a narrow 3-dB bandwidth of 0,07 nm and the optical rejection is 15 dB using MM mPOF.
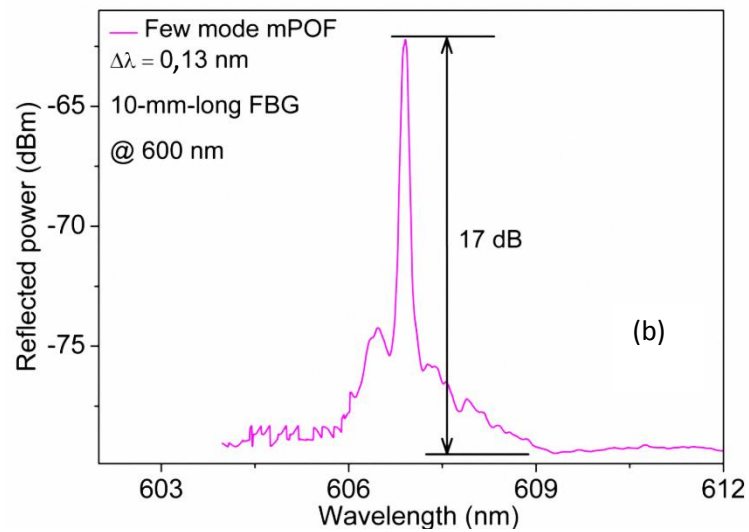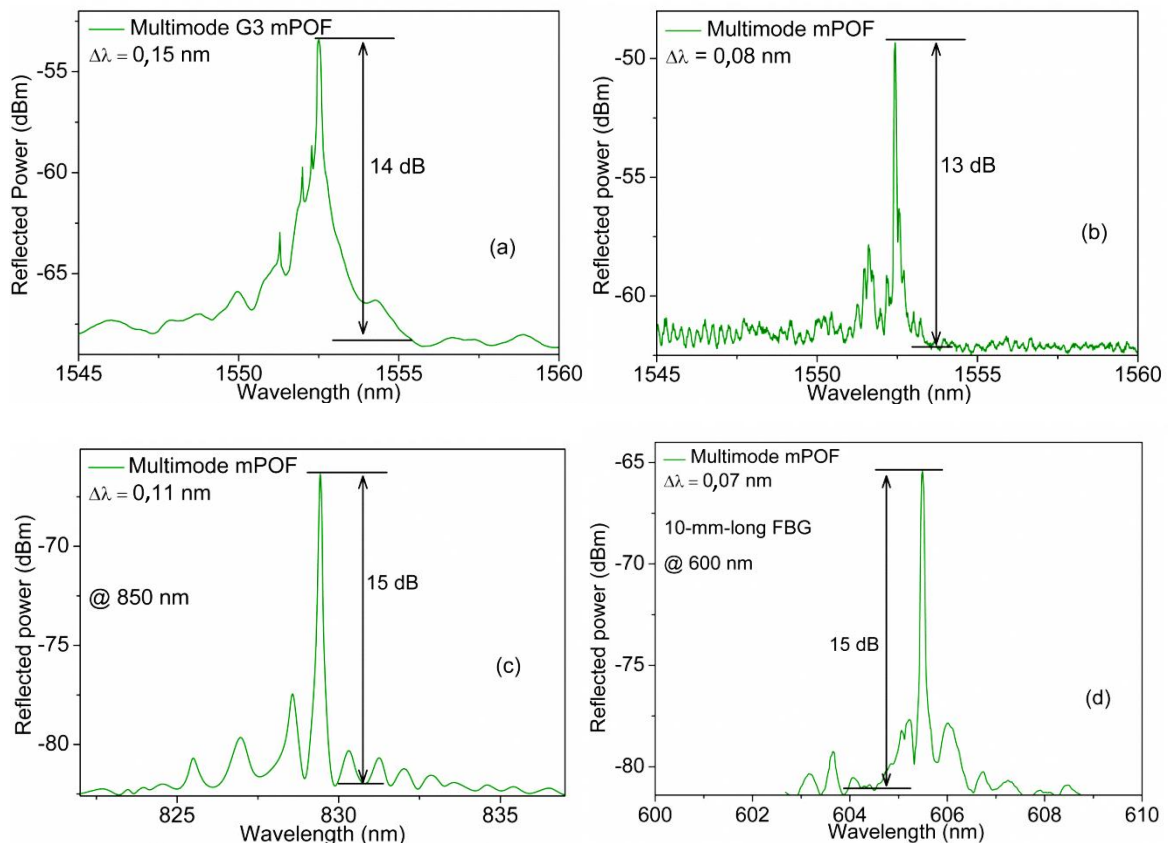

Figure 3.37 – Reflection spectrum for MM mPOF FBG at (a-b) 1550 nm, (c) 850 nm and (d) 600 nm.

It shall be noted that the measured 3-dB bandwidth of the SM mPOF is significantly higher than other fibers, which may be explained by the scatter of the laser beam due to the presence of the six rings of holes, which might induce a small chirp during the writing process.

These results show a significant improvement in amplitude response, 3-dB bandwidth as well as total exposure time when compared with those reported in the literature [Stefani2011, Yuan2011, Yuan2012]. An explanation for this fact is a better use of laser power due to the short

optical path until the fiber, and to employ the motorized linear stage to do the scanning of phase mask instead of expanding the laser beam.

Table 3.7. Loss values for @650-nm of the used POFs

Mode	Fiber name	Loss @ 650 nm (dB/m)
Few-mode	mPOF (Kiriama)	1
Single-mode	MORPOF02 (Paradigm Optics)	0,2 (manufacturer) >> 0,2 [Stefani2011]
	mPOF (Kiriama)	3,8
Multimode	mPOF G3 (Kiriama)	0,5
	mPOF (Kiriama)	0,7
	GI-POF (Chromis Fiberoptics)	0,07

The losses for the POFs used in this thesis are reported in Table 3.7. By analysis of Table 3.7 and reflection spectra of FBGs inscribed, it can be stated that the FBG inscribed in MORPOF02 presents a good spectral response coupled with low loss of this fiber. However, recent experimental measurements show that the MORPOF02 has very high losses even at short wavelengths [Stefani2011].

3.4. Chapter Summary

Gratings fabrication in silica fiber was presented in this chapter. Special attention was dedicated to the implemented methods of inscription of fiber gratings and characterization of all fiber gratings inscribed such as uniform FBG, chirped, phase-shifted, tilted, LPGs, among others. The description of this automated setup and the developed control software (in LabView) was presented, followed by the required calibration functions. Finally, gratings fabrication and characterization in different types of polymer optical fiber was described as well as the implemented methods for its inscription.

Chapter 4

Acousto-Optic Modulation in Fiber Gratings

4.1. Introduction

Predicted by L. Brillouin [Brillouin1922] and confirmed by Debye and Sears [Debye1932], the acousto-optic effect was consolidated by the end of 1930s. First, L. Brillouin proved that when a liquid, excited by a mechanical wave with short wavelength, is irradiated with visible light, a diffraction pattern is generated, similar to that obtained with a diffraction grating [Born1980]. The first experimental work on the interaction between mechanical waves and electromagnetic radiation was done by Brillouin, who studied the x-rays diffraction in a homogeneous transparent solid excited by thermic vibration, which generates elastic waves. In 1932, experiments carried out by Lucas and Biquard in France and Debye and Sears in the United States studied the optical properties of solids excited by ultra-sound waves and demonstrated the scattering of light by them. Both experiments demonstrated that the dielectric properties of a medium are modified by acoustic waves (AW) causing variation in the propagating electric field. The acousto-optic effect can be understood as a phenomenon of diffraction of electromagnetic radiation firstly observed in liquids and later on solid materials. This effect, for example, was used to measure the speed and attenuation of mechanical waves in transparent media. In 1978, Thurston presented the theory of propagation of mechanical waves in homogeneous cylindrical waveguides formed by cladding and core (clad rods), which was consequently used to model optical fibers. Thurston

showed a complete description of the mechanical resonant modes in these waveguides, and also pointed out the limitations of each case, i.e. considering guides without cladding, thin cladding, infinite cladding, etc. [Thurston1978].

After the invention of the laser and high frequency piezoelectric transducers (PZT) (in the range of hundreds of MHz), the acousto-optic interaction attracted attention, and a new and interesting research topic raised up as a promising area for telecommunications and sensing. In 1987, Roy et al. showed that, through the use of elastic waves, it is possible to rapidly change some properties of light, such as intensity and frequency. The interaction between laser beams and bulk elastic waves gave rise to new components, such as modulators [Roy1987, Paldus1997], optical deflectors [Warner1972, Gottlieb1983], optical spectrum analyzers [Gottlieb1992], tunable optical filters [Giruts1991], among others. On the other hand, the same effect can be used to sense properties of a specific solid or used in acoustic emission sensors [Perez2001, Betz2003].

4.2. The Acousto-optic Effect

The basic structure of the fiber acousto-optic modulator (AOM) is based on the device patented by Zemon and Dakss in the United States (US6068191) [Zemon1978]. Such modulator is able to modulate the intensity of light through the application of an acoustic wave. Figure 4.1 shows the schematic diagram of the device.
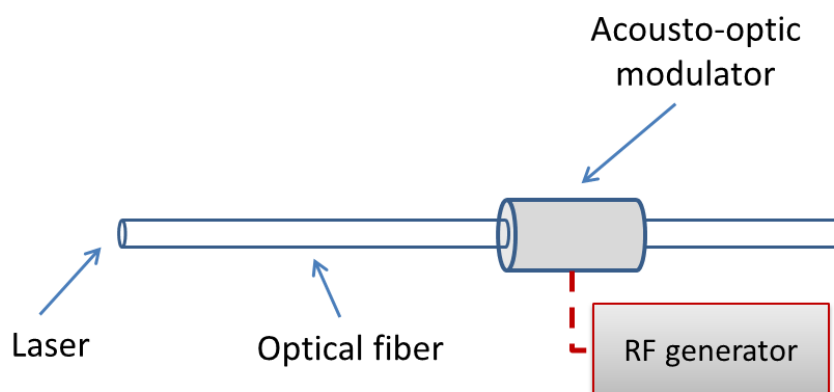

Figure 4.1 - AOM, patent number 6.068.191 – The United States [Zemon1978].

In 1986, Russell showed that the planes of an FBG can be modulated with the use of acoustic waves. He called this effect acousto-optic superlattice modulation (AOSLM), which is based on the Bragg-type Floquet-Bloch waves [Russell1986a]. The Floquet-Bloch waves are the simplest complete solutions of Maxwell's equations that exist in a periodically stratified medium such as, for example, a SM fiber with a diffraction grating written in it [Russell1986b]. In AOSLM the counter-propagating optical modes are generated by the fine pitch Bragg grating and the coarse-pitch, generated by the acoustic wave, which forms the superlattice. Coupling is maximum when the inter-Bloch-wave beat period matches the acoustic wavelength [Liu1997].

Even though various mechanical modes can be generated in fibers (for example, radial, torsional, longitudinal or flexural), effects in gratings are achieved manly through longitudinal and flexural excitation. Therefore, in this work two kinds of acoustic excitation are considered, one due to the propagation of longitudinal acoustic wave and the other due to the flexural vibration of the fiber.

4.2.1. Longitudinal Acoustic Waves

When longitudinally launched along the fiber, which contains the FBG, the acoustic wave causes a periodic compression and rarefaction strain field, causing a change in the effective refractive index of the fiber, through the photo-elastic coefficient, p_e ($p_e = \dfrac{n_{eff}^2}{2}\left[p_{12} - \sigma\left(p_{11} + p_{12}\right)\right]$ with p_{11} and p_{12} are the components of the strain-optic tensor, and σ is the Poisson's ratio [Othonos1999], while moving the modulation planes of the grating. An analytical approach by [Russell2000] defined the resulting strain field in the form:

$$
\begin{aligned}
\varepsilon\left(p\right) &= \varepsilon\left(k_s z - \omega_s t\right) \\
&= \varepsilon_0 \cos\left(k_s z - \omega_s t\right)
\end{aligned}
, \tag{4.1}
$$

where $p = \left(k_s z - \omega_s t\right)$ is the propagation phase, $k_s = 2\pi/\lambda_{acoustic}$ is the acoustic wave vector, $\lambda_{acoustic}$ is the acoustic wavelength, and ω_s is the angular frequency. For an acoustic beam of area A, carrying power P_s in a medium with Young's modulus E and acoustic group velocity u_{gs}, the peak strain has the value

$$\varepsilon_0 = \sqrt{\frac{2P_s}{EA\upsilon_{gs}}} \; . \tag{4.2}$$

The periodic strain field perturbs the grating in two ways. Firstly, the effective refractive index (n_{eff}) increases according to the elasto-optic effect, causing changes in the optical path length. Thus, the effective refractive index variation proportional to the elasto-optic changes can be expressed as

$$\Delta n_{eff} = (1 - p_e)\varepsilon(p), \tag{4.3}$$

where p_e is the the photo-elastic coefficient, also called as stress-optical coefficient of the fiber. Secondly, the grating pitch is periodically modulated, causing a spatial-frequency modulation. The resulting effective refractive change is given as

$$\Delta n_{eff}(p) = (1 - p_e)\varepsilon(p) + n_0 \left\{ 1 + C\cos\left[K\left(z - \int \varepsilon(p)dz\right)\right]\right\}, \tag{4.4}$$

where C is the modulation depth of the effective refractive index n_0 in the unperturbed FBG, $K = 2\pi/\Lambda$ is the grating vector [Russell2000].

Replacing (4.1) in (4.4), one shows that the pitch modulation produces a sequence of sidebands in spatial frequency whose amplitudes are given by a standard Bessel function expansion as

$$\begin{aligned}
\cos\left[Kz - m\sin(p)\right] &= \\
&= J_0(m)\cos Kz + \sum_{n=1}^{\infty} J_n(m)\left[(-1)^n \cos(Kz + np) + \cos(Kz - np)\right], \\
&= J_0(m)\cos Kz + \sum_{n=1}^{\infty} J_n(m) \left\{ \begin{array}{l} (-1)^n \cos\left[(K + nk_s)z - n\omega_s t\right] + \\ +\cos\left[(K - nk_s)z + n\omega_s t\right] \end{array} \right\}
\end{aligned} \tag{4.5}$$

where

$$m = \frac{K\varepsilon_0}{k_s} = \frac{\lambda_{acoustic}\varepsilon_0}{\Lambda} \; . \tag{4.6}$$

Note that m changes sign with the direction of the acoustic wave. It is clear that a sequence of ghosts of the original fiber grating form at spatial frequencies given by successive spatial sidebands of K. The amplitudes of these sidebands are given for small argument ($|m| \ll 1$), as

$$J_n(m) \cong \frac{m^n}{2^n n!}.$$

(4.7)

One can illustrate this formulation with the help of Figure 4.2, which shows the forward (0) and backward (1) Bloch waves. Figure 4.2 (a) shows the behavior of the Bloch waves for an unperturbed FBG, while figure 4.2 (b) shows a longitudinal wave exciting the fiber, whose effect causes additional reflections band to appear in the FBG spectrum.
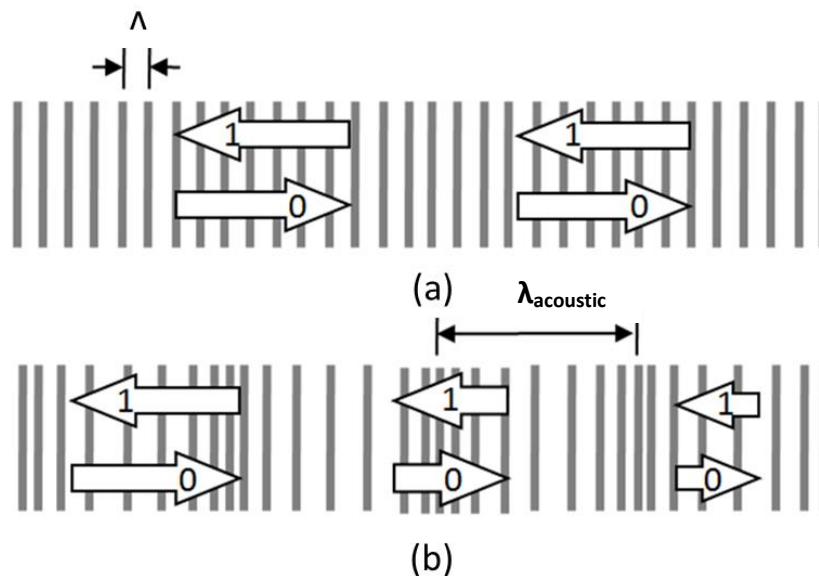
Figure 4.2 - Forward (0) and backward (1) Bloch waves of (a) unperturbed FBG and (b) longitudinally excited with acoustic wave of wavelength λacoustic. A forward Bloch wave incident from the left-hand side is gradually converted into a backward Bloch wave traveling from the right-hand side.

The disadvantage of this analytical method is the absence of information about the strain field generated in the fiber by, for example, a modulator based on the silica horn technique using a PZT. This issue can be solved by means of numerical approaches, considering the real dimensions of the device and practical boundary conditions. Oliveira et al. showed the numerical simulation of the longitudinal acousto-optic effect in FBG using the finite element method (FEM) together

with the TMM. The FEM approach allows the strain field caused by the acoustic wave to be completely characterized along the structure while the TMM is used to obtain the resulting spectrum generated by the corresponding deformed grating. Simulation results showed the formation of lateral lobules in the FBG reflection spectrum, caused by the displacement of the modulation planes of the FBG and a change of the effective refractive index, through the elasto-optic effect. Figure 4.3 shows the reflection spectrum obtained by numerical simulation of an FBG excited by a longitudinal acoustic wave with frequency f = 1 MHz and load P_0 = 1 N applied on the base of the silica horn [Oliveira2008a].
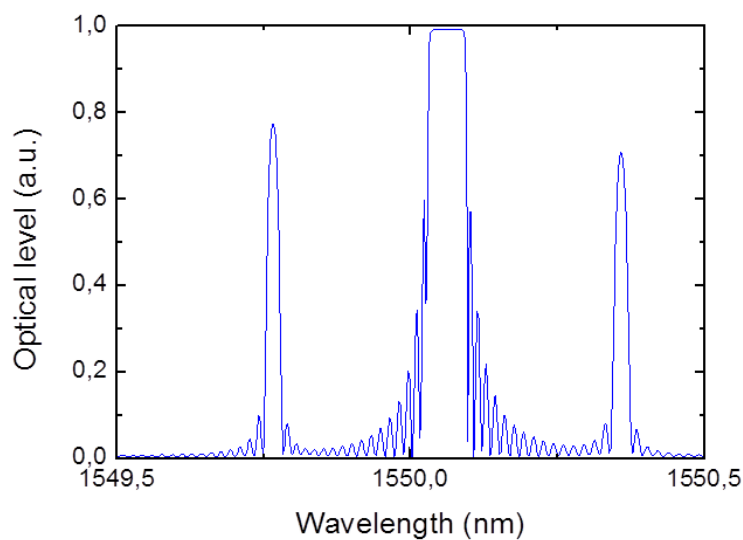
Figure 4.3 - Reflection spectrum of an FBG when excited by an acoustic wave at f = 1 MHz and load P$_0$ = 1 N [Oliveira2008a].

Figure 4.4 shows the schematic diagram of the AOM used in the numerical simulations, which is the base of the AOM used to carry out the experiments in this work. The Bragg grating AOM consists of a PZT, responsible for the generation of the acoustic wave, the silica horn, responsible for coupling the acoustic wave to the optical fiber, where the FBG is inscribed. At the end, a holder is used in order to allow the formation of a standing wave. In this model a tapered region is used in order to enhance the acousto-optic effect. However, the presence of the taper can be neglected, and the same strain field can be obtained by changing the dimensions of the silica horn [Oliveira2008a].
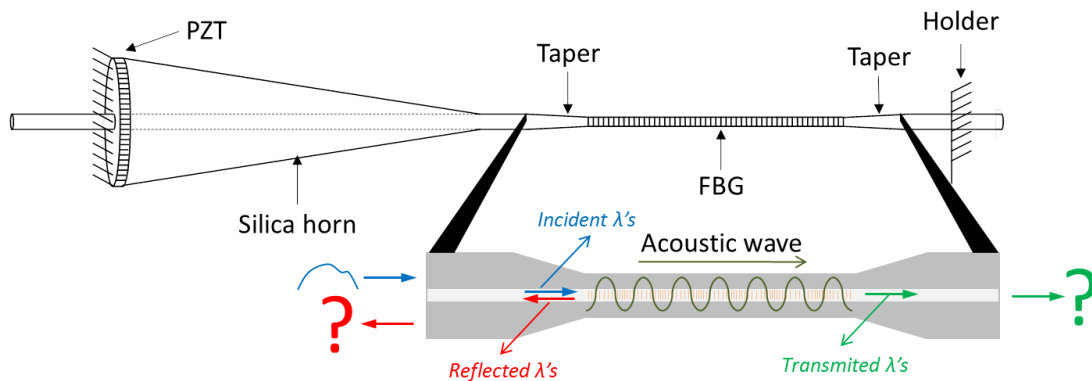
Figure 4.4 - AOM used by [Oliveira2008a] to simulate the behavior of the FBG under acousto-optic modulation.

In 2010, Oliveira et al. reported on the analysis and measurement of the acoustic vibration modes of an experimental assembly made of a silica horn with a length of silica fiber, in which the grating is inscribed (similar to the one showed in Figure 4.4, except by the absence of the taper), and demonstrated, by controlling the excitation of a particular resonance mode, that either flexural or longitudinal acoustic waves are generated [Oliveira2010a]. Regarding the longitudinal case, Figure 4.5 shows how an acoustic wave with low and high frequency (comparing the acoustic wavelength with the grating length) changes the modulation planes of the grating. Figure 4.5 (a) shows the behavior of the planes when no acoustic wave is applied, figure 4.5 (b) the case for the excitation of an acoustic wave at low frequency and figure 4.5 (c) the case for the excitation at high frequency. When the longitudinal acoustic wavelength is longer than the FBG length (low frequency regime), a compression and rarefaction strain field corresponding to less than one period extends over the entire grating and whose net result causes a small shift in the Bragg wavelength. Figure 4.5 (b) exemplifies the case where the net result of the strain field is red shifting the Bragg wavelength. On the other hand, in the high frequency regime, the longitudinal acoustic wavelength is much shorter than the grating length and the resulting compression and rarefaction strain field acts on modulating the grating planes. This creates side lobules in the reflection spectrum. However, in this case, no displacement of the wavelength occurs. This situation is depicted in figure 4.5 (c).
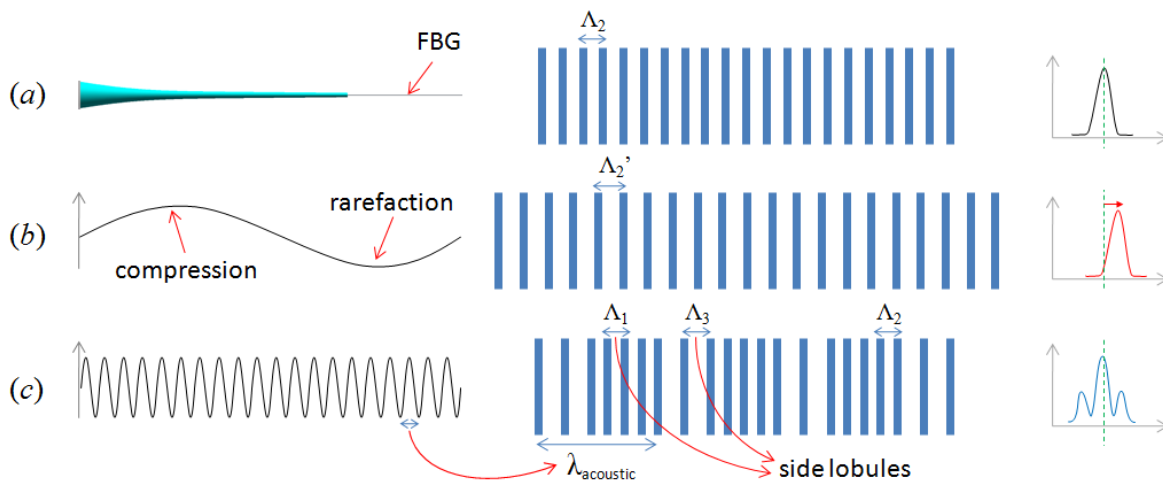
Figure 4.5 - Effect of the longitudinal acoustic wave in the FBG modulation planes when (a) no acoustic wave, (b) low frequency and (c) high frequency is applied in the fiber, respectively. The very right scheme shows the corresponding spectrum behavior (Adapted from [Oliveira2010a]).

Figure 4.6 shows the comparison of experimental and numerical simulation results under the excitation of a longitudinal wave at f = 1,089 MHz and PZT load, V_{PZT} = 30 V, which correspond to a load P_0 = 3 N [Oliveira2010a]. The FBG length is L = 50 mm, while the acoustic wavelength is $\lambda_{acoustic}$ = 5,27 mm.
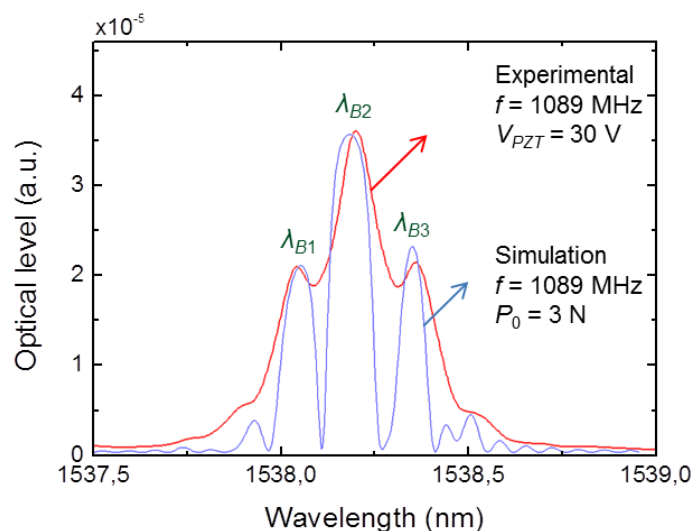
Figure 4.6 - Experimental and simulation of an FBG under excitation of a longitudinal acoustic wave at f = 1,089 MHz. Applying V$_{PZT}$ = 30 V at the PZT corresponds to a load of P$_0$ = 3 N on the basis of the silica horn [Oliveira2010a].

Regarding the applications of the longitudinal excitation of the FBG, Liu et al. in 1998 constructed a narrow band acousto-optic tunable reflector [Liu1998]. The lateral lobules are assumed as correspondent to a weak version of permanent FBGs. These unique properties lead to important applications in Q-switching of lasers [Delgado2006], wavelength shifting [Liu2000], among others.

In 2005, Minardo et al. reported the use of the acousto-optic effect in FBG as an ultrasonic sensor, showing the response of the FBG subjected to the longitudinal acoustical field theoretically and numerically [Minardo2005]. Later, Tsuda, on the other hand, showed the practical application of such sensor for ultrasonic and damage detection in carbon fiber-reinforced polymer [Tsuda2006].

4.2.2. Flexural Acoustic Waves

In the same way that longitudinal acoustic waves affects diffraction gratings in fibers, flexural acoustic waves can change the grating spectra. Flexural waves are basically bending fields that propagate along the fiber. Since the early 80's, bending effects in optical fibers have been studied. Taylor studied the bending effects in optical fibers, which cause power propagation in guided modes to be lost by coupling to radiation modes [Taylor1984]. These bends were caused by wrapping the fiber around mandrels or deploying it in flexible cables. Taylor also proposes the generation of microbendings in fiber using mechanical transducers to produce a periodic perturbation in the direction of the fiber's axis. However, in his experiments, Taylor used an apparatus illustrated in Figure 4.7, where it is assumed that the fiber path is constrained by the mechanical comb only at the points of contact separated by a distance $\Lambda/2$ in the z direction. This device, according to Taylor, can be used as an efficient $LP_{01} \leftrightarrow LP_{11}$ mode converter.
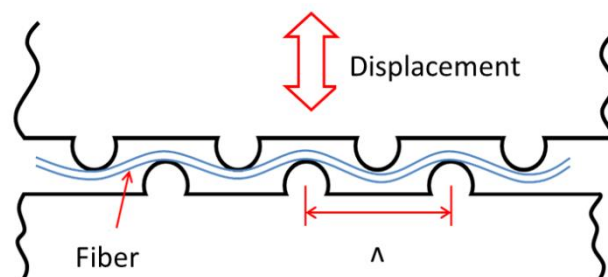
Figure 4.7 - Optical fiber subjected to spatially periodic bends [Taylor1984].

Dimmick et al. designed a flexural acoustic wave generator in fiber, using a tapered optical fiber with L_{TOF} = 4 cm and diameter d_f = 6,8 µm (see Figure 4.8). When driven with a high frequency RF signal ($f \approx$ 30 MHz), a coaxial shear mode PZT produces an acoustic vibration that is coupled to the optical fiber by a glass horn. The acoustic wave propagates as a flexural wave along the fiber. The flexural wave achieves its maximum amplitude at the tapered region. Light entering the tapered region of the fiber spreads out of the fiber core exciting the fundamental (LP_{01}) mode of the taper waist. In the absence of an acoustic wave this light travels through the taper region undisturbed and is coupled back to the fiber core as it propagates up the taper transition. When a flexural acoustic wave exists, periodic microbends in the taper region couple light from the LP_{01} mode to one or more higher order modes, which are not captured by the fiber core after the taper [Dimmick2000].
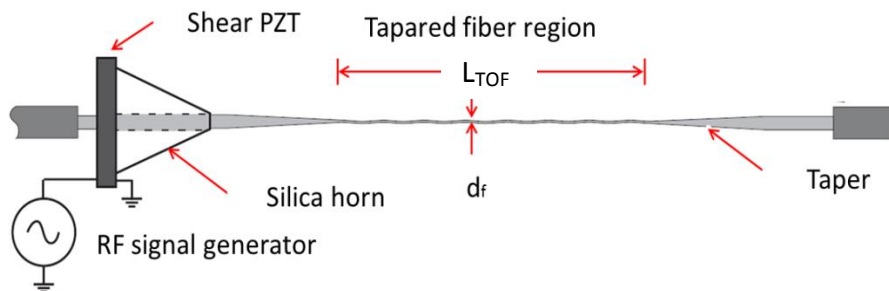
Figure 4.8 - Schematic diagram of tapered fiber acousto-optic tunable filter [Dimmick2000].

Engan et al. used the property of mode conversion through flexural acoustic wave to develop an optical frequency shifting in two-mode optical fibers, which basically converts one propagating mode to another [Engan1986], however, the flexural acoustic wave is generated by positioning the glass horn transversally to the fiber axis, as shown in Figure 4.9.

Considering the coupling between two optical modes, and denoting mode "1" as the fundamental mode, which contains all the energy before the acousto-optic interaction, and mode "2" as the one that carries a portion of the optical power after the interaction, the fraction of light coupled from mode "1" to mode "2" after the interaction length (L_i), can be written as

$$\eta = \frac{\left|k_{AO}\right|^2}{\left|k_{AO}\right|^2 + \left(\frac{\Delta\beta_{AO}}{2}\right)^2} \sin^2\left\{\left[\left|k_{AO}\right|^2 + \left(\frac{\Delta\beta_{AO}}{2}\right)^2\right]^{1/2} L_i\right\} \tag{4.8}$$

where k_{AO} is the acousto-optic coupling coefficient and $\Delta\beta_{AO}$ is the phase difference, defined as

$$k_{AO} = \frac{8\sqrt{2}\pi^2 j_{01} j_{11}}{\left(j_{11}^2 - j_{01}^2\right)^2} \frac{(1+p_e)n_{eff}}{c_{ext}} \frac{f}{\lambda} u_f \text{ and } \Delta\beta = 2\pi\left(\frac{1}{L_b(\lambda)} - \frac{1}{\lambda_s(f)}\right), \tag{4.9}$$

where j_{lm} is the *mth* zero of the Bessel function $J_{lm}(z)$ corresponding to the *lmth* mode of the fiber, c_{ext} = 5740 m/s is the speed of extensional waves in silica, p_e = -0,22 for a standard optical fiber, u_f is the transverse acoustic wave amplitude, λ_s is the flexural acoustic wavelength, L_b is the intermodal beat length, defined as the necessary length for mode "1" to acquire a phase shift of $\phi = 2\pi$ when compared with mode "2". From equation (4.8) one notices that, if $\Delta\beta_{AO}$ is much larger than $|k_{AO}|$, no light is coupled from mode "1" to mode "2", while if $\Delta\beta_{AO}$ = 0 all light is coupled to mode "2". Using these boundary conditions, the intermodal beat length can be calculated as

$$L_b = \frac{\pi}{2\left|k_{AO}\right|}. \tag{4.10}$$

From (4.9), when $\Delta\beta_{AO}$ = 0 the phase match condition is satisfied and can be expressed by

$$L_b(\lambda) \equiv \frac{\lambda}{n_1(\lambda) - n_2(\lambda)} = \lambda_s(f). \tag{4.11}$$

As L_b varies with λ, it can be assumed as a factor that determines the bandwidth of the acoustic coupling, for a given acoustic wavelength, i.e. [Blake1987]

$$\Delta\lambda L_i = 0.8 L_b^2(\lambda)\left|\frac{\partial L_b(\lambda)}{\partial\lambda}\right|^{-1}. \tag{4.12}$$

Calculations have shown that flexural waves will couple light from one mode to the other with 100 % efficiency over a length L_i given by

$$L_i = \frac{\pi}{2} L_b \frac{a_{core}}{u_f} ,$$ (4.13)

where a_{core} is the fiber core radius [Blake1987, Engan1988].
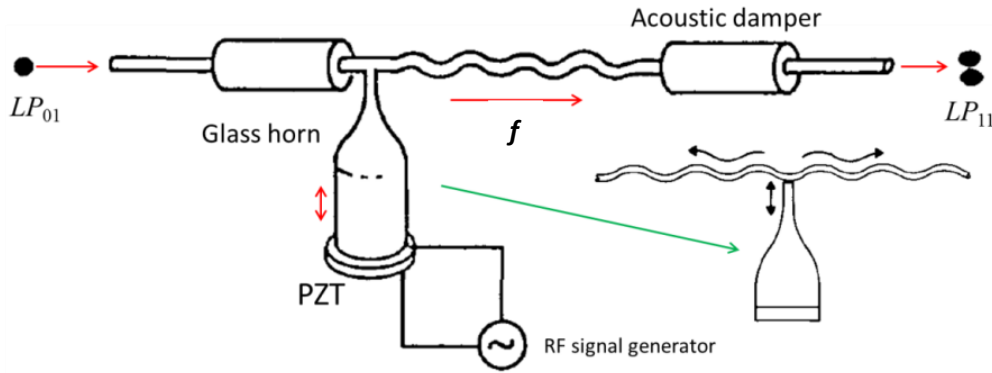
Figure 4.9 - Basic setup for generation of flexural acoustic waves. Using this particular device, a frequency shifting in a two-mode fiber was developed [Engan1986].

Most applications of flexural acoustic wave that causes changes in properties of optical fiber are based on the combination of the tapered optical fiber and the transverse excitation of a fiber. Birks et al. in 1994 introduced a low power acousto-optic device based on a tapered SM fiber. Unlike earlier designs, Birks et al. optimized the device and the overlap between the acoustic and optical waves was complete [Birks1994], so very little acoustic power was required. The resonance condition for an optimum coupling can be written with the help of formulation [Blake1987] as

$$a^3 = \frac{\left(j_{11}^2 - j_{01}^2 \right)^2}{64\pi^3} \frac{c_{ext} \lambda^2}{n_{eff}^2 f} ,$$ (4.14)

where a is the fiber radius. The k_{AO} for a maximum coupling ($k_{AO}L_i = \pi/2$) can then be calculated yielding an acoustic amplitude of

$$u_f = \frac{\left(j_{11}^2 - j_{01}^2 \right)^2}{16\sqrt{2}\pi j_{01} j_{11}} \frac{c_{ext}}{(1+p_e) n_{eff}} \frac{\lambda}{L_i f} .$$ (4.15)

As a practical example let us consider a taper carrying light from an HeNe laser at λ = 633 nm. For resonance at f = 2 MHz, the required tapered diameter is d_f = 3 μm. If L_i = 50 mm, the acoustic amplitude required for 100 % coupling is u_f = 8 nm. The expected FWHM optical bandwidth is $\Delta\lambda$ = 1,64 nm. Figure 4.10 shows the schematic diagram of the acousto-optic device, showing the fundamental (LP_{01}) mode spreading from the core to match the cladding (LP_{11}) mode after the interaction length.
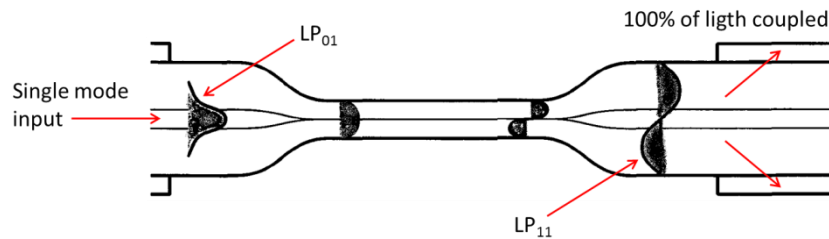
Figure 4.10 - Acousto-optic coupling in a SM fiber taper, when the acoustic amplitude is adjusted to give 100% efficient coupling from LP_{01} to LP_{11} modes [Birks1994].

The frequency f of a flexural acoustic wave is given by the RF signal driving the PZT. However, the flexural acoustic wavelength λ_s is given by the dispersion relation for flexural waves on a cylindrical rod which, in the low frequency regime, is

$$
\begin{aligned}
\lambda_s &\equiv \frac{2\pi}{k_s} \\
&= \sqrt{\frac{\pi a c_{ext}}{f}}
\end{aligned}
\quad ,
\tag{4.16}
$$

where k_s is the acoustic wave number.

The use of flexural acoustic wave together with diffraction gratings has called the attention of scientists and a large number of effects were studied and devices developed, however, only applications in FBG are found in literature. Huang et al. in 2000 acoustically generated transversal vibration of an FBG to control its reflectivity level [Huang2000] and Liu et al. demonstrated the switching of the reflection band of an FBG through the application of a flexural acoustic wave to the fiber [Liu2000]. In their work the acoustic wave is generated by positioning a silica-horn PZT set transversally to the fiber axis, causing microbends in the fiber (f = 1,3 MHz). The microbending served as an LPG for coupling the core and cladding modes and switching the reflection band between the Bragg wavelength and the cladding mode wavelength. Such switching function can

be applied to wavelength-division multiplexed add-drop operations in fiber communications. The phenomenon is illustrated in Figure 4.11, in which couplings between the forward and back-propagating core and cladding modes with their phase-matching mechanisms are shown. The forward propagating core mode is coupled with the backward propagating core mode through grating phase matching, generating the optical band with center wavelength λ_B. When the acoustic wave is applied, the forward-propagating (backward-propagating) core mode is coupled with forward-propagating (backward-propagating) cladding mode through the microbending phase matching mechanism (Figure 4.11 (a)). Although part of the signal power can be coupled back to the core modes after it is coupled into the cladding modes, most of it radiates through the propagation of cladding modes. Such a coupling process in either propagation direction leads to the reduction of reflectivity at this wavelength. On the other hand, for the signal at λ_{BS}, grating phase matching results in coupling between forward-propagating core mode and backward-propagating cladding mode. When microbending is generated, the coupling between backward-propagating cladding mode and backward-propagating core mode is phase matched and the outcoupled power at this wavelength is coupled back into the core mode and reflectivity is observed. This reflectivity increases with increasing of the microbending strength [Erdogan1997].
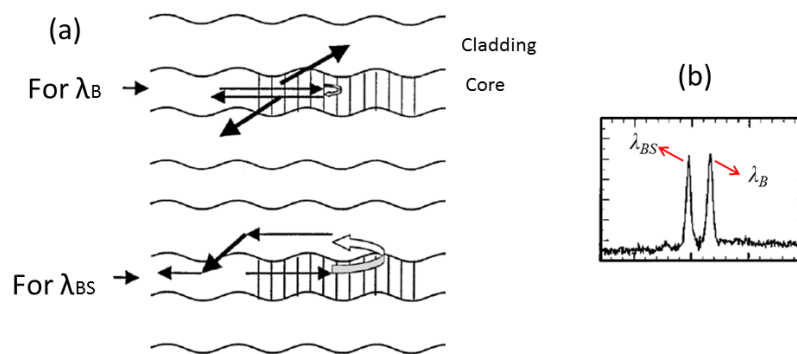
Figure 4.11 - (a) Schematic diagram showing the phase-matching mechanism for cladding to core modes coupling. (b) Bragg wavelength (λ_B) and λ_{BS} [Liu2000].

Using tilted FBG, Chen and Fu experimentally demonstrated that the induced-wavelength reflection peak can be shifted by adjusting the frequency of the flexural acoustic wave launched into the fiber [Chen2004a]. Moreover, the acoustic wave can be used to switch the induced-

wavelength peak with a wavelength-tuning rate of approximately 1 nm/MHz. Figure 4.12 shows the schematic diagram of the acousto-optic modulation in a tilted FBG.
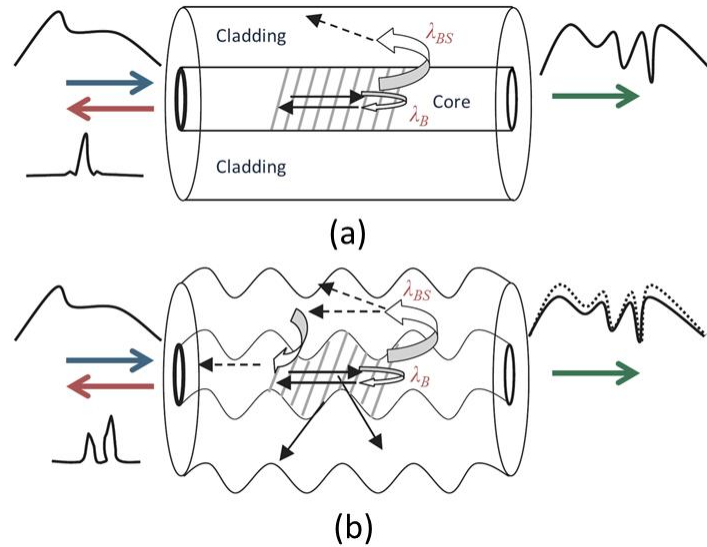
Figure 4.12 - Schematic diagram of the acousto-optic modulation in a tilted FBG: (a) without acoustic wave and (b) with acoustic wave. (Adapted from [Chen2004a])

In 2005, Abrishamian et al. presented a simple mathematical formulation to calculate the transmission and reflection spectra of propagating core and cladding modes through the acoustically induced FBG by solving MM coupling equations [Abrishamian2005]. The formulation is based on the TMM, which splits the grating into short sectioned pieces so making the process of calculation the fastest for solving two coupled-mode equations [Yamada1987]. The equation to calculate the switched wavelength generated by the acoustic wave in the FBG reflection spectrum (λ_{BS}) is written as

$$\lambda_{BS} = 2\Lambda \left[1 \pm M\left(\frac{\Lambda}{\lambda_s} \right) \right] n_{eff} \quad (M = 1,2,3,\ldots).$$

(4.17)

Other examples of the combined flexural waves and fiber diffraction gratings and/or acoustically generated gratings can be found in [Haakestad2006, Yeom2007], where PCF were explored under acousto-optic interaction using flexural acoustic waves.

4.3. Modeling and Simulation

Numerical simulations were performed to compare results obtained from experiments, to demonstrate the suitability of some numerical methods and develop a tool for design of AOMs. In 2008, Oliveira et al. showed the combination of the FEM and TMM to calculate the acousto-optic modulation of FBGs. The simulation results were compared with literature data and found to be in good agreement. Neves Jr. introduced the combination of the TMM and the assumed modes method (AMM), which gives information for the transient and steady-state regime [Neves2008]. In this work, these methods were used and experimental and practical results valued the combination of the employed numerical methods. Simulations using a commercial software package (called ANSYS) based on the FEM with a graphical interface were also performed in order to calculate the excited vibration modes of the silica horn-optical fiber set.

Both FEM and AMM are methods used to calculate the strain field experienced by the fiber when it is acoustically excited. However, there are some differences between the methods that should be clarified. FEM is a general method, used for a variety of problems such as static, dynamic, linear, nonlinear and so on. Its formulation is based on the construction of numerical matrices for each element, which causes the requirement of elevate computational performance. On the other hand, AMM is only applicable for dynamics problems where an orthonormal basis that satisfies all boundary conditions is known. This basis is composed by the natural vibration modes of the system, which are valid to the whole domain, in contrast with the interpolation equations used in FEM. As a consequence, in the AMM, the dimension of the generated matrices is smaller, because each variable is associated to a basis function, making the computational costs lower and the achieved results more accurate.

4.3.1. Numerical Modeling

The dimensions of the structure employed in the calculation are shown in Figure 4.13, which correspond to the ones of the assembled device. The length of the silica horn is l_{sh} = 46 mm, with a base diameter of d_{sh} = 8 mm and tip diameter of d_{sht} = 0,8 mm. The length of the fiber is taken as the FBG length, usually L = 50 mm.
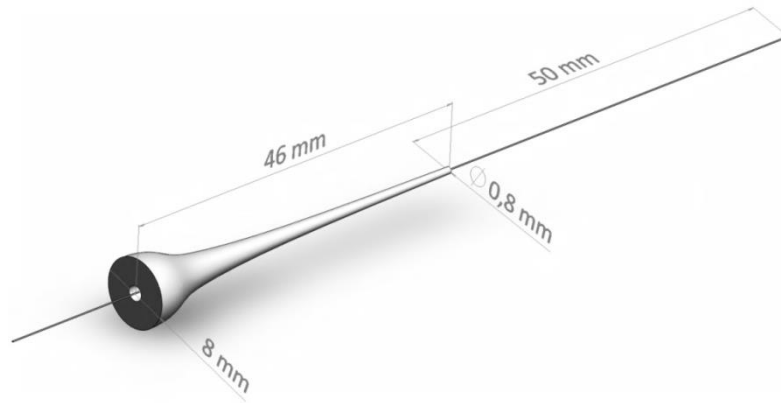
Figure 4.13 - Silica horn and FBG dimensions used in the numerical simulations (obtained from ANSYS).

4.3.2. Finite Element Method

The FEM was introduced in the late 1950s and presents several advantages, such as a widespread acceptance in the scientific and industrial community, the capability of modeling complex geometries, the consistent treatment of differential-type boundary conditions, and the possibility to be programmed in a flexible and general purpose format [Hughes1987]. Standard finite element approximations are based upon the Galerkin formulation of the weighted residuals method [Zienkiewicz2000].

The differential equation of motion that represents the acoustic wave propagation in the structure is given by

$$E \frac{\partial}{\partial z}\left(A_s(z) \frac{\partial u(z,t)}{\partial z} \right) - \rho_D A_s(z) \frac{\partial^2 u(z,t)}{\partial t^2} = 0 , \qquad (4.18)$$

where E is the Young´s modulus, u is the axial displacement, which is dependent on the position z and time t, $\frac{\partial u}{\partial z} = \varepsilon$ is the longitudinal strain and ρ_D is the density. The term $A_s(z)$ represents the variable size of the structure along the z-axis. In the current analysis, the damping of the acoustical wave in the structure is neglected.

The initial and boundary conditions are given by

$$
\begin{cases}
\left[AE \dfrac{du}{dz} \right]_{z=0} = P(t) = P_0 \exp(j\omega t) \\
u(z = L_i, t) = 0
\end{cases}
\tag{4.19}
$$

where $P(t)$ is the external excitation, composed by the harmonic load frequency ω and amplitude P_0 generated by the PZT. L_i represents the total length of the device, called as interaction length.

A classical linear basis approach for the finite elements is used in this work. After the one-dimensional discretization, the final matrix form of the problem is given by

$$
\mathbf{M\ddot{u}} + \mathbf{Ku} = \mathbf{P}.
\tag{4.20}
$$

In this expression, **M** and **K** are the mass and stiffness matrices of the structure, obtained by the superposition of the mass and stiffness matrix of each element, which are given by

$$
\mathbf{M} = \left[m_{ij}^e \right] = \frac{\rho A^e \Delta z}{2} \begin{bmatrix} 1 & 0 \\ 0 & 1 \end{bmatrix}
\tag{4.21}
$$

and

$$
\mathbf{K} = \left[k_{ij}^e \right] = \frac{A^e E}{\Delta z} \begin{bmatrix} 1 & -1 \\ -1 & 1 \end{bmatrix}
\tag{4.22}
$$

respectively. The superscript e represents an element with particular properties. Furthermore, **u** and **ü** in (4.20) represent the nodal displacement and acceleration vectors, respectively. The vector **P** is the nodal generalized force and has a null value, except for the first component, associated with the node at $z = 0$. Considering the excitation in the form of $\mathbf{P} = \mathbf{P}_0 \exp(j\omega t)$ and assuming that the system behaves linearly, the solution of the problem can be found solving the equation:

$$
\mathbf{M\ddot{u}} + \mathbf{Ku} = \mathbf{P}_0 \exp(j\omega t).
\tag{4.23}
$$

Since the time dependent load generated by the piezoelectric is harmonic, the solution has the form $\mathbf{u} = \mathbf{u}_0 \exp(j\omega t)$. This way, (4.23) is reduced to

$$\left(-\omega^2 \mathbf{M} + \mathbf{K}\right) \mathbf{u}_0 = \mathbf{P}_0 .$$ (4.24)

Note that $\mathbf{u}_0$, the displacement vector solution, is highly dependent on the amplitude $\mathbf{P}_0$ and frequency ω of the acoustic excitation. Thus, the complete solution will be given by:

$$u = u_{DC} + u_0 .$$ (4.25)

Once the displacement field is obtained, the strain field in each one of the finite elements can be found by differentiation, as

$$\varepsilon^e = \frac{\partial u}{\partial z} \cong \frac{u^{e+1} - u^e}{\Delta z} .$$ (4.26)

In this case, as the properties of the finite element are linear, u^{e+1} and u^e are the displacements in the local nodes *e+1* and *e*, respectively.

4.3.3. Assumed Modes Method

The AMM is based on the discretization of a system consisting of n elements and n degrees of freedom in order to find approximated solutions through numerical series [Neves2008]. For a particular case, where movement is only observed in one direction (for example, movements originated by pulling the fiber longitudinally), one can assume that the solution of a problem with known boundary conditions will be found through a product between a conveniently chosen spatial function and a temporal function. For a length of fiber treated as a thin cylindrical, linear, homogeneous bar, if one wishes to find the space-time dependent displacement behavior, the displacement function *u(z,t)*, and consequently the strain (*ε*), is obtained considering the solution for

$$u(z,t) = \sum_{j=1}^{n} \varphi_j(z) q_j(t) ,$$ (4.27)

where φ_j *(z)* is called the trial or assumed modes function, which is chosen in order to satisfy all boundary conditions of the problem and must be differentiable at least for half of the system order [Meirovitch1986]. Thus, for a system described as a bar of length L_i with non-uniform

transversal section, similar to the structure of the AOM showed in Figure 4.4, an appropriate trial function could be

$$\varphi_j(z)=\sin\left[\frac{(2j-1)\pi z}{2L_i}\right] \qquad j=1,2,...,n \ . \tag{4.28}$$

In equation (4.27), $q_j(t)$ is the generalized coordinates vector of a system of differential equations described by

$$\mathbf{M}\{\ddot{q}(t)\}+\mathbf{K}\{q(t)\}=\{f(t)\}, \tag{4.29}$$

where **M** and **K** are the n × n-order mass and stiffness matrixes respectively, and $\{f(t)\}$ is the generalized excitation vector. From equation (4.27), one can see that the solution is found as a linear combination of a base in the n-dimensional space. A solution for equation (4.29) can be found considering $f(t)=\sin(\omega t)$ either for transient or steady state regimes [Neves2008]. The strain field *ε(z,t)*, necessary for calculating the grating spectrum with the TMM, is simply found differentiating (4.27) with respect to *z*.

More details on the method formulation can be found in [Neves2008, Neves2008a].

4.3.4. Transfer Matrix Method

Once the strain field for the steady-state regime is known along the fiber and, particularly, along the grating, one can calculate the optical response following the schematic diagram showed in Figure 4.14.

Figure 4.14 – Schematic diagram for the calculation of the resultant grating spectra.

As mentioned in chapter 2, for a uniform grating, the effective refractive index perturbation in the core is repeated here for convenience described by

$$\delta n_{eff}(z) = \overline{\delta n_{eff}}(z)\left[1 + \nu\cos\left(\frac{2\pi}{\Lambda}z + \phi(z)\right)\right].$$

(4.30)

As the grating imposes a dielectric perturbation to the waveguide core, it forces coupling between the propagating modes. The formulation of the coupled-mode equations due to the index perturbation are found with the help of the "synchronous approximation" described by [Kogelnick1990, Hill1997, Kashyap1999].

This description represents the situation for a uniform grating, where the average refraction index change is constant. However, the onset of the acoustical wave causes a broadening in the grating, making its pitch non-uniform and changing the optical path. Considering the non-uniformity of the grating, the reflection and transmission spectra from the two-mode coupling can be calculated by considering a piecewise approach, whereby the grating is divided into discrete uniform sections that are individually represented by a matrix. The solution is found by multiplying the matrices associated with each one of the sections. The characteristic equation is solved by making the matrix determinant equal to zero and the resulting polynomial enables the eigenvalues to be found.

The FBG of length L can be treated as a quadrupole, as show in Figure 4.15, where R and S represent the co-propagating and counter-propagating modes, respectively.
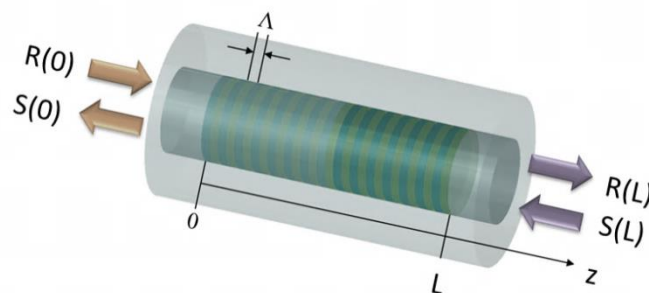
Figure 4.15 - Bragg grating schematic as a quadrupole. R and S represent the co-propagating and counter-propagating modes, respectively.

On the other hand, the TMM formulation applied for transmission gratings is similar to the one presented for reflection grating. The change is that, instead of considering the energy coupled to a counter-propagating mode, the light is coupled to a co-propagating mode, for instance light propagating in mode "1" being coupled to a co-propagating mode "2". Figure 4.16 shows the quadrupole characteristics of the LPG (Figure 4.15 modified), where now *R* represents the amplitude of the forward propagating mode and *S* the amplitude of the co-propagating field.
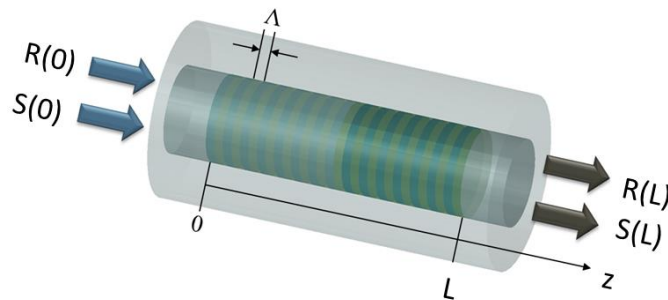
Figure 4.16 - LPG represented as a quadrupole in the TMM.

The detailed TMM formulation applied for reflection and transmission gratings can be found in Chapter 2.

4.3.5. The Combination of the Mechanical and Optical Methods

Figure 4.14 shows the steps of the algorithm for the acousto-optic effect simulation. First, one is concerned with the input of the FBG-AOM dimensions, such as the radius and the length of the silica horn and the length of the Bragg grating. In the second step the FEM is used to model the device, whereby a desired load is applied to the base of the silica horn. The result is the strain field calculated along the structure. However, only the strain field in the FBG region is used as the input to the TMM. The combination of the numerical approaches, mechanical and optical, is made through the wavelength shift in every single segment of the fiber (element) submitted to the strain field ε.

The shift of the Bragg wavelength due to changes in the temperature and longitudinal deformation is derived as

$$\Delta\lambda_B = 2\left[\Lambda\frac{\partial n_{eff}}{\partial\varepsilon} + n_{eff}\frac{\partial\Lambda}{\partial\varepsilon}\right]\Delta\varepsilon + 2\left[\Lambda\frac{\partial n_{eff}}{\partial\Theta} + n_{eff}\frac{\partial\Lambda}{\partial\Theta}\right]\Delta\Theta,$$
(4.31)

where $\Delta\varepsilon$ is the applied longitudinal strain of the grating and $\Delta\Theta$ is the change in temperature. $\partial n_{eff}/\partial\varepsilon$ represents the longitudinal stress optic coefficient (strain-optic property) and $\partial n_{eff}/\partial\Theta$ the temperature coefficient of the refractive index (thermo-optic property). Since the Bragg wavelength is a function of n_{eff} and Λ, the simplest method of altering the transfer characteristics of a FBG is to impose a temperature and/or strain profile along the length of the grating [Kashyap1999].

The term $\partial\Lambda/\partial\varepsilon$ corresponds to a change in the grating period and the strain-optic coefficient induced change in the refractive index. The strain effect term can be also expressed as [Meltz1999, Hill1997]

$$\Delta\lambda_B = \lambda_B(1 - p_e)\varepsilon_z,$$
(4.32)

where

$$p_e = \frac{n_{eff}^2}{2}\left[p_{12} - \sigma(p_{11} + p_{12})\right].$$
(4.33)

Table 4.1 shows the values for some of these coefficients, depending on the wavelength and effective refractive index.

Table 4.1 - Values for p_{11}, p_{12} and σ of silica-based materials found in literature.

Reference	λ (nm)	n_{eff}	p_{11}	p_{12}	σ	Material
Primak1959	589,2	1,458	0,121	0,27	0,164	Silica glass
Borelli1968	632,8	1,457	0,126	0,26	0,168	Fused silica

Hocker1979	633	1,456	0,121	0,17	0,17	Optical fiber
Yarin1984	630	1,46	0,121	0,27	0,21	Fused silica
Bertholds1988	633	1,458	0,113	0,252	0,16	Optical fiber
Xu1993	1533,3	1,465	0,121	0,17	0,17	Optical fiber

In the same way, the term that represents the effect of temperature can be written as

$$\Delta\lambda_B = \lambda_B \left(\alpha_\Lambda + \alpha_{n_{eff}} \right) \Delta\Theta ,$$ (4.34)

where

$$\alpha_\Lambda = \frac{1}{\Lambda} \frac{\partial \Lambda}{\partial \Theta}$$ (4.35)

is the thermal expansion coefficient for the fiber and the quantity

$$\alpha_{n_{eff}} = \frac{1}{n_{eff}} \frac{\partial n_{eff}}{\partial \Theta}$$ (4.36)

represents the thermo-optic coefficient.

Finally, considering only longitudinal strain and temperature variation, (4.31) can be rewritten as

$$\Delta\lambda_B = 2\lambda_B \left[\left(1 - p_e \right) \varepsilon_z + \left(\alpha_\Lambda + \alpha_{n_{eff}} \right) \Delta\Theta \right].$$ (4.37)

Therefore, any external perturbation of the grating, either by longitudinal strain or by temperature, will change the reflection wavelength making sensing applications potentially and practically interesting. However, only one perturbation at a time is of interest, so, the deconvolution of strain and temperature becomes necessary [Xu1994, Xu1995, James1996]. The

range of applications of the tunability property of FBG is very wide, and goes from broadband tunable optical filters [Mokhtar2003] to fiber lasers [Ball1992].

Thus, the combination of the numerical approaches, mechanical and optical, for the FBG case is made by the following equation

$$\Delta\lambda_B(z) = \lambda_B\left[1 + (1-p_e)\varepsilon_z(z)\right].$$ (4.38)

The sensitivity of LPGs to temperature and strain can be understood in the same way as the FBGs. From (2.45), the sensitivity to temperature and strain is written as

$$\Delta\lambda_m = \frac{\partial\lambda_m}{\partial(\delta n_{eff,m})} + \frac{\partial\lambda_m}{\partial\Lambda}$$
$$= \left[\frac{\partial(\delta n_{eff,m})}{\partial\Theta} + \frac{\partial(\delta n_{eff,m})}{\partial\varepsilon}\right]\Lambda + \left[\frac{\partial\Lambda}{\partial\Theta} + \frac{\partial\Lambda}{\partial\varepsilon}\right]\delta n_{eff,m}$$ (4.39)

where $\delta n_{eff,m} = n_{eff} - n_{cladding,m}$. In this equation, the first term on the right is the material contribution, and is related to changes in the differential refractive index of the core and the cladding arising from the thermo-optic and strain optic effects. This contribution is dependent upon the composition of the fiber [Shima1997] and is strongly dependent upon the order m of the cladding mode. The second term on the right is related with the waveguide effect contribution as it results from changes in the period of the LPG. Different effects are achieved if considering different gratings. For example, for coupling to low order cladding modes (achieved with longer periods, $\Lambda > 100$ μm), the material effects dominates, while for coupling to higher-order cladding modes (achieved using shorter periods, $\Lambda < 100$ μm), the material effect can be negligible [Bhatia1997]. Appropriate choice of grating period and fiber composition will thus allow the generation of attenuation bands with positive, negative or zero sensitivity to strain or temperature. This property presents several advantages if comparing with FBGs.

By differentiating (2.45), (4.39) can be simplified as

$$\frac{\Delta\lambda_m}{\lambda_m} = \left[\frac{1}{\Lambda}\frac{\partial\Lambda}{\partial\Theta} + \frac{1}{\delta n_{eff,m}}\frac{\partial\left(\delta n_{eff,m}\right)}{\partial\Theta}\right]\Delta\Theta + \left[\frac{1}{\Lambda}\frac{\partial\Lambda}{\partial\varepsilon} + \frac{1}{\delta n_{eff,m}}\frac{\partial\left(\delta n_{eff,m}\right)}{\partial\varepsilon}\right]\Delta\varepsilon$$

(4.40)

$$= \left(\alpha_\Lambda + \alpha_{neff,m}\right)\Delta\Theta + \left(1 + p_{s-o}\right)\Delta\varepsilon$$

where

$$\alpha_\Lambda = \left(\frac{1}{\Lambda}\frac{\partial\Lambda}{\partial\Theta}\right)$$

(4.41)

is the thermal-expansion coefficient,

$$\alpha_{neff,m} = \frac{1}{\delta n_{eff}}\frac{\partial\delta n_{eff,m}}{\partial\Theta}$$

(4.42)

is the thermal-optic coefficient, and

$$p_{s-o} = \frac{1}{\delta n_{eff,m}}\frac{\Delta\left(\delta n_{eff,m}\right)}{\Delta\varepsilon}$$

(4.43)

is the strain-optic coefficient. The thermal-expansion coefficient α_Λ has its value around $5,5 \times 10^{-7}$ / °C, while $\alpha_{neff,m}$, which is variable and related to the grating period and the coupled cladding mode order, generally varies from $8,6 \times 10^{-6}$ / °C for the gratings written in standard SMF-28 fiber. Consequently, as $\alpha_{neff,m} \gg \alpha_\Lambda$, the temperature term $(\alpha_\Lambda + \alpha_{neff,m})$ of LPGs mostly depends on the thermal-optic coefficient $\alpha_{neff,m}$. The strain coefficient $(1 + p_{s-o})$ is negative and varies slightly (from -0,5 to -0,7 nm/με) with the grating period and the coupled cladding mode order.

In the case of the sensitivity to external refractive index, the analytical expression derived by Chiang et al. [Chiang2000], which describe the dip wavelength shift ($\delta\lambda_0$) when the external refractive index changes from n_{ex0} to n_{ex} is written as

$$\delta\lambda_0 \approx \frac{u_\infty^2\lambda_0^3\Lambda}{8\pi^3 n_{cladding}a^3}\left[\frac{1}{\sqrt{n_{cladding}^2 - n_{ex0}^2}} - \frac{1}{\sqrt{n_{cladding}^2 - n_{ex}^2}}\right]$$

(4.44)

where u_∞ is the *mth* root of the Bessel function J_0. From (4.44) one notes that the refractive index sensitivity presents a nonlinear behavior that is more pronounced when the external refractive index is close to the cladding refractive index. Differentiating (4.44) with respect to n_{ex}, an expression for the LPG sensitivities *s* to the external media refractive indices can be written as [Kamikawachi2007]

$$s = \frac{\partial \lambda}{\partial n_{ex}} = \frac{u_\infty^2 \lambda_0^3 \Lambda}{8\pi^3 n_{cladding} a^3} \left[\frac{n_{ex}}{\left(n_{cladding}^2 - n_{ex}^2\right)^{3/2}} \right]$$

(4.45)

.

Thus, for the LPG case, the combination of the numerical approaches, mechanical and optical, is made by the following equation

$$\Delta \lambda_m(\varepsilon_z) = \lambda_m \left[1 + (1 + p_{s-0}) \varepsilon_z(z) \right].$$

(4.46)

Equations (4.38) and (4.46) accounts for both the effect of the period variation and the change in the effective refractive indices due to the strain field in each point inside the grating through the strain-optic effect. However, in the FBG case, the predominant effect is the displacement of the modulation planes, while for the LPG, changes in the effective index and optical path are the main effects. These methods simulate the excitation of longitudinal and flexural modes in the fiber through the projection of the displacement field in the one dimensional space. It is important to note that these equations establish the connection between the two methods. In the fourth step of the Figure 4.14, the TMM method gives the reflected and transmitted FBG spectra. The structure is designed using 26000 nodes/m. Each point along the structure corresponds to one element node. The quantity of nodes in the FBG region depends on its length. For example, for FBG length L = 10 mm, there are 260 elements in the grating region, which is enough to obtain an accurate strain field for resonance frequencies in study. The number of sections in the TMM is chosen to be the same as the number of elements used in the FEM for the grating region. In the example, the discrete structure is excited with different acoustic wave frequencies of load amplitudes P_0 = 1,5 N and P_{DC} = 0 N, where P_0 will vary.

On the other hand, all this process can be used for other types of fibers, such as PCF or mPOF, having different properties.

For instance, the mechanical properties of the PCF or mPOF can be achieved applying the theory of homogenization [Hassan1998] or applying concepts of mixture rules of composite materials [Vasiliev2001] used in this work. In order to adjust the FEM applied to a conventional FBG, the effective Young's modulus is calculated for the FBG-mPOF subtracting the equivalent amount of material on the homogeneous polymer fiber. Thus, the effective transversal area is given by:

$$A_{eff} = A_t - b \frac{\pi}{4}(d_h)^2 \qquad (4.47)$$

where b is the number of holes, d_h is the diameter of each hole and A_t is the transversal area of a circle with the same diameter of the fiber. This way, the effective Young's modulus for the mPOF is given by:

$$E_{eff} = E \frac{A_{eff}}{A}, \qquad (4.48)$$

$$\rho_{eff} = \rho_D \frac{A_{eff}}{A}. \qquad (4.49)$$

Knowing the effective area, the effective Young's modulus and the effective density, one can calculate the stiffness and mass matrices, used in the FEM analysis, treating the FBG-mPOF as a homogeneous conventional fiber [Oliveira2008b]. E and ρ_D are the Young modulus and density, assumed to be 72,5 GPa and 2200 kg/m^3 for the silica and 3 GPa and 1180 kg/m^3 for the POF, respectively. The application of FEM to the mPOF model can be performed assuming geometrical symmetry for both main directions within transversal section. Here, we also consider the dimensions of the fiber used silica fiber or mPOF. A thorough description of how the numerical methods and TMM are used together is found in [Oliveira2008a, Oliveira2008b, Neves2008].

4.3.6. 3-D Finite Element Simulation

The numerical approaches AMM, FEM and TMM help to calculate the optical spectra, but do not give information on the way the acoustic wave affects the fiber, i.e. which mechanical modes are generated. For this purpose the commercial finite element software package (ANSYS) with graphical interface is used in order to calculate and visualize the excited vibration modes of the

silica horn / optical fiber set used in the experiments. The model was constructed based on the device real dimensions, similar to the one shown in Figure 4.13. By means of this software, it is possible to access the natural vibration modes being excited in the fiber (radial, torsional, flexural, and longitudinal), depending on the acoustic frequency applied to the base of the silica horn [Oliveira2010a, Oliveira2009b, Marques2013a]. As mentioned in 4.2 section, these modes can be decomposed into four basic components: radial, axial, transversal and torsional. However, it must be emphasized that the torsional mode was not evidenced for this frequency range. Thus, one component may take a stronger influence than the others. A mode that is not purely radial, longitudinal, flexural or torsional is called hybrid mode, i.e., it is the combination of the four basic components.

4.4. Experimental Setup

This section describes the device and the experimental setup, which are the basis of all results obtained employing the acousto-optic modulation effect.

4.4.1. Acousto-Optic Modulator

Each one of the components of the modulator presents its particular characteristics. The main portion of the modulator is shown in figure 4.17. The device consists of a PZT disc, a silica horn and a fiber, which contains the grating, so built that it allows the transmission and reflection spectra to be measured.
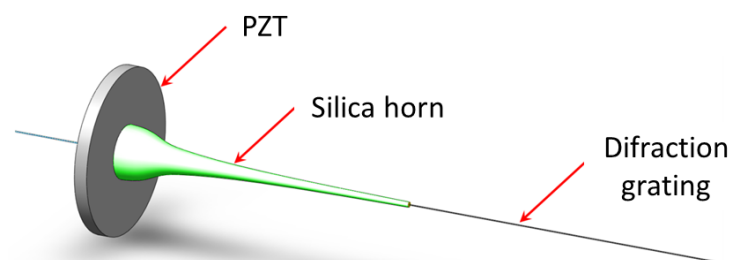

Figure 4.17 - The acousto-optic modulator (Adapted from [Oliveira2010a]).

Each part of the modulator is presented separately, and the whole experimental assembly is shown at the end. This helps to understand the function of the each one of the components.

4.4.2. Piezoelectric Disc and Silica Horn

In order to create an acoustic perturbation in the fiber it is essential to use an acoustic transducer or even an ultrasound transducer. The most common acoustic wave generator is the PZT, which is based on the piezoelectric effect, first reported by Pierre and Jacques Curie in 1880 [Lippman1881, Jaffe1958]. They described changes of the physical dimensions of specific materials when an electric field is applied on them. Additionally, the effect was found to be reversible (works the other way around), i.e. the application of strain to a piece of material generates an electrical field.

Usually, PZTs are made of a ceramic material, and it is shaped for specific applications. For example, the PZT used in this work is a ceramic disc with d_{PZT} = 25 mm diameter, and t_{PZT} = 2 mm thick, in order to achieve resonance frequencies around f = 1,2 MHz. A hole of diameter d_h = 1 mm was drilled in order to allow the fiber pass through the disc. Some of the discs were fabricated by Physik Instrumente [PI2010]. The chosen element was the PIC 151, which is a part of the so called "soft" PZTs, composed by zirconate and titanate materials with high permittivity, so high coupling factor and high piezoelectric charge constant. This material is the standard composition of most actuators and employed in low-power ultrasonic transducers and low-frequency sound transducers [PI2010].

The resonance frequencies of one of the ceramics were measured with an impedance analyzer. The used instrument was an Agilent 4294A Precision Impedance Analyzer. Figure 4.18 shows graphs of impedance and phase over frequency for the PZT used in the work. Figure 4.18 shows the behavior considering the frequency range from 0 to 1,2 MHz, while Figure 4.19 shows a zoom in low frequencies (50 to 100 kHz). Several resonances are observed, however, the most evident one is around f = 1 MHz (the condition of resonance is straightforward and it is characterized by minimum impedance and zero phase). Along this work, different aspects of the PZT disc were used, which present different resonance characteristics.
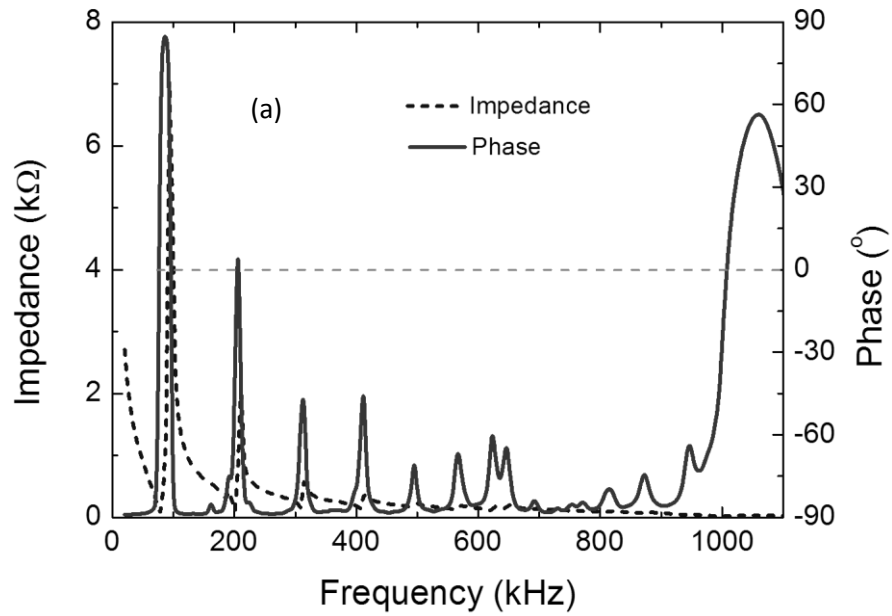
Figure 4.18 - Frequency characterization of the PZT ceramic used in the experiments in the range from 0 to 1,2 MHz.
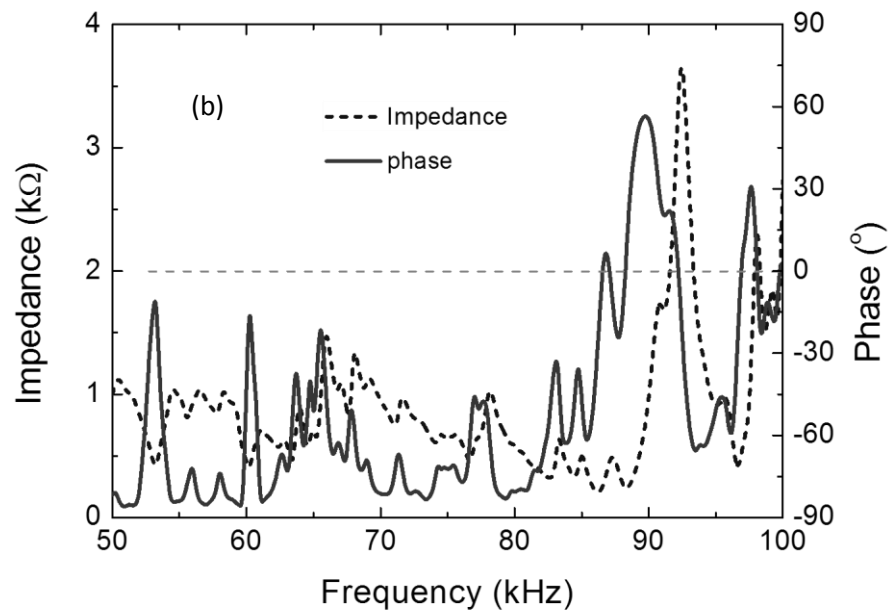

Figure 4.19 - Frequency characterization of the PZT ceramic used in the experiments: a zoom in the low frequency range, from 50 to 100 kHz.

On the other hand, the silica horn is used to couple the acoustic energy into the optical fiber, which contains the grating. Liu et al. reported the importance of such device to acousto-optic applications [Liu1997]. In Liu's device, the silica horn is attached longitudinally to the PZT, allowing the generation of longitudinal waves in the grating. The horn diameter is reduced over its l_{sh} = 70 mm length from d_{sh} = 3 mm (base diameter) to d_{sht} = 125 µm (tip diameter), and then fused to the grating.

Oliveira et al. also reported the effect on the acoustic coupling when the dimensions of the horn vary [Oliveira2008a]. It was noticed that, as the diameter of the horn base increases, keeping the density of energy applied to the base constant, the strain effect increases, while variation in its length does not affect the final strain field experienced by the grating. The silica horn used in this work was made at the chemistry department of the Universidade of Aveiro. The initial horn design was built to follow the specification: larger base diameter and small length, according to the PZT dimensions. The necessity of having a hole to allow the fiber passes though the silica horn, made the choice of a proper capillary tube crucial. Figure 4.20 shows the original capillary tube and the obtained silica horn after the process of pulling. The final dimensions of the silica horn were: base diameter d_{sh} = 8 mm, tip diameter d_{sht} = 0,8 mm and length l_{sh} = 46 mm, as shown in figure 4.13. Figure 4.21 shows a photography of some of the horns and the optimized one (highlighted).
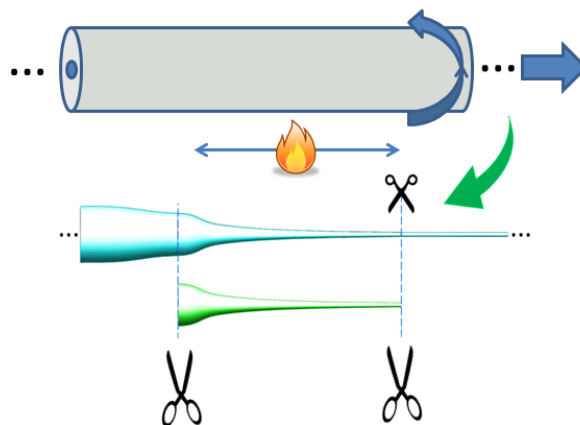

Figure 4.20 - Original capillary tube and the obtained silica horn after the process of pulling.
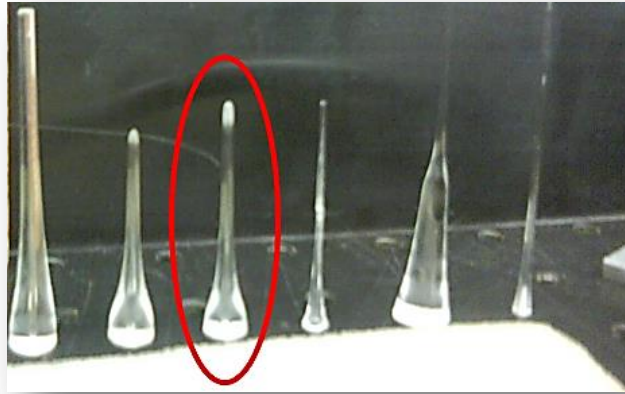
Figure 4.21 - Photography of the fabricated horns. Highlighted, the horn that presented the best performance.

All gratings used in the experiments were written at the Instituto de Telecomunicações. Usually, the gratings length was chosen to be the longest possible, so to enhance the acousto-optic interaction. However, the available phase masks presented a physical limitation. For example, the longest grating fabricated was an FBG with length of 50 mm written by means of a phase mask.

4.4.3. Fixing Stages

The fixing stages here are considered as the set formed by the PZT, the silica horn, the fiber with the grating, the holders and the translational stages. The holders are in charge to embrace the set and allow the generation of a stationary wave, i.e. the resonance conditions are given by the holders. The holder set is composed by two aluminum parts, one for the PZT and the other for the optical fiber. Figure 4.22 shows the diagram of the main part of the set, together with its dimensions. The space between the holders, lying between the silica horn and the piece of fiber length is called interaction length, L_i, and for different experiments this distance varies. In Figure 4.22 the interaction length was set to L_i = 96 mm.
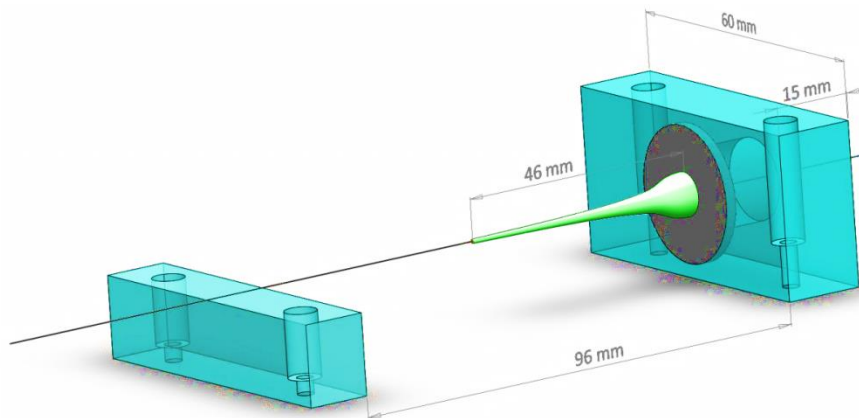
Figure 4.22 - Dimensions of the fixing stages of the AOM.

When assembled, the resonance conditions of the PZT slightly change. This can be noticed measuring again the impedance and phase of the PZT. Figure 4.23 shows the comparison before and after the modulator assembly was put in place. One observes that the resonance conditions changed and some resonances were weakened, however, the frequency of each resonance did not change. Figure 4.24 shows the modulator assembled on top of translational stages. The translational stages, however, have springs that damp the acoustic wave. This way, the translation stages have to be avoided for dynamic characterization.
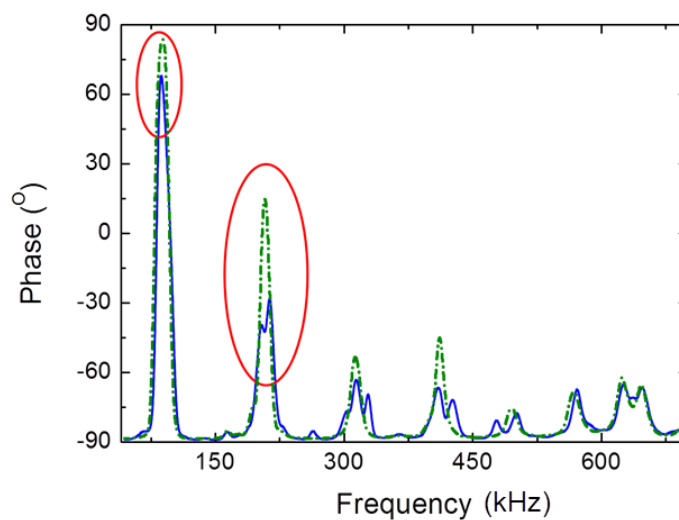
Figure 4.23 - Electrical phase measurement of the PZT before (dotted lines) and after (solid line) the assembling in the holders [Oliveira2010a].
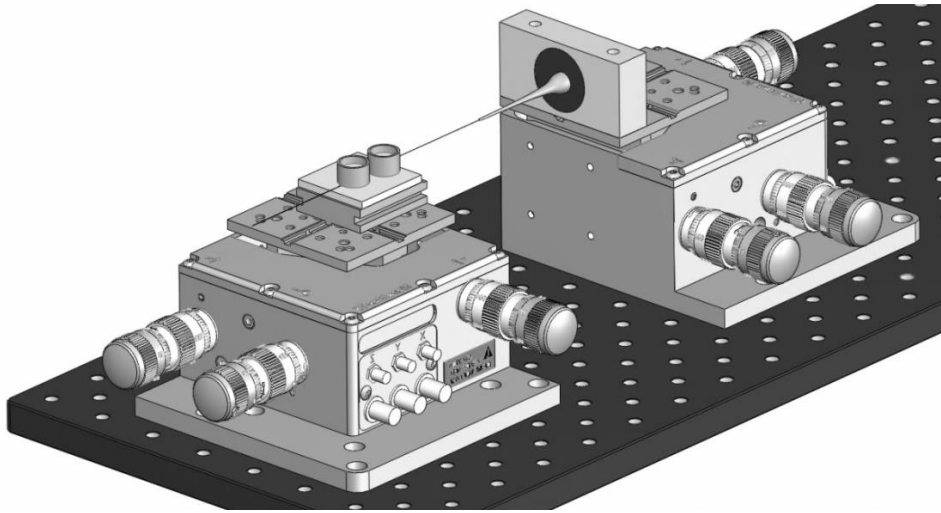
Figure 4.24 - The set PZT-silica horn-fiber assembled on top of translational stages.

The AOM consists on the fixing stages connected to an arbitrary RF signal generator for excitation of the PZT disc, an optical source for the interrogation of the grating, a polarization controller, an optical spectrum analyzer (OSA) and/or a photodetector for measuring the grating parameters, as shown in figure 4.25. The applications proposed in this work are based on this setup.
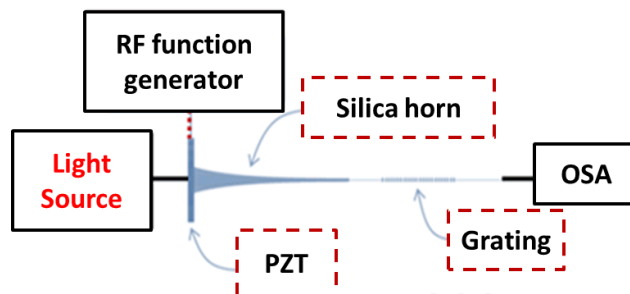
Figure 4.25 - Experimental assembly of the AOM.

4.5. Characterization

As different mechanical modes can be excited using the silica horn – fiber set, the modulator has to be characterized in order to give information about the way it affects the grating spectrum. A 3-D simulation based on FEM was done in order to show the mechanical modes excited in the

fiber [Oliveira2010a]. Using the commercial software ANSYS, different modes can be excited in the fiber, depending on the frequency applied to the PZT, considering the longitudinal excitation of the base of the silica horn. A modal analysis was first performed and showed that flexural modes are predominant in the low frequency regime, due to the buckling load that acts in the fiber, generating bends. The resultant flexural acoustic wavelength can be calculated using the equation

$$\lambda_s = \sqrt{\frac{\pi a c_{ext}}{f}} \qquad (4.50)$$

where a is the fiber radius, c_{ext} is the extensional acoustic velocity in the material and f is the acoustic frequency applied on the base of the silica horn, whose value fits well with the mechanical simulation. A detailed analysis about resonance modes of the silica horn − fiber set can be found in [Oliveira2010a].

4.5.1. Flexural Vibration of the Fiber

4.5.1.1. Fiber Bragg Grating – Reflectivity Modulation

When the fiber containing the grating is excited by flexural waves, the effects described in section 4.2.2 are achieved. Using FBGs, the main effect is the decrease of the grating reflectivity due to changes in the optical path and coupling of light to higher order modes. This decrease is observed both on reflection and transmission spectra.

Figure 4.26 shows the reflectivity and transmission behavior of a FBG, when excited with a flexural wave at f = 54 kHz. When the PZT load is varied from V_{PZT} = 0 to 10 V, the reflectivity decays 60%, following a non-linear behavior, and the transmission decreases 18 dB. More evident results are achieved by enhancing the PZT load.
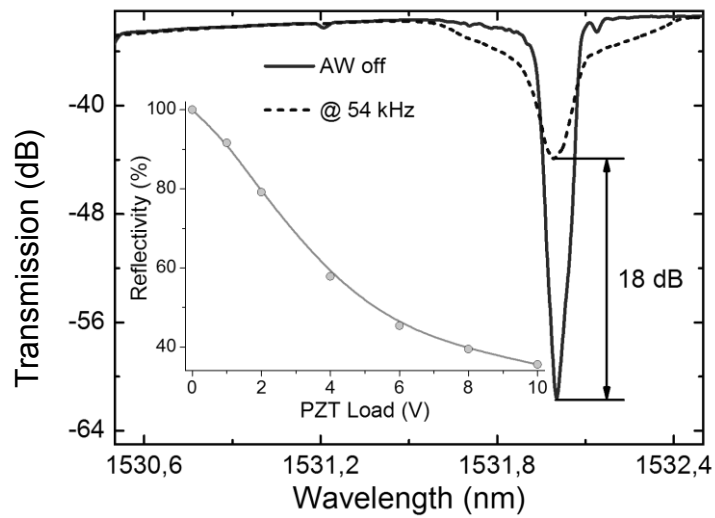
Figure 4.26 - Reflectivity and transmission behavior of a FBG. Inset: The reflectivity behavior depending on the PZT load.

Figure 4.27 shows the spectrum behavior of the FBG when a flexural wave excites the fiber at f =117 kHz. In this case, the reflectivity decay (10 dB) of the grating does not present the same attenuation observed in the example of figure 4.26, where the transmission enhancement is 18 dB. It means that the flexural acousto-optic effect is changing the reflectivity by changing the optical path and effective refractive index and the transmission by coupling light into cladding and radiation modes.
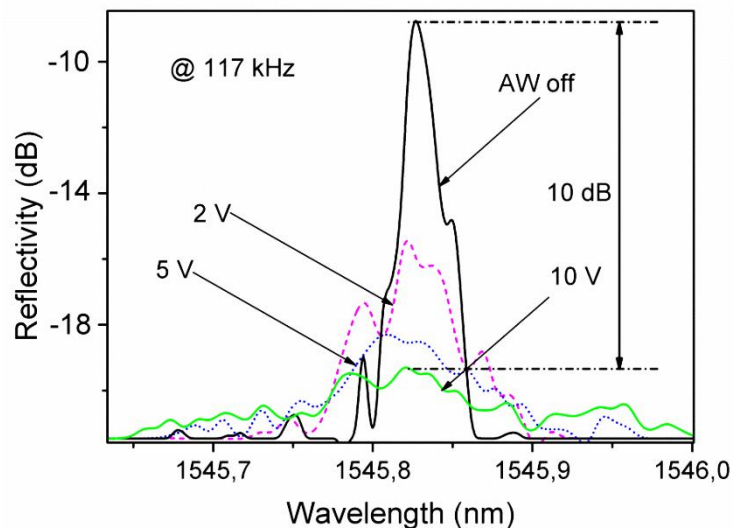
Figure 4.27 - Reflection spectrum of a FBG when excited by flexural acoustic waves at f = 117 kHz.

4.5.1.2. Long Period Grating

Using LPGs, the effect of bends on the spectrum is more evident when resonance frequencies are chosen. The periodic bend induced by the acoustic wave changes the optical path, modifies the difference between the effective refractive indices of the core and cladding modes and modulates the intermodal overlap integral, consequently reducing the coupling coefficient between them. Figure 4.28 shows the behavior of the LPG spectrum when the acoustic frequency is swept from f = 52 to 74 kHz. Particularly, the more evident effects in the LPG spectrum appears at f = 53,5 kHz and f = 60,8 kHz.
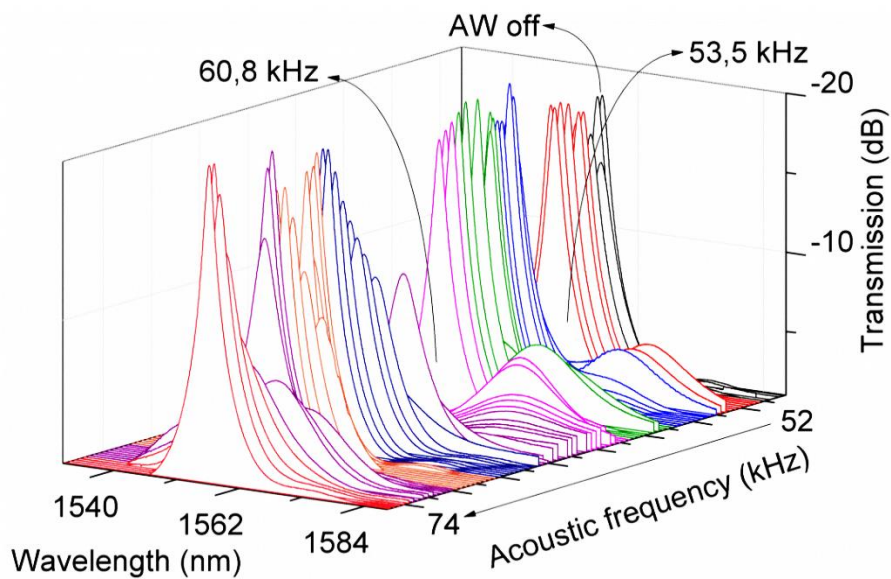
Figure 4.28 - LPG spectrum behavior when the excitation frequency is swept from f = 52 to 74 kHz, considering a PZT load at V$_{PZT}$ = 10 V (note that the y-axis (transmission) is upside down).

Figure 4.29 shows the minimum transmission and dip wavelength behavior of the LPG spectrum (projection of figure 4.28) depending on the excited frequency. It can be used in order to identify the resonance frequencies of the set.

Figure 4.30 shows the result of the modulation for an acoustic excitation at f = 60,8 kHz. The PZT load was varied from V_{PZT} = 0 to 10 V. The increase in amplitude of the acoustic wave reduces the peak transmission of the LPG attenuation band and induces a shift to longer wavelengths (red shift). A similar behavior is observed for acoustic waves generated at other resonances, however,

the magnitude of the effect is lower than that achieved at f = 60,8 and 53,5 kHz, which are the strongest observed with the silica horn – fiber set used in the experiments.
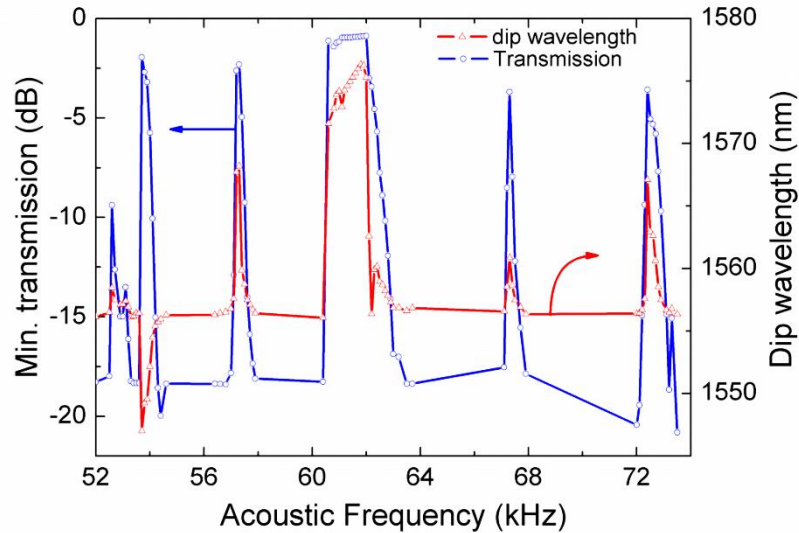
Figure 4.29 - Resonance spectrum of the modulator, measured by means of acousto-optic effect in LPG.
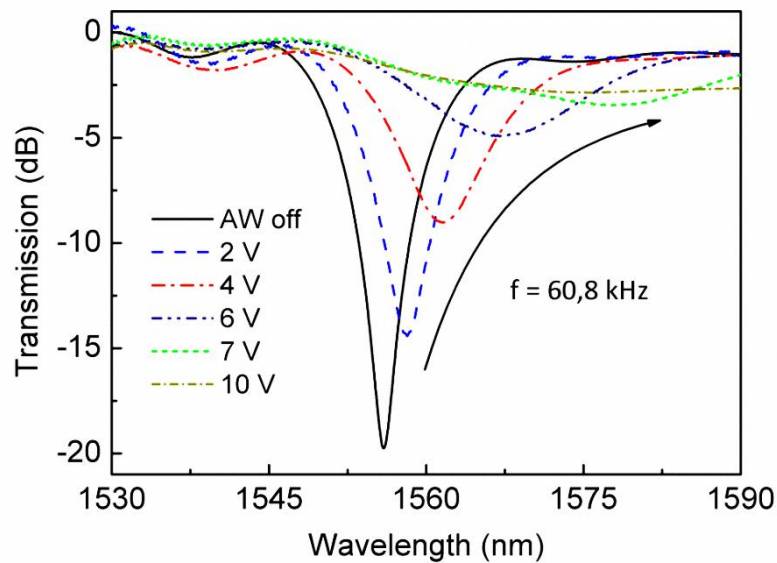
Figure 4.30 - LPG spectrum behavior when the PZT load varies from 0 to 10 V at f = 60,8 kHz.

Simulations were performed using the numerical approach presented in previous section, through the combination of the TMM and AMM. In previous section, the Figure 3.21 shows the experimental and simulated (using TMM) transmission spectrum of the LPG. The TMM provides

an excellent match of the wavelength dip for the transmission band, but delivers a slightly different behavior concerning the device bandwidth.

Figure 4.31 shows the minimum transmission of the LPG over the load range from V_{PZT} = 0 to 10 V, also related with the force applied to the horn base, at the excitation frequency of f = 60,8 kHz. At V_{PZT} = 10 V the force delivered by the PZT corresponds to P_0 = 0,042 N (verified by comparison with numerical results). Over the PZT load range, ~ 15 dB decrease of the attenuation peak is achieved, however, this relationship, between the amplitude of acoustic wave and the wavelength shift, is quasi-linear up to V_{PZT} = 6 V, and then it levels up and keeps stationary. Figure 4.32 shows the shift of the dip wavelength ($\Delta\lambda$ = 31,6 nm) over the same voltage range. At V_{PZT} = 6 V one sees a transition region, where the main peak is completely suppressed and secondary peaks appear in the spectrum. In this case, the initial conditions of the overlap integral is changed, presenting two distinct solution, so generating two attenuation bands in the transmission spectrum.
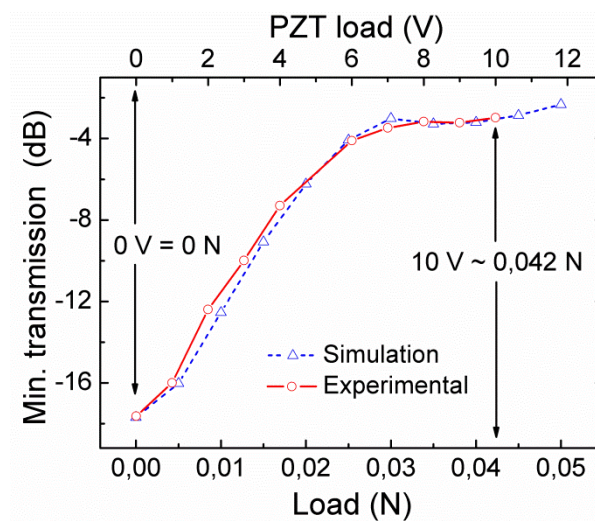
Figure 4.31 - Experimental and simulation results for the behavior of the minimum transmission at the peak wavelength versus the PZT load and the force.

The secondary peaks are more evident at the acoustic excitation f = 53,5 kHz, as shown in Figure 4.33. At this frequency for V_{PZT} = 10 V, the formation of two attenuation peaks (blue and red peaks) can be clearly seen, which are separated $\Delta\lambda$ = 34,2 nm apart. Besides the change in the optical path, changes in the difference between the effective refractive indices of core and

cladding modes, as well as the break of degeneracy of the circular cladding modes, lead to the modification of the LPG spectrum [Block2006, Allsop2004a, Allsop2004b]. Furthermore, experiments showed that no significant polarization dependence exists [Block2006, Chen1999]. The experimental behavior is confirmed by the simulation (considering P_0 = 0,06 N due now to a different mechanical resonance), whose result fits well the experimental curve, particularly at the long wavelengths (red peak). A total shift of Δλ = 20,6 nm is achieved by driving the PZT from V_{PZT} = 0 to 10 V in relation to the peak at rest (no acoustic wave).
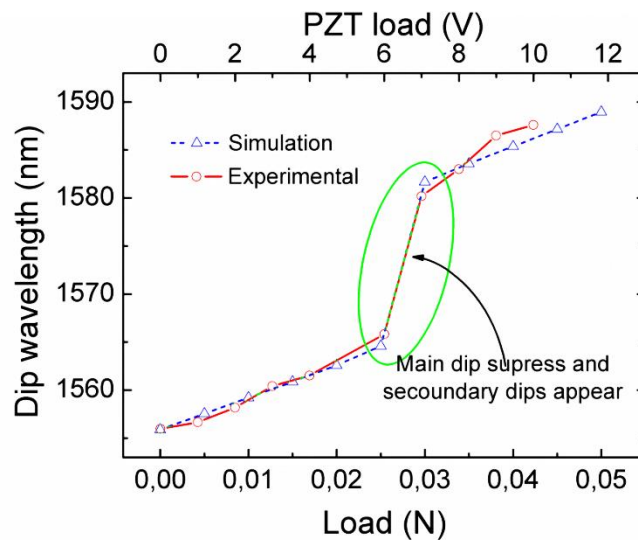

Figure 4.32 - Experimental and simulation results for the behavior of peak wavelength when the acoustic wave at f = 60,8 kHz excites the grating.
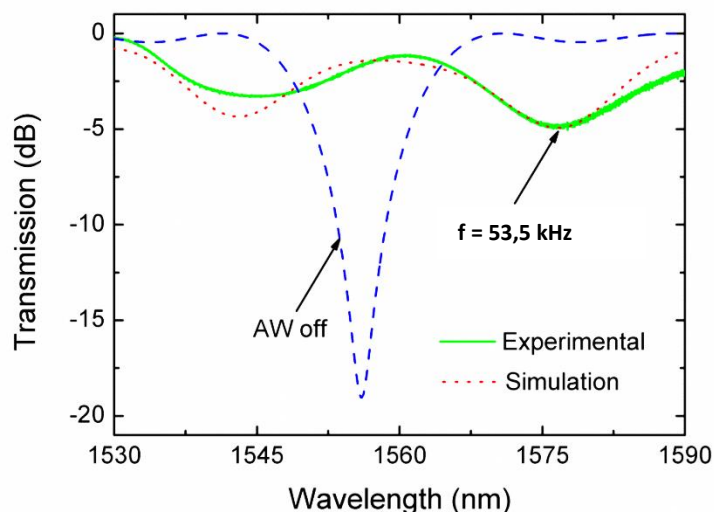
Figure 4.33 - LPG spectrum behavior for PZT load at V_{PZT} = 10 V (P_0 = 0,06 N) at f = 53,5 kHz.

During the experiments, it was noticed that for higher frequencies (in the $f \sim$ 1 MHz range), where the predominant vibration mode is longitudinal [Oliveira2010a] no such effect takes place in the LPG spectrum. The explanation for this absence of grating modulation is that the induced changes in the refractive indices are negligible and the longitudinal displacement of the grating planes does not affect the LPG spectrum. However, at this point, it is interesting to compare with the FBG case, for which the period is much smaller. In FBGs small changes in the grating modulation planes do change the spectrum, resulting in the modulation of the grating at higher frequencies [Oliveira2008a, Oliveira2010a].

4.5.2. Longitudinal Vibration of the Fiber

In the high frequency regime (frequencies higher than $f \sim$ 500 kHz) the predominant vibration modes in the fiber are longitudinal. However, even though the predominant resonant modes when low frequencies are applied are flexural, particular frequencies can generate longitudinal vibration modes in the fiber as well. In fact, different resonant modes have been excited in the fiber depending on the applied frequencies. From simulation results obtained with ANSYS [Oliveira2010a] and from the behavior of grating spectra, one can see which mode (flexural or longitudinal) is predominant at a particular frequency.

For frequencies around 200 kHz, a flexural effect was expected in the grating spectrum, however, for some particular frequencies a side lobe generation was obtained. For example, Figure 4.34 (a) shows the reflection spectrum of the FBG when f = 223,3 kHz excites longitudinally the grating with PZT load at V_{PZT} = 5 and 10 V. Thus, when a hybrid mode is found at a particular frequency, one needs to take into account which effect will be dominant, that is, if either flexural or longitudinal waves are dominant. In most cases, the lowest order longitudinal mode is always present, but with a weaker amplitude. As referred in [Silva2013], Figure 4.34 (b) shows the modulator response in terms of fiber displacements, which is decomposed into axial (z direction) and transversal displacements (xy directions). Although all analyzed acoustic modes present components of both XYZ displacements, the longitudinal acoustic waves are characterized by the larger displacements in z direction. The transversal displacements are composed by lower amplitude flexural oscillations which are polarized in xy plane transversally to the fiber axis. The proximity between the axial-transversal displacements observed in some resonances (for example

in the narrow frequency band around 1,150 MHz) can produce complex acoustic waves that are not useful for grating modulation.
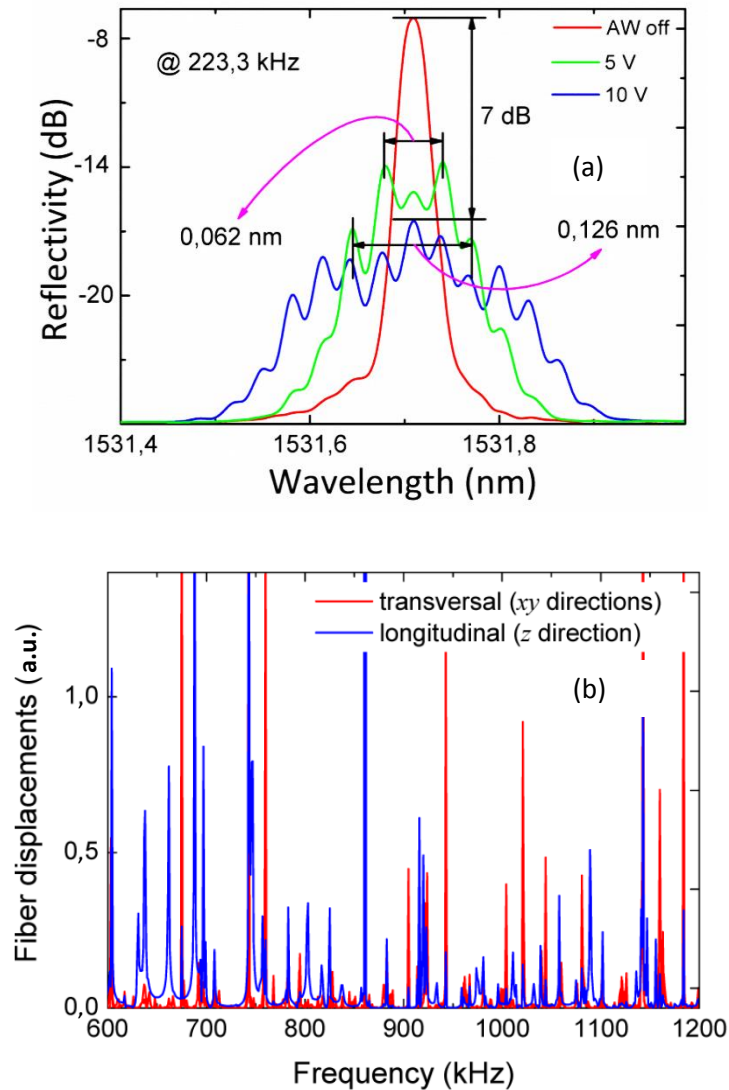
Figure 4.34 – (a) FBG reflection spectrum of the FBG when excited by f = 223,3 kHz longitudinal acoustic wave [Pohl2013]. (b) Modulator frequency response in terms of the fiber transversal and axial displacements [Silva2013].

Sweeping the frequency from 0 to f = 1 MHz, other longitudinal modes can be found, and the behavior of the side lobes can be tracked (considering the first and second symmetrical lobes from the center peak – called primary and secondary lobes) as shown in Figure 4.35. The behavior

follows the theoretical curve calculated in [Oliveira2008a]. Figure 4.36 shows a comparison of the experimental and theoretical FBG spectrum considering an acoustic excitation at f = 1,021 MHz with V_{PZT} = 10 V, which correspond to P_0 = 1 N applied to the base of the silica horn, considering the silica horn – fiber set presented in Figure 4.13. The theoretical curve fits well the experimental one in wavelength and reflectivity. As for the characterization, different experimental assemblies (silica horn, fiber tension, FBG length, holders, etc.) were used to perform the experiments and, in addition to different physical conditions (temperature, humidity, etc.), slightly different results are obtained through this thesis for the same frequencies.
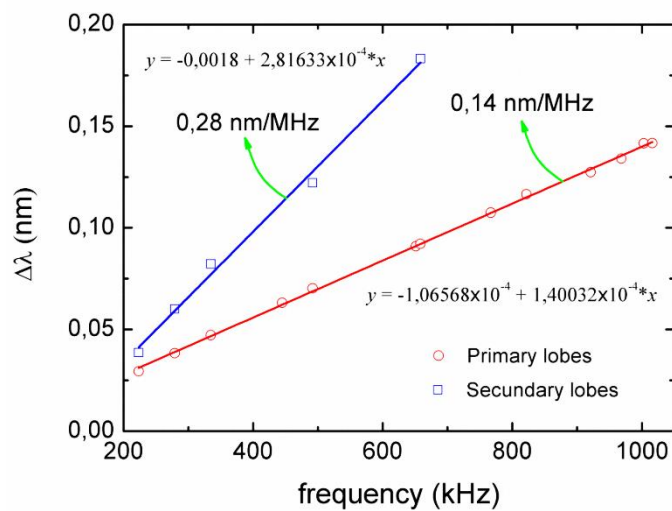
Figure 4.35 - Linear behavior of the primary and secondary lobes of the FBG spectrum, depending on the applied frequency.
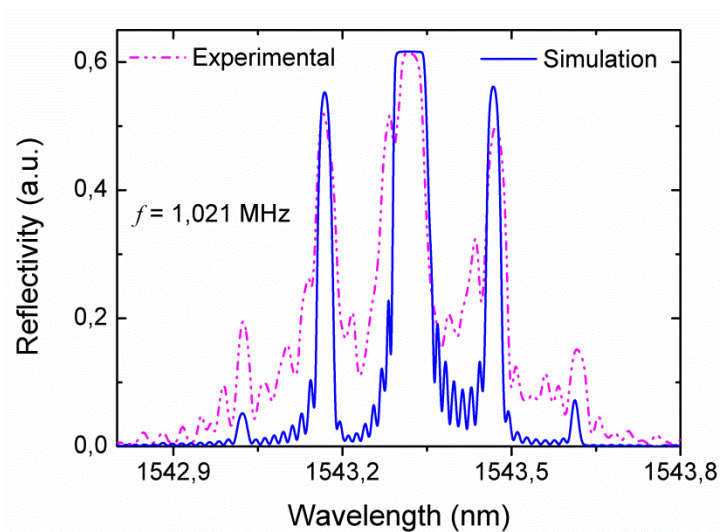
Figure 4.36 - Experimental and simulated results for f = 1,021 MHz acoustic wave excitation.

The capability of generating side lobes in the FBG spectrum opens up the possibility of having a tunable sampled grating, where the period of the side lobes is dependent on the applied acoustical frequency and the intensity of the PZT load. Figure 4.37 shows a 3-D graph that shows the behavior of the side lobes reflectivity, when the applied load varies from V_{PZT} = 1 to 10 V. This behavior is founded to be nonlinear and is characterized by an increase of the side lobes reflectivity while central wavelength peak decreases, as shown in Figure 4.38.
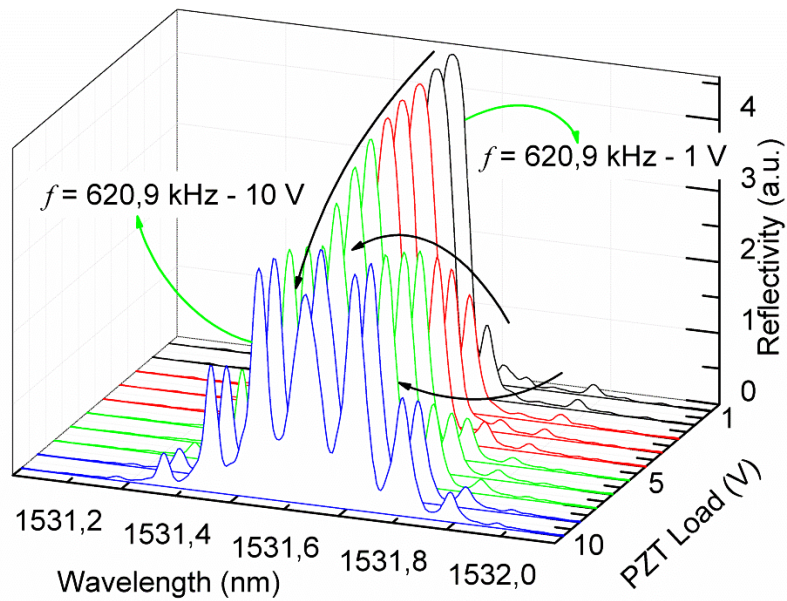
Figure 4.37 - Growing of side lobes as the PZT load increases.
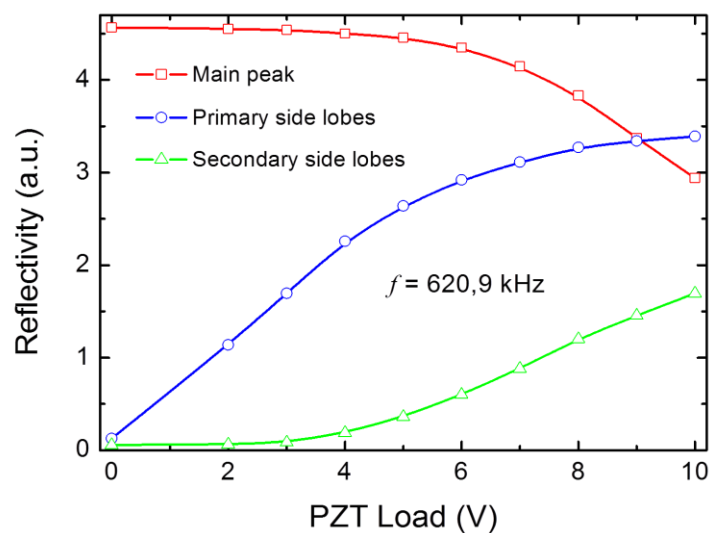
Figure 4.38 - Side lobes growing and peak wavelength decreasing behavior.

4.5.3. Temporal Analysis

The significant development of FBG technology has ultimately contributed to lowering the costs of systems employed in optical communications and sensing. One weakness associated with FBG technology is the difficulty to develop fast tunable devices. Therefore, the time response of Bragg gratings is of great concern in the design of fast photonic devices. The tuning methods presented so far based on strain [Lee2007] or temperature [Eggleton2000a] are slow and bulky, with tuning times of milliseconds. This drawback has been partially overcome using acousto-optic modulation, as will be shown in this section.

The switching time is the time necessary to change the grating optical response from 10 to 90% of its final value. This time depends on a variety of factors, such as the mechanical setup, temperature and fiber tension. However, every assembled modulator presents a particular behavior depending on the excited frequency.

4.5.3.1. Silica Optical Fiber

For example, pure longitudinal modes usually take the time correspondent to the acoustic wave to travel at c_{ext} = 5740 m/s, which corresponds to the speed of sound in the silica optical fiber, calculated using the equation:

$$c_{ext} = \sqrt{\frac{E}{\rho_D}} = \sqrt{\frac{72{,}9 \text{ GPa}}{2200 \text{ kg/m}^3}} \; . \tag{4.51}$$

However, when the excited mode is flexural, the propagating time is higher, which correspond to a lower speed of sound. For a given frequency, the speed of flexural wave can be measured using the follow relation:

$$v_f = \sqrt{\pi a c_{ext} f} \; . \tag{4.52}$$

Even though in these equations the external and mechanical conditions are not included, the speed of sound is strongly dependent on them. Another factor is the damping of the acoustic wave, which makes the measured time differ from the theoretical value.

The modulator showed in Figure 4.25, when operating in reflection for side lobes generation (high frequency regime), can be used to be a measure of the switching time. A photodetector is used to interrogate the reflection of an optical channel positioned on the same wavelength of a primary side lobe of a FBG, considering a longitudinal excitation at f = 617 kHz. When the acoustic wave is turned 'on', the acoustic excitation takes approximately t_{st} = 44 µs to change the FBG reflectivity. This time represents the period taken to allow the optical channel to be reflected by the primary side lobe and to be detected by the photodetector. Figure 4.39 (a) shows this time, measured when the acoustic wave is 'on' and taken at the point where the reflectivity response grows and remains constant. Indeed, the time that can be considered for practical applications, in this case, is t_s = 22 µs, which corresponds to the time the standing acoustic wave takes to be generated in the region between the tip of the horn and the fiber holder (which corresponds to the grating length). The delay observed between the RF and optical signal is related to the time the acoustic wave takes to propagate along the interaction length (silica horn + fiber) and the inertia of the system. Optimizing the experiment through the suppression of the mechanical damping that acts on the modulator, for instance, removing the device from any positioning stage (which always have a damping spring), faster switching time can be achieved. For example, by fixing the modulator on a stable optical table, a shorter time can be achieved. Thus, this configuration can be applied in a series of devices where fast dynamic control is required as will be seen in the next chapter.

In the case of excitation of flexural waves, the time taken to change the spectrum characteristics is larger, as seen in Figure 4.39 (b). A tunable laser has its center wavelength tuned to the dip wavelength of a LPG and, when excited by f = 87 kHz acoustic wave, the transmission at that wavelength is enhanced, and an increase on the photodetector signal is experienced. The acoustic wave takes approximately t_{st} = 596 µs to change the spectrum. Furthermore, the switching time for practical applications is around t_s = 211 µs.
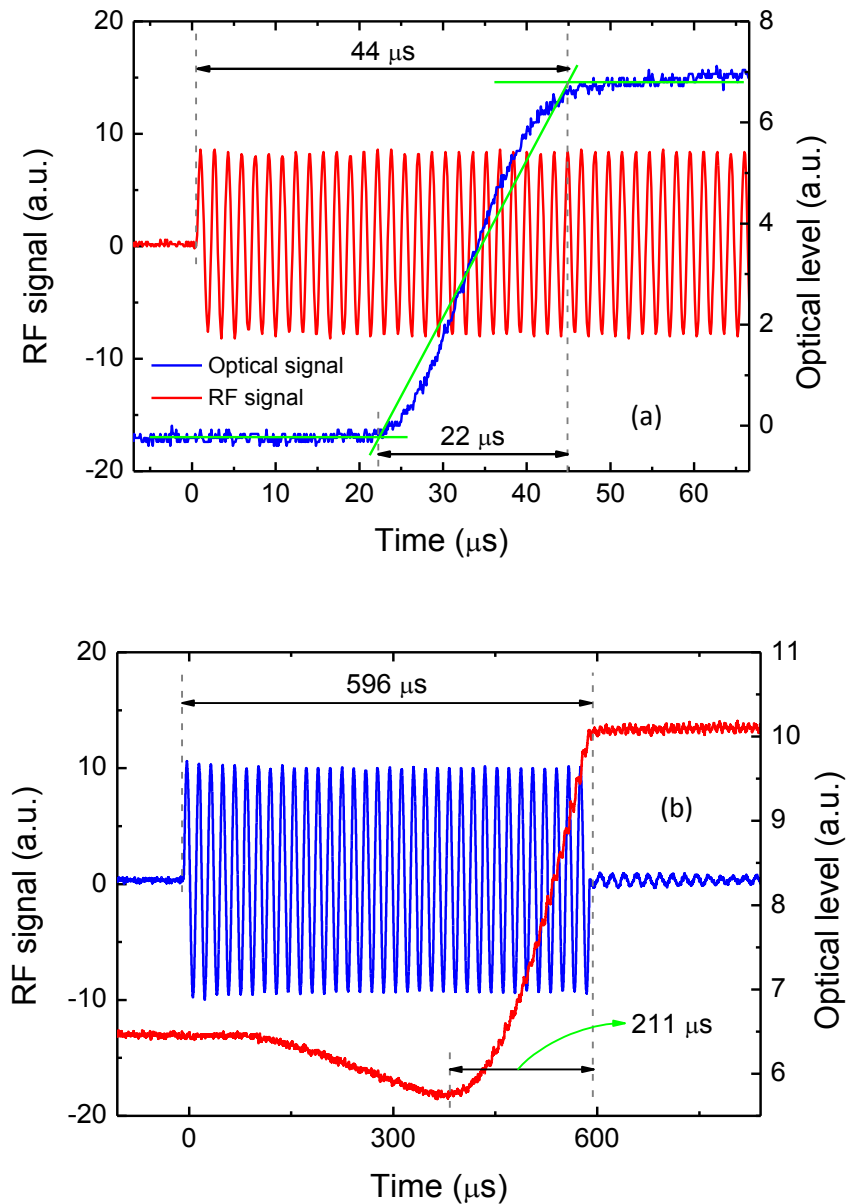
Figure 4.39 – (a) The time response of the modulator when driven by f = 617 kHz longitudinal acoustic wave. (b) Switching time of the modulator when driven by f = 87 kHz flexural acoustic wave.

4.5.3.2. Polymer Optical Fiber

In POF, the E and ρ_D values are 3 GPa and 1180 kg/m^3, respectively, so that the pure longitudinal modes take the time corresponding to the acoustic wave to travel at c_{ext} = 1595 m/s, which corresponds to the speed of sound in the POF, calculated using the equation (4.51). However,

when the excited mode is flexural, the propagating time is higher and consequently corresponds to a lower speed of sound, following the equation (4.52).

A similar modulator as showed in Figure 4.25 was used to investigate and measure the time response of the FBG-mPOF. Operating in reflection and for low frequency regime, it can be used to be a measure of the switching time. The time response is assessed using a fast photodetector coupled to an oscilloscope from which important parameters such as the response delay and the grating switching time can be retrieved. The photodetector is used to interrogate the reflection of an optical channel positioned on the same wavelength of the central wavelength of the FBG-mPOF with a fiber radius of 62,5 μm, considering a flexural excitation at f = 76,5 kHz. It shall be noted that similar behaviors are observed for acoustic waves generated at other resonance frequencies; however, the magnitude of the effect is lower.

The experimental setup used to evaluate the time response is shown in Figure 4.40. First, by using the 2-mm FBG-mPOF (Figure 4.41 (a)), the acoustic effect takes approximately t_s = 350 μs to change the grating spectrum, which corresponds to the time the standing acoustic wave takes to be generated. After the excitation reaches the maximum value, the measured stabilization time (τ_{sta}) is around τ_{sta} = 250 μs (see Figure 4.41 (c)). By using the 10-mm long FBG-mPOF (see Figure 4.41 (b)), the times are substantially improved as is shown in Figure 4.41 (d). The acoustic effect takes approximately t_s = 215 μs to change the grating spectrum and the measured stabilization time is around τ_{sta} = 200 μs. This improved behavior can be caused basically due to a better coupling of the acoustic wave between the horn and the fiber due to the interaction length (horn + mPOF containing the FBG) to be longer than the previous case. It shall be noted that the acoustic wave velocity is the same in both cases according to expression (4.52). However, due to the fact that the length of the two gratings is different, the interaction length of the acoustic wave in the gratings will cause the switching time to be different. These results can still be improved if acoustic waves of higher frequency (higher flexural frequencies or longitudinal frequencies) were employed.

 In POF, the best result was achieved with a 10-mm long FBG length. It should be noted that the best results obtained in the silica fiber were performed with FBG lengths greater than 25 mm [Pohl2013].
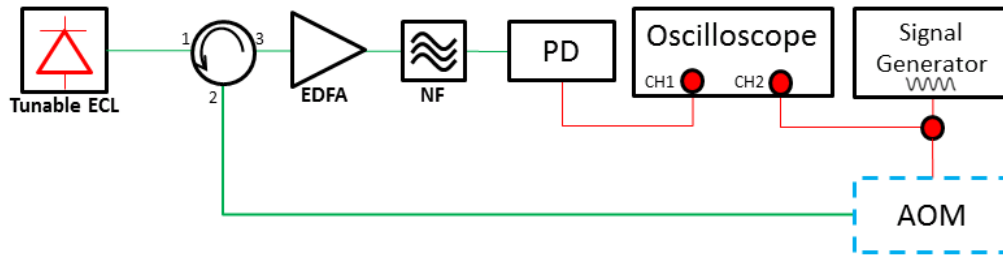
Figure 4.40 - Experimental setup used for time response measurements. ECL – external cavity laser; EDFA – Erbium doped fiber amplifier; NF – noise filter; PD – photodetector.
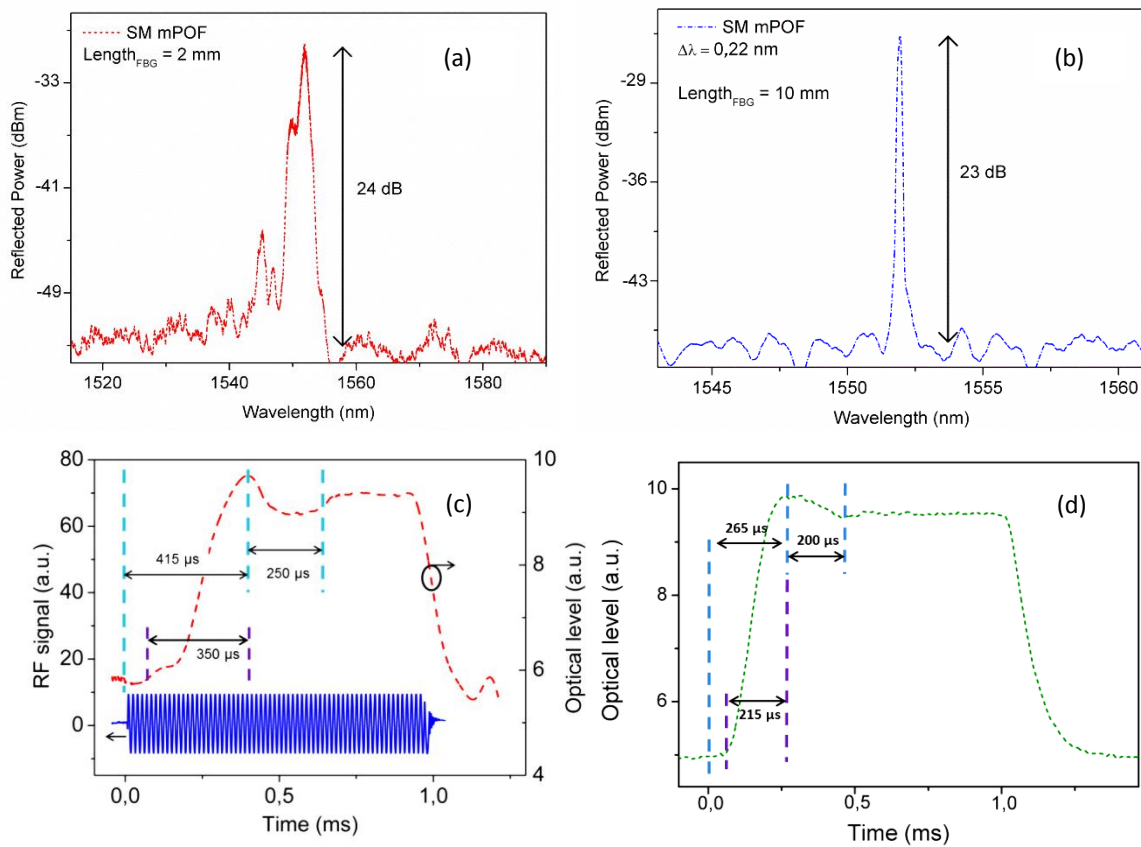
Figure 4.41 - Reflection spectra of the SM FBG-mPOF with length of (a) 2mm and (b) 10 mm. Switching time of the modulator when driven by a flexural acoustic wave in an FBG-mPOF with length of (c) 2 mm and (d) 10 mm.

4.6. Acousto-optic Effect in mPOF vs. Silica Fiber

A detailed analysis of the acousto-optic effect in mPOF in order to discuss and compare with silica fiber ones existing in literature is one of goals in this thesis. This study is a key for potential applications in optical communications, such as short distance transmissions [Shi2013, Shao2012], and sensing [Yuan2011a, Luo2011] due to a large interest in POF technology nowadays.

When an AW is coupled into a fiber where an FBG is inscribed it generates a standing mechanical wave, either in silica fiber or POF. As already mentioned, the FEM modal analysis showed that: (i) most low frequency resonant modes generate flexural acoustical waves; (ii) longitudinal resonant modes are mostly observed in high frequency regimes (the acoustic longitudinal wavelength is small and the structure does not support the existence of flexural waves); (iii) at low frequency regimes, in an hybrid mode the flexural regime is dominant but there is also an interaction with a low frequency longitudinal acoustic wave.

4.6.1. Strain Field Behavior

Figure 4.42 shows the modulator response (PZT is coupled to the horn-fiber system) in terms of fiber displacements, which is decomposed into axial and transversal displacements. Although all analyzed acoustic modes have both components of the displacement field, the longitudinal acoustic waves are characterized by the larger displacements in z direction. The transversal displacements are due to lower amplitude flexural oscillations which are polarized in xy plane, transversally to the fiber axis. Also, at lower frequencies (flexural regime) the flexural acoustic waves are mostly characterized by the larger displacements in xy direction however, some displacements in z direction are observed in this regime. These simulations predict strong flexural modes for acoustic frequencies below 400 KHz and longitudinal modes predominant for higher frequencies.
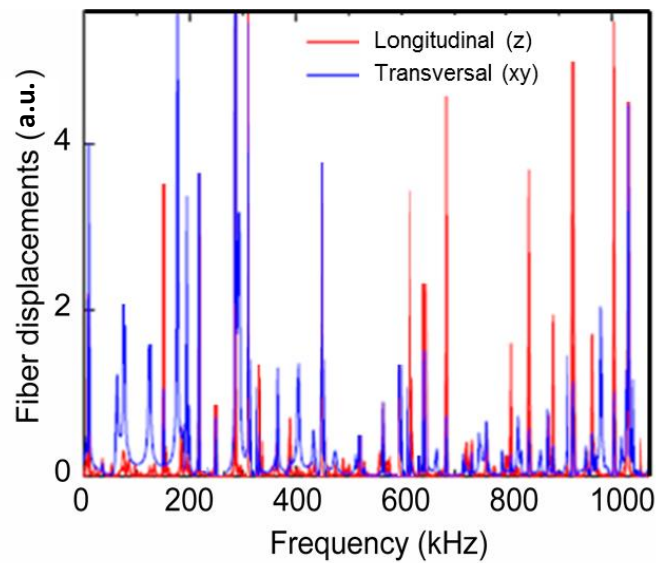
Figure 4.42 - AOM frequency response in terms of the fiber transversal and axial displacements.

A numerical comparison of the mechanical properties along FBG-mPOF-AOM and the similar structure with silica FBG (SFBG) is performed. Figures 4.43 (a) and (b) detail the dimensions of the FBG-AOM used in the FEM model (similar to the experimental structure). A comparison of the strain field along the FBG-mPOF-AOM length and the similar structure with SFBG-AOM is shown in Figures 4.43 (c,e)-(d,f), when the grating length is L = 2 mm and 10 mm, respectively. The strain field was achieved by FEM considering a sinusoidal excitation source applied on the base of the silica horn with resonance frequencies, f, of 302 kHz and 1 MHz, and load amplitudes P_0 = 1,5 N and P_{DC} = 0 N. According to the results presented in Figure 4.42 and also considering a decomposition of the strain field, for 302 kHz and 1 MHz the strain field is presented by its transversal and longitudinal component, respectively. As can be seen in Figure 4.43, the strain field amplitude is higher for the FBG-mPOF than for SFBG due to its smaller stiffness. It is also verified that the acoustic wavelength is shorter for the mPOF, as expected. The behavior of the structure can be studied under the influence of parameters such as the frequency of the acoustic wave, the applied load or its dimensions. Using the dimensions given in Table 4.2 the following sections detail the behavior of the reflected grating spectrum as these parameters are varied.

L = 2 mm   **L = 10 mm**
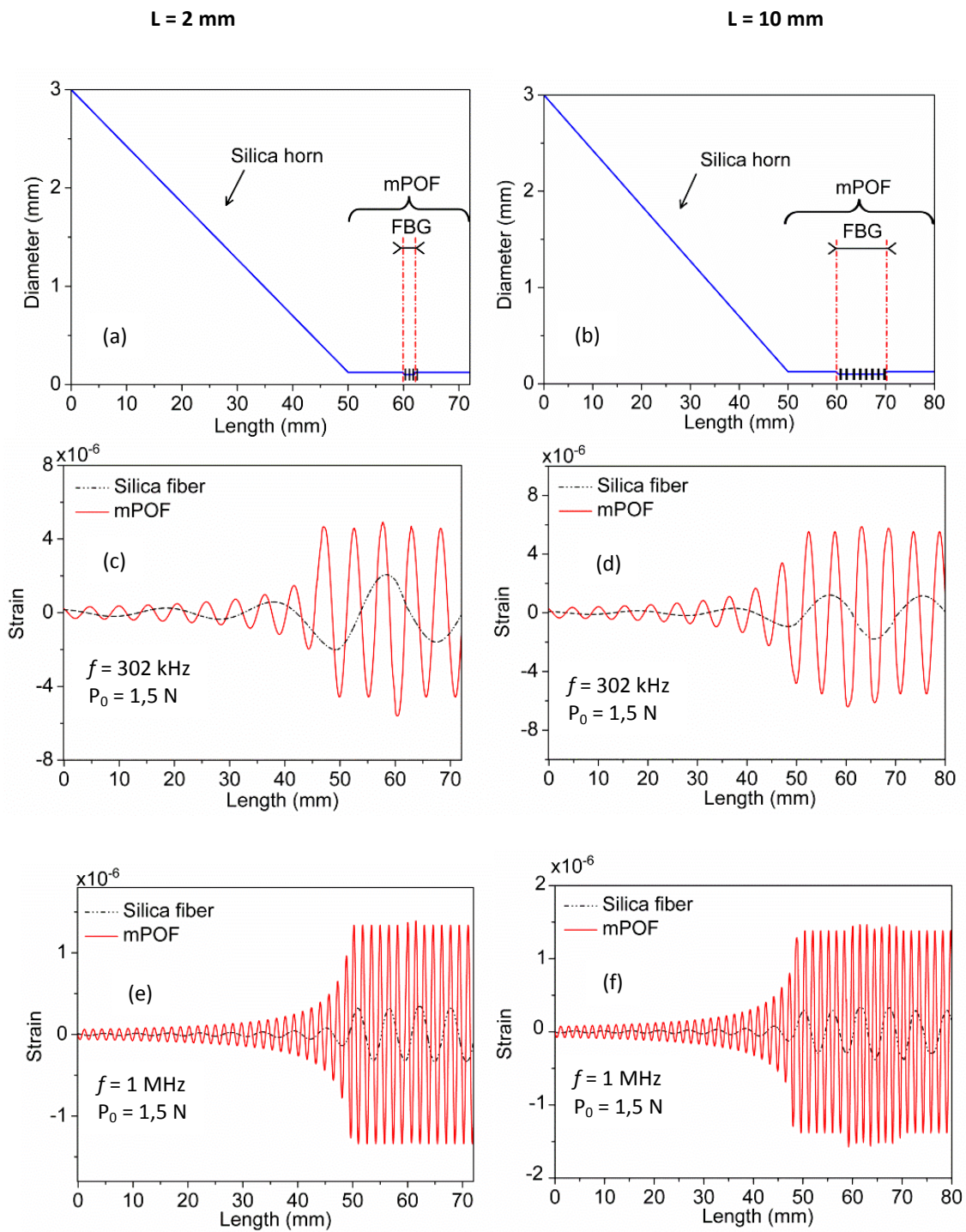
Figure 4.43 - Diameter of the AOM structure as function of the FBG length: (a) 2 mm and (b) 10 mm. Superposition of strain fields for FBG-mPOF and SFBG under the influence of the acousto-optic effect when grating length is (c,e) 2 mm and (d, f) 10 mm.

Table 4.2 - FBG length and respective acoustic wave interaction length of the horn-fiber

FBG length (mm)	2	10
Interaction length: horn-fiber (mm)	72	80

For a given device dimension the strain also varies with the PZT excitation frequency. The acousto-optic effect in the fiber will be enhanced when the excitation of the natural resonant modes of the silica horn–fiber structure are best matched to the frequencies delivered by the PZT. Previous results show that all resonant modes measured in the PZT are again observed in the combined structure, but with slight changes in frequency values because the anisotropic constants used in simulations did not include the PZT losses [Oliveira2010a]. Those losses reduce the impedance-phase amplitude, which affects the localization of some resonances by the condition of minimum impedance and null phase. Figure 4.44 shows strain variation as a function of the PZT excitation frequency for the dimensions detailed in Table 4.2 (in this case for 72 mm of interaction length). When a longer piece of mPOF is added on the set (the case of 80 mm interaction length - Table 4.2), it reduces the stiffness of the fiber, and a small shifting of the resonance frequencies range happens. Also, comparing these data with the results obtained in [Oliveira2008a] for silica fiber, the resonance frequencies are distinct for mPOF, as expected, due to the different mechanical properties (mPOF and silica fiber). The strain fields are much higher than for silica fiber, with more than two orders of magnitude.
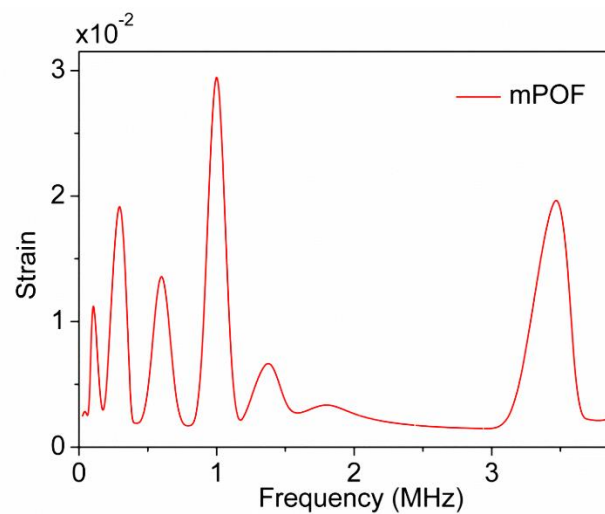
Figure 4.44 - Strain variation versus the PZT excitation frequency.

4.6.2. Frequency and Load Variation

Figure 4.45 shows the grating reflection spectra calculated using the theory and computational simulation described in previous sections. By exciting the structure with acoustic waves of different frequencies the grating spectrum shows other characteristic wavelengths. The grating reflection spectra in mPOF were simulated for three different scenarios: (i) using flexural regime at 126 kHz (Figure 4.45 (a)); (ii) using longitudinal regime at 1 MHz (Figure 4.45 (b)) and 3,5 MHz (Figure 4.45 (c)); (iii) to obtain similar spectral shape in silica fiber and mPOF (Figure 4.45 (d)). For these scenarios the preload P_{DC} is chosen to be null and the amplitude of the harmonic load P_0 is changed. The FBG length is L = 2 mm. In the first scenario the PZT actuator works in the bending regime at 126 kHz as seen in Figure 4.45 (a). It shall be noted that P$_0$ is much lower for FBG-mPOF due to smaller stiffness in comparison with the SFBG (inset of Figure 4.45 (a)). As expected, a decrease of the grating reflectivity was achieved. In the second scenario the PZT actuator works in the stretching and compression regime, with symmetric displacement amplitude as seen in Figure 4.45 (b) and (c). Figure 4.45 (b) shows also the grating reflection spectrum when P_0 = 0 N is applied at 1 MHz showing one central peak, λ_{B0}. Applying load, side bands appear and if P_0 is increased, more side bands appear but the central band is attenuated. The wavelength difference between the central band and the side bands is estimated as $\Delta\lambda = \lambda_{B2}$-$\lambda_{B0} = \lambda_{B1}$-$\lambda_{B0} = \lambda_{B3}$-$\lambda_{B1} = \lambda_{B4}$-$\lambda_{B2}$ = 1.08 nm. The same difference is obtained between consecutive side bands. Figure 4.46 (c) shows a similar behavior with a higher resonance frequency. The figure also shows a greater difference between the side bands due to the frequency increase. To obtain similar spectral shape in the silica fiber and mPOF, it was necessary to apply a lower resonance frequency as well as lower PZT load to the mPOF as shown in the Figure 4.45 (d). It shows that the FBG-mPOF requires less effort from the PZT actuator.
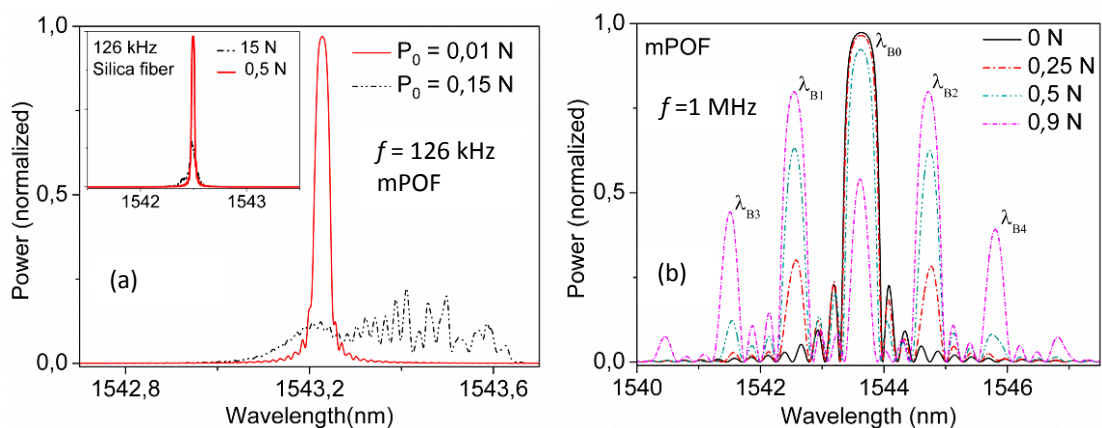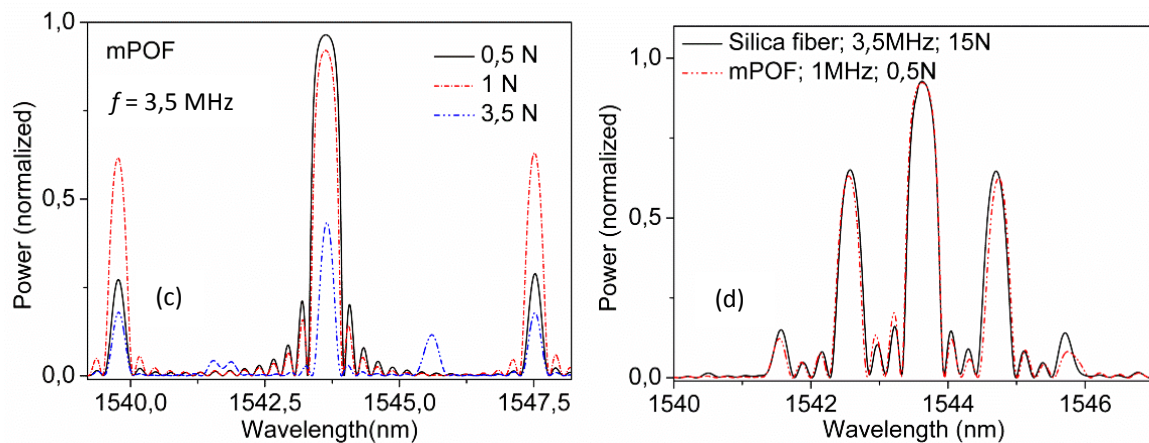
Figure 4.45 - Reflected spectra when excitations are applied with frequency at (a) 126 kHz, (b) 1 MHz and (c) 3,5 MHz. (d) Similar spectral shape silica fiber and mPOF. The FBG length is 2 mm.

4.6.3. Influence of the Dimensions

The influence of the horn dimensions on the strain observed along the structure allows the optimization of each of its parts. Applying different resonance frequencies and PZT loads, the strain field seen by the grating can be modified through changes in the dimensions of the silica horn. Figure 4.46 shows the strain behavior as a function of the diameter and of the length of the silica horn for silica fiber and mPOF. A modification of the horn dimensions causes changes in the resonance frequencies of the device. Numerical results show that an increase of the silica horn base diameter causes an increase in the stiffness and mass of the system, leading to a decrease of the displacement and strain fields along the FBG (Figures 4.46 (a) and (b)). Figure 4.46 (c) shows the results when a low amplitude load of P_0 = 0,05 N is applied and we concluded that the strain fields are higher for mPOF, regardless of the applied voltage and resonance frequency. By simulation results, the silica horn with 1 mm of base diameter presents the best result in terms of strain field. On the other hand, a change of the silica horn length does not cause significant variations in these fields, as shown in Figure 4.46 (d), and, once more, the mPOF strain fields are much higher than for silica fiber regardless the resonance frequency and FBG length. The strain field is also higher (more than one order of magnitude in relation to Figure 4.46 (a)) when long FBGs are used as shown in Figure 4.46 (b).
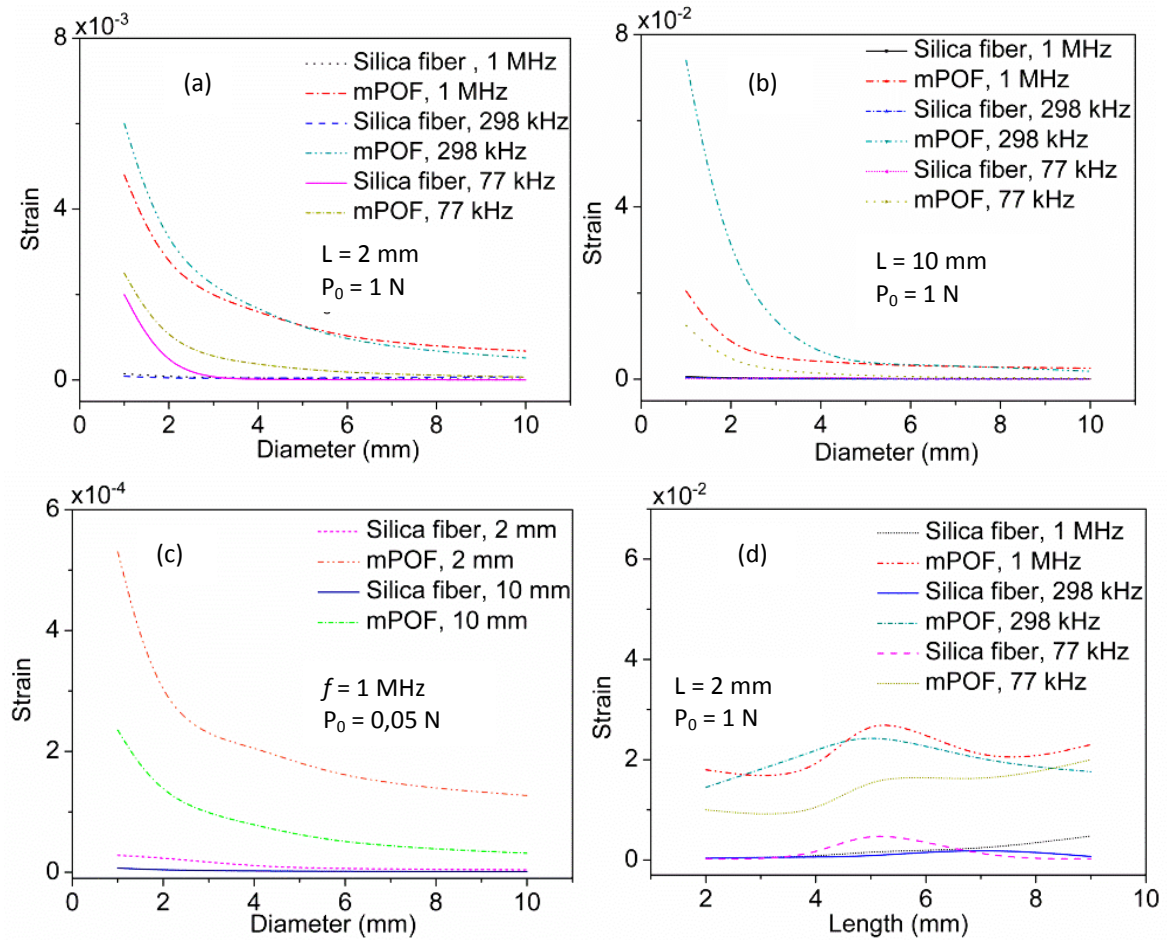
Figure 4.46 - Strain behavior versus the silica horn (a, b, c) diameter and (d) length.

In fact, the observation of the acousto-optic effect in a 2 mm grating is already a significant result when compared to the same effect in a silica fiber, which requires a length of few centimeters to be noticed. Furthermore, from the simulation results we can observe effects of the different FBG lengths (such as 10 mm length), allowing optimisation for POF applications that require FBGs with different characteristics such as bandwidth and/or reflected power, among others.

4.6.4. Experimental Realization and Results

The Bragg gratings used to perform the experiments were inscribed in PMMA-based few mode mPOF through the phase mask technique, using the CW HeCd laser with an output wavelength of

325 nm and a power of 30 mW. The mPOF has an outer diameter of 150 µm and a core diameter of 15 µm. The core is bounded by four rings of holes as shown in Figure 4.47 (a). Details of the production process of the mPOF are described in [Barton2004]. The laser beam was focused vertically downward using a 10-cm focal length cylindrical lens, through a 1061 nm period phase mask and onto the fiber as mentioned in Chapter 3. The mPOF was laid on a v-groove and taped down using polyimide tape. This type of fiber has a typical inscription time of 15 to 60 min depending of FBG length. The Bragg wavelength of the inscribed grating was in the region of 1570 nm with a length of 2 mm, determined by the width of the UV laser beam. The inscription process was monitored using a 1550 nm MM 50∕125 µm silica fiber coupler, a broadband light source, and an OSA. For the inscription, a temporary connection was made using a FC/APC contact connector on a 50∕125 µm silica fiber which was then butt coupled to the bare POF using an XYZ translation stage. A small amount of index matching gel was used in the coupling to reduce Fresnel reflections.
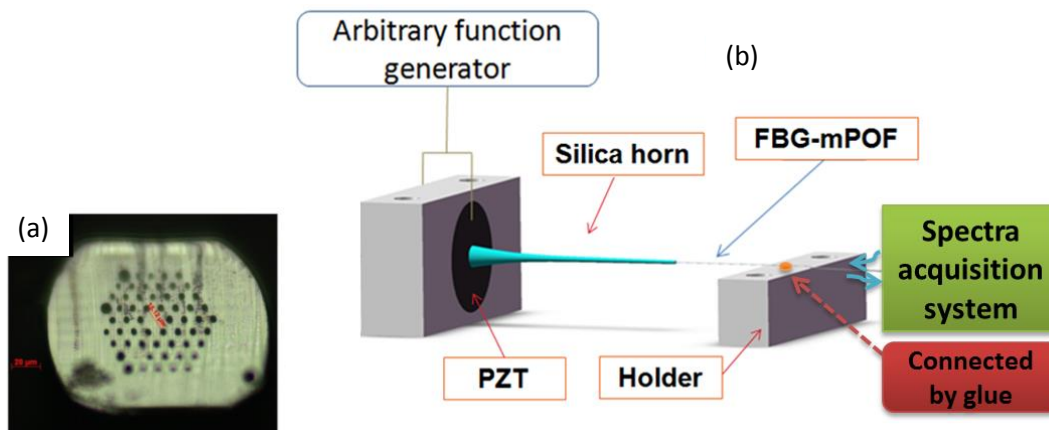
Figure 4.47 - (a) Microscope image of end face of few mode mPOF. (b) Schematic apparatus used to excite acoustic waves in the structure (silica horn + FBG-mPOF).

On the other hand, the AOM is composed of a PZT, a silica horn and the mPOF containing the Bragg grating (see Figure 4.47 (b)). The silica horn length is L_{sh} = 50 mm, with a base diameter d_{sh} = 3 mm, a tip diameter d_{sht} = 1 mm and central hole diameter d_h =150,5 µm. The initial tension of the FBG is adjusted using micro-resolution translation stages. The acoustic wave interaction length of the horn-fiber is 72 and 80 mm when the FBG length is 2 and 10 mm, respectively, as shown in the Table 4.2. It should be note that the acoustic wave interaction length is the total

length of the FBG-AOM, L_i. The set was swept over the range from 1 kHz to 1,2 MHz to investigate the acoustic effects on the FBG-mPOF and to compare with FBG in silica fiber. As one can see in Figure 4.47 (b), the AOM is connected to an arbitrary function generator and the reflected spectrum was monitored by an OSA with wavelength accuracy of 0,01 nm.

Figure 4.48 (a) shows that the acoustic excitation at 77 kHz leads to a broadening of the FBG spectrum, which can be controlled by means of the V_{PZT}. When the PZT load is set at 20V, the FBG amplitude is totally suppressed. This result can be explained considering the coupling mechanism of the propagating modes. The lower reflectivity of the grating is due to changing period along the grating length that disrupts the phase matching, leading to a lower coupling to the counter-propagating mode [Oliveira2010a]. For example, this behavior can be used for add-drop multiplexers in low frequency regimes. It should be noted that maximum amplitude measurement of each spectrum is made between the values of noise background and main peak (Figure 4.48 (a)).

Figure 4.48 (b) shows the spectral behavior of the grating when the applied V_{PZT} is changed between 0 V and 20 V and with the acoustic wave frequency set at 77 kHz. It is possible to control the 3-dB bandwidth of the reflected spectrum by tuning the applied V_{PZT}. As the PZT load is increased the phase mismatching effect also increases. In the case of 3-dB bandwidth measurements, results are presented for PZT loads up to 17 V, the maximum measurable 3-dB bandwidth value. For higher loads, the FBG is suppressed.

Figures 4.48 (c-e) show the measured-simulated FBG spectra when the grating is excited with the 77 kHz resonance for different V_{PZT}. The measured spectra are compared to the modelled TMM spectra obtained from previously assessed FEM simulations. At V_{PZT} = 10 V the amplitude of the harmonic load delivered by the PZT is P_0 = 0,63 N (verified through simulations).

The differences in reflectivity and wavelength bandwidth between measured-simulated results are due to grating variations originating in the grating inscription process. The experimental results show a good agreement with the simulated data.
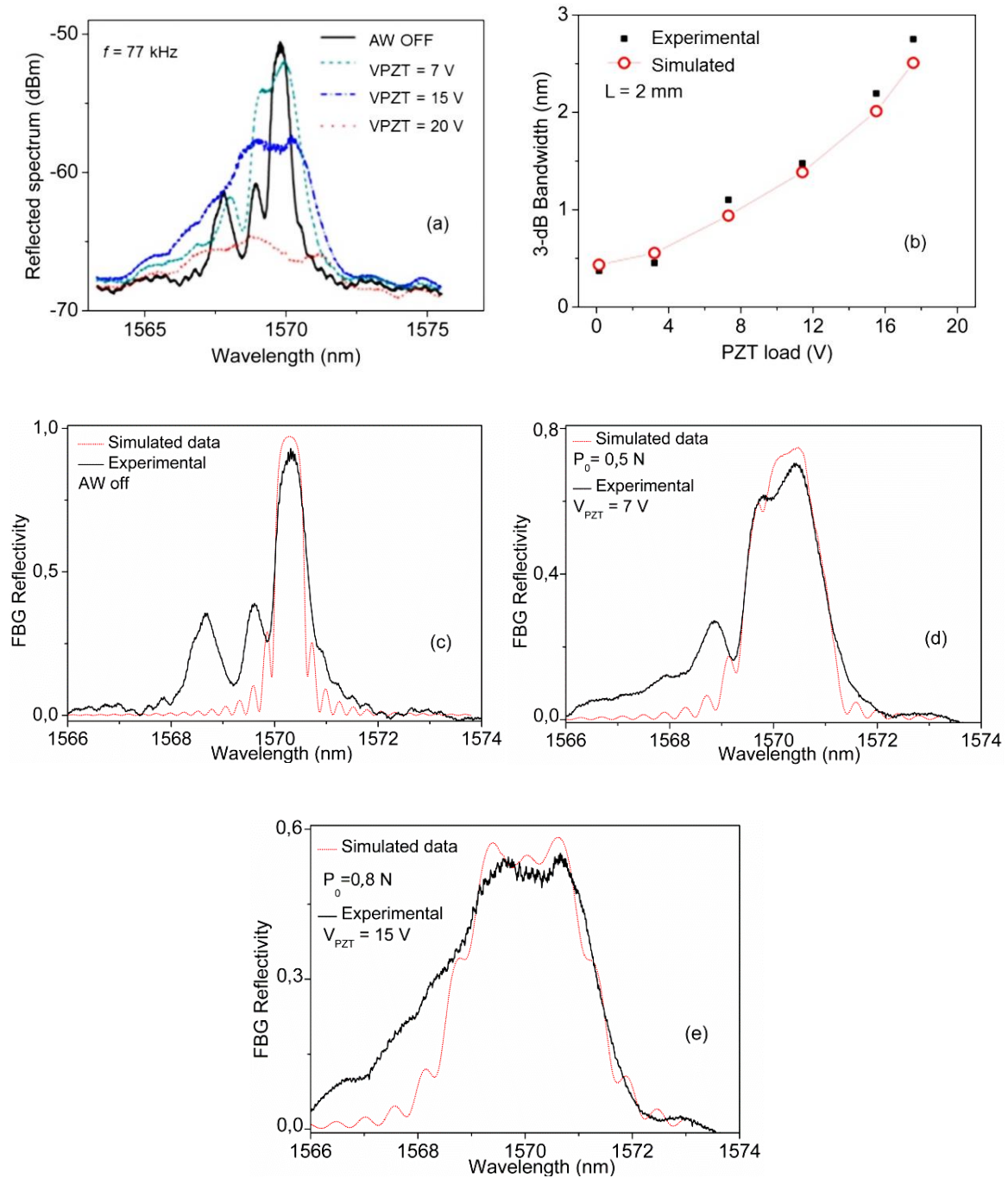
Figure 4.48 - (a) Spectrum behavior when a 77 kHz frequency acoustic wave excites the FBG-mPOF, varying V_{PZT} from 0 to 20 V. (b) 3-dB FBG bandwidth behavior as a function of the PZT load (experimental results and simulated data) for an acoustic excitation of 77 kHz. FBG measured-simulated spectra when (c) Acoustic wave is 'off', (d) V_{PZT} is 7 V (corresponding an amplitude of the harmonic load P_0 = 0,5 N) and (e) V_{PZT} is 15 V (P_0 = 0,8 N).

Figure 4.49 (a) shows an example of spectral shaping when an acoustic excitation of 193 kHz is turned 'on'. In this example, the side lobe of the reflection spectrum of the FBG is suppressed, due to an induced apodization, leading to a better filter response. At 193 kHz, the flexural acoustic wavelength ($\lambda_s \sim 3{,}09$ mm) is larger than the grating length ($L = 2$ mm). Once the length between the PZT and the beginning of the FBG (60 mm) and the acoustic wavelength are known, the wave position relatively to the FBG can be estimated, i.e. the ratio between them give us the wave position relatively to the FBG as shown in Figure 4.49 (b). When acoustic wave is turned 'on' there is a maximum of the standing acoustic wave at z = 0. Taking into account the calculated standing wave period, it is possible to write the FBG in a wave zone which induces an apodization such as the center of the FBG is positioned in a node (zero displacement – see Figure 4.49 (b)).

In Figure 4.49 (c), the acoustic excitation of 214 kHz results in a spectral broadening of the FBG. This may be a result of the grating being in the transition between the compression and rarefaction strain fields, corresponding to both blue and red shifting of the λ_B. Therefore, this behavior demonstrates a bandwidth tuning structure as a function of the PZT load.

In this experimental work the acoustic excitation is only observed in low-frequency regime, i.e. when the longitudinal acoustic wavelength is longer that the FBG length (2 mm). Indeed, from Figure 4.44 we can conclude that for a device using mPOF, mostly resonance frequencies are located below 1 MHz (shorter acoustic wavelength). At this particular frequency and for 3,5 MHz, the appearance of additional bands on both sides of the grating reflection spectrum should be experimentally observed. Therefore, further developments will be focused in the increasing of the FBG length in order to increase the acoustic-optic interaction length and thus improve the peak reflectivity of the secondary lobules.

Results show that it is possible to dynamically control the properties of the grating spectra even with a grating length of 2 mm through the AOM, which has not been possible in silica fibers.

The FEM and the TMM present the advantage of calculating the strain along the whole structure allowing the determination of the influence of the structure dimensions (horn, fiber and FBG sizes) on the grating reflected spectrum when an acoustic wave propagates along its axis. Furthermore, the physical characteristics of the structure can be adjusted in order to obtain the desired strain and FBG spectrum. The approach takes into account the load induced by the acoustic wave, which can be associated with the characteristics of the PZT actuator used for its

excitation. The simulation results obtained using the method correlate well with experimental data. The strain field along an FBG-mPOF–AOM and a similar structure with SFBG-AOM was determined, showing that the strain field amplitude is higher along the FBG-mPOF due to its smaller mechanical stiffness.

The obtained results can be used in the development of fine-tuned optical filters using low voltage sources and low frequency regimes, to obtain tunable optical filters and to control the shape of the spectrum.
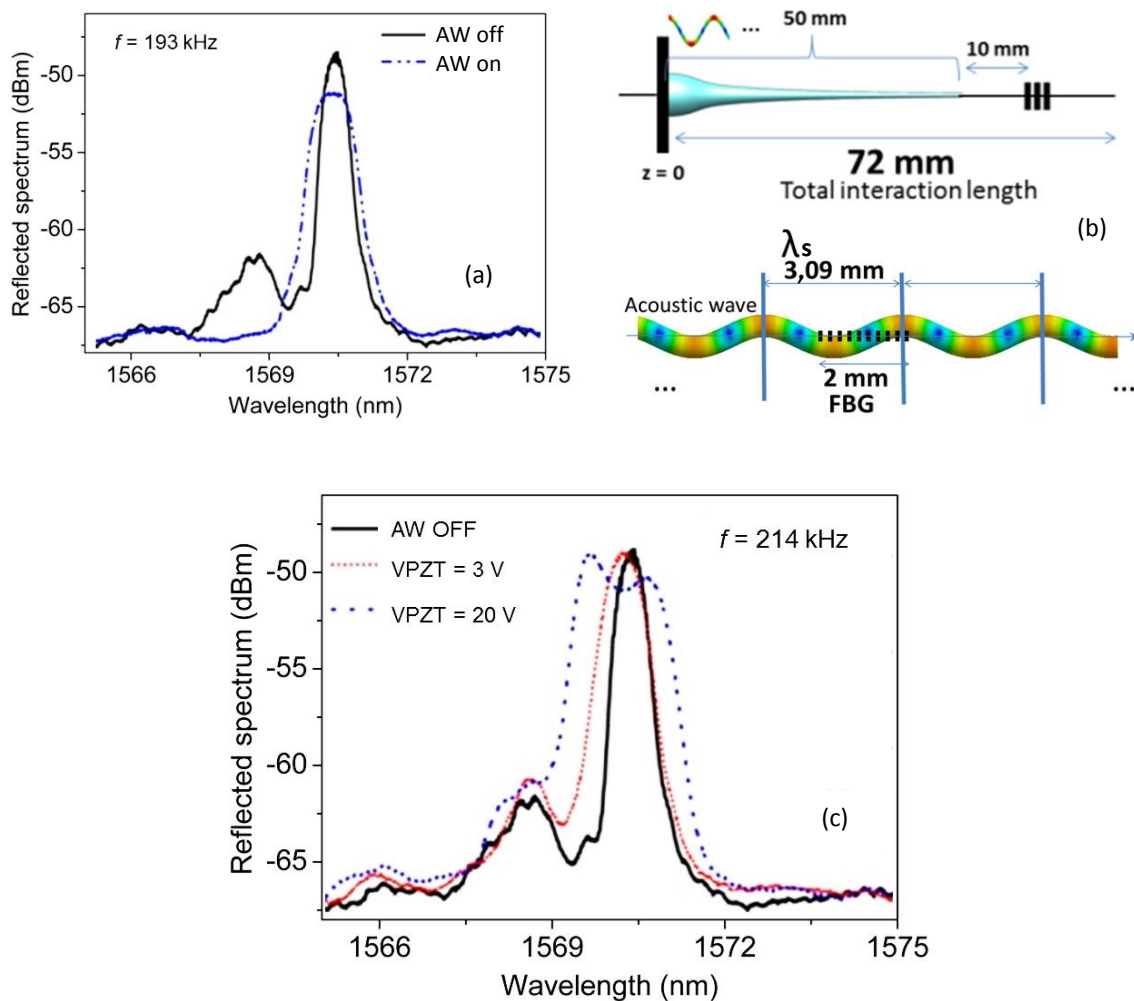
Figure 4.49 - (a) Grating reflection spectrum behavior when the acoustic wave is switched 'on' (20 V) and 'off' considering a frequency at 193 kHz. (b) Diagram showing the wave position relatively to the FBG. (c) Reflected spectrum behavior when the acoustic wave is switched 'on' and 'off' considering a frequency at 214 kHz.

4.7. Chapter Summary

A detailed description of the acousto-optic modulation in silica and polymer optical fiber was presented. The methods used to simulate the mechanical structure and the experimental assemblies are also presented in this chapter. This chapter ends up with the experimental characterization of the modulator and; numerical simulations and experimental evidences are used to verify the way acoustic waves modulates the diffraction grating spectra, giving emphasis also to results of this effect in the POF technology.

Chapter 5

Applications

5.1. Introduction

In this chapter, applications based on the concepts explored previously are proposed and their performance verified experimentally. For applications using the acousto-optic effect, which are based on the assembled silica-horn structure, they consist of a fast optical add-drop multiplexer (OADM) [C6], tunability of the FBG group delay - tunable dispersion compensator for WDM channels and optical delay lines [J14], an adjustable notch filter [J5,C8], a new method for writing complex FBG profiles [J8,J12,C27], an adjustable EDFA gain equalization filter for DWDM channels [J11,C34] and tunable mode coupler [C29]. For applications using regenerated FBGs, the fabrication of optical notch filters with fine parameter control [J9,C32] was achieved.

The design of these devices is presented and the main results summarized.

5.2. Fast Acousto-Optic Add-Drop Multiplexer

OADMs are important components in WDM systems. OADMs enable great connectivity and flexibility and play an important role in wavelength-routing techniques. Several types of fiber-optic OADMs based on different configurations such as Mach–Zehnder interferometers, grating-assisted mismatched couplers, and multiport circulators have been reported [Nykolak1997,

Kewitsch1998, Tran2001]. Most of them include Bragg gratings because of their optimum spectral characteristics for WDM. Diez et al. reported a dynamic fiber OADM that combines the properties of Bragg gratings and the acousto-optic effect in optical fibers [Diez2003]. It is a noninterferometric, nonfrequency shifting device that allows adding/dropping a certain optical channel when it is required. The prototype presented exhibits a time response of 95 μs.

Experimental assembly

The modulator itself works as an acousto-optic ADM (AO-ADM), as one can see from the schematic diagram shown in Figure 5.1. The AO-ADM is based on the use of acoustic waves to decrease the FBG reflectivity (using both flexural and longitudinal modes - see figures 4.27 and 4.34 (a)), by changing the optical path and coupling coefficients. A uniform FBG (FBG length, L = 25 mm) was inscribed using the direct writing technique through the use of a phase mask and the 248 nm UV laser.
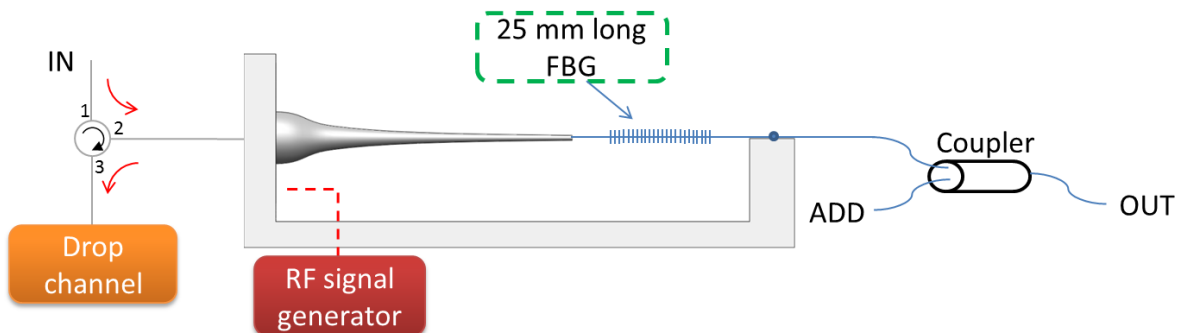
Figure 5.1 - AO-ADM schematic diagram.

"IN" and "Drop channel" correspond to port 1 and port 3 of the circulator, respectively, and "OUT" is port 2. The grating of Bragg wavelength λ_B was written at the center of a section of fiber, on which the acousto-optic effect will be implemented. When no acoustic wave is present, a carrier signal of wavelength λ_B entering by "IN" is reflected by the grating, and it goes through the circulator to "Drop channel". The carrier signal is dropped when an acoustic wave (satisfying phase-matching condition) propagates along the fiber, causing that the light bypasses the grating and propagates beyond it. In the same way, a carrier signal of wavelength λ_B entering the "OUT"

channel can be added to the main line. In the 'off' state (no acoustic wave present) the optical channel λ_B, whose bandwidth is much narrower than the grating bandwidth, is inserted through port 1, reflected by the grating and exited through port 3 (Drop channel - left hand side of the modulator in Figure 5.1). The modulator is attached to port 2. When the acoustic wave is turned 'on', the resonance condition of the grating is weakened and no coupling between the counter- and co-propagating modes takes place.

Results

The performance of the fast AO-ADM was tested using the property of suppressing the reflectivity of the FBG through longitudinal waves (for a slower device, flexural waves can be used as well). In the "off" state the ADM works dropping the channel in port 3. In this case, Figure 5.2 shows the FBG reflection spectrum and the reflected optical channel λ_B exiting "Drop channel" port with a power of P_c = 0 dBm when the acoustic wave was 'off'. The Bragg wavelength was 1543,46 nm, and the maximum reflectivity was 23 dB. . On the other hand, Figure 5.3 shows the transmission spectrum of the FBG and the P_c = -20 dBm transmitted signal (OUT port) when the acoustic wave is switched 'off'. A transmission FBG band of 14 dB is observed.
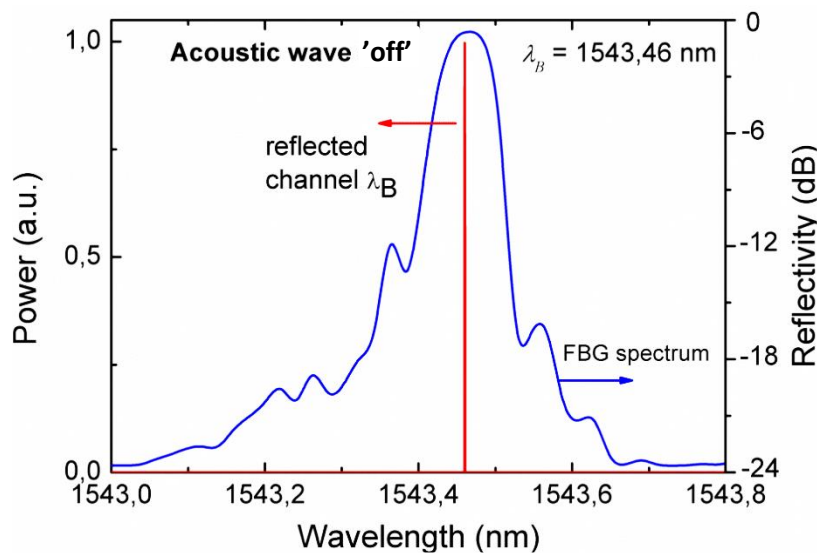
Figure 5.2 – "Drop channel" port: reflected spectrum of the FBG and reflected optical channel $\boldsymbol{\lambda_B}$ when the acoustic wave was 'off'.
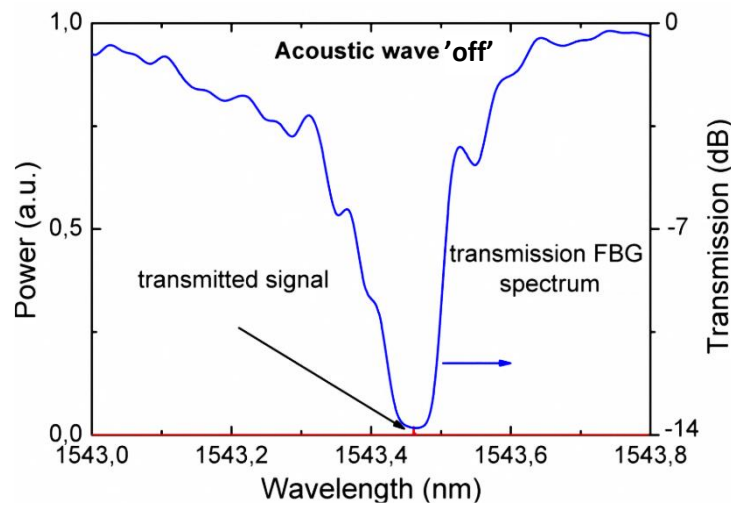
Figure 5.3 – "OUT" port: transmission spectrum of the FBG and transmitted optical channel when the acoustic wave was 'off'.
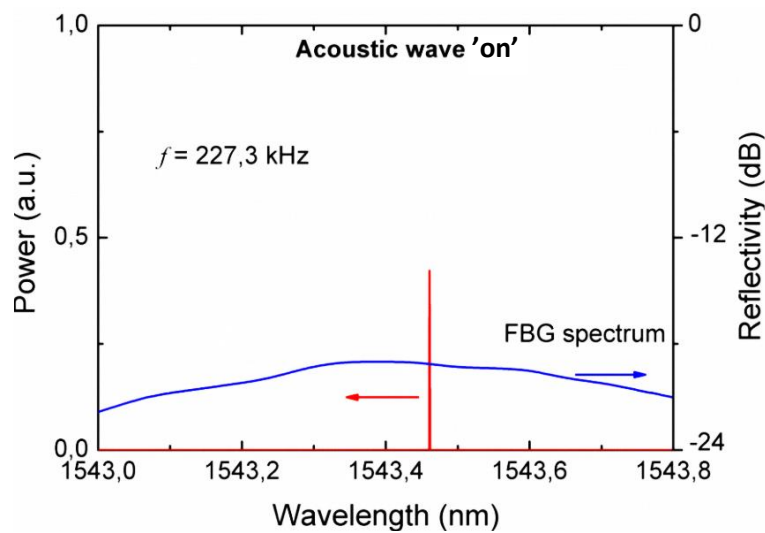
Figure 5.4 – "Drop channel" port: reflected spectrum of the FBG and the undesired signal reflected by the grating and exited through the Drop channel port when acoustic wave is switched 'on'.

Figure 5.4 shows the optical spectra in "Drop channel" port when f = 227,3 kHz acoustic wave excites the fiber. Figure 5.4 shows the corresponding decrease of the FBG reflectivity together with the undesired ~40% channel, as the suppression of the reflectivity is not 100 %. Measurements of the signal at the "Drop channel" port confirm that a significant percentage of the power remains undropped (see Figure 5.4).

Figure 5.5 shows the optical spectra in "OUT" port when acoustic wave is turned 'on'. As one can be seen, the transmission does not reach 0 dB, which means that not all the light bypasses the grating. The reasons for this are losses induced by the acousto-optic process and a significant percentage of light that is still reflected by the FBG (as shown in Figure 5.4). About 60% of the input power was detected when the acousto-optic effect was running as observed in Figure 5.5.
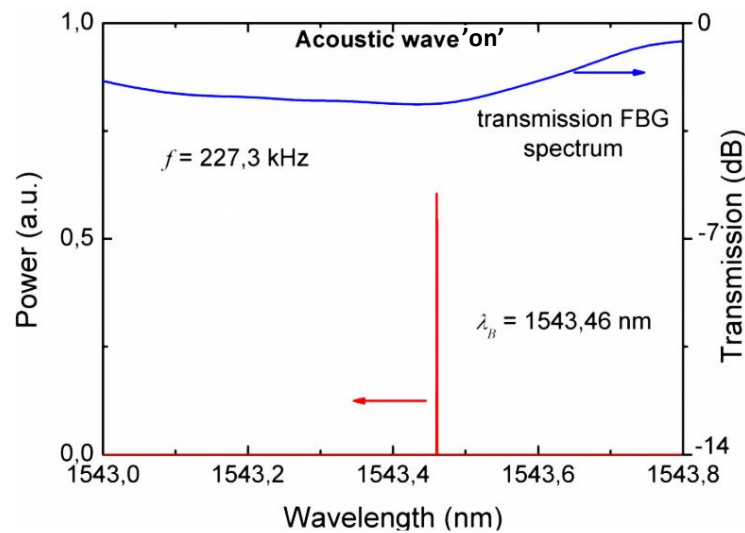
Figure 5.5 – "OUT" port: transmission spectrum of the FBG and transmitted optical channel when the acoustic wave is turned 'on'.

Response time

The response time was measured using a fast photodetector with the help of an EDFA to enhance the power of the optical channel. The photodetector is positioned at the transmission end of the grating. The acousto-optic effect took approximately t_{st} = 61 μs to change the FBG reflectivity, having the on-set of the RF frequency as the initial time reference, as shown in figure 5.6. Indeed, the switching time for practical devices is t_s = 26 μs. This result is comparable to the fastest result achieved using this modulator. The fast switching time is due to an optimal coupling of the acoustic wave between the horn and the fiber by placing both parallel to each other. Moreover, it can be substantially improved by operating at higher frequencies, as mentioned in previous chapter. Finally, the FBG reflectivity decay is strongly dependent on the PZT applied load, i.e. increasing the voltage the reflectivity can be decreased and a suppression of the reflectivity close to 100 % can be achieved.
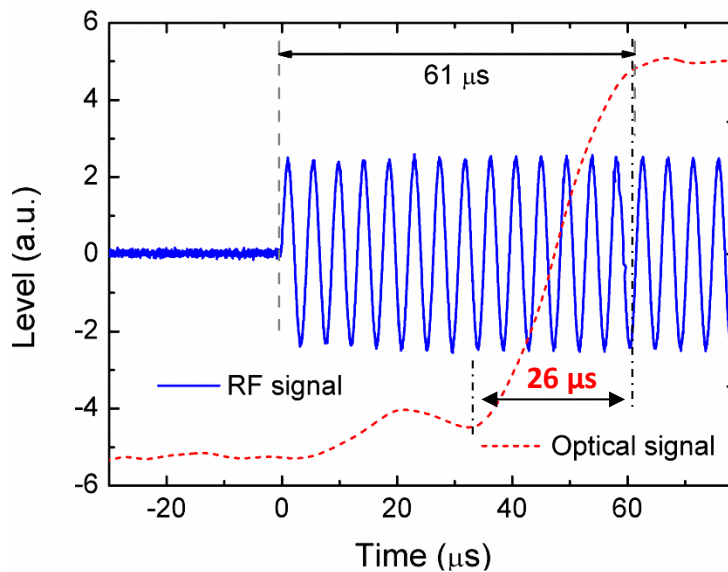
Figure 5.6 - Switching time of the AO-ADM.

5.3. Tunability of the FBG Group Delay

Currently, due to the dynamism of telecommunication links, different channels travels through different optical paths, making the dispersion characteristics differ for each case. Because of this, a dispersion compensator with reconfigurable parameters is necessary. It was noticed that, by using the acousto-optic effect, this goal can be achieved.

Optical telecommunication networks require components and/or techniques that have the capability of buffering, delaying information and dispersion compensation. In ultra-high speed transmission systems, where information is encoded in pulses, optical/electronic conversion of information is a bottleneck for increasing the data transmission rate. While information is transmitted using optical fibers in current communication networks, components for data processing must follow the development of optical networks for providing high-speed data transfer. As the data rate increases and device size decreases, it is becoming more difficult for the industry to follow Moore's law. One solution to this electronic bottleneck problem is the development of an all-optical network [Saruwatari2000]. All-optical components will eliminate the bandwidth limitation due to optical/electronic signal conversion and reduce the noise and errors due to the conversion.

In the high-bit-rate optical communication systems, chromatic dispersion (CD) compensation is necessary [Giles1997]. The CD in fiber causes a pulse broadening and degrades the transmission quality, limiting the distance a digital signal can travel before needing regeneration or compensation. Several optical and electrical tunable chromatic dispersion compensation techniques have been proposed over the last years [Li2008, Kawashima2006, Doerr2008, Lee2007]. Even though electrical dispersion compensation can be tuned close to real-time, it requires coherent detection, which is costly, complex, and power consuming. On the other hand, low cost optical dispersion compensation techniques based on chirped FBGs are very attractive [Ennser1998, Litchinitser1997]. The tuning methods presented so far, however, are based on strain [Lee2007] or temperature [Eggleton2000a] both of which are slow (in order of the milliseconds) and bulky. Recently, another technique based in an arrayed waveguide grating with air trench output waveguides and waveguide-type phased modulators based on thermo-optical effect was presented to alleviate the mentioned issues of bulkyness and slowlyness [Wang2011]. However, there is a disadvantage that higher electrical power consumption is needed for channel-by-channel tuned optical dispersion compensation fabricated in silica-on-silicon material.

On the other hand, many communication applications require fine tuning of the delay, and several proposed delay lines [Yoo2006] will not have the granularity that is necessary as the data rates increase. In addition, several delay lines have slow switching times (few milliseconds) [Pisco2006, Italia2005, Wei2009].

Thus, in a proof of principle demonstration it was shown how this effect can transform a uniform FBG into a narrow band dispersion compensator, potentially allowing WDM compensators with each channel having independent tuning. This is important for multichannel systems where different distances may be covered by different channels.

As mentioned in the previous chapter, a longitudinal acoustic wave traveling along a uniform FBG inscribed in a single-mode fiber induces a spatial sinusoidal phase modulation of the grating, which produces an effective sinusoidal chirp, moving synchronously with the acoustic wave. The phase modulation amplitude depends linearly on the acoustic wave amplitude [Russell2000].

From the phase ϕ of the amplitude reflection coefficient ρ, and since the first derivate $d\phi/d\omega$ is directly proportional to the optical frequency ω, the dispersion group delay τ (given in picoseconds) across the grating bandwidth can be determined. The dispersion coefficient D is

presented by equation (2.28), which is defined as the rate of change of τ (given by equation 2.27 – Chapter 2) with wavelength. Furthermore, with the second derivate of $d\phi/d\omega$, it can be estimated the second order dispersion coefficients.

Experimental Procedure

An AOM set is used to generate the tunable acoustic wave within the fiber and therefore a tunable strain profile. It is composed of a PZT, a 53,7 mm length silica horn and an optical fiber containing the Bragg grating. The FBG used to carry out the experiments was inscribed in a single mode photosensitive fiber using the 248 nm KrF laser. The length of the uniform FBG is $L = 25$ mm, leading to a reflection peak wavelength at $\lambda = 1544,32$ nm. The interaction length, which corresponds to the length between the base of the horn and the fixed stage where the fiber is fixed, is $L_i = 95$ mm. The AOM is similar to the Figure 4.25 however, without optical source and OSA. An ONA is used to measure the amplitude and group delay responses of the FBG, as shown in Figure 5.7.
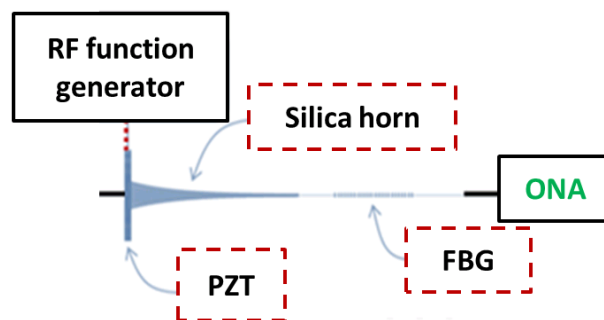
Figure 5.7 - Scheme of the experimental setup.

Results

By adjusting the resonance frequencies of the PZT, the group delay profile as well as the bandwidth can be changed. Since the group delay has specific profile (typical shape of a uniform FBG) and spectral response in terms of bandwidth does not change significantly for resonance frequencies below 117 kHz, the group delay response is not linear, so the coefficient of second order dispersion was estimated. In this work, it is noticed that for resonance frequencies above

117 kHz, a significant broadening of the spectrum due to the acousto-optic effect and, consequently, the response of the group delay becomes linear. Figures 5.8 (a), (b) and (c) show the reflection and group delay behavior when different acoustic frequencies excite the grating – at 58, 117 and 220 kHz, respectively. The resultant group delay is measured and the first and second order dispersion coefficients are estimated. When the acoustic frequency is set at 58 kHz, the second order coefficient is measured as 2252 ps/nm^2 while for an acoustic excitation at 117 and 220 kHz, the measured first order dispersion slope is -287 and -857 ps/nm, respectively, considering 10 V PZT load. Note that, these resonance frequencies are low enough to keep the system in the flexural regime. Table 5.1 shows the behavior for the variation of first order dispersion slope versus the frequency of the acoustic excitation, considering in all cases 10 V PZT load. Table 5.2 shows the behavior for the variation of the second order coefficients as a function of the resonance frequency. It shows that each resonance frequency causes a change in its spectrum, both in spectral shaping and consequently the group delay, obtaining different dispersion values. It shall be noted that a similar behavior is observed for acoustic waves generated by other resonances frequencies. However, the magnitude of the observed effect is lower than those achieved but other values of dispersion coefficients (first and second order) can be achieved if different PZT (with different resonance frequencies) was used or by setting different PZT load values [Marques2011].

Table 5.1 - Behavior for the variation of first order dispersion slope as function of the resonance frequency of the flexural acoustic excitation

Resonance Frequency (kHz)	First Order Dispersion Slope (ps/nm)
117	-287
185	-440
220	-857
407	-1230

Table 5.2 - Behavior for the variation of second order coefficients versus the resonance frequency

Resonance Frequency (kHz)	Second Order Dispersion coefficients (ps/nm^2)
46	2723
58	2252
92	1687
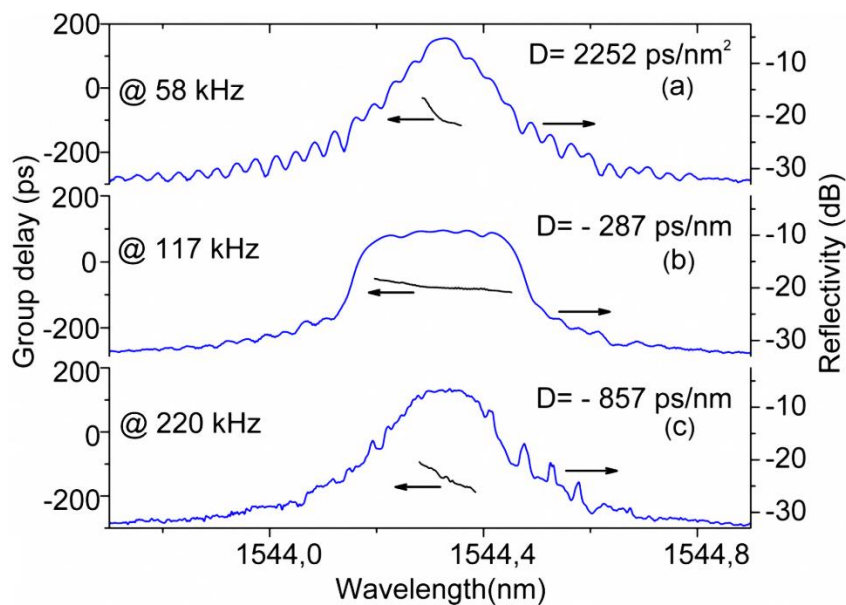
Figure 5.8 - FBG spectrum and group delay behavior when the acoustic wave is set at (a) 58 kHz, (b) at 117 kHz, and (c) at 220 kHz.

For longitudinal regime (for higher frequencies), compression and rarefaction zones are generated, so creating additional bands to appear on both sides of the grating reflection spectrum as is shown in the Figures 5.9 (a) and (b). From Figure 5.9 (a) and (b), one can conclude that the group delay of the sidebands can be controlled by adjusting the PZT load.
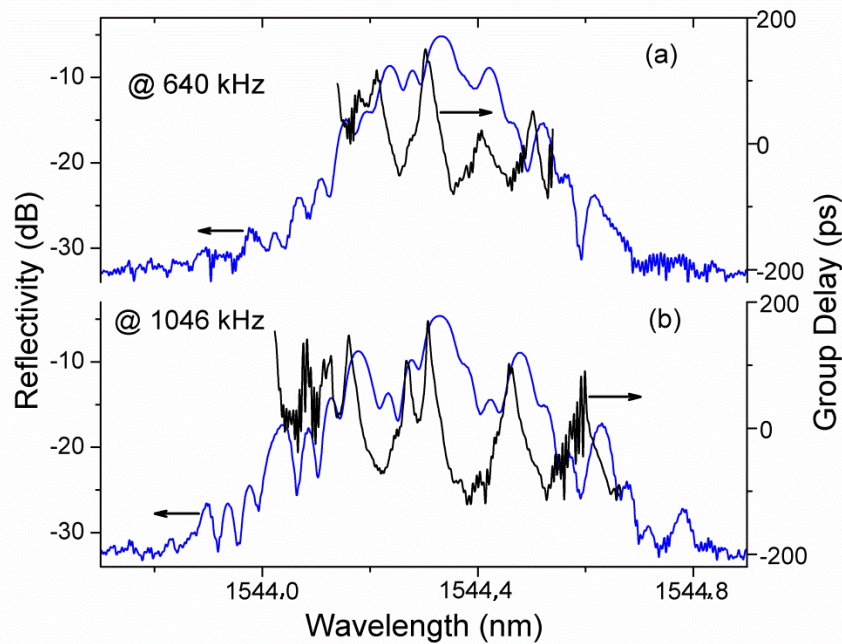
Figure 5.9 - FBG spectrum and group delay behavior when the acoustic wave is set at, (a) 640 kHz, and (b) 1046 kHz.

On the other hand, adjusting the amplitude of the acoustic wave, the group delay profile as well as the bandwidth can also be changed. Figure 5.10 (a) shows the group delay behavior when no acoustic wave excites the FBG and with 117 kHz acoustic frequency is applied to the PZT, with different voltages, i.e., from V_{PZT} = 5, 6, 8 and 10 V (Figures 5.10 (b), (c), (d) and (e), respectively). The results show a good agreement between simulation and experimental data. It is clear from these results that the dispersion can be tuned by adjusting the applied piezo voltage. The useful bandwidth, over which the slope presents a linear behavior (from V_{PZT} = 6 to 10 V) is $\Delta\lambda \sim 0,21$ nm.

Since the group delay at 117 kHz acoustic excitation presents the most linear behavior (see Figure 5.10) for the range between 1544,25 and 1544,46 nm (0,21 nm), this frequency was selected for more detailed analysis. Hence, this linearity can be controlled by varying the PZT load. At 117 kHz excitation, the dispersion can be controlled from -546 ps/nm (at V_{PZT} = 6 V) to -132 ps/nm (V_{PZT} = 10 V), as shown in Figure 5.10 (f). In this case, for PZT loads below 6 V, the group delay follows a higher order polynomial behavior and it is not considered for measurements of dispersion. Figure 5.10 (f) shows a comparison of simulated and experimental results for dispersion when the acoustic wave excites the fiber at 117 kHz, as a function of the PZT load. A

good agreement between theory and experimental data is achieved. Thus, by changing the PZT load, it is possible to control dynamically the dispersion.
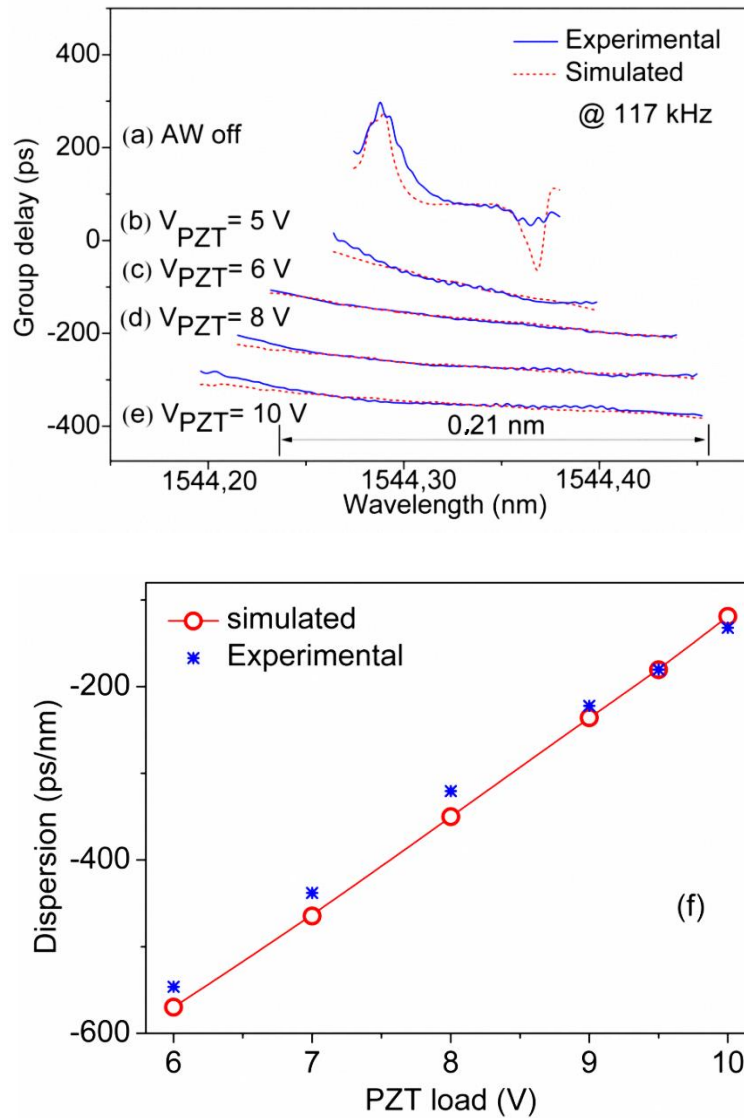
Figure 5.10 - Group delay simulation and experimental behavior when (a) no acoustic wave excites the FBG and when the acoustic wave is set at 117 kHz, driven by (b), V$_{PZT}$ = 5 V , (c) 6 V, (d) 8 V and (e) 10 V PZT load. (f) Dispersion simulation and experimental behavior as function of PZT load.

The group delay ripple (GDR) coefficient (t_{GDR}) is caused by weak reflections occurring at the edges and along the grating and it is a critical parameter if considering a communication link. The GDR coefficient is measured as the peak-to-peak time variation of the group delay (in this case, the values were obtained for excitation at 117 kHz, for PZT load varying from 6 to 10 V). Results show

values with tuning from ±11 ps to ±6 ps as shown in Figure 5.11 (a). Figure 5.11 (b) shows in details how the GDR can be estimated when the PZT load is set at 10 V. The acoustically induced strain wave reduces the GDR, which can be explained as a "dc" apodization of the grating, similar to that reported for "dc" apodization with a tailored UV writing profile [Ashton2004]. For instance, in the cases of the Figures 5.9 (a) and (b) (longitudinal regime) the ripple level is similar to the value achieved at 117 kHz (between ±6 ps and ±9 ps). Acceptable values for commercial applications vary from t_{GDR} = ±2 to ±10 ps, however, the average of GDR found in datasheet of commercial equipment is t_{GDR} = ±5 ps.
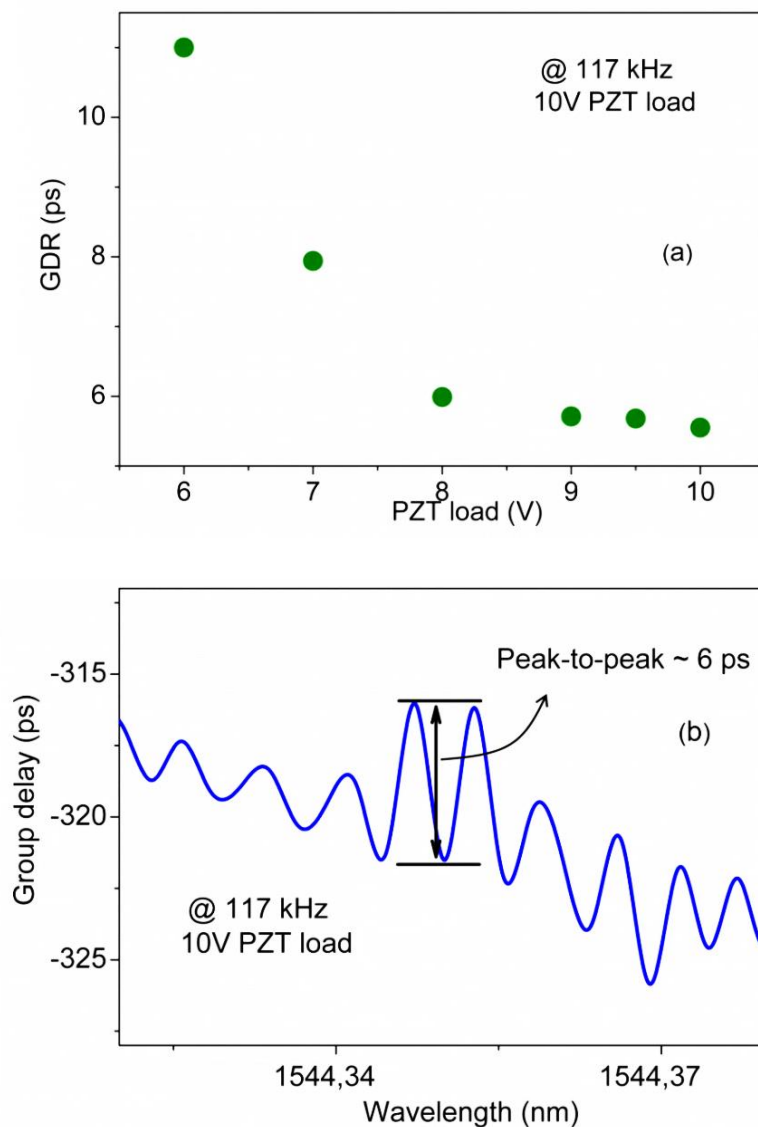
Figure 5.11 - (a) GDR behavior when the PZT load is set from 6 V to 10 V. (b) GDR spectrum when the PZT load is set at 10 V.

The time response of the device was also investigated and measured. The results displayed in Figure 5.12. In order to verify the device time response an experimental setup with a photodetector is used, whose configuration is described elsewhere [9]. When the acoustic wave is 'off', no signal in the photodetector is measured, whereas when the acoustic wave is 'on', the acoustic signal excites the grating and the optical signal is transmitted, making the photodetector experience a high optical level. The acoustic effect takes approximately 42 µs to change the gratings properties. Indeed, the time that can be considered for practical applications, in this case, is t_s = 17 µs. Taking the interaction length as 95 mm, the measured acoustic speed in the fiber is 5588 m/s, which is comparable with values found in the literature [Elmore1985]. As already mentioned, this fast behavior is achieved basically due to a good coupling of the acoustic wave between the horn and the fiber, which reduces the mechanical damping. This configuration can be applied in a series of devices where fast dynamic control is required.
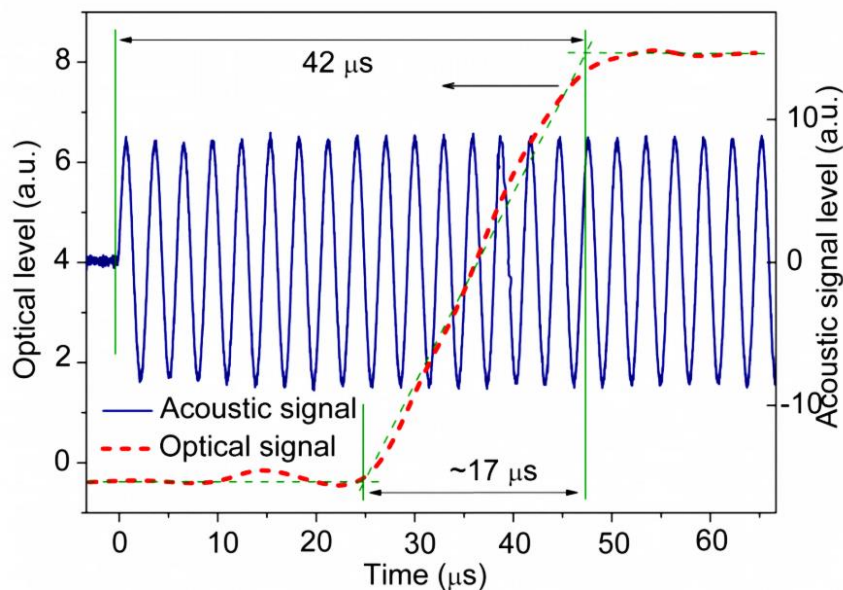
Figure 5.12 - The time response of the device. When the acoustic wave is ON, it takes approximately 17 µs to change the optical level experienced by the photodetector (this is measured as the 5-95% confidence level of the rise).

Notably, the response time of 17 µs is faster than existing grating tuning techniques. By ensuring the induced strain profile is positioned properly over the grating length, an effective "dc apodization" is achieved. If the broadening of the bandwidth over which the device work is equal or less than the channels bandwidth itself (as in coarse WDM) then this technique opens up an opportunity for the dispersion compensation of individual channels. In very complex systems where different channels travel different lengths and experience differing group delays and dispersion, this unique form of active channel control turns up to be an important solution. Further, it can be conceivably used to encode the channel with another parameter, potentially enabling much broader channel integration on coarse WDM systems. Finally, this technology can be applied to tune much broader band devices including existing chirped FBGs compensators to enhance their tunability and performance as well as apply it for optical delay lines.

5.4. Adjustable Notch Filter

The need to tailor the transmission FBG spectrum to obtain very narrow stop bands has led to the introduction of a phase shift across the grating. The principle of phase shifts was first demonstrated in periodic structures made from semiconductor materials [Alferness1986]. Techniques were then developed to produce phase-shifts in fiber gratings [Canning1994, Kashyap1978]. More recently, the control of phase shifts by acoustic waves has gained attention as a means of controlling the Q-switching in DFB fiber lasers [Delgado2006, Delpado2007]. A detailed study on the characteristics of uniform PSFBG under the excitation of acoustic waves is presented. Weak PSFBGs are used to ensure sufficient resolution of the phase shift so that the phenomenological changes are readily observed on an OSA without the use of other higher resolution methods required to properly characterize strong phase shifted gratings. It is also demonstrated that for higher acoustic frequencies, when longitudinal waves are excited, the sampling modulation of the grating is achieved with the generation of multiple peaks.

Experimental assembly

The L = 50 mm long ϕ = π PSFBG used was inscribed in standard single mode photosensitive fiber with the phase mask technique, using the 248 nm KrF laser. The same experimental setup shown in Figure 5.7 is used to characterize the phase-shifted grating.

Results

Figure 5.13 shows a comparison of simulated and experimental results when (a) no acoustic wave is applied in the device and when the wave excites the fiber at (b) 113 and at (c) 621 kHz. The results show a good agreement between simulation and experimental data. For f = 621 kHz (see Figure 5.13 (c)), an excitation is applied to the grating creating side lobes on the PSFBG spectrum. This is an example of the excitation with a longitudinal mode. However, when a flexural acoustic mode acts on the fiber, the effect is a reduction of the reflectivity of the grating, and, consequently, the reduction of the phase-shift strength (Figure 5.13 (b)).
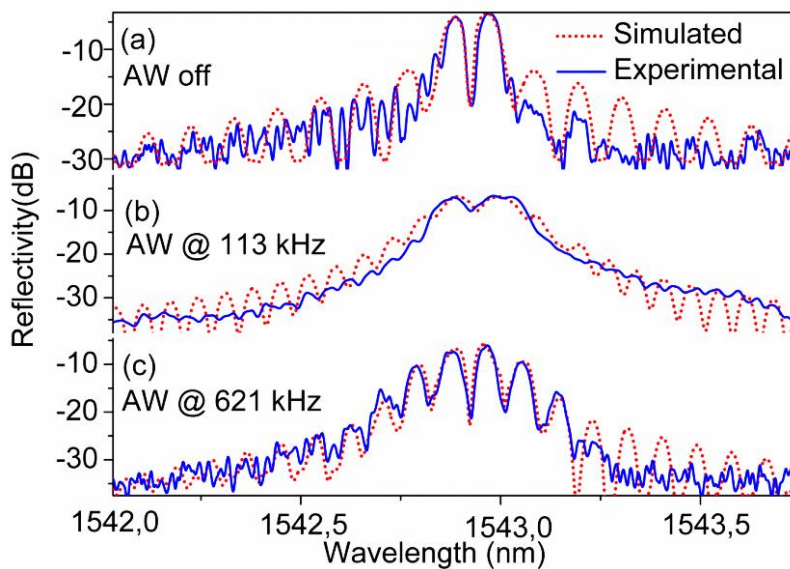
Figure 5.13 - Simulated (dotted lines) and experimental (solid lines) reflected spectrum of a π phase shifted FBG (a) at rest, and when (b) 113 and (c) 621 kHz acoustic wave, at constant PZT load excite the fiber.

Figure 5.14 (a) and (b) show, respectively, the reflection and transmission spectra of the PSFBG when the PZT load varies for an acoustic excitation at 113 kHz. Figure 5.14 (a) shows that the acoustic excitation at 113 kHz leads to a broadening of the PSFBG, which can be tuned with increasing PZT load. When the load is set at 5 V, the notch is totally suppressed, thus values above that are not considered. Therefore, as the load is increased the notch depth decreases as shown in figure 5.14 (a). In the same way, Figure 5.14 (b) shows the transmission spectra when the PZT

load is varied for the same frequency. It is also noticed that the left and right rejection bands depth decrease when the PZT load increases. The flexural acoustic wave leads to the destruction of the grating phase matching condition, turning the grating weaker. In summary, this device acts as a tunable rejection band as well as a narrow notch filter, when used in transmission and reflection, respectively.
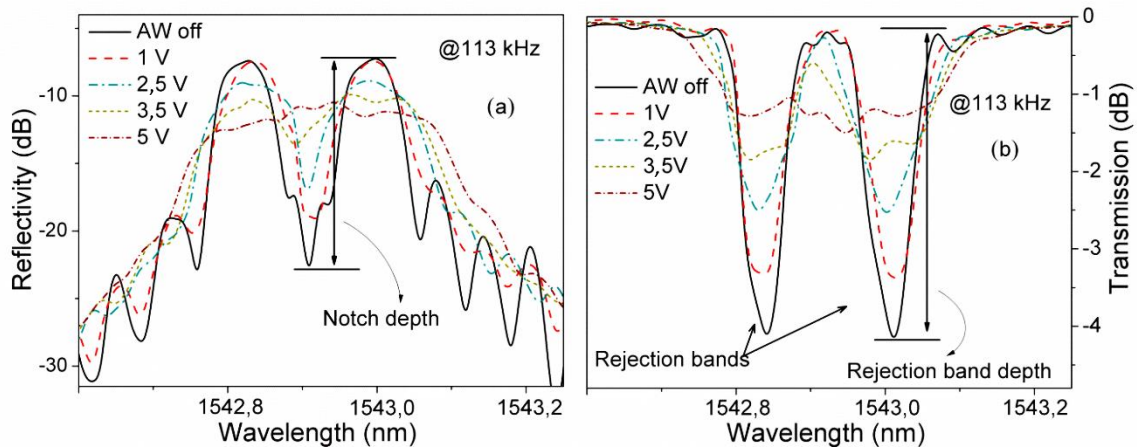
Figure 5.14 - PSFBG (a) reflection and (b) transmission spectra behavior when the PZT load varies for an acoustic excitation at 113 kHz.

On the other hand, it is possible to control the 3-dB bandwidth of left and right peaks by adjusting the applied piezo voltage. As the PZT load is increased the side lobes (left and right peak) bandwidth increase as observed in Figure 5.14 (a). This particular behavior is detailed in Figure 5.15. The results show an excellent agreement between left and right peak. In the same way, Figure 5.15 shows also a fine control of the 3-dB bandwidth of left and right rejection bands that is achieved by varying the PZT load. In this case, the results are presented for piezo loads up to 2,5 V, the maximum measurable 3-dB bandwidth value for the rejection bands. The results show a good agreement between both rejection bands, showing that the effect is symmetrically observed on both bands.

The notch depth and the rejection band depth can also be changed. It is noticed that the notch depth parameter is linearly dependent on the acoustic intensity for a particular frequency, in this case 113 kHz, as shown in Figure 5.16 (a). Increasing the PZT load adjusts the notch depth from 14 to 0 dB. For higher loads (above 5V), the notch is completely suppressed. Figure 5.16 (a) shows also a comparison of simulated and experimental results, showing a good agreement data. Figure

5.16 (b) shows the simulated and experimental behavior of the rejection band depth and a fine control of the rejection band depth are achieved by varying the PZT load when the wave excites the fiber with the same acoustic frequency.
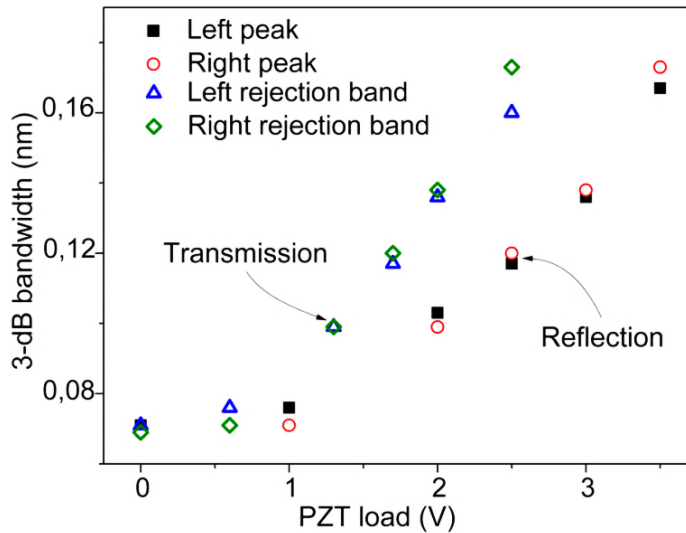
Figure 5.15 - 3-dB bandwidth behavior of left and right peak (reflection) of the PSFBG depending on the PZT load at 113 kHz and 3-dB bandwidth response for left and right rejection band (transmission) of the grating by varying the PZT load for the same frequency.
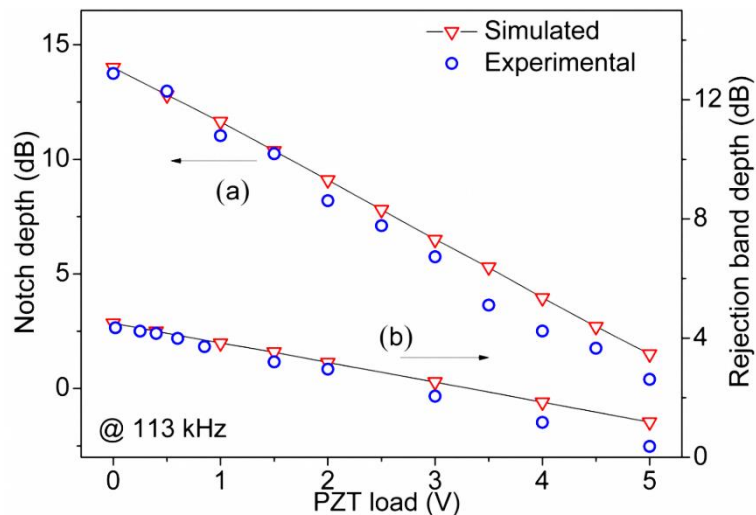
Figure 5.16 - (a) Notch depth (reflection) simulation and experimental behavior as function of PZT load up to 5V. (b) Linear variation of the rejection band depth (transmission) as function of the PZT load up to 5V (when the rejection band is totally suppressed).

5.5. Acousto-Optic Method for Writing Complex FBG Profiles

The inscription of FBGs using the method of direct writing through a phase mask has been employed and to allow the efficient inscription of uniform and non-uniform Bragg gratings [Hill1997]. This technique has made possible the development of a vast range of telecommunication and sensing devices that are based on, for example, sampled gratings [Eggleton1994] and phase-shifted gratings [Canning1994]. The range of applications of such grating structures can be extended through the use of the acousto-optic effect. However, the modulation caused by this effect disappears in the absence of the acoustic wave. Thus, the excitation control of an acoustic flexural wave during the inscription of permanent Bragg grating structures is investigated. This mechanism was first demonstrated for the inscription of permanent sampled gratings using longitudinal acoustic waves [Oliveira2010b]. Here, one is expanded to the case where flexural waves are excited leading to dithering of the fiber.

Experimental assembly

For inscription of acoustic induced gratings, the writing technique through the phase mask was modified by placing the AOM in positioning rigs and aligning it within the interferometer setup. Figure 5.17 shows a diagram of the setup containing the AOM.
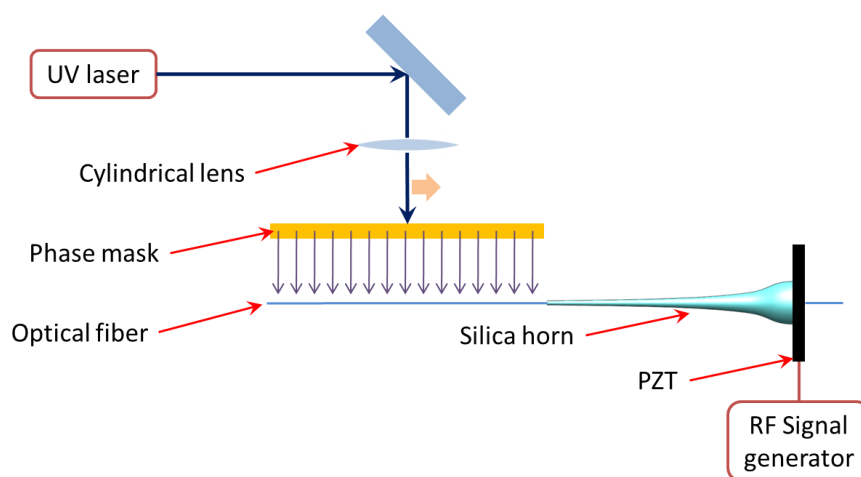
Figure 5.17 – FBG writing setup showing the modulator positioned in the assembly.

Depending on the nature of the acoustic wave (longitudinal or flexural) different properties can be adjusted. Longitudinal waves generate a periodic strain in the fiber, which gives rise to the creation of side bands in the grating spectrum (called sampled gratings [Eggleton1994], due to its non-periodic grating planes profile. The period of the generated side bands is strongly dependent on the acoustic frequency applied to the PZT, and its amplitude, on the load (PZT voltage) of the RF signal. On the other hand, flexural waves can be used to create resonant cavities, for instance, in DFB, due to the insertion of a phase-shift in the FBG spectrum [Kringlebotn1994], and in Fabry-Pérot interferometers based on Bragg mirrors [Wan2002]. Flexural waves can be used to switch the grating imprinting course while the laser beam is swept over the fiber. In this case, the light from the UV source is scattered and no light reaches the core of the fiber.

Thus, this new technique leads to fabrication of special gratings such as sampled gratings [Oliveira2010b], leading to profiles that form spectral combs, resonant cavities and phase-shifted gratings.

Results

The possibility of modulating the fiber during the writing process leads to other special gratings, depending on the nature of the acoustic excitation. In recent work, the discussion about the excitation of longitudinal waves, giving rise to the generation of permanent sampled gratings, showed the feasibility of the technique [Oliveira2010b]. As shown in chapter 4, section 4.2.1, Figure 4.5 (c) shows a diagram that helps to explain the resultant modulated periodic index modulation of the grating planes. The period of the sampled gratings is strongly dependent on the longitudinal acoustic wavelength. After inscription, the resultant FBG modulation planes profile is no-uniform, indeed, is modulated by the acoustic wave.

In the same way, by means of controlling the flexural excitation, it is possible to inscribe special types of gratings. Basically, the idea is to use the acoustic wave to switch the writing process, whose mechanism is based on the scattering of the light and misalignment of the fiber core. The diagram shown in figure 5.18 exemplifies the expected effect. When the fiber is at rest, the UV light induces a refractive index change in the core (Figure 5.18 (a)), whereas when the fiber is flexurally excited (Figure 5.18 (b)), there is no photoinduced changes because the core in relation to the interferometric pattern makes the light scatter, avoiding the UV light to reach the fiber

core, only to the stationary points of the fiber (nodes).. This effect can be used to create interferometric cavities, formed by a comb of gratings (Bragg grating mirrors), intrinsic fiber Fabry-Pérot interferometers and phase-shifted FBGs.
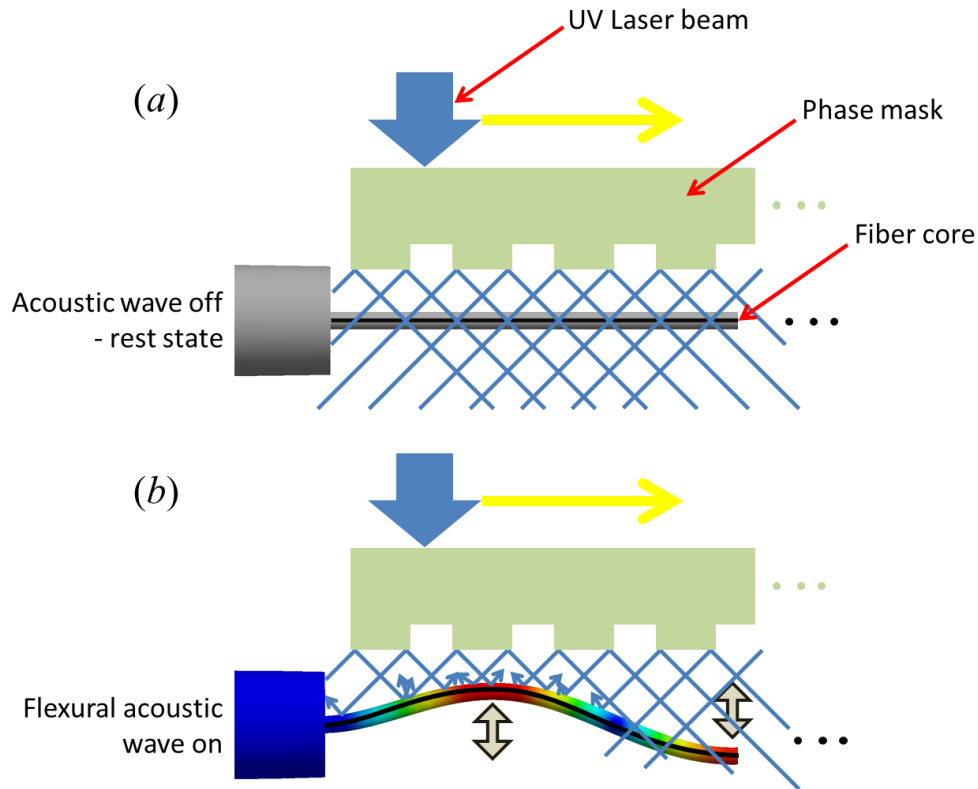
Figure 5.18 - Diagram of the photoinduced refractive index change through the phase mask technique (a) when the fiber is at rest and (b) when a flexural acoustic wave excites the fiber.

Figure 5.21 shows the FBG spectrum inscribed using the same setup of Figure 5.17, considering the excitation of a flexural wave during the sweep of the UV beam over the fiber. In this case, the acoustic wave is not constantly 'on', but periodically turned 'on' and 'off' for a certain period of time, t_b (using the burst function of the RF signal generator). Considering a RF signal with 100 cycles, for different frequencies, the burst mode of the RF generator creates a signal that switches the acoustic excitation, for a certain period of time, 'on' and 'off'. The schematic that represents the RF excitation time is shown in Figure 5.19, where the t_b corresponds to the interval between bursts of 100 cycles, since the RF frequency at f = 40,9 kHz is considered. T_{bt} is the duration of the burst.
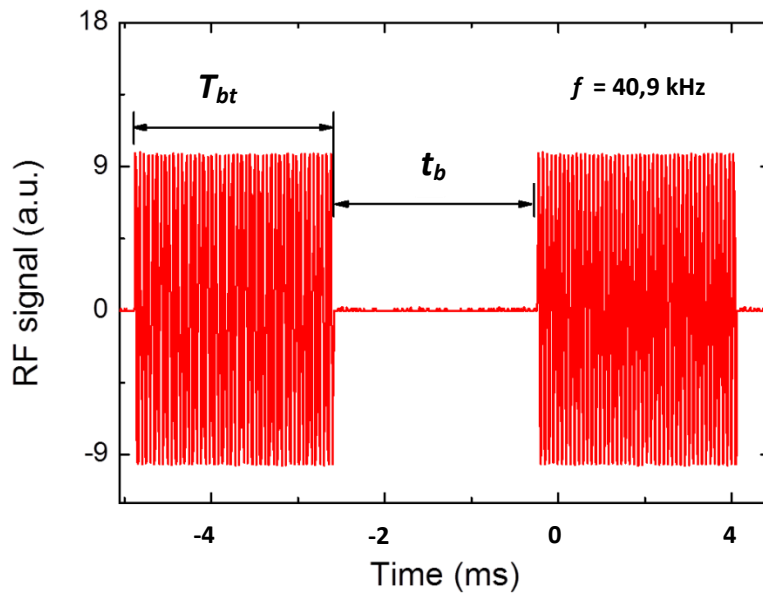
Figure 5.19 - Burst mode excitation of the PZT. The burst time, t_b, corresponds to the time between bursts of 100 cycles.

When the acoustic wave is 'on', no grating is inscribed in the fiber. By using the frequency generator in the burst mode, it is possible to set the distance between the gratings, which can be controlled over the acoustic frequency and the burst time. 100 cycles of the acoustic wave were first chosen randomly. The sweep time of the UV beam over the phase mask is also critical. Therefore, a good control of these parameters allows the generation of special fiber gratings. Figure 5.20 shows a schematic of the technique adopted for writing Fabry-Pérot interferometers using Bragg gratings mirrors.
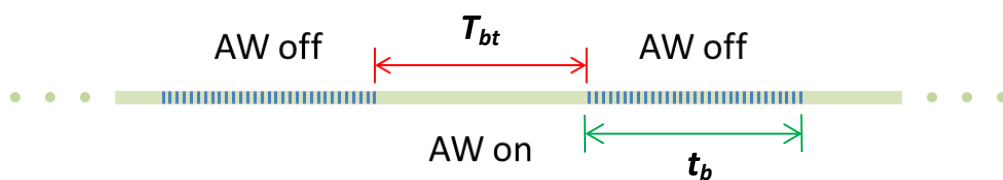
Figure 5.20 - Schematic diagram of the Fabry-Pérot interferometers writing process under excitation of flexural acoustic waves.

Figure 5.21 shows the fabricated Fabry-Pérot interferometer considering different frequencies applied on the modulator. The solid curve represents a standard Fabry-Pérot interferometer formed by six gratings of approximately $L \approx 4.5$ mm uniformly separated, obtained by sweeping the modulated UV beam over the phase mask length ($l_{pm} = 50$ mm). The sweep velocity (v_{sc}) was set at $v_{sc} = 10$ mm/min. Depending on the acoustic frequency, the number of Bragg mirrors of each segment can be set. When $f = 306$ kHz, the achieved supergrating corresponds to approximately four Bragg mirrors on each section inscribed in the 5 cm long piece of fiber, which means that a four planes Fabry-Pérot interferometer is generated, whereas for $f = 75$ kHz, the structure corresponds to the generation of two planes, i.e. two Bragg mirrors on each section. This proves it can be used to inscribe customized Fabry-Pérot interferometers directly.
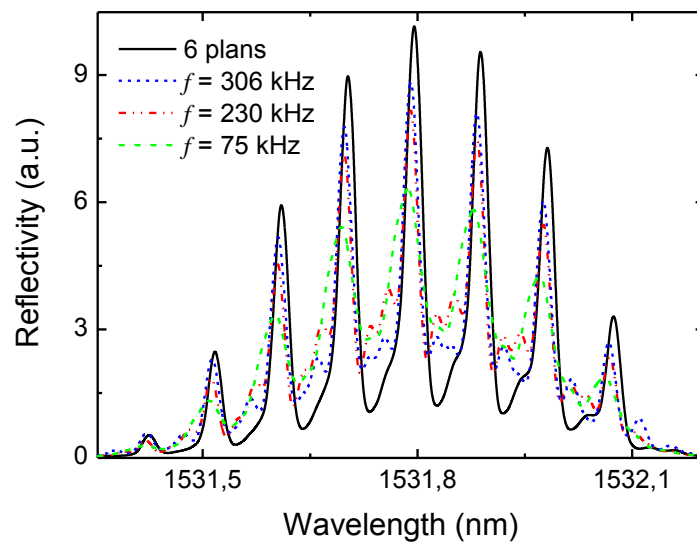
Figure 5.21 - Fabry-Pérot interferometers inscribed using a direct UV beam modulation methodology (solid curve) and by means of acoustic waves.

On the other hand, if the burst time is tuned, keeping the frequency constant, the modulation conditions are changed and different configuration of resonant cavities can be obtained. For example, the number of planes and length of the Bragg mirrors is related to the period of the modulation. Figure 5.22 shows the resultant FBG spectrum when $f = 113$ kHz acoustic frequency excites the PZT using the burst function, setting the modulation period at $t_b = 0{,}5$ s, 1 s, 2 s, 3s and 4 s, giving rise to sampled period, $\Lambda_{sampled}$, between 83 and 600 µm. This gives rise to a peak separation of $\Delta\lambda = 1{,}17$, $0{,}57$, $0{,}29$, $0{,}18$, and $0{,}14$ nm, respectively, consistent with that

estimated using the standard sampled grating equation described in [Jayaraman1993]. Increasing the period, the side lobes period decreases which is expected from the Fourier transform of the superperiod [Jayaraman1993]. Note that the T_{bt} must be $T_{bt} < 4,5$ s for this frequency.
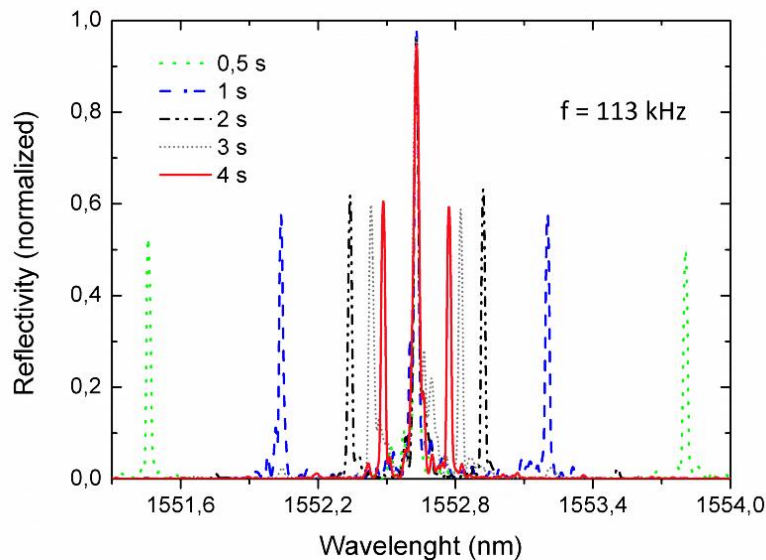
Figure 5.22 - Permanent resonant cavities achieved through the acousto-optic modulated FBG writing process methodology.

5.6. Acoustic Bursts for Customized Tapered Fiber Bragg Structures

In the previous section, the effect of applying an acoustic flexural wave longitudinally to an optical fiber during the process of Bragg grating inscription using the direct writing method through a phase mask was demonstrated and showed that it can be used to obtain precise control over the grating parameters in order to achieve sampled gratings and Fabry-Pérot cavities. However, regarding the generation of cavities for phase-shift, only preliminary result had been achieved. Basically, it was investigated how to control the PSFBG inscription process, in order to add customized phase-shifts (such as π/2, π, 3 π /2, 4 π/5) on Bragg structures by means of excitation of specific acoustic flexural wave excitation in burst mode. The experimental results show a good agreement with simulation. By means of the control of the burst time and duration, cavities within the Bragg structure are inserted, due to the fact that when the fiber is acoustically excited

with flexural waves no photo-induced index change is achieved in the core of the fiber (Figure 5.18), similar to the case when the phase mask is dithered instead [Canning2005]. Thus, it is avoided the need of using an optical switch or a beam modulator.

Experimental setup

The experimental setup shown in Figure 5.23 (a) is similar to the one used in previous section, where the modified method of direct writing through a phase mask was employed to inscribe the gratings. The tapered optical fiber (TOF) was fed-through a silica horn which was attached to a PZT, in order to make possible the excitation of the optical fiber and consequently, switch the writing process along the fiber so creating defects within the grating structure [Oliveira2010b].

Since the tapering of optical fibers can be used to increase the coupling of acoustic waves within the optical fiber, TOF samples were used to enhance the expected effects. The diameter of the waist region of the tapered fiber is 40 μm. More details about TOF production can be found in [Niehus2010].

After the production of tapers, the fiber samples were subjected to a hydrogenation process that occurred at a pressure of 150 bars during two weeks, in order to enhance its photosensitivity. The inscription was carried out using UV light from a KrF excimer laser @ 248 nm. A cylindrical lens with f_c = 20 mm was used to focus the laser beam on the optical fiber in order to increase the power density into the core of the fiber. The pulse energy was E_{pulse} = 3 mJ and repetition rate of 500 Hz. The laser was scanned along a phase mask with a period of Λ_{pm} = 1,073×10^3 nm. The scanning of the laser beam is made by a translation stage with a velocity v_{sc} = 0,5 mm/s and 20 mm FBGs were produced, with Bragg wavelength at λ_B ~ 1553 nm.

For demonstration purposes, phase shifted Bragg gratings with ϕ = π, ϕ= π / 2 and ϕ = 3π / 2, where ϕ is the phase-shift coefficient, were inscribed. In order to do so, the position of the defects inserted in the Bragg structures have to be set to be respectively at *l = L / 2, l = L / 4* and *l = 3L / 4*, as shown in Figure 5.23 (b), (c) and (d). It can be set using the burst function of an arbitrary RF signal generator. *l* is the defect position inserted in the Bragg grating and *L* is the Bragg grating length. The duration of the burst depends on the desired length of the defect. In this case, the burst duration was chosen to be T_{bt} = 50 ms, which results on l_b = 25 μm. T_{bt} and l_b

are the burst time and cavity length respectively. The acoustic frequency was set at f = 87 kHz (which is one of the flexural acoustic resonance of the set PZT-silica horn-fiber). When the burst is set on continuous mode, the induced phase-shift is ϕ = 2π.
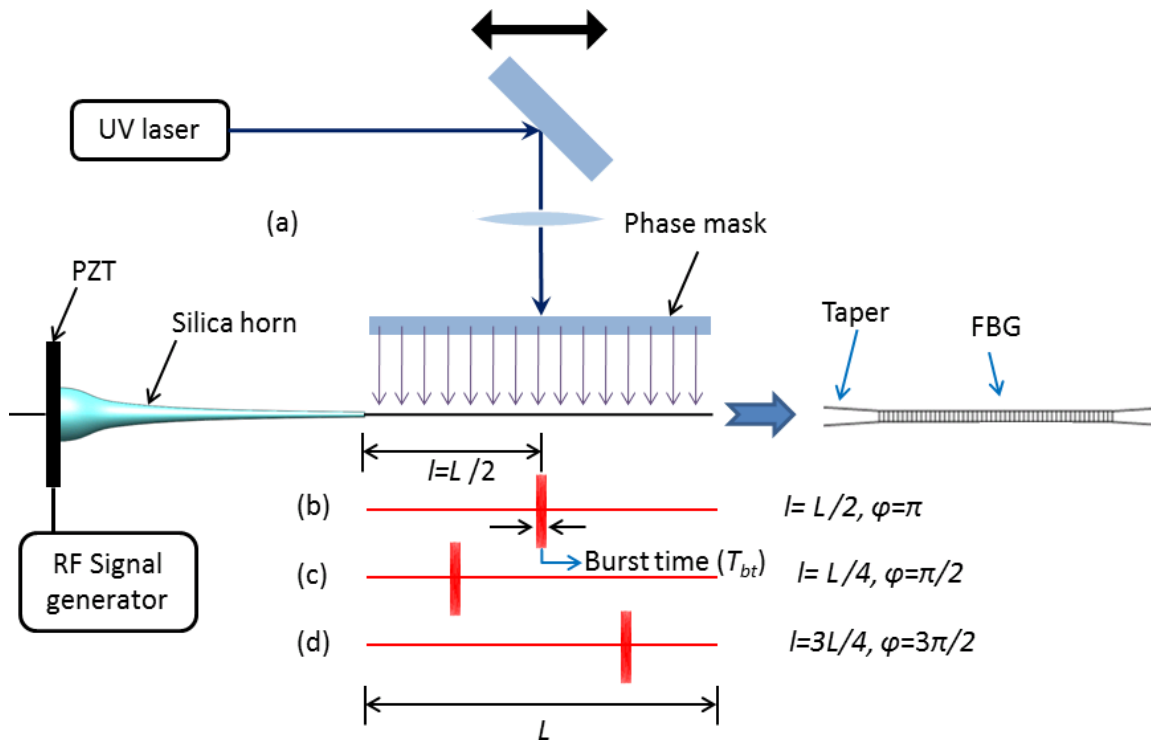
Figure 5.23 – (a) Schematic of the grating writing setup. (b)-(d) Time diagram for the burst characteristics.

Results

The introduction of complex phase shifts has been proposed in several contexts, and detailed analysis of complex transversal time based Feynman paths have been successfully applied to a simple Fabry-Pérot cavity [Lee2000]. The introduction of phase-shifts in different positions will affect different wavelengths to different degrees [Ghiringghelli2001]. If random phase errors distributions are inserted, the longitudinal dependence is averaged and all the wavelengths will be affected in the same way, obtaining a resulted spectral response.

Figure 5.24 shows the reflected spectrum when no phase shift is introduced in the Bragg grating, showing a good agreement with simulated data.

Figure 5.24 - Simulated (dotted lines) and experimental (solid lines) reflected spectra when no defect is introduced in the Bragg structure.

On the other hand, Figure 5.25 shows the reflected spectrum resulted from the defect introduced in the Bragg structure, considering the application of an acoustic burst of 50 ms in the central region of the tapered fiber length (20 mm) during the scanning of the UV-beam (see wave configuration showed in Figure 5.23 (b)), so creating a π phase-shifted. The 3-dB bandwidth of the narrow transmission band of the π-PSFBG was measured to be ~ 47 pm, showing a good agreement with simulated result (~ 44 pm). The result also presents a maximum notch depth around 22 dB and, if the acoustic wave is post turned 'on', after the inscription process, the phase-shift can be suppressed, as shown in Figure 5.26, depending on the acoustic PZT load (by adjusting the voltage applied on the PZT). It shall be noted that the inscription of phase shifts by this technique in conventional (not tapered) fibers is equal to the presented; however the notch depth is not so deep, for instance. Through the use of the combined finite element and transfer matrix methods [Marques2013], the resultant grating spectrum, when a defect is inserted along the *z*-axis in the FBG, was calculated numerically and compared with the experimental data (Figure 5.25), showing a good agreement between them. The flexural wave was set at frequency of *f* = 87 kHz.
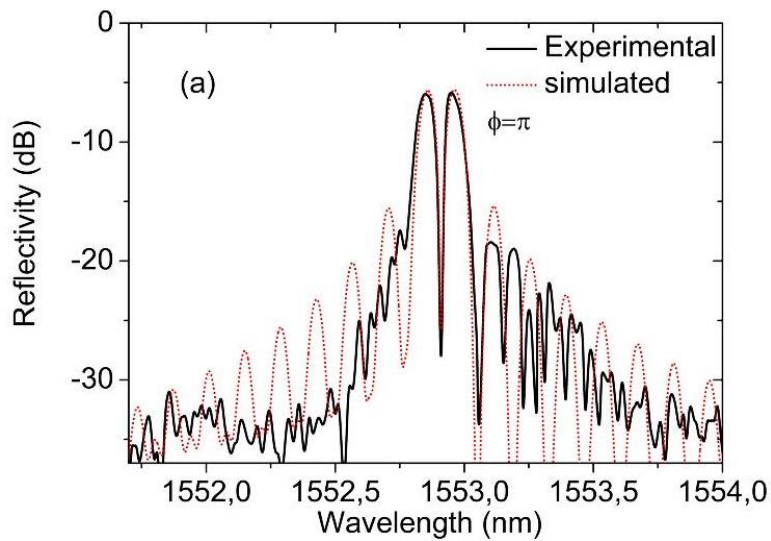
Figure 5.25 - Simulated (dotted lines) and experimental (solid lines) reflected spectra when a defect is introduced in the Bragg structure creating a phase-shift of φ= π.
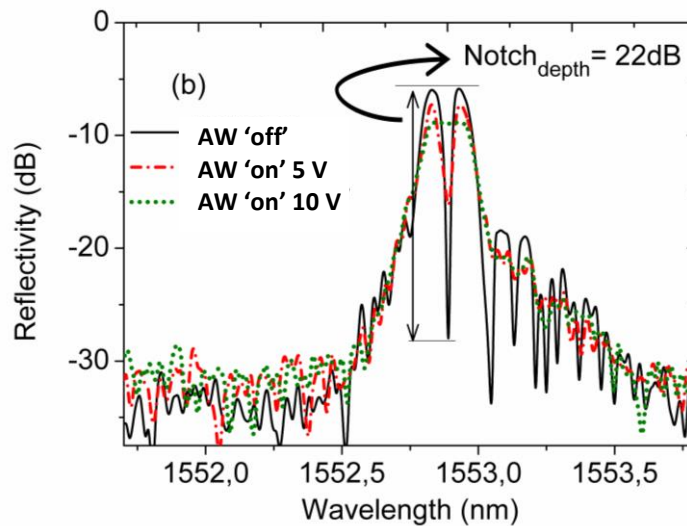
Figure 5.26 - After the inscription process, when the acoustic wave is turned on, the phase-shift can be suppressed, depending on the PZT loads. The FBGs were inscribed by fixing the acoustic frequency (f = 87 kHz).

In the same way, Figure 5.27 (a) and (b) shows the resultant reflection spectrum when the defect is inserted in the structure following the acoustic wave burst characteristics shown in Figures 5.23 (c) and (d) respectively – phase shifts of ϕ = π / 2 and ϕ= 3π / 2, in that order.
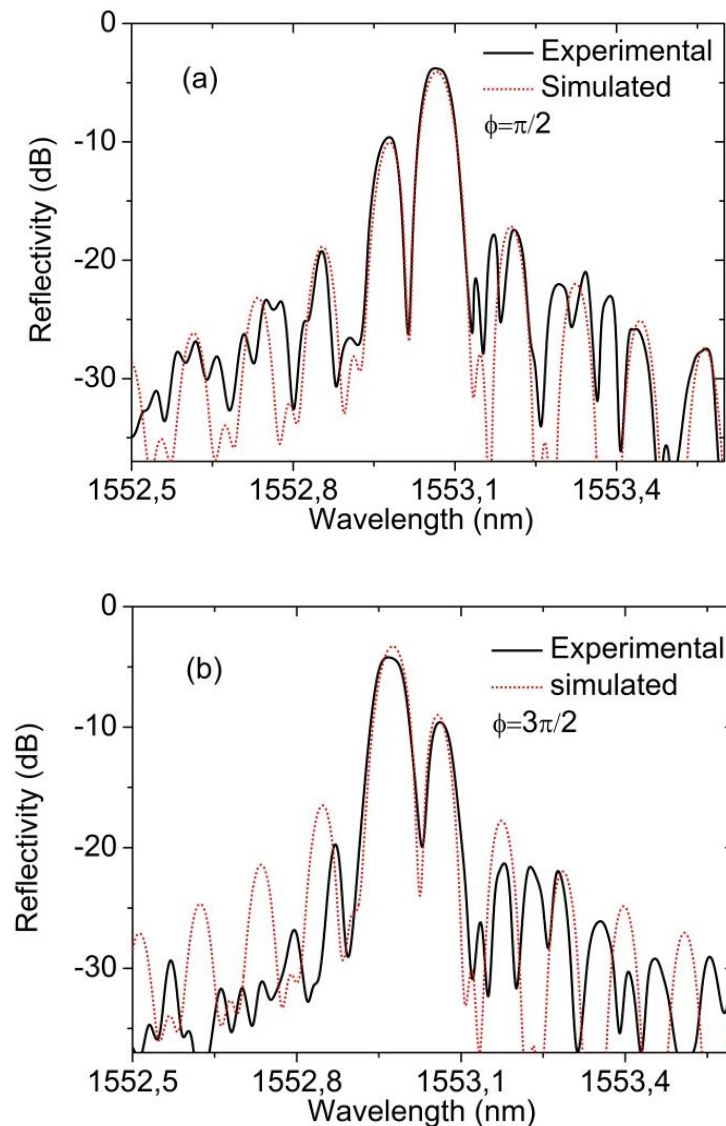
Figure 5.27 - Reflected spectra when the defects of (a) ϕ = π / 2 and (b) ϕ = 3π / 2 are inserted in the structure following the acoustic wave burst characteristics shown in Figures 5.23 (c) and (d), respectively.

Using the relationship $P_\phi = \phi l/2\pi$, where P_ϕ is position of the value of ϕ on the FBG, it is possible to achieve a phase shift of $\phi = 4\pi/5$ if a burst acoustic wave is generated in the position $P_\phi = 2l/5$, as is shown in Figure 5.28(a). Thus, it is possible the customization of Bragg structures for several photonic and/or microwave-photonic applications, where specific Bragg structures are needed [Palaci2010].

When more than one defect is inserted in the structure (considering $t_b \geq 0{,}5$ s) a sampled grating is created [Oliveira2010b]. However, if a continuous burst is applied in the fiber, a $\phi = 2\pi$ is achieved, as shown in Figure 5.28 (b).

On the other hand, Figure 5.28 (c) shows the reflective spectra when multiple phase shifts are inserted in the grating (considering a $T_{bt} = 50$ ms). The dotted line of Figure 5.28 (c) shows the insertion of two defects in the Bragg structure, one at $l = L / 4$ and other at $l = 3L / 4$ (as shown in Figure 5.29), while the dotted-dashed curve shows the spectrum when three defects in the grating is introduced (at $l = L / 4$, $l = L / 2$ and $l = 3L / 4$).
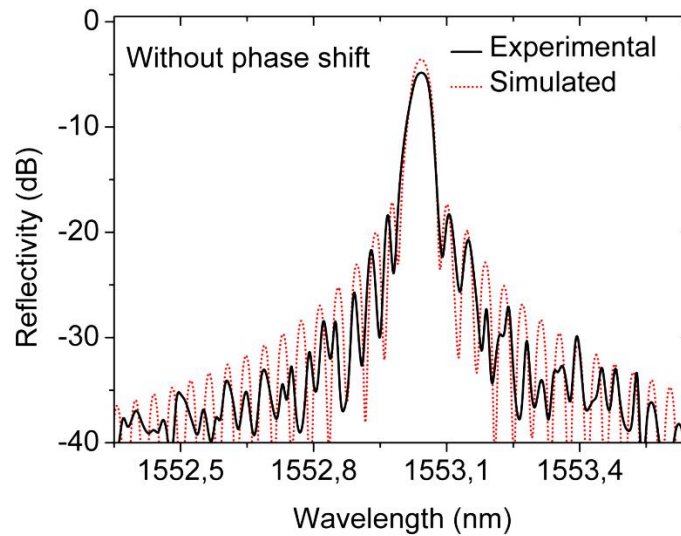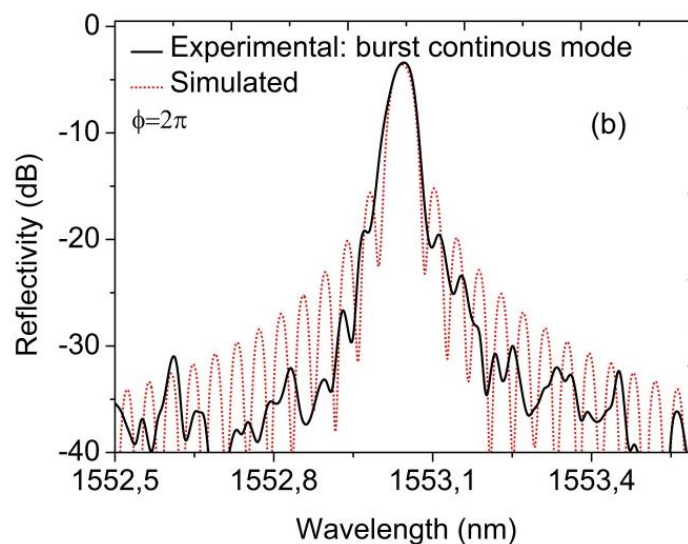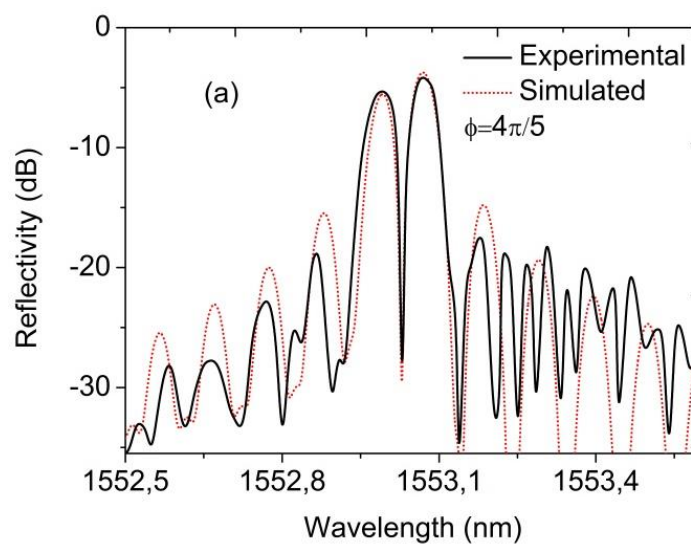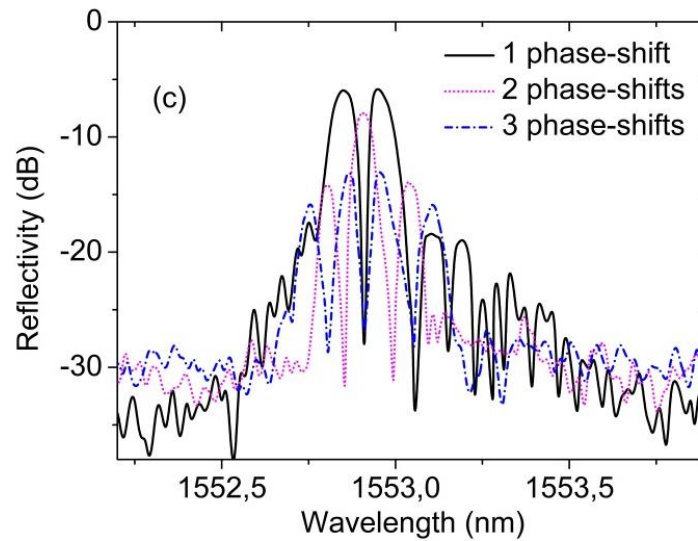
Figure 5.28 - (a) Simulated (dotted lines) and experimental (solid lines) reflected spectra when a defect is introduced in the Bragg structure creating a phase-shift of ɸ= 4π/5. (b) Reflected spectrum when the burst is set on continuous mode, inducing a phase-shift of ɸ = 2π. (c) Optical spectra when multiple phase shifts are introduced in the fiber.
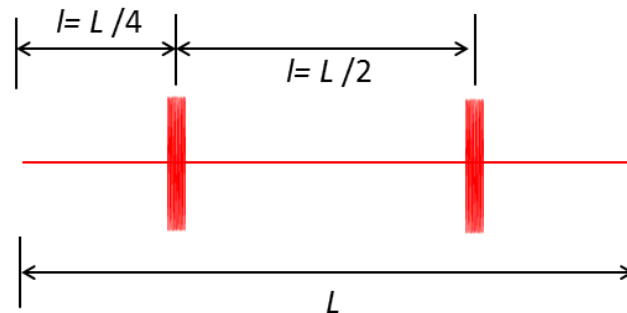
Figure 5.29 - Time diagram for produce multiple phase shifts. The positions of 2 defects inserted in the fiber are l = L / 4 and l = 3L / 4.

For the case with two phase shifts, the channel space of these two transmission bands is about 0,14 nm, and the notch depths are about 18 dB. For the case with three defects, the channel space of these three transmission bands is about 0,11 nm, and the notch depths are about 14 dB. It shows also that when one phase shift is inscribed, a notch depth about 22 dB is achieved as shown in Figure 5.26. The bandwidth of each transmission band increases slightly as the number of the phase shifts introduced in the structure increases, as one can see when comparing spectra

of FBGs with different number of phase-shifts. This characteristic is helpful to choose special transmission peak wavelength as using in dense WDM (DWDM) systems, comb filters, among others. It is also seen that the reflectivity of the Bragg structures decreased when increasing the number of phase shifts. The obtained results exhibits a full-width at half maximum of 13 pm, 27 pm and 52 pm bandwidth of their transmission bands for the cases of one, two and three phase shifts, respectively. Thereby, the obtained spectra for multiple phase-shifts show that technique is also promising for applications that required more than one phase shift.

5.7. Adjustable EDFA Gain Equalization Filter for DWDM Channels

The complexity of modern DWDM systems requires that under dynamic operation conditions, the EDFA gain profile is maintained flat, so that equal power levels are achieved for different channels. However, the intrinsic non-uniform gain profile of the EDFA limits this accomplishment. Over the C-band the gain spectrum exhibits a peak in the 1530~1532 nm region, leading to a significant difference in the signal power level of DWDM channels, thereby causing severe penalties in the optical signal-to-noise ratio of a link containing a cascade of EDFAs, thus limiting significantly the transmission distance and the useful amplifier working range. Although the compensation of such undesired characteristics can be done by demultiplexing all channels and using a variable optical attenuator (VOA) at each channel, the method depends on the use of extra optical devices (VOAs). This way, an adjustable wavelength-independent gain flattening filter is more desirable for the correction of the accumulated gain asymmetry in an optical network.

In order to solve this problem, active gain shape controllers have evolved along the years. Several approaches were proposed, including the use of discrete gain equalization systems and optical filters, such as the Mach-Zehnder (MZ) [Pan1995], the fiber-loop mirror (FLM) [Li2001, Kumar2005], the FBG [Dung1998], the LPG [Liu1999, Harumoto2002, Bae2007], acousto-optic filters [Kim1998], and side-polished fiber half-coupler block loaded with a displaceable tapered multimode overlay waveguide (SPF-MMOW) [Varshney2007]. Comparing the above solutions, MZ filters are relatively expensive and usually require extra compensation while FLM ones normally

present relatively high insertion loss. Previous works based on optical fiber gratings (FBG or LPG) use, in some cases, more than one grating and also more than one type of grating. On the other hand, the SPF-MMOW method is more complex because its tunability is highly dependent on several parameters, such as, for instance, the coupling between the SPF half-coupler and the MMOW, not to say that the device also exhibits a slow tuning time.

Experimental procedure

The LPG used to carry out the experiments was inscribed in a hydrogen loaded standard single mode photosensitive fiber using the 248 nm KrF laser. The LPG was inscribed by means of the point-by-point technique with pulse energy E_{Pulse} = 3 mJ, t_{exp} = 17 s and repetition rate of 500 Hz. The LPG period is Λ = 409 µm and the exposure length is L_{exp} = 200 µm. The length of the LPG is L = 51 mm, leading to an attenuation peak wavelength at $\lambda \approx$ 1532 nm. The AOM consists of a PZT disc, a silica horn and the fiber containing the LPG.

The experimental setup consists of the LPG-AOM connected to an arbitrary RF signal generator for excitation of the PZT, an optical source (an EDFA) and an OSA to measure the LPG transmission spectrum, as shown in Figure 5.30. A translation stage is used to generate a pre-tension in the fiber. It can also be used for fine adjustment of the LPG peak wavelength.
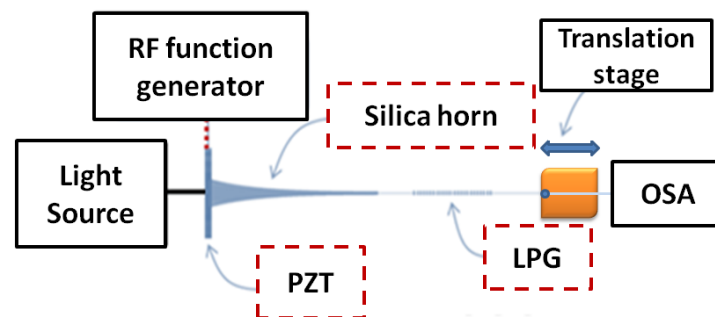
Figure 5.30 - Scheme of the experimental setup.

The LPG is placed outside the horn with the fiber clamped on a fixed stage. The silica horn has L_{sh} = 53,2 mm length, d_{sh} = 4,5 mm base diameter, d_{sht} = 1 mm tip diameter and d_h = 125 µm

central hole diameter. The interaction length, which corresponds to the length between the base of the horn and the fixed stage where the fiber is fixed, is L_i = 105 mm.

Experimental results

When the acoustic wave excites the LPG, various effects are achieved, depending on the characteristics of the driving signal. For instance, one can dynamically adjust the peak loss and intensity, as mentioned in Chapter 4.

Figure 5.31 (a) shows the acoustic effect when the resonance frequency is set at f = 65 kHz (the strongest resonance frequency observed with the employed PZT). The PZT load was swept from V_{PZT} = 0 to 10 V.

Periodic fiber bends generated with the flexural acoustic wave changes the optical path, modifies the difference between the effective refractive indices of the core and cladding modes and modulates the intermodal overlap integral. By doing so it reduces the coupling coefficient between the modes thus leading to a reduction of the LPG attenuation transmission peak and also inducing a red shift of the spectrum, as one can see in Figure 5.31 (a). Besides the change in the optical path, the break of degeneracy of the circular cladding modes also leads to the modification of the LPG spectrum [Block2006, Allsop2004a]. Furthermore, it should be noted that experiments show that no significant polarization dependence exists, as expected [Chen1999]. A similar behavior is observed for acoustic wave generated at other resonance frequencies; however, the magnitude of the effect is lower. In order to compensate this, or to better adjust the wavelength of the filter, the translation stage can be used to stretch or compress the fiber, which adds another degree of control to the device.

The top curve of Figure 5.31 (b) shows the LPG transmission peak power dependence on the PZT load, while the bottom curve shows the peak wavelength shift. This experimental behavior is confirmed by the numerical simulation and a good agreement between simulated and experimental data is noticed. This experiment clearly demonstrates that depth and position of the LPG peak can be tuned over a large wavelength range.
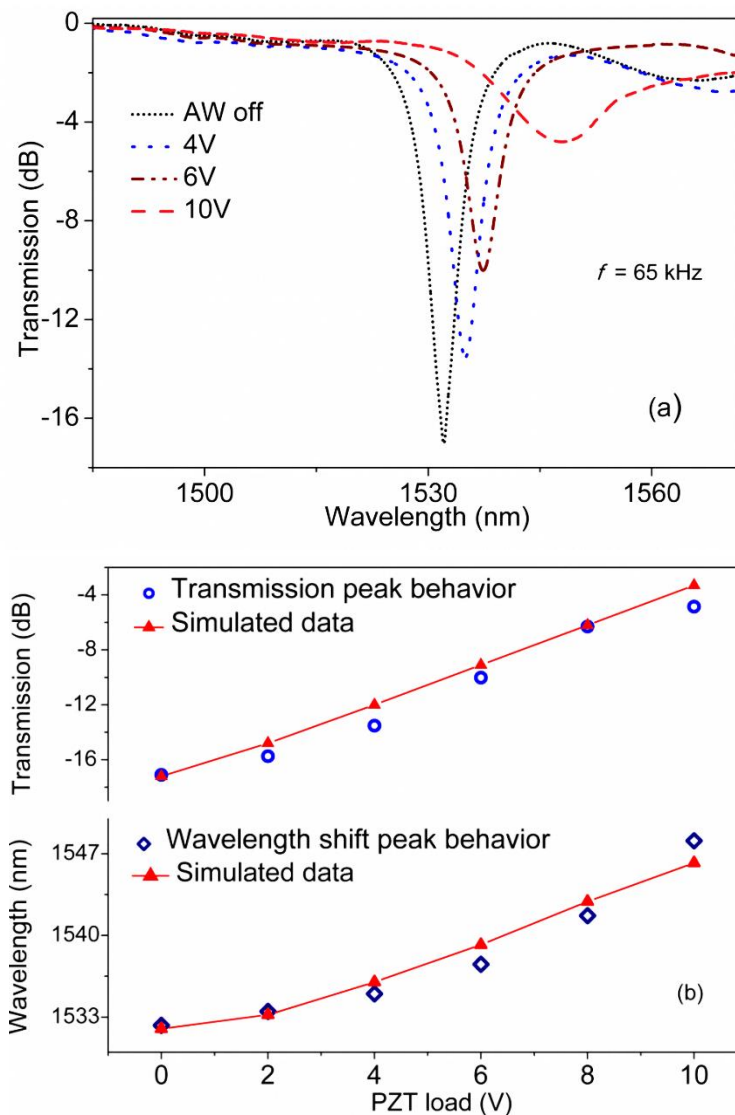
Figure 5.31 - (a) LPG transmission spectrum behavior when f = 65 kHz acoustic wave excites the fiber. The PZT load varies from V$_{PZT}$ = 0 to 10 V. (b) LPG transmission peak and wavelength shift behavior depending on the PZT load.

When the LPG is used as in-line filter in the EDFA, its impact on the flatness of the ASE profile is noticed. The EDFA is pumped with a 980 nm laser diode at a pump power of P_{ASE} = 110 mW. The solid curve of Figure 5.32 (a) represents the ASE spectrum without the filter. The dotted curves of Figure 5.32 (a) show the behavior of the ASE spectra when the LPG is excited and the PZT load varied. At $V_{PZT} \approx$ 2 V the ASE spectrum shows an efficient equalization. To reach an optimum performance, a fine adjustment of the load was performed and at V_{PZT} = 2,24 V (see inset graph of

Figure 5.32 (b)) the maximum observed ripple of the ASE profile presented a value around ~0,3 dB over the ~32 nm bandwidth, which represents a significant improvement over the uncompensated gain variation, which is more than 8 dB in the same wavelength range (C-band).
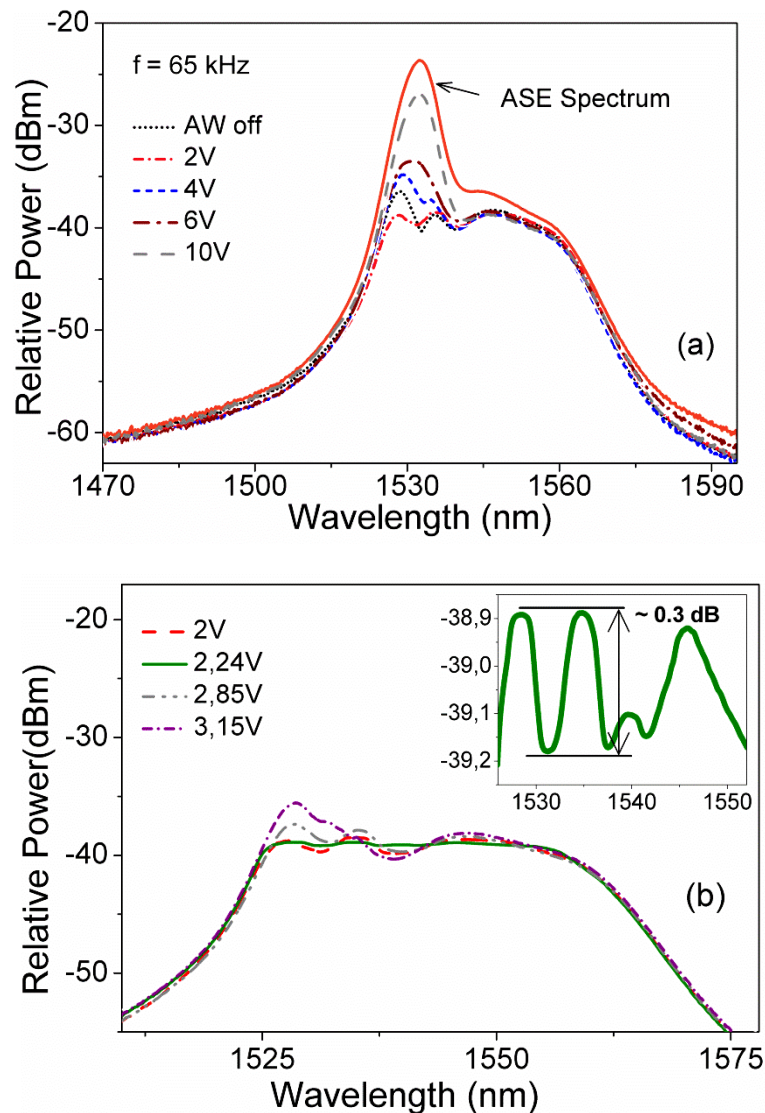
Figure 5.32 - (a) Unequalized ASE spectrum and equalized spectra when a 65 kHz acoustic wave excites the fiber. PZT load varies from 0 to 10 V. (b) The fine control of the PZT load improves the equalization of the ASE spectrum.

In order to test the mechanism performance, 8 (eight) DWDM channels over the wavelength range from 1525 to 1557 nm were generated from CW sources with average power of +13 dBm and multiplexed into the fiber. Initially, the EDFA, inserted after the optical mux, was pumped

with a power of P_{ASE} = 110 mW. Figure 5.33 (a) shows the measured output spectra of the EDFA without the flattener filter. The peak-to-peak power variation among the amplified channels was ΔP = 8,3 dB. If the acousto-optic filter is used, a flattening in the output power of the channels is achieved. Figure 5.34 (a) shows the equalized amplified signals with a fluctuation of ΔP ~0,3 dB.
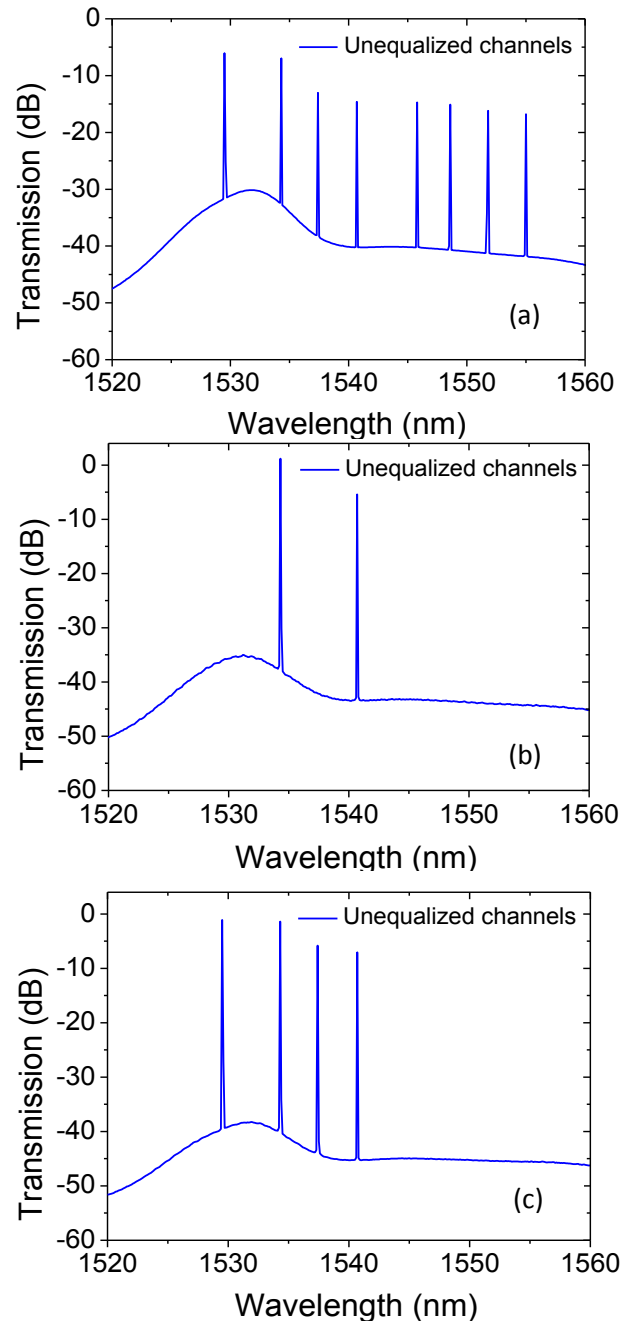
Figure 5.33 - (a) Measured signal output spectrum for 8 DWDM channels amplified with the EDFA without (unequalized spectrum) the device. Unequalized signal output spectra from the EDFA when (b) six DWDM channels are dropped and when (c) another two DWDM channels are added.
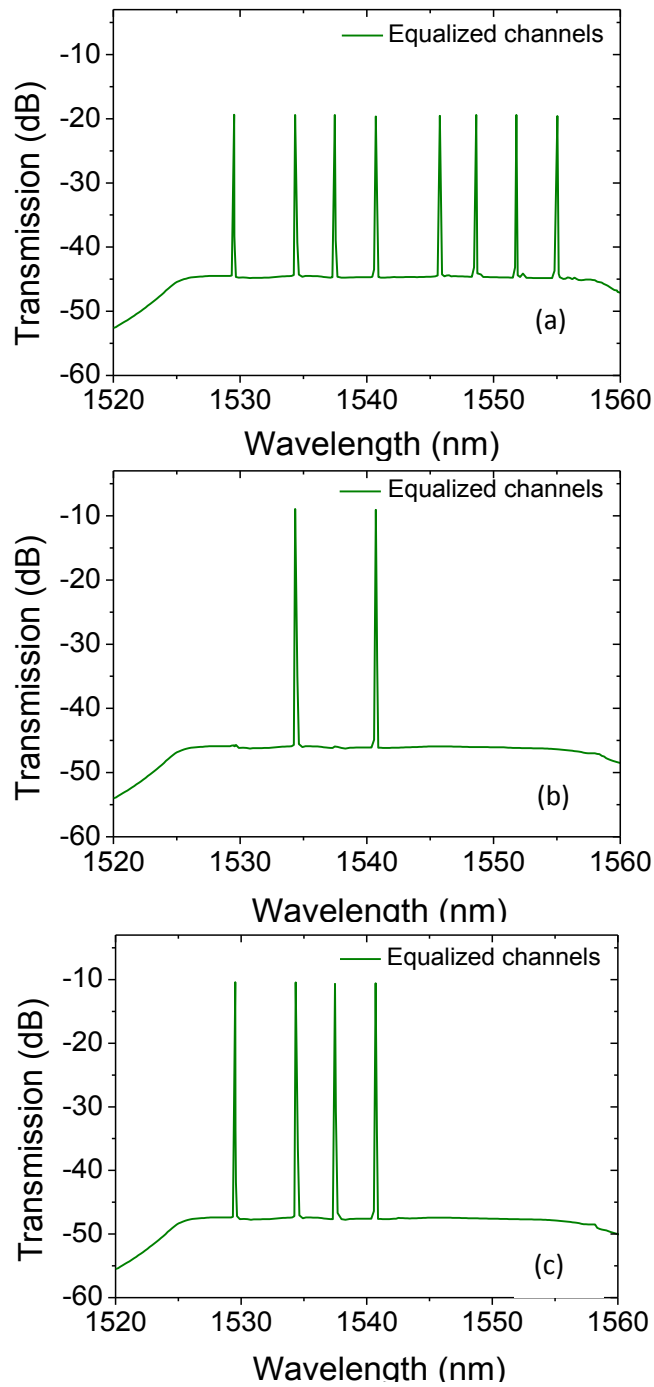
Figure 5.34 - (a) Measured signal output spectrum for eight DWDM channels amplified by the EDFA with (equalized spectrum) device. Equalized signal output spectra from the EDFA when (b) six DWDM channels are dropped and when (c) another two DWDM channels are added.

It is well known that the shape of the gain spectrum of an EDFA varies with changes in the pump and signal powers [Srivastava2006]. In dynamic DWDM transmission systems, when channels are dropped (Figure 5.33 (a)) or added (Figure 5.33 (b)) in the link, significant variations in the gain spectrum of an EDFA are noticed. Figures 5.34 (b) and 5.34 (c) depict the gain equalization for different channels when 6 (six) out of 8 (eight) channels were dropped and, right after, when 2 (two) channels were added, respectively. The experiments show that the peak-to-peak power variation is kept less than ~0,3 dB when DWDM channels are dropped or added, which shows an improvement over previous results [Varshney2007]. Additionally, considering the case of dropped channels, the gain spectrum was flattened by ~0,21 dB, which is the best obtained result observed in the literature and in the case of channel addition, the gain spectrum was flattened by ~0,25 dB.

The performance of the device in flattening the EDFA gain profile for different pump and channel power was also verified. The obtained gain spectra exhibit ripples within the above obtained values, not only when there is a change in pump power but also when channel powers are changed. However, it shall also be noted that when the number of channels changes, it is not necessary to make a large adjustment of the PZT load. But to correct for the changing shape of the EDFA gain spectrum it is only necessary to make a very slight adjustment on the PZT load to keep the system flatness < 0,3 dB. The experimental setup used to evaluate the system is shown in Figure 5.35 (a). Three CW sources with wavelengths of λ_1 = 1529,55, λ_2 = 1546,12 and λ_3 = 1552,52 nm and average power of +13 dBm were multiplexed. A Mach-Zehnder modulator with an electrical bandwidth of 30 GHz was used to obtain a 40 Gb/s NRZ optical signal. A pseudorandom binary sequence (PRBS) with 2^{31} – 1 bits was used.

The eye diagrams for the back-to-back and after equalization are presented in Figure 5.35 (b) and (c), respectively. The eye of the signal with the LPG-AOM is similar to the eye of the back-to-back signal, showing that our device does not cause distortion in the signal. The amplified signal is undistorted but noisier in comparison to the back-to-back case, due to the noise figure of the amplifier.

The system performance was then assessed using bit error rate (BER) measurements. The results are shown in Figure 5.36. The equalization performed by the LPG-AOM induces no significant power penalty in comparison to the back-to-back case. The comparison shows that the equalized signals presented a power penalty lower than 0,84 dB considering a BER of 10^{-9}.
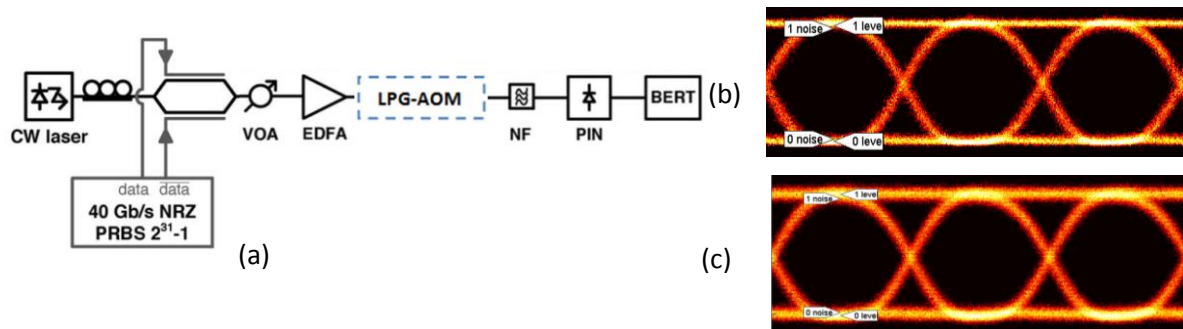
Figure 5.35 - (a) Experimental setup used for BER measurements. NF – noise filter; PIN – photoreceiver; BERT – bit error rate tester. (b) Eye diagrams for the back-to-back signal and when (c) LPG-AOM is introduced.
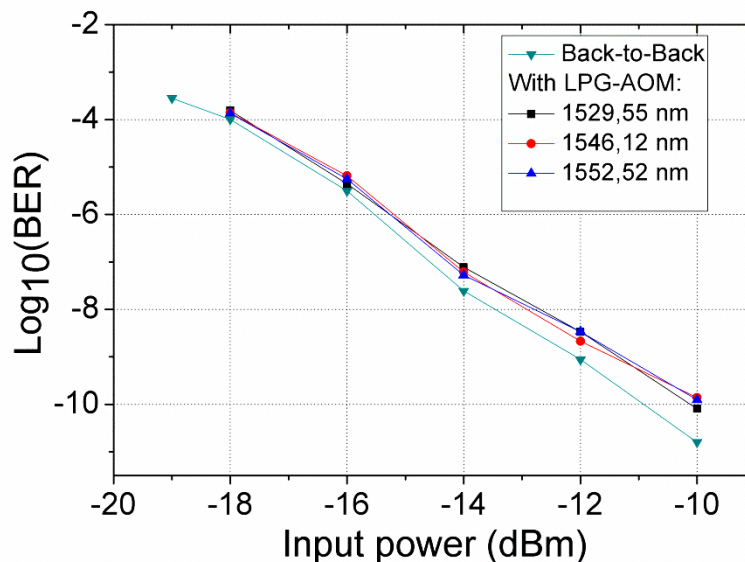
Figure 5.36 - BER results for different input powers at the output of the VOA.

5.8. Acousto-Optic Tunable Mode Coupler

With the advent of massive digital signal processing, mode-division-multiplexing (MDM) has been catching more and more attention from the research community, as an alternative way to keep up with the capacity demands over a single fiber [Saitoh2010, Jung2013]. The technological advances pushed the capacity limit up to a record above of 109 Tb/s. The current and crushing limitations for SSMF based systems are originated from several impairing circumstances that rise

from the increased bit rates. The research community has been working on fibers with large cores, fibers with multiple cores, or fibers that support multiple spatial modes to improve the nonlinear tolerance. MM fibers can also be used to increase the transmission capacity through spatial MDM. Using MM fibers with a higher core effective area, to reduce nonlinear effects is viable. In the last years, the interest in few-mode [Ip2013] or multicore fibers [Takahashi2013] has increased exponentially, allowing an increase of the total capacity per fiber.

Principle

Basically, it was investigated how the acousto-optic effect can be useful for MDM conjugated with a TOF. Jung et al. demonstrated how a TOF with appropriate designed transition region can act as a fixed mode filter for MM fibers [Jung2008]. On the other hand, an acoustic wave induces a periodic refractive index perturbation in the TOF. The acoustic wavelength matches the beat-length between the two modes, there is resonant forward coupling between them [Feced1999a]. The resonance point can be spectrally tuned by changing the acoustic frequency, and the coupled light can be adjusted due to the change of refractive index perturbation. The resonant forward coupling between the two modes is found, and the change of the spatial field distribution can be observed. In this way, the acousto-optic effect [Feced1999a] can be applied in TOF adding a degree of freedom. However, only the LP_{1m} modes can exchange power with the LP_{01} mode through a flexural acoustic wave, due to symmetry considerations.

Thus, a tunable mode coupler can be produced exploring the acousto-optic effect in TOF. High order modes can be excited by the appropriate choice of the acoustic frequency. This device allows to select the output mode as function of the acoustic frequency applied.

Results

The used optical fiber is the SSMF (SMF-28, Corning), which is SM fiber in C-band however the fiber is MM fiber in the VIS spectral window presenting only a few modes. This fiber has a quoted NA of 0,14 at 1310 nm. Taking into account the V-parameter (in this case 5,74 at 630 nm), one indicates that the fiber will support 6 modes [Okamoto2006]. The TOF was produced by a process based on the flame brushing technique, where the fiber is heated above its softening point by an

acetylene flame of 2 mm width, while it is stretched mechanically by two linear stages in several oscillatory "brushing" movements controlled by precision stepper motors (Newport UTS-150-pp), with a predefined velocity sequence. This tapering setup allows us to control the fiber taper transition regions shape and length, as well as, the diameter and length of the central waist region [Niehus2010]. The used TOF was then produced from a MM optical fiber at 630 nm. This has a tapering angle of 4,5 mrad, and a length and diameter of waist region of 11 mm and 22 µm, respectively. The taper angle chosen is great enough in order to approximating this to the adiabatic criteria. Figure 5.37 (a) depicts the measured taper profile and target profile. In this way, the adiabatic TOF only allows the fundamental mode, without acoustic excitation as displayed in Figure 5.37 (b).
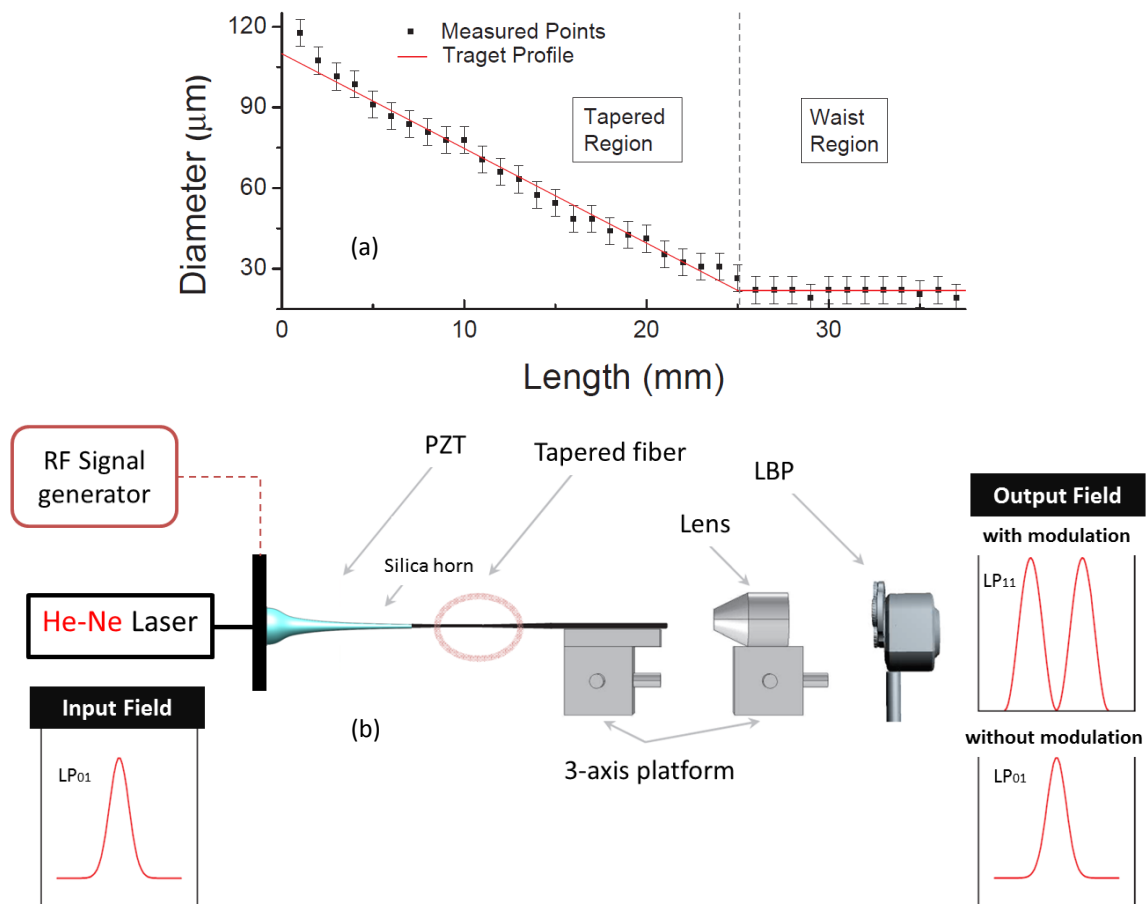
Figure 5.37 – (a) Measured taper profile and target profile. (b) The tapered fiber is fixed to the silica horn. The fiber end is cleaved and aligned with an objective lens (40x) and the laser beam profiler thought the 3-axis platform. The RF signal is applied to the PZT and the spacial mode distribution is projected onto the laser beam profiler (LBP).

Figure 5.37 (b) shows the experimental setup used. A silica horn, with a PZT disc fixed to its base, was attached to a bare but unnarrowed portion of fiber near the TOF. The end of the fiber is cleaved, the laser (λ = 630 nm) is launched in the TOF and the spatial field distribution is projected in the objective lens (40x). The spatial mode distribution is consequently obtained in an LBP. The cleaved fiber, the objective and the LBP are precisely aligned using a XYZ platform. One must to ensure that the input field is in the fundamental mode (LP_{01}), as shown in Figure 5.38 (a). Posteriorly, an acoustic wave was applied to the PZT disc, and high order modes can excited as function of the acoustic frequency (see Figure 5.37). The change of the spatial field distribution is observed "in situ". Figure 5.38 (a) shows the spatial mode distribution for the fundamental mode before the acoustic wave applied. Figures 5.38 (b)-(d) display the spatial mode distribution for the three degenerated LP_{11} modes: TE_{01}, HE_{21} and TM_{01}. The resonance coupling is observed for the acoustic frequencies of (b) 387,8 kHz, (c) 462,1 kHz, and (d) 465,7 kHz, for the modes TE_{01}, HE_{21} and TM_{01}, respectively.

f= 0 kHz   f = 387,8 kHz   f = 462,1 kHz   f = 465,7 kHz
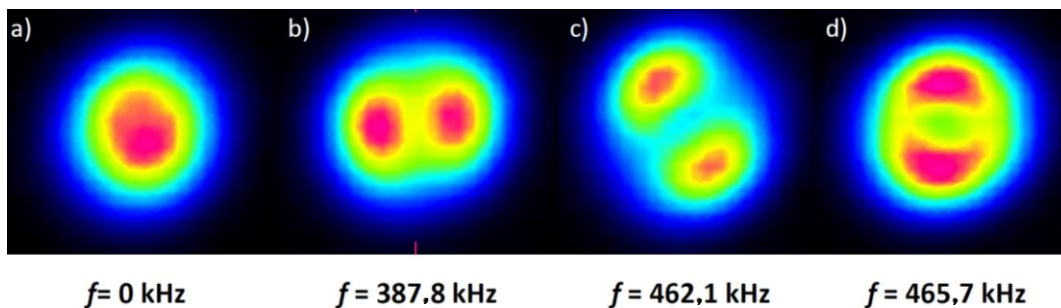
Figure 5.38 - Special mode distribution experimentally measured with the LBP, (a) for the fundamental mode without acousto-optic effect, (b), (c) and (d) for the three degenerated LP_{11} (TE_{01}, HE_{21} TM_{01} and respectively).

The transmission spectra of the TOF shows the characteristic beating due to the mode coupling, as is shown in Figure 5.39 (a). Despite the intrinsic TOF mode coupling, one only observes the fundamental mode in the output fiber. Figures 5.39 (b)-(d) display the transition spectra after the acoustic wave be applied. The measured losses are 2,42, 0,67 and 0,93 dB for the acoustic excitation of 387,8, 462,1, and 465,7 kHz, respectively.
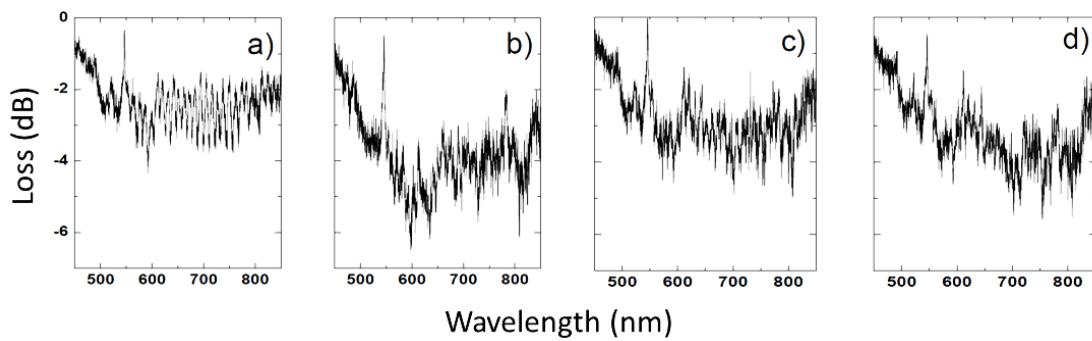
Figure 5.39 - Spectrum for the tapered fiber, a) before the acoustic excitation, b), c) and d) spectra with acoustic frequency of 387,8 kHz, 462,1 kHz, and 465,7 kHz, respectively.

Figure 5.40 show the theoretical spatial mode distribution for a wavelength of 630 nm for the same multimodal fiber used in the experimental approach. A three layer vector model was considered, in which the fiber core and cladding regions are surrounded by a layer of air. The spatial mode distribution was calculated using a FEM in the Comsol Multiphysics software. From Figure 5.40 the numerical results are in agreement with the experimental data. In principle the device proposed can be used to select other high order modes. This would require starting from high order modes, taking into account the symmetry conditions must be respected. The TE_{01} and TM_{01} members of the set closely resemble the azimuthally and radially polarized vector beams have several applications including laser drilling, particle trapping, and microscopy. The tunable coupling of these modes can find interesting applications in these topics. Another challenge in MDM is the efficient combining and splitting of higher-order spatial modes from and to the fundamental LP_{01} mode of SMF components. Based in this study, an hibrid TOF can be developed allow splicing the SMF with the MMF and select dynamically the output mode.
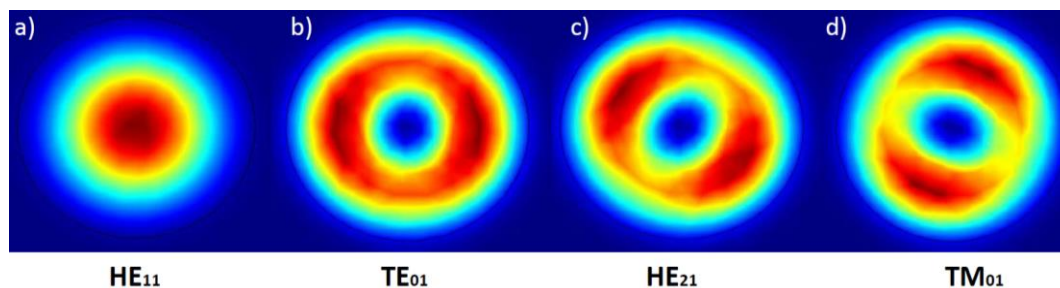
Figure 5.40 - Special mode distribution calculated with Comsol Multiphysics for the MM fiber for the wavelength of 630 nm. In (a), (b), (c) and (d) is represented the fundamental mode, TE_{01}, HE_{21} and TM_{01}, respectively.

5.9. Optical Notch Filters with Fine Parameter Control using RFBGs

To date, there has been a major progress in the development of microwave and/or photonics devices. Optical transport and processing of microwave band signals by means of different optical devices, exploiting their characteristics has been one of the main stimuli. In this context, optical filters are a key enabler of these systems, among which, notch filters can play a critical role in photonic and microwave-photonic systems to enable the blocking or attenuation of undesired spectral content [Capmany2006, Yao2009], signal monitoring or sub carrier processing [Zhao2008, Madsen2004]. To satisfy the most demanding applications, unconventional levels of notch filter performance are required in terms of attenuation level, 3-dB bandwidth consistency and cost. Several applications have been proposed using optical filters [Zhang2009, Zhao2008], to attenuate one of the two sidebands or to attenuate only one sideband without affecting the optical carrier and the other sideband. However, these optical devices have relatively broad bandwidth for systems which operate at a few GHz. Another techniques using a narrow π phase-shifted FBG [Li2010] does not have this problem; however, the ability to control the attenuation level of the central rejection band is very limited due to difficulty of fabricating such precise FBG.

As previously stated in Chapter 2, regenerated gratings are obtained from strong FBGs written in highly photosensitive optical fibers by heating the grating to a suitable temperature (usually of the order of 700–900°C) [Canning2010]. The heating causes the FBG spectral reflection band to initially disappear or decrease dramatically, followed by the growth of another spectral reflection band normally close to the same central wavelength. A possible explanation of this effect which is responsible for the second increase of the refractive index modulation is crystallization in the doped material caused by UV radiation together with the thermal heating and maybe diffusion effects [Linder2009].

This method to produce optical notch filters, which allows us to overcome the typical limitations of previous approaches, it is ideally suited to operate on optical signals with bandwidths up to a few GHz. Specifically, it is demonstrated that a fine control of the rejection band is achieved and it is based on the regeneration process of strongly saturated FBGs.

Experimental procedure

Strongly saturated FBGs were inscribed in standard ITU G.652 single-mode fiber using the phase mask technique. The illumination was carried out using UV light from a KrF excimer laser at 248 nm. A cylindrical lens with f_c =20 mm is used to focus the laser light on the optical fiber in order to increase the power density onto the fiber's core. The FBGs were inscribed with pulse energy E_{Pulse} = 3 mJ and repetition rate of 500 Hz. The fiber samples were previously subjected to a hydrogenation process that occurred at a pressure of 150 bars, during two weeks, in order to enhance its photosensitivity. After the production, the FBGs were initially characterized in terms of their spectral response and afterwards put in an electrical oven for heating [Valmir2011]. During the period between production and thermal characterization, the gratings were kept at dark. Two thermocouples were used to monitor and control the oven temperature. One of them was put at the center of the usable volume of the oven and the FBGs were placed surrounding it. The oven temperature can be kept with a fluctuation bellow ±0,5 °C.

Results

Regeneration was obtained by heating the seed gratings in the oven laboratory to temperatures in the range of 850°C until the seed signal vanishes and the regenerated grating signal stabilizes. The initial spectrum of the grating was obtained at room temperature before starting the heating cycle, whereas the final spectrum is measured at the end of the process, after the grating cooled to room temperature again. Figure 5.41 shows the reflectivity of one seed FBG with a length L = 4 mm together with that of the respective regenerated grating. The reflectivity spectra of the seed show characteristics of a strongly saturated grating The Bragg wavelength at room temperature of the regenerated grating lies at 1546,32 nm and the 3-dB bandwidth is 0,2 nm. The considerable shift in the Bragg wavelength can be assigned to the changes in the refractive index profile [Canning2010].
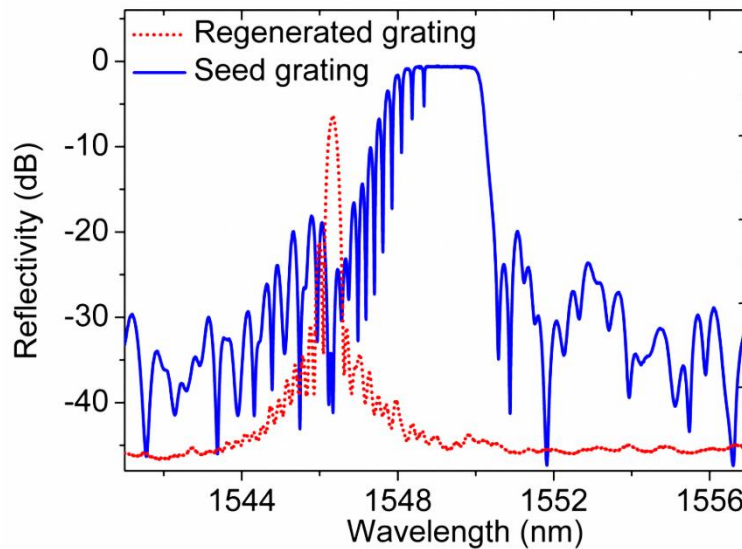
Figure 5.41 - Optical reflection spectra from one obtained grating at 22°C.

However, it shall be mentioned that the obtained gratings with very high saturation level showed always a Bragg wavelength blue shift of the order of 2,8 nm, regardless of grating length, slightly different from the value presented in [Canning2008]. One explanation for this fact is the use of hydrogen-loaded fiber. Furthermore, the UV laser wavelength, exposure conditions and composition of the fiber differ from those used in [Canning2008].

The regeneration cycle for the mentioned grating is shown in Figure 5.42 (a). The grating was annealed at 850 °C and afterwards it was kept in the oven. The evolution of the grating reflectivity is representative of the UV-induced refractive index modulation during isothermal annealing. The grating reflectivity decreases during the first 60 min before a secondary growth This secondary growth leads to an index change in the fiber core which is more temperature-stable than normal Type I FBGs. The reflection spectra show that the grating has been regenerated in approximately 84 % of reflection relatively to the initial saturated grating, which corresponds to a signal ~40 dB above noise background. This presents the typical behavior for any regeneration process using strongly saturated FBGs, regardless of grating length and fiber saturation level.

Figure 5.42 (b) shows the evolution of the reflection spectra of a FBG during the regeneration process. When the temperature increases the narrowing of the bandwidth and the decrease of reflected signal from the FBG peak can be seen. The temperature was maintained in 850 $^{\circ}$C and the formation of a notch is observable.
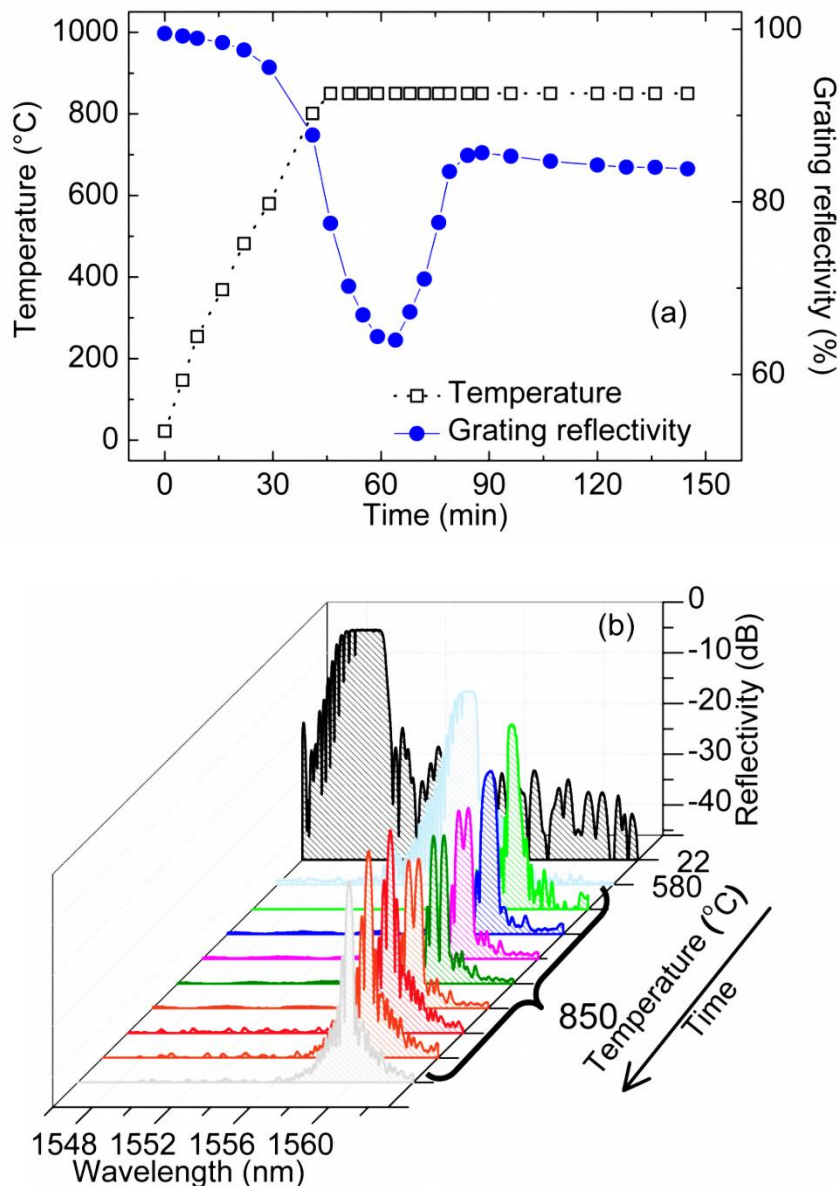
Figure 5.42 – (a) Grating reflectivity behavior and temperature variation as a function of time. (b) Changes in the spectral response of saturated grating in hydrogenated fiber when subjected to temperature variations along of the time.

A possible cause for this effect is an overlap between contributions from different mechanisms such as crystallization and specific changes of diffusion properties in the doped material in the fiber, changes in the defect structure due to the high level of UV radiation for creating saturated FBGs and centers linked to the hydrogen used to enhance photosensitivity in fibers. Another

plausible explanation is that phase information of the seed grating cannot be preserved, indicating there is evidence that a diffusive process could alter the phase relationship anywhere over the grating length. This explanation is based on group delay spectra before and after of the notch filters formation as shown in the Figure 5.43, whose behavior is similar to the phase-shifted FBGs.   When the notch depth reaches its maximum, the reverse process starts and the regeneration phenomenon proceeds normally until the grating is completely regenerated.

The process can be interrupted anytime, when the desired notch depth is reached. Thereby, Figure 5.44 shows the evolution of the notch depth as a function of time. A fine adjust of the notch depth is achieved by control of the time of regeneration process. The process time depends of the fiber saturation level and it can last between 3 to 15 min since the beginning of the notch formation until its maximum depth, allowing precise depth control.
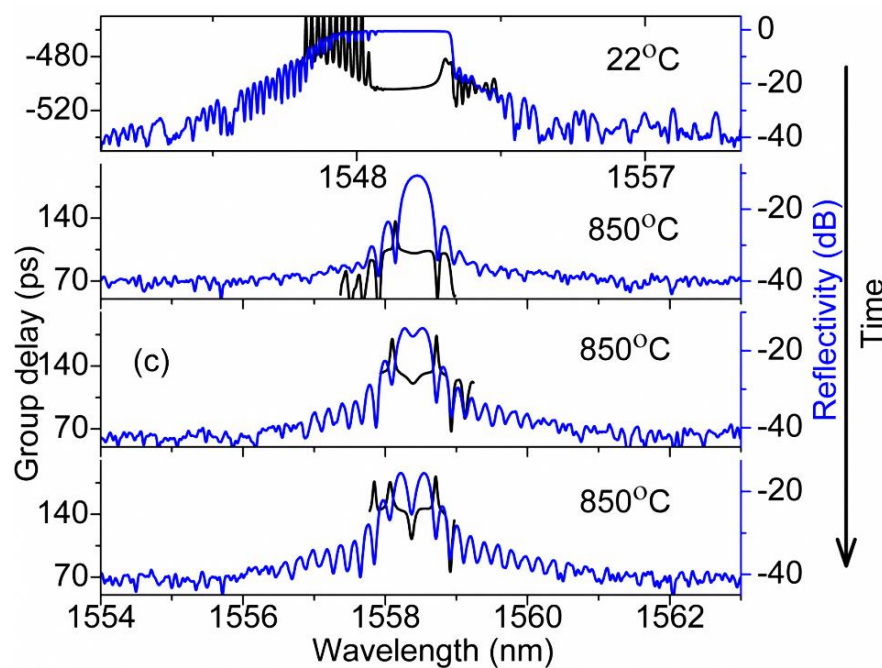
Figure 5.43 –Phase information during the regeneration process. Behavior similar to the phase-shifted FBGs.

The result shown in Figure 5.44 was obtained with a FBG with length L = 50 mm, which presents a maximum notch depth around 24 dB and a Bragg wavelength of λ_B = 1553,6 nm. The excess

insertion loss is approximately −4 dB. It shall be noted that maximum depth of the notch depends on the saturation level of the FBG. So, the higher the saturation level of FBG the greater its depth.
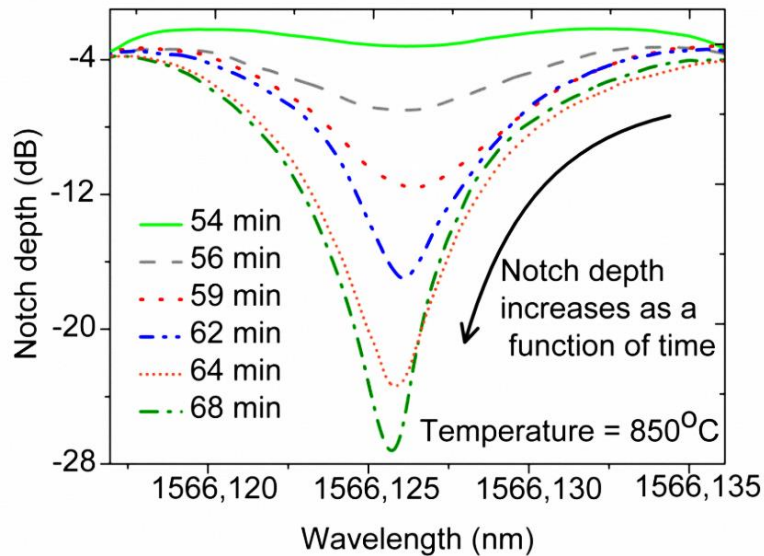
Figure 5.44 - Evolution of the notch depth over of the responsible mechanism for its formation. In this case, the maximum depth occurs at 68th min of the regeneration process time. FBG with length L = 50 mm was produced. This figure is a zoom of the reflection spectrum from of FBG showing the notch´s region.

When the fiber returns to the oven for subsequent heating at the regeneration temperature, the regeneration process continues normally, as if the heat treatment had not been interrupted. Thus, different adjustments with the same Bragg grating can be achieved by subsequent processes. To obtain also a fine control of the 3-dB bandwidth, FBGs with different lengths were inscribed and their spectra were characterized, after exposed to the regeneration process, in terms of 3-dB notch filter bandwidth, as shown in Figure 5.45. The 3dB notch filter bandwidth varies between 0,33 and 0,01 nm considering a Bragg grating length between 2 and 50 mm, respectively. Thus, it is possible to create optical notch filters with a fine control of its depth and bandwidth. When the filter is removed from the oven and returns to ambient temperature, both notch depth and bandwidth remain stable, as can be confirmed with the reflection spectra shown in Figure 5.46.
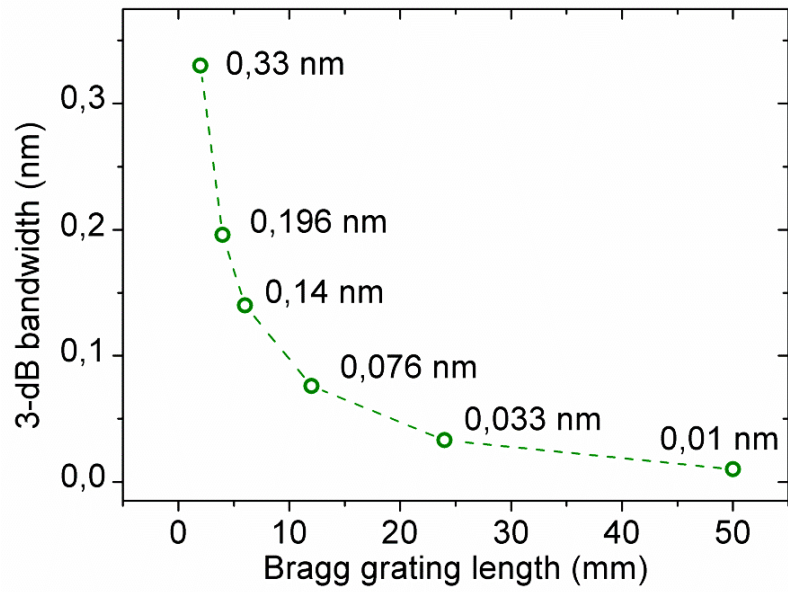
Figure 5.45 - 3-dB notch filter bandwidth as function of Bragg grating length.
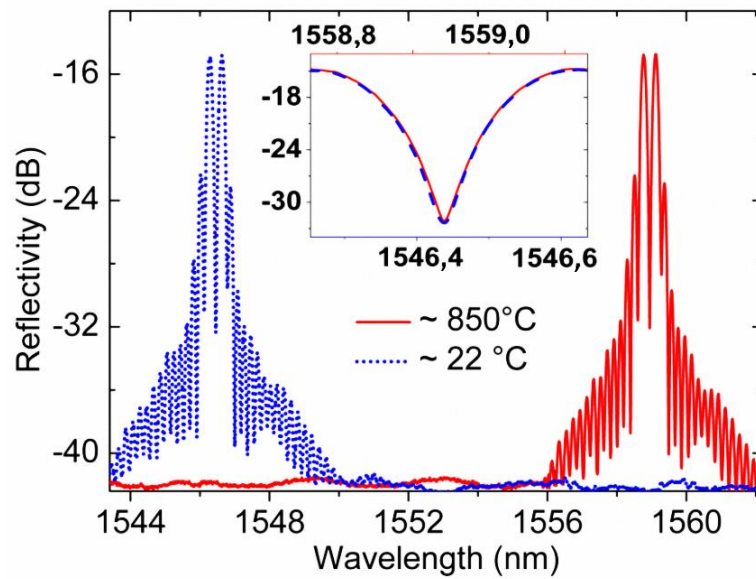
Figure 5.46 - Reflection spectra showing the notch depth when the oven temperature was set at 850 ^{o}C and when it is at 22 ^{o}C. No significant changes were verified in the notch depth and bandwidth (inset figure).

5.10. Chapter summary

In this chapter, several novel applications based on acousto-optic modulation and regeneration phenomenon in fiber gratings are presented. Applications are described and their respective experimental assemblies detailed. The devices performance are also presented and discussed in this chapter.

Chapter 6

Conclusions and Further Works

Conclusions

The central issue treated in this document is a comprehensive study of fiber grating technology from fundamentals to photonic applications. The PhD thesis collects in a single document, a group of topics that aim to provide a solid description of the fiber grating technology assisted by a selected number of experiments that strengthen the theoretical background.

In this thesis, several aspects of the Bragg grating in silica and polymer optical fiber were studied. In this context, the work addressed four areas: theoretical fundamentals, inscription, characterization and application of fiber gratings. In most cases, a good approximation of the theory and experimental results were achieved.

The background knowledge relating to fiber gratings is introduced at the second Chapter of the thesis. The third Chapter is related with fiber gratings fabrication in silica and polymer optical fiber. The fourth Chapter collects the acousto-optic effect with original theoretical and experimental works in both type of fibers and on fifth chapter is focused potential applications using not only the acousto-optic effect but also the regeneration process in fibers. The outcomes and further works of these works are concluded in following sub-topics.

Fiber Grating Inscription Workstations in Silica and Polymer Optical Fiber

Since the optimization of any fabrication and characterization system is a never ending task, especially the fiber grating fabrication workstations, have certainly useful features to explore and improvements to be further developed. Nevertheless, the activity reported in Chapter 3 was an important step towards accurate and tailored fabrication of fiber gratings in silica and polymer fiber. Another point to be emphasized is the priority put into the software control interface in order to make it comprehensive, easy to operate, while at the same time keeping it flexible enough to allow new functionalities to be added.

Achievements:

1. A fiber grating inscription setup based on 248nm KrF UV laser using four techniques of inscription has been developed for fabricating fiber gratings in silica optical fibers, including uniform FBG, PSFBG, chirped FBG, Fabry-Pérot cavities, LPGs, and so on. Fiber gratings are successfully written in different kinds of silica optical fibers, including photosensitive single mode silica optical fiber, standard silica optical fiber, HiBi optical fiber, double-cladding fiber, with or without hydrogen loaded to an improvement of photosensitivity. The station incorporates multi-parameter and accurate control assisted by user friendly control software. It should be noted that this setup has contributed with many and different devices to satisfies the requirements of various works. These contributions can be found in several papers published (see list of publications – Chapter 1).

2. A Bragg grating inscription setup based on 325 nm HeCd UV laser using two writing techniques has been developed for fabricating Bragg gratings in POFs. Bragg gratings are successfully written in different kinds of POFs, including PMMA based SM and MM mPOF, PMMA based photosensitive SM step-index POF. Bragg gratings also were successfully inscribed in different spectral windows such as 1550 nm, 850 nm and, for first time, at 600 nm, which is important for future applications, because polymers, in particular PMMA, have low loss in that wavelength regime. The FBGs have narrow bandwidths from 0,22 down to 0,045 nm with short total exposure times, achieving rejection levels of

21 dB. The main aspect is the use of scanning method with a very short optical path. The narrow low attenuation window at a lower wavelength is definitely a candidate for future POF transmission systems using CMOS technology, in particular when taking into account that the loss can be further reduced by improvement of the fabrication technology. In addition, the fabricated POFBGs with particular characteristics (such as narrow 3-dB bandwidth and amplitude response) can be potentially used as optical devices in POF link, overcoming limitations existing at lower wavelength.

Further works:

Other types of gratings such as PSFBGs and chirped FBGs will be investigated to be used in POF applications for VIS-NIR window. The use of other types POF such as mPOF, graded-index POF (best transmission POF), step-index POF for inscription of Bragg gratings are in progress with aim to obtain devices for optical filtering.

Due to the lack of regular success of the connection between silica fiber and mPOF/POF using UV curable epoxy glue (NOA 78), and considering recent developments in the fabrication of demountable connection between silica fiber and an mPOF [Abang2012], eliminating the limitations of UV glued connections, new developments shall be done. This last approach only had yet success for MM fiber, which presents a large core size providing tolerance to core misalignment. For SM fibers, which have few micron of core (~3-8 µm), the core alignment is a complex task and with a low success.

Acousto-Optic Modulation in Diffraction Gratings

As mentioned along this PhD Thesis, the possibility of writing diffraction gratings in optical fiber opens up a vast field of research. In the same way, the study of the interaction between sound and light arises as an alternative for increasing the range of optical fiber technology applications. This interaction is the key to construct several all-fiber photonic devices. Thus, the AOM has been explored regarding the excitation of different resonant modes in the silica horn – fiber set. Numerical approaches based on finite elements, assumed modes and transfer matrix methods were used in order to model the devices and simulate the effect. Flexural and longitudinal

excitation modes can be excited using a single AOM device, which opens up a large range of applications using silica and polymer optical fiber.

By using FBG and LPG, the acousto-optic effect was employed in several situations. In the low frequency regime, when flexural modes predominate, the effect experienced by FBGs is a reflectivity decay, due to a mismatch between the co-propagating and counter propagating modes as a consequence of bends generated in the fiber. In the LPG case, the increase of the flexural acoustic wave intensity reduces the transmission peak of the LPG attenuation band and induces a shift to longer wavelengths. By changing the optical path and the difference between the effective refractive indices of the core and cladding modes and the overlap between them, the acoustic wave causes a reduction of the coupling coefficient and, consequently, a reduction of the transmission peak. In the high frequency regime, where the excitation of compression and rarefaction strain fields in the fiber predominates, the acousto-optic effect is noticeable only when applied to FBGs, because its refractive index modulation period has the same order of magnitude of the induced longitudinal displacement of the planes. It leads to the superlattice modulation of the grating. In LPG, due to its larger modulation period, the longitudinal modulation does not change significantly the grating spectrum. However, the effect of induced bends in the fiber (flexural waves) is more evident in LPGs.

The complete characterization in the low and at high frequency regime made it possible to apply the modulator in different devices, by controlling the effect that is most suitable for the particular application.

Hereupon, several devices were proposed, demonstrated and characterized using AOM, such as: fast acousto-optic add-drop multiplexer, tunability of the FBG group delay (tunable dispersion compensator for WDM channels and optical delay lines), an adjustable notch filter , a method for writing complex FBGs, an adjustable EDFA gain equalization filter for DWDM channels and a tunable mode coupler.

Achievements:

1. A detailed analysis of this effect in POF was also studied as presented in fourth Chapter. It was demonstrated that the excitation of an FBG written in mPOF through acoustic waves can

be achieved. It is possible to dynamically control the properties of the grating spectra (such as maximum reflected power and 3-dB bandwidth) even with a grating length of 2 mm through the AOM, which has not been possible in silica fiber. The FEM and the TMM present the advantage of calculating the strain along the whole structure allowing the determination of the influence of the structure dimensions (horn, fiber and FBG sizes) on the grating reflected spectrum when an acoustic wave propagates along its axis. Furthermore, the physical characteristics of the structure can be adjusted in order to obtain the desired strain and FBG spectrum. The approach takes into account the load induced by the acoustic wave, which can be associated with the characteristics of the PZT actuator used for its excitation. The strain field along an mPOF FBG–AOM and a similar structure with SFBG-AOM was determined, showing that the strain field amplitude is higher along the mPOF FBG due to its smaller mechanical stiffness. The obtained results can be used in the development of new devices for optical communications and sensing.

2. An OADM with fast switching times was presented. The response time of such device is limited by the speed of the acoustical wave through the entire modulator. A switching time of t_s = 26 µs was measured. This can still be improved, if the interaction length and the acoustical frequency are optimized. Yet, this switching time is one of the smallest found in literature, which makes the device very promising for practical applications. Also, the time response of mPOF FBG is experimentally assessed, for the first time, using flexural acoustic waves, taking approximately 215 µs to change the grating spectrum. The best result was achieved with a 10-mm long FBG length.

3. It was demonstrated that both the amplitude and frequency of an acoustic wave can be used to tune the first and second order dispersion coefficients and to reduce the group delay ripple of a uniform FBG. This technique can be used for the implementation of photonics delay lines and dispersion compensator for independent coarse WDM channels controlled by the frequency and PZT load applied to the PZT that generates the acoustic wave. By ensuring the induced strain profile is positioned properly over the grating length, an effective "dc apodization" is achieved. If the broadening of the bandwidth over which the device works is equal or less than the channels bandwidth itself then this technique opens up an opportunity for the dispersion compensation of individual channels. In very complex systems where

different channels travel different lengths and experience differing group delay and dispersion, this unique form of active channel control turns up to be an important solution. The achieved results can be improved by tailoring the uniform grating profile (including partial apodization) to help reduce the GDR and to flatten the dispersion slope further. Additionally, this technique can be applied to tune much broader band devices, including existing chirped FBG compensators to enhance their tunability and performance. A good response time t_s = 17 μs was measured. Considering an interaction length L_i = 95 mm, the measured acoustic speed in the fiber is 5588 m/s, comparable with values found in literature [Elmore1985].

4. The properties of a PSFBG under the influence of AOM were investigated. The acoustic effect allowed a fine tuning of the notch depth and bandwidth until its suppression due to the generation of bends in the fiber, breaking the phase matching condition of the grating. The experimental results were obtained both in reflection and transmission and were validated by theory and simulation. The time response of the device was also characterized. Whilst weak gratings were used explicitly to study the effects of the acoustic signal directly on an optical spectrum analyzer with only moderate resolution, the technique can clearly be applied to much stronger gratings. The obtained results can be used in the development of fine-tuned optical filters with very fast response times. The method allows for an actively tunable cavity Q, with potential applications in DFB fiber laser that use active gratings for controlling the laser pulse power and the linewidth broadening.

5. It was demonstrated the technique of exciting an optical fiber by flexural waves during the process of Bragg grating inscription and shown that it is possible to create Fabry-Pérot cavities and sampling modulation of uniform Bragg gratings, by switching 'on' and 'off' the acoustic wave and tunability of bursts during the writing process, respectively. The method shows great potential in various applications where precise and fast control of the grating parameters is desired. It is an acoustic equivalent to past processes where the writing tools, such as phase masks, are dithered or the laser beam modulated.

6. The possibility of using burst acoustic waves to create defects along the Bragg grating, so generating customized phase-shifts was demonstrated. As an example of application, phase-shifted Bragg gratings were recorded, achieving values of φ = π, φ = π / 2, φ = 3π / 2,

φ = 4π/5 and φ = 2 π, opening up the possibility of complex structures writing. It can be further extended to generate multiple phase-shifts in optical fiber and/or waveguides, if the defects are inserted at different positions. The method was proved to be a relative low cost alternative, in terms of translation stages, controllers, laser modulators, switches and so on, comparing with conventional permanent grating defects insertion systems. Moreover, a uniform phase mask can be used making possible the customization of Bragg structures, as the characteristics is set through the acoustic signal generation. It shows great potential in several applications where precise phase-shift control is desired, generating narrow pass-bands in controlled positions of the Bragg stop band.

7. A filter for the gain equalization of an EDFA in an optical link using a single LPG was reported. The work was supported by theoretical simulation and experimental results. The applied methodology is based on the acousto-optic effect in fiber diffraction gratings and the LPG resonance peak is adjusted through the setting of the PZT load. A flattening of the EDFA gain profile by means of the in-line positioned filter with very fine control of the PZT load is achieved. The power equalization of DWDM channels over a bandwidth of 32 nm in the C-band, in the presence of the LPG based acousto-optic filter and the EDFA, was found to be at maximum 0,3 dB even under operating conditions, where the addition and drop of channels was implemented. An experiment was performed using a 40 Gb/s NRZ signal and a BER lower than 10^{-9} was achieved for different channels, with a maximum power penalty of 0,84 dB relatively to the signal in the back-to-back situation. Since the device is based on a single LPG, it has the advantages of a simple and fine adjustment, fast time response and good mechanical stability and can be implemented in DWDM systems with very good performance.

8. A tunable mode coupler based on flexural acoustic waves was developed. Numerical results agree with the experimental data. The acousto-optic effect in TOF can be used for select the spatial fiber modes with high speed and accuracy. This device shows a great configurability, and a robustness response. This device can be used in conjugation with MM optical fibers to filer or multiplexing information in different spatial modes.

Further works:

Developments focused on the acousto-optic behavior in different gratings in polymer fiber (such as PSFBGs and LPGs) and different lengths for photonic applications, such as tunable notch filters or tunable cavities, need to be done. Also, the technique of exciting an optical fiber by acoustic waves during the process of PFBGs inscription can be applied and investigated.

The fast AO-ADM will be subject to improvements because a significant leakage of the drop signal was observed. Some improvements about it are in progress considering a suppression of the reflectivity close to 100 % and a significant increase of the transmission at the Bragg wavelength around 26 dB. Experiments when channels are added to the link already also are in progress. Moreover, the response time can be substantially improved by operating at higher frequencies. The device also will be evaluated in terms of performance using BER measurements and the eye diagrams analysis.

The acousto-optic tunable mode coupler will be a subject of improvement for its application in MM systems in C-band. The device will be integrated as a multiplexer in transmission systems and evaluated its performance using advanced modulation formats and bit rates available at Instituto de Telecomunicações. News tunable mode couplers will also be developed and based on tuning the properties of a LPG used for mode coupling.

Fabrication of Optical Notch Filters with Fine Parameter Control using RFBGs

Achievements:

It was demonstrated the possibility of using regeneration process in saturated Bragg gratings to create very controlled optical notch filters. During the regeneration process of saturated FBGs, a reflective notch filter is produced and its depth can be finely controlled as function of the regeneration process time. Depending on the application, FBG writing with specific lengths is possible to obtain different 3 dB notch filter bandwidths. The new method for fabrication of notch filters can be potentially used for optical monitoring or to attenuate specific bands in photonic, overcoming the limitations of existing approaches. This new method to obtain specific notch filters can be an option for several photonic and microwave-photonic applications.

Further works:

A detailed theoretical analysis about the effects that occurs in regeneration process in FBGs and optical notch formation need to be made for a better explanation of this effect in optical fibers to be given and discussed.

In conclusion, after its first demonstration in 1978, optical fiber grating technology continues to offer a broad range of challenges and opportunities, which will certainly be subject to exciting exploration in the coming years.

References

[Abang2012] A. Abang and D. J. Webb, "Demountable connection for polymer optical fiber grating sensors", Opt. Eng. 51, 080503 (2012).

[Abdi2009] O. Abdi, K. C. Wong, T. Hassan, K. J. Peters and M. J. Kowalsky, "Cleaving Of Solid Single Mode Polymer Optical Fiber For Strain Sensor Applications," Opt.Commun. 282, 856 (2009).

[Abe2004] I. Abe, H. J Kalinowski, O.Frazão, J. L. Santos, R. N. Nogueira and J. L Pinto, "Superimposed Bragg Gratings in High-Birefringence Fibre Optics: Three-Parameter Simultaneous Measurements" Meas. Sci. Technol. 15, 1453 (2004).

[Abrishamian2005] F. Abrishamian, S. Sato, M. Imai, "A New Method Of Solving Multimode Coupled Equations For Analysis Of Uniform And Non-Uniform Fiber Bragg Gratings And Its Application To Acoustically Induced Superstructure Modulation," Optical Review, 12, 467 (2005).

[Agrawal1994] G. P. Agrawal E S. Radic, "Phase-Shifted Fiber Bragg Gratings and Their Application for Wavelength Demultiplexing", IEEE Photon. Technol. Lett. 6, 995 (1994).

[Alberto2010] N. J. Alberto, C. A. F. Marques, J. L. Pinto, and R. N. Nogueira, "Three-parameter optical fiber sensor based on a tilted fiber Bragg grating," Appl. Opt. 49, 6085 (2010).

[Alberto2011] N. J. Alberto, "Sensores de Bragg para Bioaplicações", Universidade de Aveiro, PhD Thesis, Portugal (2011).

[Albuquerque2009] A. A. C. Albuquerque, "Cavidades de Fabry-Pérot com Redes de Bragg para Recuperação de Relógio", Universidade De Aveiro, Bachelors Thesis, Portugal, (2009).

[Alferness1986]   R. C. Alferness, C. H. Joyner, M. D. Divino, M. J. R. Martyak, L. L. Buhl, "Narrowband grating resonator filters in InGaAsP/InP waveguides", Applied Physics Letters 49, 125 (1986).

[Allsop2004]   T. Allsop, A. Gillooly, V. Mezentsev, T. E.-Gould, R. Neal, D. J. Webb, and I. Bennion, "Bending and Orientational Characteristics of Long Period Gratings Written in D-Shaped Optical Fiber", IEEE Trans. Instrum. Meas. 53, 130 (2004).

[Allsop2004a]   T. Allsop, T. Earthrowl, R. Reeves, D. J. Webb, I. Bennion, "The Interrogation And Multiplexing of Long Period Grating Curvature Sensors Using a Bragg Grating Based, Derivative Spectroscopy Technique," Meas. Sci. Technol. 15, 44 (2004).

[Allsop2004b]   T. Allsop, A. Gillooly, V. Mezentsev, T. Earthgrowl-Gould, R. Neal, D. J. Webb, I. Bennion, "Bending and Orientational Characteristics of Long Period Gratings Written in D-Shaped Optical Fiber," IEEE Transactions On Instrumentation and Measurement, 53, 130 (2004).

[Anderson1993]   D. Z. Anderson, "Production of in-Fiber Gratings Using a Diffractive Optical-Element" IEE Electron. Lett. 29, 566 (1993).

[Andre2004]   P. S. André, R. N. Nogueira, A. T. Teixeira, M. Lima, R. F. Rocha, J. L. Pinto, "Multi Wavelength Rational Harmonic Mode Locked Source For Polarization Division Multiplexing Based on a Reflective Semiconductor Optical Amplifier and Bragg Grating Written in a High Birefringent Fiber", Laser Physics Letters 1, 613 (2004).

[Archambault1993]   J. L. Archambault, L. R. Eekie and P. St. Russell, "100% Reflectivity Bragg Reflectors Produced In Optical Fibres By Single Excimer Laser Pulses", IEE Electron. Lett. 29, 453 (1993).

[Argyros2004]   A. Argyros, M. A. van Eijkelenborg, S. D. Jackson and R. P. Mildren, "A microstructured polymer fibre laser," Optics Letters, 29, 1882 (2004).

[Argyros2006]   A. Argyros, "Bragg Reflection and Bandgaps in Microstructured Optical Fibres", PhD thesis, University of Sydney, (2006).

[Argyros2013]   A. Argyros, "Microstructures in Polymer Fibres for Optical Fibres, THz Waveguides, and Fibre-Based Metamaterials", ISRN Optics - Hindawi Publishing Corporation, Article ID 785162, 1-22 (2013).

[Ashton2004]   B. Ashton, J. Canning, N. Groothoff, "Two-Point Source Interferometric Grating Writing", Applied Optics, 43, 3140 (2004).

[Aslund2000]   M. L. Åslund, and J. Canning, "Annealing Properties of Gratings Written Into UV-Presensitized Hydrogen-Out Diffused Optical Fiber", Optics Letters 25, 692 (2000).

[Aslund2010]   M. L. Åslund, N. Jovanovic, J. Canning, S. D. Jackson, G. D. Marshall, A. Fuerbach, and M. J. Withford, "Rapid Decay of Type-II Femtosecond Laser Inscribed Gratings Within Q-switched Yb3+-Doped Fiber Lasers", IEEE Photon. Technol. Lett. 22, 504 (2010).

[Atef2012a]   M. Atef, R. Swoboda, H. Zimmermann, "1.25 Gbit/s over 50 m step-index plastic optical fiber using a fully integrated optical receiver with an integrated equalizer", J. Lightwave Technol. 30, 118 (2012).

[Atef2012b]   M. Atef, R. Swoboda, H. Zimmermann, "Real-Time 1.25-Gb/s Transmission Over 50-m SI-POF Using a Green Laser Diode", IEEE Photon. Technol. Lett. 24, 1331 (2012).

[Bae2007]   J. K. Bae, D. Koh, S. H. Kim, N. Park, And S. B. Lee, "Automatic EDFA Gain Spectrum Equalization using LPFGs on Divided Coil Heaters", Optical Fiber Communication Conference and Exposition and The National Fiber Optic Engineers Conference – OFC, Anaheim, Jtha22 (2007).

[Ball1992]   G. A. Ball, W. H. Glenn, "Design of A Single-Mode Linear-Cavity Erbium Fiber Laser Utilizing Bragg Reflectors," J. Lightwave Technol. 10, 1338 (1992).

[Barmenkov2010] Y. O. Barmenkov, J. L. Cruz, A. Díez, and M. V. Andrés, "Electrically tunable photonic true-time-delay line," Optics Express 18, 17859 (2010).

[Barton2004]   G. Barton, M. A. van Eijkelenborg, G. Henry, M. C. J. Large and J. Zagari, "Fabrication of Microstructured Polymer Optical Fibres", Opt. Fiber Technol. 10, 325 (2004).

[Bates2001]   R. J. Bates, "Optical Switching and Networking Handbook". New York: McGraw-Hill, (2001).

[Bennion1996]   I. Bennion, J.A.R. Williams, L. Zhang, K. Sugden, and N. J. Doran, "UV-Written In-Fibre Bragg Gratings", Optical and Quantum Electronics, 28, 93 (1996).

[Berthold1995] J. W. Berthold, "Historical Review of Microbend Fiberoptic Sensors", J. Lightwave Technol. 13, 1193 (1995).

[Bertholds1988] A. Bertholds, R. Dändliker, "Determination of the Individual Strain-Optic Coefficients In Single-Mode Optical Fibres," J. Lightwave Technol. 6, 17 (1988).

[Betz2003]   D. C. Betz, G. Thursby, B. Culshaw, W. J. Staszewski, "Acousto-Ultrasonic Sensing Using Fiber Bragg Gratings," Smart Materials and Structures, 12, 122 (2003).

[Bhatia1996]   V. Bhatia and A. M. Vengsarkar, "Optical Fiber Long-Period Grating Sensors," Optics Letters, 21, 692 (1996).

[Bhatia1997]   V. Bhatia, D. K. Campbell, D. Sherr, T. G. D'alberto, N. A. Zabaronick, G. A. Teneyck, K. A. Murphy, and R. O. Claus, "Temperature-Insensitive and Strain Insensitive Long-Period Grating Sensors for Smart Structures," Opt. Eng. 36, 1872 (1997).

[Bhatia1999]   V. Bhatia, "Applications of Long-Period Gratings to Single and Multi-Parameter Sensing", Optics Express, 4, 457 (1999).

[Birks1994]   T. A. Birks, P. St. J. Russell, C. N. Pannell, "Low Power Acousto-Optic Device Based on a Tapered Single Mode Fiber," IEEE Photon. Technol. Lett. 6, 725 (1994).

[Birks1996]   T. A. Birks, P. St. J. Russel, D. O. Culverhouse, "The Acousto-Optic Effect in Single--Mode Fiber Tapers and Couplers" J. Lightwave Technol. 14, 2519 (1996).

[Blake1987]   J. N. Blake, B. Y. Kim, H. E. Engan, H. J. Shaw, "Analysis of Intermodal Coupling in a Two-Mode Fiber with Periodic Microbends," Optics Letters, 12, 281 (1987).

[Block2006]   U. L. Block, V. Dangui, M. J. F. Digonnet, and M. M. Fejer, "Origin of Apparent Resonance Mode Splitting in Bent Long-Period Fiber Gratings", J. Lightwave Technol. 24, 1027 (2006).

[Bock2007]   W. J. Bock, J. Chen, P. Mikulic, and T. Eftimov, "A Novel Fiber-Optic Tapered Long-Period Grating Sensor for Pressure Monitoring", Transactions on Instrumentation and Measurement, 56, 1176 (2007).

[Borelli1968] N. Borelli, and R. Miller, "Determination of the Individual Strain-Optic Coefficients of Glass by an Ultrasonic Technique," Applied Optics, 7, 745 (1968).

[Born1980]   M. Born, and E. Wolf, "Principles of Optics," Pergamon Press, Oxford, England, 6º Ed., Chap. 12, 593 (1980).

[Born1987]   M. Born and E. Wolf, "Principles of Optics". New York: Pergamon, Sec. 8.6.1, Eq. (8) (1987).

[Brillouin1922]   L. Brillouin, "Diffusion of light and x-rays by a transparent homogeneous body," Ann. Phys.17, 88 (1922).

[Butov2006]   O. V. Butov, E. M. Dianov and K. M. Golant, "Nitrogen-Doped Silica Core Fibres for Bragg Grating Sensors Operating at Elevated Temperatures," Meas. Sci. Technol. 17, 975 (2006).

[Caldas2011]   P. S. Caldas, "Fiber Optic Sensing Evanescent Field Interaction", Universidade do Porto, PhD Thesis, Portugal (2011).

[Canning1994]   J. Canning, and M. G. Sceats, "Pi-phase shifted periodic distributed structures in optical fibres by UV post-processing", IEE Electron. Lett. 30, 1344 (1994).

[Canning2005]   J.Canning, H.-J. Deyerl, and M. Kristensen, "Precision Phase- Shifting Applied to Fibre Bragg Gratings," Optics Communications, 244, 187 (2005).

[Canning2006]   J. Canning, "Fibre Lasers and Related Technologies", Opt. and Las. in Eng. 44, 647 (2006).

[Canning2008a]   J. Canning, "Fibre Gratings and Devices for Sensors and Lasers", Lasers and Phot. Rev. 2, 275 (2008).

[Canning2008b]   J. Canning, S. Bandyopadhyay, M. Stevenson, and K. Cook, "Fiber Bragg Grating Sensor for High Temperature Application", ACOFT/OECC (2008).

[Canning2010]   J. Canning, S. Bandyopadhyay, P. Biswas, M. Aslund, M. Stevenson, and K. Cook, "Regenerated Fibre Bragg Gratings," in Frontiers in Guided Wave Optics and Optoelectronics, Intech, 363–384 (2010).

[Canning2013]   K. Chen, J. Canning, K. Cook, Q. Q. Wang, T. Chen, M. Li, R. Chen, and A. Yang, "Regenerated distributed Bragg reflector fiber lasers for high-temperature operation", Optics Letters, 38, 2490 (2013).

[Capmany2006]   J. Capmany, B. Ortega and D. Pastor, "A Tutorial on Microwave Photonic Filters", J. Lightwave Technol. 24, 201 (2006).

[Cardenas2009]   G. A. C.-Sevilla, D. M.-Hernandez, I. T. -Gomez, and A. M.-Rios, "Mechanically Induced Long-Period Fiber Gratings on Tapered Fibers", Optics Communications, 282, 2823 (2009).

[Cardozo2007]   J. C. Cardozo Da Silva, C. Martelli, H. J. Kalinowski, E. Penner, J. Canning and N. Groothoff, "Dynamic Analysis and Temperature Measurements of Concrete Cantilever beam using Fibre Bragg Gratings", Opt. and Las. in Eng. 45, 88 (2007).

[Carroll2007]   K. E. Carroll, C. Zhang, D. J. Webb, K. Kalli, A. Argyros, and M. C. Large, "Thermal response of Bragg gratings in PMMA microstructured optical fibers," Optics Express, 15, 8844 (2007).

[Castro2004]   J. M. Castro, D. F. Geraghty, B.R. West, and S.Honkanen, "Fabrication and Comprehensive Modeling of Ion-Exchanged Bragg Optical Add-Drop Multiplexers," Appl. Opt. 43, 6166 (2004).

[Chen1999]   Z. Chen, K. S. Chiang, M. N. Ng, Y. M. Ke, H. Chan, "Bent Long Period Fiber Gratings for Sensor Applications," Proceedings SPIE, Advanced Photonic Sensors and Applications, 3897, 94 (1999).

[Chen2004]   K. Chen, Q.Q. Sheng, and X.Y. Dong, "Band-Rejection and Bandpass Filters Based on Mechanically Induced Long-Period Fiber Gratings", Microwave and Optical Tech. Letters, 42, 15 (2004).

[Chen2004a]   T. C. Chen, M. Y. Fu, "Acoustic-Induced Tunable Wavelength in a Tilted Fiber Bragg Grating," Japanese Journal of Applied Physics, 43, L200 (2004).

[Chen2011]   T. Chen, R. Chen, C. Jewart, B. Zhang, K. Cook, J. Canning, and K. P. Chen, "Regenerated gratings in air-hole microstructured fibers for high-temperature pressure sensing," Optics Letters, 36, 3542 (2011).

[Chiang2000]   K. S. Chiang, Y. Liu, M. N. Ng, X. Dong, "Analysis of Etched Long-Period Fibre Grating and Its Response to External Refractive Index," IEE Electron. Lett. 36, 966 (2000).

[Cho2002]   J. Y. Cho, and K. S. Lee, "A Birefringence Compensation Method for Mechanically Induced Long-Period Fiber Gratings", Optics Communications, 213, 281 (2002).

[Chun2005]   Y. Chun, W. Yong, and X. C.-Qing "A Novel Method to Measure Modal Power Distribution in Multimode Fibers Using Tilted Fiber Bragg Gratings", IEEE Photon. Technol. Lett. 17, 2146 (2005).

[Cole1995]   M. J. Cole, W. H. Loh, R. I. Laming, M. N. Zervas, and S. Barcelos, "Moving Fibre/Phase Mask-Scanning Beam Technique for Enhanced Flexibility in Producing Fiber Gratings with Uniform Phase Mask". IEE Electron. Lett. 31, 1488 (1995).

[Curatu2002]   G. Curatu, S. Larochelle, C. Paré, and E. P. A. Bélanger, "Antisymmetric Pulse Generation Using Phase-Shifted Fibre Bragg Grating", IEE Electron. Lett. 38, 307 (2002).

[Daum2001]   W. Daum, J. Krauser, P. Zamzow, and O. Ziemann, POF Polymer Optical Fibers for Data Communication (Springer-Verlag, 2001).

[Debye1932]   F. S. P. Debye, "On the scattering of light by supersonic waves," Proc. Nat. Acad. Sci. USA, 6, 409 (1932).

[Delgado2006]   M. Delgado-Pinar, D. Zalvidea, A. Díez, P. P.-Millán, and M. V. Andrés, "Q-Switching of An All-Fiber Laser by Acousto-Optic Modulation of a Fiber Bragg Grating," Optics Express, 14, 1106 (2006).

[Delgado2007]   M. Delgado-Pinar, A. Díez, P. P.-Millán, and M. V. Andrés,, "Single frequency active Q-switched distributed fiber lasers using acoustical waves", Applied Physics Letters, 90, 171110 (2007).

[Diez2003]   A. Diez, M. Delgado-Pinar, J. Mora, J. L. Cruz, and M. V. Andrés, "Dynamic Fiber-Optic Add-Drop Multiplexer using Bragg Gratings and Acousto-Optic-Induced Coupling", IEEE Photon. Technol. Lett. 15, 84 (2003).

[Dimmick2000]   T. Dimmick, G. Kakarantzas, T. A. Birks, and P. St. J. Russell, "Narrow-Band Acousto-Optic Tunable Filter Fabricated from Highly Uniform Tapered Optical Fiber," Optical Fiber Communication Conference, OSA Technical Digest Series, (Optical Society Of America), Paper Fb4 (2000).

[Dobb2005]   H. Dobb, D. J. Webb, K. Kalli, A. Argyros, M. C. J. Large, and M. A. Van Eijkelenborg, "Continuous Wave Ultraviolet Light-Induced Fiber Bragg Gratings in Few- and Single-Mode Microstructured Polymer Optical Fibers," Optics Letters, 30, 3296 (2005).

[Doerr2008]   C. R. Doerr, S. Chandrasekhar, and L. L. Buhl, "Tunable Optical Dispersion Compensator with Increased Bandwidth via Connection of a Mach–Zehnder Interferometer to an Arrayed-Waveguide Grating," IEEE Photon. Technol. Lett. 20, 560 (2008).

[Drummond2011]   M. V. Drummond, C. A. F. Marques, P. Monteiro, R. N. Nogueira, "Photonic Instantaneous Frequency Measurement System Using Complementary Modulation", IEEE Photon. Technol. Lett. 23, 143 (2011).

[Dung1998]   J.-C. Dung, S. Chi, and S. Wen, "Gain Flattening of Erbium-Doped Fiber Amplifier Using Fiber Bragg Gratings," IEE Electron. Lett. 34, 555 (1998).

[Dupuis2007]   A. Dupuis, N. Guo, Y. Gao, N. Godbout, S. Lacroix, C. Dubois, and M. Skorobogatiy, "Prospective for biodegradable microstructured optical fibers," Optics Letters 32, 109 (2007).

[Eggleton1994]   B. J. Eggleton, P. A. Krug, L. Poladian E F. Ouellette, "Long Period Superstructure Bragg Gratings in Optical Fibres", Electron. Lett. 30, 1620 (1994).

[Eggleton2000a]   B. J. Eggleton, A. Ahuja, P. S. Westbrook, J. A. Rogers, P. Kuo, T. N. Nielsen, and B. Mikkelsen, "Integrated Tunable Fiber Gratings For Dispersion Management In High-Bit Rate Systems," J. Lightwave Technol. 18, 1418, (2000).

[Eggleton2000b]   B. J. Eggleton, P. S. Westbrook, C. A. White, C. Kerbage, R. S. Windeler and G. L. Burdge, "Cladding-Mode-Resonances in Air-Silica Microstructure Optical Fibers", J. Lightwave Technol. 18, 1084 (2000).

[Eijkelenborg2004]   M. A. van Eijkelenborg, W. Padden, and J. A. Besley "Mechanically Induced Long-Period Gratings in Microstructured Polymer Fibre", Optics Communications, 236, 75 (2004).

[Eijkelenborg2008]   M. A. van Eijkelenborg, A. Argyros, and S. G. L.-Saval, "Polycarbonate hollow-core microstructured optical fibre," Optics Letters 33, 2446 (2008).

[Elmore1985]   W. C. Elmore, and M. A. Heald "Physics Of Waves," Dover, New York, (1985).

[Emiliyanov2007]   G. Emiliyanov, J. B. Jensen, O. Bang, P. E. Hoiby, L. H. Pedersen, E. M. Kjaer, and L. Lindvold, "Localized biosensing with topas microstructured polymer optical fiber," Optics Letters, 32, 460 (2007).

[Engan1986]   H. E. Engan, B. Y. Kim, J. N. Blake, and H. J. Shaw, "Optical Frequency Shifting In Two-Mode Optical Fibers By Flexural Acoustic Waves," IEEE Ultrasonic Symposium, 435 (1986).

[Engan1988]   H. E. Engan, B. Y. Kim, J. N. Blake, and H. J. Shaw, "Propagation and Optical Interaction of Guided Acoustic Waves in Two-Mode Optical Fibers," J. Lightwave Technol. 6, 428 (1988).

[Ennser1998]   K. Ennser, M. N. Zervas and R. I. Laming, "Optimization of Apodized Linearly Chirped Fiber Grating for Optical Communications" IEEE Journal of Quantum Electronics, 34, 770 (1998).

[Epaarachchi2009]   J. Epaarachchi, J. Canning, and M. Stevenson "The Response of Embedded NIR (830nm) FBG sensors in Glass Fibre Composites under Fatigue Loading", J. of Composite Materials, 44, 809 (2009).

[Erdogan1996]   T. Erdogan, and J. E. Sipe, "Tilted Fiber Phase Gratings," Opt. Soc. Am. A13, 296 (1996).

[Erdogan1997a]   T. Erdogan, "Fiber Grating Spectra", J. Lightwave Technol. 15, 1277(1997).

[Erdogan1997b]   T. Erdogan, "Cladding-Mode Resonances in Short- and Long- Period Fiber Grating Filters," Opt. Soc. Am. A14, 1760 (1997).

[Feced1999]   R. Feced, M. Zervas, and M. Muriel, "An Efficient Inverse Scattering Algorithm for The Design of Nonuniform Fiber Bragg Gratings," IEEE J. Sel. Top. Quantum Electron. 35, 1105 (1999).

[Feced1999a]   R. Feced, C. Alegria, M. N. Zervas, and R. I. Laming, "Acoustooptic attenuation filters based on tapered optical fibers," J. Lightwave Technol. 5, 1278 (1999).

[Fermann1995]   M. E. Fermann, K. Sugden, and I. Bennion, "High-Power Soliton Fiber Laser Based on Pulse Width Control with Chirped Fiber Bragg Gratings," Optics Letters, 20, 172 (1995).

[Fernandes2012]   G. M. Fernandes, M. Niehus, C. A. F. Marques, R. N. Nogueira, and A. Pinto, "Acousto-Optic Tunable Mode Coupler," Optical Fiber Communication Conference and Exposition and The National Fiber Optic Engineers Conference – OFC, Anaheim, paper JTh2A.2. (2012).

[Fokine2002]   M. Fokine, "Formation of Thermally Stable Chemical Composition Gratings in Optical Fibers", J. Opt. Soc. Am. B 19, 1759 (2002).

[Fujimaki2000]   M. Fujimaki, Y. Ohki, J. L. Brebner, and S. Roorda, "Fabrication of Long-Period Optical Fiber Gratings by use of Ion Implantation", Optics Letters, 25, 88 (2000).

[Gao2006]   Y. Gao, N. Guo, B. Gauvreau, M. Rajabian, O. Skorobogata, E. Pone, O. Zabeida, L. Martinu, C. Dubois, and M. Skorobogatiy, "Consecutive Solvent Evaporation and Co-Rolling Techniques for Polymer Multilayer Hollow Fiber Preform Fabrication," J. Mat. Res. 21, 2246 (2006).

[Garrett1998]   L. D. Garrett, A. H. Gnauck, Forgherieri, and E D. Scarano, "8 X 20 Gb/S-315 Km- 480 Km WDMTransmission over Conventional Fiber Using Multiple Broad-Band Fiber Gratings", Optical Fiber Communication Conference and Exposition and The National Fiber Optic Engineers Conference – OFC, PDP18 (1998).

[Ghatak1998]   A. Ghatak and K. Thyagarajan, "Introduction to Fiber Optics". Cambridge University Press (1998).

[Ghiringhelli2001]   F. Ghiringhelli, C. Alegria, and M. N. Zervas, "Effect of Phase Shift Perturbations and Complex Local Time Delay in Fiber Bragg Gratings," In

Bragg Gratings, Photosensitivity, and Poling in Glass Waveguides - BGPP, Paper Bwa3. 269 (2001).

[Giles1997] C. R. Giles, "Lightwave Applications of Fiber Bragg Gratings" J. Lightwave Technol. 15, 1391 (1997).

[Giruts1991] E. L. Giruts, and S. M. Kopylov, "Emission Spectra of Dye Lasers Which Use Acoustooptic Tuning" Journal of Applied Spectroscopy, 54, 454 (1991).

[Gottlieb1983] M. S. Gottlieb, C. L. M. Ireland, and J. M. Ley, "Electro-Optic and Acousto-Optic Scanning and Deflection," Marcel Dekker, Inc., New York, (1983).

[Gottlieb1992] M. S. Gottlieb, N. T. Melamed, J. B. Goodell, "Rapid Spectral Analysis Using Acousto-Optical Devices," Proceedings of SPIE, 1704, 168 (1992).

[Grobnic2006] D. Grobnic, C.W. Smelser, S.J. Mihailov, and R. B. Walker, "Long Term Thermal Stability Tests at 1000°C of Silica Fibre Bragg Gratings Made with Ultrafast Laser Radiation," Meas. Sci. Technol. 17, 1009 (2006).

[Groothoff 2004] N. Groothoff, and J. Canning, "Enhanced Type IIA Gratings for High-Temperature Operation", Optics Letters, 29, 2360 (2004).

[Haakestad2006] M. W. Haakestad, and H. E. Engan, "Acoustooptic Properties of a Weakly Multimode Solid Core Photonic Crystal Fiber," J. Lightwave Technol. 24, 838 (2006).

[Harumoto2002] M. Harumoto, M. Shigehara, and H. Suganuma, "Gain-Flattening Filter Using Long-Period Fiber Gratings," J. Lightwave Technol. 20, 1027 (2002).

[Hassan1998] B. Hassan and E. Hinton, "A Review of Homogenization and Topology Optimization I-Homogenization Theory for Media with Periodic Structure," Comput. Struct. 69, 707 (1998).

[Hill1974] K. O. Hill, "Aperiodic distributed-parameter waveguides for integrated optics", Applied Physics Letters, 32, 647 (1974).

[Hill1978] K. O. Hill, Y. Fujii, D. C. Johnson, and B. S. Kawasaki, "Photosensitivity in Optical Fibre Waveguides: Application to Reflection Filter Fabrication," Applied Physics Letters, 32, 647 (1978).

[Hill1990] K. O. Hill, B., Malo, K.A. Vineberg, F. Bilodeau, D.C., Johnson and I. Skinner, "Efficient Mode Conversion In Telecommunication Fiber Using Externally Written Gratings", IEE Electron. Lett. 26, 1270 (1990).

[Hill1993]   K. O. Hill, B. Malo, F. Bilodeau, D.C. Johnson, and J. Albert, "Bragg Gratings Fabricated in Monomode Photosensitive Optical Fiber By UV Exposure through a Phase Mask". Applied Physics Letters, 62, 1035 (1993).

[Hill1993a]   K. O. Hill, B. Malo, F. Bilodeau, and D. C. Johnson, "Photosensitivity in Optical Fibers," Annual Review of Materials Research, 23, 125 (1993).

[Hill1997]   K. O. Hill, and G. Meltz, "Fiber Bragg Grating Technology Fundamentals and Overview," J. Lightwave Technol. 15, 1263 (1997).

[Hocker1979]   G. B. Hocker, "Fiber-Optic Sensing of Pressure and Temperature," Applied Optics, 18, 1445 (1979).

[Huang2000]   D. W. Huang, W. F. Liu, C. W. Wu, and C. C. Yang, "Reflectivity-Tunable Fiber Bragg Grating Reflectors," IEEE Photon. Technol. Lett. 12, 176 (2000).

[Huber1991]   D. R. Huber, "1.5 nm Narrow Bandwidth In-Fiber Gratings", Proc. of IEEE LEOS Annual Meeting, Paper Oe3.1 (1991).

[Hughes1987]   T. J. R. Hughes, "The Finite Element Method – Linear Static and Dynamic Finite Element Analysis," Englewood Cliffs, Nj, Prentice-Hall (1987).

[Humbert2002]   G. Humbert and A. Malki, "Electric-Arc-Induced Gratings in non-hydrogenated Fibres: Fabrication and High-Temperature Characterizations", Journal of Optics A-Pure and Applied Optics, 4, 194 (2002).

[Ip2013]   E. Ip, M. Li, Y. Huang, A. Tanaka, E. Mateo, W. Wood, J. Hu, Y. Yano, and K. Koreshkov, "146λx6x19-Gbaud Wavelength-and Mode-Division Multiplexed Transmission over 10x50-km Spans of Few-Mode Fiber with a Gain-Equalized Few-Mode EDFA" Optical Fiber Communication Conference and Exposition and The National Fiber Optic Engineers Conference – OFC, paper PDP.5.A (2013).

[Italia2005]   V. Italia, M. Pisco, S. Campopiano, A. Cusano, and A. Cutolo, "Chirped Fiber Bragg Gratings for Electrically Tunable Delay Lines," J. Sel. Top. Quantum Electron. 11, 408 (2005).

[Jaffe1958]   H. Jaffe, "Piezoelectric Ceramics," Journal of the American Ceramic Society, 41, 494 (1958).

[James1996]   S. W. James, M. L. Dockney, and R. P. Tatam, "Simultaneous Independent Temperature and Strain Measurement Using In-Fibre Bragg Grating Sensors," IEE Electron. Lett. 32, 1133 (1996).

[James2003]   S. W. James, and R. P. Tatam, "Optical Fibre Long-Period Grating Sensors: Characteristics and Application," Meas. Sci. Technol. 14, 49 (2003).

[Jayarman1993]   V. Jayaraman, Z.-M. Chuang, and L.A. Coldren, "Theory, design, and performance of extended tuning range semiconductor lasers with sampled gratings," IEEE J. Sel. Top. Quantum Electron. 29, 1824 (1993).

[Jiang2002]   C. Jiang, M. G. Kuzyk, J.-L. Ding, W. E. Johns, and D. J. Welker, "Fabrication and mechanical behavior of dye-doped polymer optical fiber," Journal of Applied Physics 92, 4 (2002).

[Johnson2010]   I. P. Johnson, D. J. Webb, K. Kalli, M. C. J. Large, and A. Argyros, "Multiplexed FBG sensor recorded in multimode microstructured polymer optical fibre", Proc. SPIE 7714, 77140D (2010).

[Jung2008]   Y. Jung, G. Brambilla, and D. J. Richardson, "Broadband single-mode operation of standard optical fibers by using a sub-wavelength optical wire filter," Optics Express 19, 14661 (2008).

[Jung2013]   Y. Jung, R. Chen, R. Ismaeel, G. Brambilla, S.-U. Alam, I. P. Giles, and D. J. Richardson, "Dual mode fused optical fiber couplers suitable for mode division multiplexed transmission," Optics Express 21, 24326 (2013).

[Kamikawachi2007] R. C. Kamikawachi "Dispositivos Sensores em Fibra para uso em Refratometria," Federal University Of Technology – Paraná, PhD Thesis, Brazil (2007).

[Kashyap1990]   R. Kashyap, J. R. Armitage, R. W. Wyatt, S. T. Davey, and D. L. Williams, "All-Fibre Narrow-Band Reflection Gratings at 1550 nm," IEE Electron. Lett. 26, 730 (1990).

[Kashyap1994]   R. Kashyap, P.F. McKee, and D. Armes, "UV written reflection grating structures in photosensitive optical fibres using phase-shifted masks", IEE Electron. Lett. 30, 1977 (1994).

[Kashyap1998]   R. Kashyap, "Assessment of Tuning the Wavelength of Chirped and Unchirped Fibre Bragg Grating with Single Phase-Masks" IEE Electron. Lett. 34, 2025 (1998).

[Kashyap1999]   R. Kashyap, "Fiber Bragg Gratings" Academic Press (1999).

[Kashyap2010]   R. Kashyap, "Fiber Bragg Gratings", 2nd Ed, Optics and Photonics Series, Academic Press, Boston (2010).

[Kawasaki1978]   B. S. Kawasaki, K. O. Hill, D. C. Johnson, and Y. Fujii, "Narrow-Band Bragg Reflectors in Optical Fibers," Optics Letters, 3, 66 (1978).

[Kawashima2006]   H. Kawashima, N. Matsubara, and K. Nara, "Tunable Dispersion Compensator Using PLC Type Optical Transversal Filter," Furukawa Rev. 29, 13 (2006).

[Kewitsch1998]   A. S. Kewitsch, G. A. Rakuljic, P. A. Willems, and A. Yariv, "All-fiber zero-insertion-loss add-drop filter for wavelength-division multiplexing," Optics Letters, 23, 106 (1998).

[Kibler2004]   T. Kibler, S. Poferl, G. Böck, H.-P. Huber, and E. Zeeb, "Optical data buses for automotive applications," J. Lightwave Technol. 22, 2184 (2004).

[Kim1986]   B. Y. Kim, J. N. Blake, H. E. Engan, and H. J. Shaw, "All-fiber acousto-optic frequency shifter" Optics Letters, 11, 389 (1986).

[Kim1998]   H. S. Kim, S. H. Yun, H. K. Kim, N. Park, and B.Y. Kim, "Actively Gain-Flattened Erbium-Doped Fiber Amplifier over 35 nm By Using All-Fiber Acousto-Optic Tunable Filters," IEEE Photon. Technol. Lett. 10, 790 (1998).

[Kogelnick1990]   H. Kogelnick, "Theory of Optical Waveguides" Guided-Wave Optoelect., T. Tamir, Ed. New York: Springer-Verlag, (1990).

[Kogelnik1972]   H. Kogelnik, and C. W. Shank, "Coupled Wave Theory of Distributed Feedback Lasers," Appl. Phys., 43, 2327 (1972).

[Kogelnik1976]   H. Kogelnik, "Filter Response of Nonuniform Almost-Periodic Structures," Bell Sys. Tech. J. 55, 109 (1976).

[Koike2004]   S. Kondo, T. Ishigure, and Y. Koike, "Fabrication of polymer photonic crystal fiber," In Proc. of the Micro-Optics Conference, 10, B–7 (2004).

[Koike2009]   Y. Koike, M. Asai, "The future of plastic optical fiber", NPG Asia Mat. 1, 22 (2009).

[Kringlebotn1994]   J. T. Kringlebotn, J. L. Archambault, L. Reekie, and D. N. Payne, "Er^{3+}:Yb^{3+}-Co-Doped Fiber Distributed-Feedback Laser," Optics Letters, 19, 2101 (1994).

[Kuhlmey2002]   B. Kuhlmey, R. C. Mcphedran, and C. M. De Sterke "Modal Cutoff in Microstructured Optical Fibers," Optics Letters 27, 168 (2002).

[Kumar2005]   N. Kumar, M. R. Shenoy, and B. P. Pal, "A Standard Fiber-Based Loop Mirror as a Gain-Flattening Filter for Erbium-Doped Fiber Amplifiers," IEEE Photon. Technol. Lett. 17, 2056 (2005).

[Laffont2001]   G. Laffont and P. Ferdinand, "Tilted Short-Period Fibre-Bragg-Grating Induced Coupling to Cladding Modes for Accurate Refractometry", Measurements, 12, 765 (2001).

[Laming1997]   R. I. Laming, M. Ibsen, M. Durkin, M. J. Cole, M. N. Zervas, K. E. Ennser, and E V. Gusmeroli, "Dispersion Compensation Gratings", Proc. of Bragg Gratings, Photosensivity, and Poling in Glass Fibers And Waveguides: Applications and Fundamentals, 17, Paper Btua7, 271 (1997).

[Large2004]   M. C. Large, S. Ponrathnam, A. Argyros, N. S. Pujari, and F. Cox, "Solution doping of microstructured polymer optical fibres," Optics Express 12, 1966 (2004).

[Large2011]   M. C. Large, R. Lwin, A. Argyros, and S. G. L.-Saval, "Low loss microstructured Polymer Optical Fibre (mPOF)," Optical Fiber Communication Conference and Exposition and The National Fiber Optic Engineers Conference – OFC, paper OWS6 (2011).

[Large2012]   C. J. Large, "Low loss and temperature stable microstructured polymer optical fibers," J. Lightwave Technol. 30, 192 (2012).

[Law2006]   S. H. Law, M. A. van Eijkelenborg, G. W. Barton, C. Yan, R. Lwin, and J. Gan, "Cleaved End-Face Quality of Microstructured Polymer Optical Fibres," Optics Communications, 265, 513 (2006).

[Lee2000]   J. Y. Lee, H.-W. Lee, and J. W. Hahn, "Complex Traversal Time for Optical Pulse Transmission in a Fabry–Perot Cavity," J. Opt. Soc. Am. B 17, 401 (2000).

[Lee2007]   Y. J. Lee, J. Bae, K. Lee, J-M. Jeong, And S. B. Lee, "Tunable Dispersion and Dispersion Slope Compensator Using Strain-Chirped Fiber Bragg Grating" IEEE Photon. Technol. Lett. 19, 762 (2007).

[Lethien2005]   C. Lethien, C. Loyez, and J.-P. Vilcot, "Potentials of radio over multimode fiber systems for the in-buildings coverage of mobile and wireless LAN applications," IEEE Photon. Technol. Lett. 17, 2793 (2005).

[Lethien2011]   C. Lethien, C. Loyez, J. Vilcot, N. Rolland, and P. Rolland, "Exploit the bandwidth capacities of the perfluorinated graded index polymer optical fiber for multi-services distribution," Polymers, 3, 1006 (2011).

[Li2001]   S. Li, K. S. Chiang, And W. A. Gambling, "Gain Flattening of an Erbium-Doped Fiber Amplifier Using A High-Birefringence Fiber Loop Mirror", IEEE Photon. Technol. Lett. 13, 942 (2001).

[Li2002]   Q. Li, C. H. Lin, A. A. Au, and H. P. Lee, "Compact All-Fibre on-line Power Monitor Via Core-to- Cladding Mode Coupling", IEE Electron. Lett. 38, 1013 (2002).

[Li2008]   X. Li, X. Chen, G. Goldfarb, E. Mateo, I. Kim, F. Yaman, and G. Li, "Electronic Post-Compensation of WDM Transmission Impairments Using Coherent Detection and Digital Signal Processing", Optics Express, 16, 880 (2008).

[Li2010]   M. Li and J. P. Yao, "Experimental Demonstration of a Wideband Photonic Temporal Hilbert Transformer Based on a Single Fiber Bragg Grating," IEEE Photon. Technol. Lett. 22, 1559 (2010).

[Liaw2007]   S. -K. Liaw, W. Y. Jang, C.-J. Wang, and K. L. Hung, "Pump efficiency improvement of a C-band tunable fiber laser using optical circulator and tunable fiber gratings," Applied Optics, 46, 2280 (2007).

[Linder2009]   E. Linder, C. Chojetski, S. Brueckner, M. Becker, M. Rothhardt, and H. Bartelt, "Thermal Regeneration of Fibre Bragg Gratings in Photosensitive Fibres", Optics Express, 17, 12523 (2009).

[Lippman1881]   G. Lippman, "Principe de la Conservation de L'électricité," Annales de Chimie et de Physique, 24, 145 (1881).

[Litchinitser1997] N. M. Litchinitser, B. J.Eggleton and D. V. Patterson "Fiber Bragg Gratings for Dispersion Compensation in Transmission: Theoretical Model and Design Criteria for Nearly Ideal Pulse Recompression" J. Lightwave Technol. 15, 1303 (1997).

[Liu1997]   W. F. Liu, P. St. J. Russell, and L. Dong, "Acousto-Optic Superlattice Modulator Using a Fiber Bragg Grating," Optics Letters, 22, 1515 (1997).

[Liu1998]   W. F. Liu, P. St. J. Russell, L. Dong, "100% Efficient Narrow-Band Acoustooptic Tunable Reflector Using Fiber Bragg Grating," J. Lightwave Technol. 16, 1006 (1998).

[Liu1999]   Y. Liu, J.A.R. Williams, L. Zhang, and I. Bennion, "Phase Shifted and Cascaded Long-Period Fiber Gratings," Optics Communications 164, 27 (1999).

[Liu2000]   W. F. Liu, I. M. Liu, L. W. Chung, D. W. Huang, and C. C. Yang, "Acoustic-Induced Switching Of The Reflection Wavelength In A Fiber Bragg Grating," Optics Letters, 25, 1319 (2000).

[Liu2001]   H. Y. Liu, G. D. Peng, and P. L. Chu, "Thermal Tuning of Polymer Optical Fiber Bragg Gratings," IEEE Photon. Technol. Lett. 13, 824 (2001).

[Liu2002]   H. Y. Liu, G. D. Peng, and P. L. Chu, "Polymer Fiber Bragg Gratings with 28 DB Transmission Rejection," IEEE Photon. Technol. Lett. 14, 935 (2002).

[Liu2003]   H. B.Liu, H. Y. Liu, G. D. Peng, and P. L. Chu, "Strain and temperature sensor using a combination of polymer and silica fiber Bragg gratings", Optics Communications, 219, 139 (2003).

[Loh1996]   W. H. Loh, R. I. Laming, N. Robinson, A. Cavaciuti, Vaninetti, C. J. Anderson, M. N. Zervas and E M. J. Cole, "Dispersion Compensation Over Distances In Excess of 500 Km for 10 Gb/S Systems Using Chirped Fibre Gratings", IEEE Photon. Technol. Lett. 8, 944 (1996).

[López2005]   M. Silva-López, A. Fender, W. N. MacPherson, J. S. Barton, J. D. C. Jones, D. Zhao, H. Dobb, D. J. Webb, L. Zhang, and I. Bennion, "Strain and temperature sensitivity of a single-mode polymer optical fiber," Optics Letters, 30, 3129 (2005).

[Luo2011]   Y. Luo, B. Yan, M. Li, X. Zhang, W. Wu, Q. Zhang, and G. D. Peng, "Analysis of multimode POF gratings in stress and strain sensing applications," Opt. Fiber Technol. 17, 201 (2011).

[Madsen2004]   C. K. Madsen, M. Cappuzzo, E. Chen, L. Gomez, A. Griffin, E. J. Laskowski, L. Stulz, And A. W-Foy, "A Tunable Ultra-Narrowband Filter For Subcarrier Processing And Optical Monitoring," Optical Fiber Communication Conference and Exposition and The National Fiber Optic Engineers Conference – OFC, 431 (2004).

[Makino2012]   K. Makino, T. Kado, A. Inoue, and Y. Koike, "Low loss graded index polymer optical fiber with high stability under damp heat conditions", Optics Express 20, 12893 (2012).

[Makovejs2010]   S. Makovejs, D. S. Millar, D. Lavery, C. Behrens, R. I. Killey, S. J. Savory, and P. Bayvel, "Characterization of long-haul 112Gbit/s PDM-QAM-16 transmission with and without digital nonlinearity compensation," Optics Express 18, 12939 (2010).

[Malo1993]   B. Malo, K.O. Hill, F. Bilodeau, D.C. Johnson, and J. Albert, "Point-By-Point Fabrication Of Micro-Bragg Gratings In photosensitive Fiber Using Single Excimer Pulse Refractive-Index Modification Techniques" IEE Electron. Lett. 29, 1668 (1993).

[Marques2008]   C. A. F. Marques, "Gravação de Redes de Bragg avançadas em Fibra Óptica", Universidade De Aveiro, Master's thesis, Portugal 2008.

[Marques2011]   C. A. F. Marques, R. A. Oliveira. A. Pohl, J. Canning and R. N. Nogueira, "Dynamic Control of a Phase-Shifted FBG through Acousto-Optic Modulation", Optics Communications, 284, 1228 (2011).

[Marques2013]   C. A. F. Marques, L. Bilro, L. Khan, R. A. Oliveira, D. J. Webb, and R. N. Nogueira, "Acousto-Optic Effect in Microstructured Polymer Fiber Bragg Gratings: Simulation and Experimental Overview", J. Lightwave Technol. 31, 1551 (2013).

[Marshall2007]   G. D. Marshall, D. J. Kan, A. A. Asatryan, L. C. Botten, and M. J. Withford, "Transverse Coupling to the Core of a Photonic Crystal Fiber: The Photo-Inscription of Gratings," Optics Express 15, 7876 (2007).

[Martin1994]   J. Martin, and F. Ouellette, "Novel Writing Technique of Long and Highly Reflective In-Fibre Gratings", IEE Electron. Lett. 30, 811 (1994).

[Matsuhara1974]   M. Matsuhara, and K. O. Hill, "Optical-waveguide band-rejection filters: design", Applied Optics, 13, 2886 (1974).

[Meirovitch1986] L. Meirovitch, "Elements of Vibration Analysis," Singapore: Mcgraw-Hill, (1986).

[Melloni2000]   A. Melloni, M. Chinello, and E. M. Martinelli, "All-Optical Switching In Phase-Shifted Fiber Bragg Grating", IEEE Photon. Technol. Lett. 12, 42 (2000).

[Meltz1988]   G. Meltz, W. W. Morey, W. H. Glenn, and J. D. Farina, "In-Fiber Bragg-Grating Sensors," Optical Fiber Sensors Conference - OFS, Paper Thbb5-1, 63 (1988).

[Meltz1989]   G. Meltz, W. W. Morey, and W. H. Glenn, "Formation of Bragg Gratings in Optical Fibers by a Transverse Holographic Method," Optics Letters, 14, 823 (1989).

[Meltz1991]   G. Meltz, and W. W.Morey, "Bragg Grating Formation and Germanosilicate Fiber Photosensitivity," Proceedings of SPIE, 1516, 185 (1991).

[Miao2009]   Y. Miao, B. Liu, and Q. Zhao, "Refractive index sensor based on measuring the transmission power of tilted fiber Bragg grating", Opt. Fiber Technol. 15, 233 (2009).

[Mihailov2001]   S. Mihailov, R. Walker, T. Stocki and D. Johnson, "Fabrication of Tilted Fibre-Grating Polarization-Dependent Loss Equaliser", IEE Electron. Lett. 27, 284 (2001).

[Mihailov2002] S. Mihailov, R. Walker, P. Lu, H. Ding, X. Dai, C. Smelser and L. Chen, "UV-Induced PDL in Tilted Fibre Bragg Gratings: Application of a PDL Equaliser", IEE Proc. Optoelectronics, 49, 211 (2002).

[Mihailov2006] S. J. Mihailov, D. Grobnic, D. Huimin, C.W. Smelser, and B. Jes, "Femtosecond IR Laser Fabrication of Bragg Gratings in Photonic Crystal Fibers and Tapers", IEEE Photon. Technol. Lett. 18, 1837 (2006).

[Millar2011] D. S. Millar, D. Lavery, S. Makovejs, C. Behrens, B. C. Thomsen, P. Bayvel, and S. J. Savory, "Generation and long-haul transmission of polarization-switched QPSK at 42.9 Gb/s," Optics Express, 19, 9296 (2011) .

[Minardo2005] A. Minardo, A. Cusano, R. Bernini, L. Zeni, and M. Giordano, "Response of Fiber Bragg Gratings to Longitudinal Ultrasonic Waves," IEEE Transactions on Ultrasonics, Ferroelectrics And Frequency Control, 52, 304 (2005).

[Mishra2011] V. Mishra, N. Singh, U. Tiwari, and P. Kapur, "Fiber grating sensors in medicine: current and emerging applications", Sens. Actuator A - Phys. 167, 279 (2011).

[Mohanty2007] L. Mohanty, S. Tjin, D. Lie S. Panganiban, and P. Chow, "Fiber grating sensor for pressure ampping during total knee arthroplasty", Sens. Actuator A - Phys. 135, 323 (2007).

[Mokhtar2003] M. R. Mokhtar, C. S. Goh, S. A. Butler, S. Y. Set, K. Kikuchi, D. J. Richardson, and M. Ibsen, "Fibre Bragg Grating Compression-Tuned Over 110nm," IEE Electron. Lett. 39, 509 (2003).

[Möllers2009] I. Möllers, D. Jäger, R. Gaudino, A. Nocivelli, H. Kragl, O. Ziemann, N. Weber, A. M. J. Koonen, C. Lezzi, A. Bluschke, and S. Randel, "Plastic optical fiber technology for reliable home networking: overview and results of the EU project POF-ALL," IEEE Commun. Mag. 47, 58 (2009).

[Mortensen2003] N. A. Mortensen, J. R. Folkenberg, M. D. Nielsen, and K.P. Hansen, "Modal cutoff and the V parameter in photonic crystal fibers", Optics Letters, 28, 1879 (2003).

[Mortensen2005] N. A. Mortensen, "Semianalytical approach to short-wavelength dispersion and modal properties of photonic crystal fibers", Optics Letters, 30, 1455 (2005).

[Morton1993] P. A. Morton, V. Mizrahi, P. A. Andrekson, T. Tanbun-Ek, R. A. Logan, P. Lemaire, D. L. Coblentz, A. M. Sergent, K. W. Wecht, and P. F. Sciortino, Jr., "Mode-Locked Hybrid Soliton Pulse Source with Extremely Wide Operating Frequency Range," IEEE. Photon. Technol. Lett. 5, 28 (1993).

[Morton1994]   P. A. Morton, V. Mizrahi, T. Tanbun-Ek, R. A. Logan, P. J. Lemaire, H. M. Presby, T. Erdogan, S. L. Woodward, J. E. Sipe, M. R. Phillips, A. M. Sergent, and K. W. Wecht, "Stable Single Mode Hybrid Laser With High Power and Narrow Linewidth," Applied Physics Letters, 64, 2634 (1994).

[Neves2007]   P. T. Neves, and A. A. P. Pohl, "Time Analysis of the Wavelength Shift in Fiber Bragg Gratings", J. Lightwave Technol. 25, 3580 (2007).

[Neves2008a]   P. T. Neves Jr., "Análise Temporal do Espectro Óptico em Redes de Bragg em Fibra," Federal University Of Technology – Paraná, PhD Thesis, Brazil (2008a).

[Neves2008b]   P. T. Neves Jr., C. A. Bavastri, R. A. Oliveira, A. A. P. Pohl, "Combinação Dos Métodos dos Modos Assumidos E Matriz de Transferência em Dispositivos Ópticos Baseados em Redes de Bragg sob Deformação Longitudinal," Proceedings of The XXVI Simpósio Brasileiro de Telecomunicacões – Sbrt (2008).

[Niehus2010]   M. Niehus, G. G. M. Fernandes, A.N. Pinto, "Design of a Tunable Single Photon Interferometer Based on Modal Engineered Tapered Optical Fibers," in Proceedings of SPIE Photonics Europe, (2010).

[Nogueira2005]   R. N. Nogueira, "Redes de Bragg em Fibra Óptica", Universidade de Aveiro, PhD Thesis, Portugal (2005).

[Nogueira2006]   R.N. Nogueira, A. Teixeira, J. L. Pinto, R. F. Rocha, "Polarization assisted OCDMA using fiber Bragg gratings written in highly birefringent fibers", IEEE Photon. Technol. Lett. 18, 841 (2006).

[Nogueira2013]   R. N. Nogueira, L. Bilro, C.A.F. Marques, R. Oliveira, J. Heidarialamdarloo, "Optical Filtering in Plastic Optical Fibers," in 15th International Conference on Transparent Optical Networks (ICTON 2013), Th.B2.2. *Invited paper* (2013).

[Nykolak1997]   G. Nykolak, M. R. X. de Barros, T. N. Nielsen, and L. Eskildsen, "All-fiber add-drop wavelength router," IEEE Photon. Technol. Lett. 9, 605 (1997).

[Okamoto2006]   K. Okamoto, "Fundamental of Optical Waveguides", Elsevier Inc., second edition (2006).

[Oliveira2008a]   R. A. Oliveira, P. T. Neves Jr., J. T. Pereira, and A. A. P. Pohl, "Numerical Approach for Designing a Bragg Grating Acousto-Optics Modulator using Finite Element and Transfer Matrix Methods," Optics Communications, 281, 4899 (2008a).

[Oliveira2008b]   R. A. Oliveira, P. T. Neves Jr., J. T. Pereira, and A.A.P. Pohl, "Analysis of Mechanical Properties of a Photonic Crystal FBG Acousto-Optic Modulator," In Proc. AIP Conf. 1055, 117 (2008).

[Oliveira2009a]   R. A. Oliveira, C. A. F. Marques, R. N. Nogueira, J. Canning, and A. A. P. Pohl "Fast Acousto-Optic Add-Drop Based On Fiber Bragg Grating," LEOS Annual Meeting Conference Proceedings, 573 (2009a).

[Oliveira2009b]   R. A. Oliveira, C. A. F. Marques, C. E. N. Mayer, J. T. Pereira, R. N. Nogueira, and A. A. P. Pohl, "Single Device For Excitation of Both Flexural and Longitudinal Acousto-Optic Effects in Fiber Bragg Gratings," Proceedings of the Microwave and Optoelectronics Conference - IMOC, SBMO/IEEE International, 546 (2009b).

[Oliveira2010a]   R. A. Oliveira, P. T. Neves Jr., J. T. Pereira, J. Canning, and A. A. P. Pohl, "Vibration Mode Analysis of a Silica Horn Fiber Bragg Grating Device," Optics Communications, 283, 1296 (2010a).

[Oliveira2010b]   R. A. Oliveira, K. Cook, J. Canning and A. A. P. Pohl, "Complex Bragg Grating Writing Using Direct Modulation of the Optical Fiber With Flexural Waves" Applied Physics Letters, 97, 041101 (2010b).

[Ortega1999]   B. Ortega, J. Capmany, and J. L. Cruz, "Wavelength Division Multiplexing All-Fiber Hybrid Devices Based on Fabry-Perot's and Gratings," J. Lightwave Technol. 17, 1241 (1999).

[Othonos1999]   A. Othonos, and K. Kalli, "Fiber Bragg Gratings: Fundamentals and Applications In Telecommunications and Sensing". Artech House (1999).

[Ouellette1987]   F. Ouellette, "Dispersion Cancellation Using Linearly Chirped Bragg Grating Filters In Optical Waveguides," Optics Letters, 12, 847 (1987).

[Palaci2010]   J. Palací, P. Pérez-Millán, G. E. Villanueva, J. L. Cruz, M. V. Andrés, J. Martí, and B. Vidal, "Tunable Photonic Microwave Filter With Single Bandpass Based on a Phase-Shifted Fiber Bragg Grating," IEEE Photon. Technol. Lett. 22, 1467 (2010).

[Palai2001]   P. Palai, M.N. Satyanarayan, M. Das, K. Thyagarajan, and B.P. Pal, "Characterization and Simulation of Long Period Gratings Fabricated Using Electric Discharge", Optics Communications, 193, 181 (2001).

[Paldus1997]   B. A. Paldus, J. S. Harris Jr, J. Martin, J. Xie, and R. N. Zarec, "Laser Diode Cavity Ring-Down Spectroscopy Using Acousto-Optic Modulator Stabilization," Journal of Applied Physics, 82, 3199 (1997).

[Pan1995]   J. Y. Pan, M. A. Ali, A. F. Elrefaie, and R. E.Wagner, "Multiwavelength Fiber-Amplifier Cascades With Equalization Employing Mach-Zehnder Optical Filter," IEEE Photon. Technol. Lett. 7, 1501 (1995).

[Park2011]   K. -Y. Park, W. -S. Oh, J.-C. Choi, W. -Y. Choi, "Design of 250-Mb/s Low-Power Fiber Optic Transmitter and Receiver ICs for POF Applications," J. Semicond. Technol. Sci. 11, 221 (2011).

[Peng1999]   G. D. Peng, Z. Xiong, and P. L. Chu, "Photosensitivity and Gratings in Dye-Doped Polymer Optical Fibers," Opt. Fiber Technol. 5, 242 (1999).

[Perez2001]   I. Perez, H. L., Cui, and E. Udd, "Acoustic Emission Detection Using Fiber Bragg Gratings," Proceedings of SPIE (2001).

[Petrovic2007]   J. S. Petrovic, H. Dobb, V. K. Mezentsev, K. Kalli, D. J. Webb, and I. Bennion, "Sensitivity Of LPGs in PCFs Fabricated By an Electric Arc to Temperature, Strain, and External Refractive Index", J. Lightwave Technol. 25, 1306 (2007).

[Pi2010]   Pi, Physik Instrumente, "Piezoceramic Materials," Available in www.Piceramic.com Accessed In: December, (2010).

[Pisco2006]   M. Pisco, S. Campopiano, A. Cutolo, and A. Cusano, "Continuously Variable Optical Delay Line Based on a Chirped Fiber Bragg Grating," IEEE. Photon. Technol. Lett. 18, 2511 (2006).

[Plougmann2004] N. Plougmann and M. Kristensen, "Efficient Iterative Technique for Designing Bragg Gratings", Optics Letters, 29, 23 (2004).

[Pohl2013]   A. A. P. Pohl, R. A. Oliveira, R. E. Silva, C. A.F. Marques, P.T. Neves, K. Cook, J. Canning, and R. N. Nogueira, "Advances and new applications using the acousto-optic effect in optical fibers - review paper", Photonic Sensors, 3, 1 (2013).

[Polishuk2006]   P. Polishuk, "Plastic optical fibers branch out," IEEE Commun. Mag. 44, 140 (2006).

[Pratas2013]   A. Pratas, C. A. F. Marques, R. N. Nogueira, and P. S André, "OSNR Monitoring Using Fiber Bragg Grating in High Birefringent Optical Fibers", Microwave and Optical Tech. Letters, 55, 6 (2013).

[Primak1959]   W. Primak, and D. Post, "Photoelastic Constants of Vitreous Silica and its Elastic Coefficient of Refractive Index," Journal of Applied Physics, 30, 779 (1959).

[Probst1989]   C .B. Probst, A. Bjarklev, and S. B. Andreasen, "Experimental-Verification of Microbending Theory Using Mode-Coupling to Discrete Cladding Modes", J. Lightwave Technol. 7, 55 (1989).

[Prohaska1993]   J. D. Prohaska, E. Snitzer; S. Rishton and V. Boegli, "Magnification of mask fabricated fibre Bragg gratings", IEE Electron. Lett. 29, 1614 (1993).

[Provo2011]   R. Provo, S. G. Murdoch, J. D. Harvey, R. Lwin, S. G. Leon-Saval, and A. Argyros, "Error free 9. 5Gb/s transmission over 50m of multimode microstructured polymer optical fibres," in Proceedings of the Quantum Electronics Conference and Lasers and Electro-Optics Conference, 784 (2011).

[Rego2001]   G. Rego, O. Okhotnikov, E. Dianov, and V. Sulimov, "High-Temperature Stability of Long-Period Fiber Gratings Produced Using an Electric Arc", J. Lightwave Technol. 19, 1574 (2001).

[Rego2003]   G. Rego, J. R. A. Fernandes, J. L. Santos, H. M. Salgado, and P. V. S. Marques, "New Technique to Mechanically Induce Long-Period Fibre Gratings", Optics Communications, 220, 111 (2003).

[Rego2005]   G. Rego, P. V. S. Marques, J. L. Santos, and H. M. Salgado, "Arc-Induced Long-Period Gratings", Fiber and Integrated Optics, 24, 245 (2005).

[Rourke1994]   H. N. Rourke, S. R. Baker, K. C. Byron, R. S. Baulcomb, S. M. Ojha, and S. Clements, "Fabrication and Characterisation of Long, Narrowband Fibre Gratings By Phase Mask Scanning", IEE Electron. Lett. 30, 1341 (1994).

[Roy1987]   R. Roy, P. A. Schulz, and A. Walther, "Acousto-Optic Modulator as an Electronically Selectable Unidirectional Device in a Ring Laser," Optics Letters, 12, 672 (1987).

[Russell1986a]   P. St. J. Russell, "Bragg Resonance of Light in Optical Superlattices," Physical Review Letters, 56, 596 (1986a).

[Russell1986b]   P. St. J. Russell, "Optical Superlattices for Modulation and Deflection of Light," Journal of Applied Physics, 59, 3344 (1986b).

[Russell2000]   P. St. J. Russell, and W. F. Liu, "Acousto-Optic Superlattice Modulation in Fiber Bragg Gratings," Journal of the Optical Society of America A, 17, 1421 (2000).

[Saitoh2013]   F. Saitoh, K. Saitoh, and M. Koshiba, "A design method of a fiber-based mode multi/demultiplexer for mode-division multiplexing," Optics Express 18, 4709 (2010).

[Saruwatari2000]   M. Saruwatari, "All-Optical Signal Processing For Terabit/Second Optical Transmission," IEEE J. Sel. Top. Quantum Electron. 6, 1363 (2000).

[Saval2005]   S. G. L.-Saval, T. A. Birks, J. B.-Hawthorn, and M. Englund, "Multimode fiber devices with single-mode performance," Optics Letters, 30, 2545 (2005).

[Savin2000]   S. Savin, M. J. F. Digonnet, G. S. Kino, and H.J. Shaw, "Tunable Mechanically Induced Long-Period Fiber Gratings", Optics Letters, 25, 710 (2000).

[Shao2012]   Y. Shao, R. Cao, Y.-K. Huang, P. N. Ji, and S. Zhang, "112-Gb/s transmission over 100 m of graded-index POF for optical data center applications," Optical Fiber Communication Conference and Exposition and The National Fiber Optic Engineers Conference – OFC, Paper OW3J.5 (2012).

[Shi2012]   Y. Shi, C. Okonkwo, A. Argyros, S. G. Leon-Saval, R. Lwin, E. Tangdiongga, and A. M. J. Koonen, "7.3Gbit/s transmission over microstructured polymer optical fiber for in-home networks," IEEE Photon. Technol. Lett. 24, 1257 (2012).

[Shi2013]   Y. Shi, C. Okonkwo, D. Visani, E. Tangdiongga, and T. Koonen, "Distribution of Broadband Services Over 1-mm Core Diameter Plastic Optical Fiber for Point-to-Multipoint In-Home Networks", J. Lightwave Technol. 31, 874 (2013).

[Shima1997]   K. Shima, K. Himeno, T. Sakai, S. Okude, and A. Wada, "A Novel Temperature-Insensitive Long-Period Grating Using a Boron-Codoped Germanosilicate Core-Fibre," Optical Fiber Communication Conference and Exposition and The National Fiber Optic Engineers Conference – OFC, 347 (1997).

[Silva2007]   J. C. Cardozo da Silva, C. Martelli, H. J. Kalinowski, E. Penner, J. Canning and N. Groothoff, "Dynamic analysis and temperature measurements of concrete cantilever beam using fibre Bragg gratings", Opt. and Las. in Eng. 45, 88 (2007).

[Silva2013]   R. E. Silva, M. A. R. Franco, P. T. Neves, H. Bartelt, and A. A. P. Pohl, "Detailed analysis of the longitudinal acousto-optical resonances in a fiber Bragg modulator," Optics Express, 21, 6997 (2013).

[Skaar1998]   J. Skaar and K. Risvik, "A Genetic Algorithm for the Inverse Problem in Synthesis of Fiber Gratings," J.Lightw. Technol. 16, 1928 (1998).

[Skaar2001]   J. Skaar, L. Wang, and T. Erdogan, "On the Synthesis of Fiber Bragg Gratings By Layer Peeling," J. Quantum Electron, 37, 165 (2001).

[Sohn2004]   I. -B. Sohn, and J. -W. Song, "Gain Flattened and Improved Double-Pass Two-Stage EDFA Using Microbending Long-Period Fiber Gratings", Optics Communications, 236, 141 (2004).

[Srivastava2006]   A. Srivastava and Y. Sun, "Erbium Doped Fiber Amplifiers for Dynamic Optical Networks," In Guided Wave Optical Components and Devices: Basics, Technology and Applications, B. P. Pal., Ed. Academic Press, Chapter 12 Elsevier, Burlington, 181 (2006).

[Stefani2011]   A. Stefani, W. Yuan, C. Markos, and O. Bang, "Narrow bandwidth 850nm fiber Bragg gratings in few-mode polymer optical fibers," IEEE Photon. Technol. Lett. 23, 660 (2011).

 [Suo2008]   R. Suo, X. Chen, K. Zhou, L. Zhang and I. Bennion, "800nm WDM Interrogation System for Strain, Temperature, and Refractive Index Sensing Based on Tilted Fiber Bragg Grating", IEEE Sensors Journal, 8, 1273 (2008).

[Takahashi2013]   H. Takahashi, T. Tsuritani, E. L. T. de Gabory, T. Ito, W. R. Peng, K. Igarashi, K. Takeshima, Y. Kawaguchi, I. Morita, Y. Tsuchida, Y. Mimura, K. Maeda, T. Saito, K. Watanabe, K. Imamura, R. Sugizaki, and M. Suzuki, "First demonstration of MC-EDFA-repeatered SDM transmission of 40 x 128-Gbit/s PDM-QPSK signals per core over 6160-km 7-core MCF," Optics Express 21, 789 (2013).

[Teixeira2005]   A. L. Teixeira, R. N. Nogueira, P. S. André, M. Lima, and J. F. Rocha, "Optimized Wavelength Interleaved Radio-Over-Fibre System Based on Highly Birefringent Fiber Bragg Gratings" IEE Electron. Lett. 41, 30 (2005).

[Thurston1978]   R. N. Thurston, "Elastic Waves in Rods and Clad Rods," Journal of the Acoustical Society of America, 64 , 1 (1978).

[Tran2001]   A. V. Tran, W. D. Zhong, R. S. Tucker, and K. Song, "Reconfigurable multichannel optical add-drop multiplexers incorporating eight-port optical circulators and fiber Bragg gratings," IEEE Photon. Technol. Lett. 13, 1100 (2001).

[Tsuda2006]   H. Tsuda, "Ultrasound and Damage Detection in CFRP Using Fiber Bragg Grating Sensors," Composite Science and Technology, 66, 676 (2006).

[Valmir2010]   Valmir Oliveira, and H. J. Kalinowski, "Strongly Regenerated Bragg Gratings in Standard Single-Mode Fibres", Proc. SPIE 7653, 765312 (2010).

[Valmir2011]   Valmir Oliveira, M. Muller, and H. J. Kalinowski, "Bragg gratings in standard nonhydrogenated fibers for high-temperature sensing," Applied Optics, 50, E55 (2011).

[Valmir2012]   Valmir Oliveira "Redes de Bragg para medições em altas temperaturas," Federal University Of Technology – Paraná, PhD Thesis, Brazil (2012).

[Varshney2007]   R. K. Varshney, B. Nagaraju, A. Singh, B. P. Pal, and A. K. Kar, "Design and Realization of an All-Fiber Broadband Tunable Gain Equalization Filter for DWDM Signals," Optics Express, 15, 13519 (2007).

[Vasiliev2001]   V. V. Vasiliev and E. V. Morozov, "Mechanics and Analysis of Composite Materials" Amsterdam: Elsevier (2001).

[Vengsarkar1996] M. Vengsarkar, P. J. Lemaire, J. B. Judkins, V. Bhatia, T. Erdogan, and J. E. Sipe, "Long-Period Fiber Gratings as Band-Rejection Filter," J. Lightwave Technol. 14, 58 (1996).

[Wan2002]   X. Wan, and H. F. Taylor "Intrinsic Fiber Fabry-Perot Temperature Sensor with Fiber Bragg Grating Mirrors," Optics Letters, 27, 1388 (2002).

[Wang2010]   Y.P. Wang, "Review of Long Period Fiber Gratings Written By CO_2 Laser", Journal of Applied Physics, 108, 081101 (2010).

[Wang2011]   W. Wang, W. Liu, S. Wang, J. Shao, Z. Xu, and C. Guan, "Integrated Tunable Optical Dispersion Compensator Consisting of Arrayed Waveguide Grating with Air Trench Output Waveguides", J. Lightwave Technol. 29, 2039 (2011).

[Warner1972]   A. W. Warner, D. L. White, and W. A. Bonner, "Acousto-Optic Light Deflectors Using Optical Activity in Paratellurite," Journal of Applied Physics, 43, 4489 (1972).

[Wei2009]   L. Wei, W. Xue, Y. Chen, T. T. Alkeskjold, and A. Bjarklev, "Optically Fed Microwave True-Time Delay Based on a Compact Liquid-Crystal Photonic-Bandgap-Fiber Device," Optics Letters, 34, 2757 (2009).

[Xie1993]   W. X. Xie, P. Niay, P. Bernage, M. Douay, J. F. Bayon, T. Georges, M. Monerie, and B. Poumellec, "Experimental Evidence of Two Types of Photorefractive Effects Occurring during Photo Inscriptions of Bragg Gratings Within Germanosilicate Fibers", Optics Communications, 104, 185 (1993).

[Xiong1999]   Z. Xiong, G .D. Peng, B. Wu and P. L. Chu, "Highly Tunable Bragg Gratings in Single-Mode Polymer Optical Fibers." IEEE Photon. Technol. Lett. 11, 352 (1999).

[Xu1993]   M. G. Xu, L. Reekie, Y. T. Chow, and J. P. Dakin, "Optical in Fibre Grating High Pressure Sensor" IEE Electron. Lett. 29, 398 (1993).

[Xu1995]   M. G. Xu, L. Dong, L. Reekie, J. A. Tucknott, and J.L. Cruz, "Temperature-Independent Strain Sensor Using a Chirped Bragg Grating in a Tapered Optical Fibre," IEE Electron. Lett. 31, 823 (1995).

[Yamada1987]   M. Yamada, and K. Sakoda, "Analysis of Almost-Periodic Distributed Feedback Slab Waveguides via a Fundamental Matrix Approach," Applied Optics, 26, 3474 (1987).

[Yang2009]   H. Yang, S. C. Lee, E. Tangdiongga, F. Breyer, S. Randel, and T. Koonen, "40-Gb/s Transmission over 100m Graded-Index Plastic Optical Fiber Based on Discrete Multitone Modulation," in Optical Fiber Communication Conference and National Fiber Optic Engineers Conference - OFC, paper PDPD8 (2009).

[Yao2009]   J. Yao, "Microwave Photonics," J. Lightwave Technol. 27, 314 (2009).

[Yariv1973]   A. Yariv, "Coupled-Mode Theory for Guided-Wave Optics," IEEE Quantum. Electron. 9, 919 (1973).

[Yariv1984]   A. Yariv, and P. Yeh, "Optical Waves in Crystals," John Wiley & Sons, Inc, New York (1984).

[Yeom2007]   D. I. Yeom, P. Steinvurzel, B. J. Eggleton, S. D. Lim, and B. Y. Kin, "Tunable Acoustic Gratings in Solid-Core Photonic Bandgap Fiber," Optics Express, 15, 3513 (2007).

[Yokota2002]   M. Yokota, H. Oka, and T. Yoshino, "Mechanically Induced Long Period Fiber Grating and its Application for Distributed Sensing", Optical Fiber Sensors Conference - OFS, 135 (2002).

[Yoo2006]   S. J. B. Yoo, "Optical Packet and Burst Switching Technologies for the Future Photonic Internet," J. Lightwave Technol. 24, 4468 (2006).

[Yu2004]   J. M. Yu, X. M. Tao, and H. Y. Tam, "Fabrication of UV Sensitive Single-Mode Polymeric Optical Fiber," Optics Letters, 29, 156 (2004).

[Yuan2011a]   W. Yuan, L. Khan, D. J. Webb, K. Kalli, H. K. Rasmussen, A. Stefani, and O. Bang, "Humidity insensitive TOPAS polymer fiber Bragg grating sensor," Optics Express, 19, 19731 (2011).

[Yuan2011b]   W. Yuan, A. Stefani, M. Bache, T. Jacobsen, B. Rose, N. H. Rasmussen, F. Nielsen, S. Andresen, O. Sørensen, K. Hansen, and O. Bang "Improved Thermal and Strain Performance of Annealed Polymer Optical Fiber Bragg Gratings," Optics Communications, 28, 176 (2011).

[Yuan2012]   W. Yuan, A. Stefani, and O. Bang, "Tunable Polymer Fiber Bragg Grating (FBG) Inscription: Fabrication of Dual-FBG Temperature Compensated Polymer Optical Fiber Strain Sensors," IEEE Photon.Technol. Lett. 24, 401 (2012).

[Zemon1978]   S. A. Zemon, and M. L. Dakss, "Acoustoptic Modulator For Optical Fiber Waveguides," United States Patent, 4.068.191 (1978).

[Zhang1993]   Q. Zhang, D. A. Brown, L. Reinhart, T. F. Morse, J. Q. Wang, and X. Gang, "Tuning Bragg Wavelength By Writing Gratings on Prestrained Fibers" IEEE Photon. Technol. Lett. 6, 839 (1994).

[Zhang1999]   L. Zhang, Y. Liu, L. Everall, J.A.R. Williams, and I. Bennion, "Design and Realization of Long-Period Grating Devices in Conventional and High Birefringence Fibers and Their Novel Applications as Fiber - Optic Load Sensors", IEEE J. Sel. Top. Quantum Electron. 5, 1373 (1999).

[Zhang2007]   B. Zhang, and M. Kahriziet, "High Temperature Resistance Fiber Bragg Grating Temperature Sensor Fabrication", IEEE Sensor J. 7, 586 (2007).

[Zhang2009]   X. Zhang, S. Zheng, L. Liu, X. Liu, X. Zhang, and X. Jin, "Frequency Response Equalization Using Fiber Bragg Grating Tilted Filter in RoF Systems", J. Lightwave Technol. 27, 2465 (2009).

[Zhang2012]   W. Zhang, D. J. Webb, and G.-D. Peng, "Investigation into Time Response of Polymer Fiber Bragg Grating Based Humidity Sensors", J. Lightwave Technol. 30, 1090 (2012).

[Zhang2012a]   F. Z. Zhang and M. Xiao, "Synergetic Effects of Humidity and Temperature on PMMA Based Fiber Bragg Gratings," J. Lightwave Technol. 30, 841 (2012).

[Zhao2008]   X. Zhao, K. Hasebe, T. Sakaguchi, F. Koyama, C. J. Chasnain, N. Nishiyama, C. Caneau, and C.-E. Zah, "Tunable Optical Equalizer Using Diffraction Grating Filters", IEEE Photon. Technol. Lett. 20, 1590 (2008).

[Zhao2012]   C. Zhao, Y. Chen, S. Zhang, J. Li, F. Zhang, L. Zhu, and Z. Chen, "Experimental demonstration of 1.08 Tb/s PDM CO-SCFDM transmission over 3170 km SSMF," Optics Express, 20, 787 (2012).

[Zheng2005]   S. L. Zheng and X. M. Zhang, "Simultaneous Realization of Optical Carrier-Suppression and SSB Modulation in Wireless Fiber Links Using Fiber Bragg Grating," Microwave and Optical Tech. Letters, 46, 336 (2005).

[Zhu2008]   Y. Zhu, Z. He, and H. Du, "Detection of refractive index change with high sensitivity using long period gratings in photonic crystal fiber", Sens. Actuator B – Chem. 31, 265 (2008).

[Ziemann2008]   O. Ziemann, J. Krauser, P. E. Zamzow, and W. Daum, POF Handbook - Optical Short Range Transmission Systems, 2nd ed. Berlin, Heidelberg: Springer, (2008).

[Zienkiewicz2000] O. C. Zienkiewicz, and R. L. Taylor, "The Finite Element Method," The Basis, 1, Oxford, Butterworth-Heinemann (2000).